Study of the Micro Oven at the Linac3 Heavy Ion Source

Dissertation
zur Erlangung des Doktorgrades
an der Fakultät für Mathematik, Informatik und Naturwissenschaften
Fachbereich Physik
der Universität Hamburg

vorgelegt von
Toke Kay Thomas Kövener

Hamburg
2020

Gutachter der Dissertation:	PD Dr. Bernhard Schmidt Prof. Dr. Wolfgang Hillert
Zusammensetzung der Prüfungskommission:	Prof. Dr. Dieter Horns PD Dr. Bernhard Schmidt Prof. Dr. Wolfgang Hillert Prof. Dr. Grudrid Moortgat-Pick Prof. Dr. Eckhard Elsen
Vorsitzender der Prüfungskommission:	Prof. Dr. Dieter Horns
Datum der Disputation:	23.06.2020
Vorsitzender des Fach-Promotionsausschusses PHYSIK:	Prof. Dr. Günter Hans Walter Sigl
Leiter des Fachbereichs PHYSIK:	Prof. Dr. Wolfgang Hansen
Dekan der Fakultät MIN:	Prof. Dr. Heinrich Graener

Zusammenfassung

In der vorliegenden Arbeit wird eine Studie des Mikro-Ofens zur Verdampfung von Blei an der Schwerionenquelle GTS-LHC des Linearbeschleunigers Linac3 am CERN vorgestellt.

Die Heizleistung des Ofens ist einer der Hauptparameter für das Tuning an der Ionenquelle und bisher beruht die Wahl der Heizleistung ausschließlich auf der Erfahrung des Quellenoperateurs. Plötzliches Absinken des Ionenstroms der Ionenquelle verlangt außerdem häufig nicht planbare Variationen der Heizleistung. Zusätzlich konnte im Regelbetrieb nicht erreicht werden, dass die gesamte Bleifüllung im Tiegel des Ofens aufgebraucht wird, bevor eine Verringerung des Quellenstroms eine Neubefüllung nötig macht. Da die Neubefüllung eine Ausfallzeit für die Quelle darstellt, ist eine Verlängerung des Ofenbetriebs bis zum vollständigen Aufbrauchen der Bleifüllung wünschenswert.

Die Studie beinhaltet thermische und Gasflusssimulationen sowie Messungen an einem Teststand. In einer Reihe von Messungen wurde der Ofen in unterschiedlichen Bedingungen betrieben um sein Verhalten zu charakterisieren. Instabilitäten der Verdampfungsrate konnten so dokumentiert und Gründe für deren Auftreten gefunden werden. Außerdem wurde das Entstehen einer Blockade untersucht, die in ähnlicher Form auch an der Schwerionenquelle beobachtet wurde.

Durch Veränderungen des Ofenaufbaus konnten am Teststand sowohl die Verdampfungsrate stabilisiert, als auch die Entstehung der Blockade vollständig verhindert werden. Ohne das Auftreten der Blockade konnte der Ofen bis zur vollständigen Entleerung des Tiegels betrieben werden. Aus den Ergebnissen der Studie ergeben sich Vorschläge für eine Veränderung des Ofenaufbaus an der Schwerionenquelle von Linac3.

Abstract

This work presents a study of the micro oven that is used for the lead evaporation at the heavy ion source GTS-LHC of the linear accelerator Linac3 at CERN.

The heating power of the oven is one of the main tuning parameters at the ion source and so far the choice of the heating power is solely based on operator experience. Sudden drops of the source current regularly require not foreseen modifications of the heating power. Additionally during normal operation it could so far not be achieved that the complete lead sample contained in the crucible of the oven is consumed before the decrease of the ion current delivered from the ion source made a refill of the oven necessary. As the refills are causing downtime of the heavy ion source an extension of the oven runtime until the complete lead sample is consumed is desirable.

The study includes thermal and gas flow simulations as well as measurements at a test stand. In a series of measurements the oven was operated in different conditions to characterize its behaviour. Instabilities of the evaporation rate could be documented and reasons for these instabilities were found. Additionally the formation of a blockage was studied that was observed in a similar form at the heavy ion source.

By changing the oven setup the evaporation rate could be stabilized at the test stand. Also the formation of the blockage could be completely prevented. Without the blockage formation the oven could then be operated until the crucible was completely empty. From the result of the study recommendations for a change of the oven setup at the heavy ion source of Linac3 can be deduced.

Contents

1. Introduction **1**

2. The GTS-LHC Ion Source, Functionality and Setup **5**

2.1. Ionization principle 5
2.2. Plasma confinement 7
2.3. Electron heating 10
2.4. Gas mixing 11
2.5. GTS-LHC Ion Source 12
2.6. The micro oven 14

3. Theory and Simulations **19**

3.1. Vapour pressure and evaporation rate 19
3.2. Flow regime of the lead gas jet 23
3.3. Knudsen's cosine law 25
3.4. Molflow+ simulation model 27
3.5. Thermal transport mechanisms 36
3.6. 2D model of the micro oven in ANSYS 39
3.7. 3D model in ANSYS 44
3.8. Conclusion from the thermal simulations 63

4. Oven Characterization at the Test Stand **65**

4.1. Setup of the oven test stand 65
4.2. Outer thermal profile at stable power levels 80
4.3. Divergence of the lead gas jet 88
4.4. Calibration: From the deposition to an evaporation rate 91

5. Temporal Evaporation Behaviour **97**

5.1. Operation simulation at the test stand 97
5.2. Active gas injection 106

5.3. Unstable evaporation rates 121
5.4. Oven insulation modifications 132
5.5. Stable oven operation 139
5.6. Conclusion of the measurement series 150

6. Conclusion and Outlook 153

A. Nitrogen Test at the GTS-LHC Ion Source 155
A.1. Low energy beam transfer line and instrumentation 155
A.2. Measurements 156
A.3. Discussion 160

B. Finite Elements Method 163
B.1. Example for the FEM 163
B.2. Non linear systems 166

List of Symbols and Abbreviations 169

Bibliography 173

Acknowledgements 181

Eidesstattliche Versicherung 183

List of Figures

1.1. Sketch of the accelerator chain at CERN that is involved in the heavy ion beam acceleration. 2
1.2. A possible lead ion beam production scheme for the LHC. 3

2.1. Sketch of the loss cone of a magnetic mirror in velocity space. 9
2.2. Sketch of the magnetic field lines for the magnetic bottle created by two solenoids and the field lines of a sextupole. 10
2.3. Sketch of the GTS-LHC ion source and its basic components around the plasma chamber. 13
2.4. Sketch of the general setup of the micro oven that is used at the GTS-LHC ion source. 14
2.5. Sketch and photo of the crucible that contains the lead sample for the oven. 15
2.6. Photo of the filament holder, the filament and the filament protection around it. 16
2.7. Photo of the layers outside of the filament and a photo of the fully assembled oven. 17
2.8. Scheme of the electrical connection of the filament, the cane and the power supply. 17

3.1. Vapour pressure of lead. 21
3.2. Knudsen number, when the vapour pressure of lead is assumed and the characteristic length is the diameter of the crucible. 25
3.3. Geometry of Lamberts cosine law in 2D 26
3.4. The geometry for a Molflow+ simulation prepared with the ANSYS Design-Modeler. 28
3.5. Simulation of the lead gas jet from the oven in Molflow+. 29
3.6. Photo of the remaining lead in the crucible after a measurement and the positions of the emitting surface that where used to calculate the evaporation rate from the oven at a range of temperatures. 31

3.7. Evaporation rates per surface area for the different positions of the lead surface within the crucible. 31
3.8. Total evaporation rates of the Linac3 lead oven, from the Molflow+ model and of an estimation using the Hertz-Knudsen equation. 32
3.9. Normalized impingement rate on a facet, placed 5 cm away from the oven for the 3 cases shown in figure 3.6. 33
3.10. Geometry used to calculate the transversal gas profile. 34
3.11. Outline of the transversal profile of the lead gas jet 50 mm away from the oven tip. 35
3.12. Mean free path of the gas particles calculated from equation (3.12) using the pressure, given by the Molflow+ model. 36
3.13. Derivation of the two dimensional geometry for the thermal 2D model of the oven. 39
3.14. Temperature of the oven cover and a copper pin within the crucible, against heating power. 42
3.15. Geometry of the surface representing the cylindrical lead sample in the 2D simulation. 43
3.16. Lead temperature from the thermal 2D simulation for two bodies that resemble a full and an empty crucible. 44
3.17. Appearance of the mesh for the three dimensional oven model in ANSYS. . . 46
3.18. The material assignments at the 3D model of the oven. 47
3.19. Thermal emissivities of the materials that are used in the 3D model. 48
3.20. Loads and contacts of the 3D oven model, apart from the radiation. 48
3.21. Temperature span of the crucible and the oven cover in the 3D model compared to the 2D model for the same heating power in the filament. 49
3.22. Temperature on a path within the crucible derived from the 3D and the 2D simulation. 50
3.23. Comparison of the thermal distribution of the micro oven at 10 W predicted by the two models in ANSYS. 50
3.24. Comparison of a reduced 2D model of the oven with a 3D model that was derived by rotating the 2D model around its symmetry axis, 3Dy. 52
3.25. Geometry used for a 3D and 2D comparison of simpler structures. 53
3.26. Thermal distribution of the filament holder in all six simulations. 54
3.27. Geometry of the simplified oven model in 3D. 55

3.28. Temperature span of the crucible and the oven cover from the simplified 3D model compared to the full 3D model. 56
3.29. The body representing the reflective tantalum foil as a cylinder and the new body where the foil is thin and has windings 57
3.30. Temperature profile of the tantalum foil for a heating power of 5 W. On the left the foil is represented as a thick cylinder and on the right with several windings. 57
3.31. All temperature values within the thermal distribution of the crucible (left plot) and the oven cover (right plot) at a certain heating power level. 58
3.32. Temperature on a path along the crucible for three different simulation models at 5W. 59
3.33. Temperature span from two 3D simulations. In one the filament was set on a fixed temperature while the other used the heat generation. 60
3.34. Simple model of the injection plug at the GTS-LHC ion source. 61
3.35. Temperature span of the crucible and the oven cover with and without the injection plug. 62
3.36. The left plot shows the temperature span of the injection plug plotted against the heating power of the oven. The right picture shows the temperature profile of the plug. 63

4.1. Sketch of the inside of the oven test stand vacuum chamber as seen from the side and from the top. 66
4.2. Sketch of the connections outside of the oven test stand. 68
4.3. Photos of the oven feedthrough with the cooling pipes, the bellow and the motorized stage that allows to move the oven. 69
4.4. Photos of the gas injection at the test stand. 69
4.5. Principle of a thermocouple. 70
4.6. Photo of the thermocouples inside the oven test stand. 71
4.7. Setup of a temperature measurement with clamping rings and thermocouples. 72
4.8. Geometry of the holder ring for ANSYS thermal simulations. 73
4.9. Temperature distribution of the oven cover and the holder ring for two different simulations. 74
4.10. Temperature along a path in the oven cover, shown on the right, for ANSYS simulations at 10 W of heating power, including a thermocouple holder ring. 74
4.11. Sketch of the oscillator circuit that lets the crystal oscillate at its resonance frequency. 76

4.12. Photos of the deposition sensor and its feedthrough. 77
4.13. Setup of an evaporation rate measurement. 77
4.14. Visualization of how the deposition data after the SQM-160 is distributed. . 78
4.15. Reading of the deposition sensor when the shutter opens and closes. 79
4.16. Example of a temperature scan with different oven powers over time. 81
4.17. Temperature at the reference position shown in figure 4.7 for the full power range of the oven at several scans. 82
4.18. Averaged stable readings of the thermocouple positioned at the reference position during all presented thermal scans at all used power steps. 83
4.19. Thermal profile of the Linac3 oven at all operational power levels. 85
4.20. The measured outer thermal profile of the oven together with the result of the 2D and the detailled 3D simulation. 86
4.21. Outer thermal profile of simulations, where the oven cover and the cane share a conducting connection together with the measurement. 87
4.22. Temperature along a path within the crucible, for two thermal 2D simulations, with and without conduction between cane and oven cover. 87
4.23. Reading of the deposition sensor over time when the oven distance to the detector is increased. 89
4.24. .Geometry of the solid angle taken up by the deposition detector. 90
4.25. The corrected normalized deposition sensor reading ($D_{\mathrm{corr,norm}}$) at different distances between the oven tip and the detector (s). 91

5.1. Power values of different oven runs at the GTS-LHC ion source in 2016, set to a common starting time. 98
5.2. Subset of the power-time curves that was used to derive the model for the typical oven operation at the source. 99
5.3. Two examples for manipulation of the power-time curves. 99
5.4. Selected power-time curves where the longer interruptions at below 5 W where cut out. 100
5.5. Evaporation rate during the oven operation replication at the oven test stand. 102
5.6. Resulting evaporation rate R and the uncalibrated deposition rate D of the operation replication at the test stand for three consecutive runs. 103
5.7. First 120 h of the evaporation rate measurement S1. The different colors represent fixed heating power levels. 104
5.8. Power to evaporation rate relation for the measurements S1-S3. 104

5.9. Measured evaporation rate of the oven with a nitrogen atmosphere at a pressure of 1×10^{-5} mbar. 107
5.10. Power to evaporation rate relation for the measurements S3 and N1. 108
5.11. Evaporation rate and power during run N2, in a nitrogen atmosphere where the power was adjusted to keep the evaporation stable. 109
5.12. Power to evaporation rate relation for the measurements N1 and N2. 110
5.13. Appearance of the oven tip after two individual runs at the GTS-LHC ion source. 111
5.14. Effect of the oxygen atmosphere of 1×10^{-5} mbar on the oven. 113
5.15. The two crucible positions that were simulated with Molflow+ to derive the fractions of the gas jet that hit the inner walls of the oven cover. 115
5.16. Oven run in 1×10^{-6} mbar of oxygen. 116
5.17. Measurement O3 at the oven test stand, using chemically clean lead at an oxygen pressure of 1×10^{-5} mbar. 118
5.18. Crucible modification with the goal to prevent lead deposition on the outer oven cover. 119
5.19. Evaporation rate and power during measurement O4 at the oven test stand. 120
5.20. Evaporation rate and power during measurement I1, with chemically clean lead, a reduced tantalum foil and without external thermocouples. 123
5.21. Evaporation rate and filament resistance r plotted for the two time windows D1 and D2. 124
5.22. The evaporation rate together with $|r'_{\text{neg,norm}}|$ which indicates a negative derivation of the filaments resistance. 126
5.23. The upper plot shows the evaporation rate together with peaks indicating negative resistance changes. 127
5.24. Evaporation rate and power of a measurement where the filament current is automatically adjusted to keep the filaments resistance at a desired value. . 129
5.25. Evaporation rate of the oven together with drops of the resistance during measurement I2. 130
5.26. Filament resistance, oven current and oven power together with the evaporation rate in the time frame of the first evaporation rate drop. 131
5.27. Resistance setpoint together with the measured resistance and the evaporation rate. 131
5.28. Tantalum insulation rings at the front of the oven to enhance the heat reflection at the oven tip. 133

5.29. Evaporation rate and oven power over the time of the measurement T1. . . . 134
5.30. Several parameters during an evaporation rate drop that where recorded in measurement T1. 135
5.31. Removing the tantalum foil can cause a misalignment of the inner oven parts.137
5.32. Evaporation rate and oven power during the measurement T2. 137
5.33. Evaporation rate and applied oven oven power during measurement U1. The photo shows the tip of the oven after the run. 140
5.34. Evaporation rate and the filament resistance for time windows of stable power at the end of measurement U1. 141
5.35. Evaporation rate and power during measurement U2. 143
5.36. Photos of the oven with an empty and turned crucible, the thermocouple with a copper pin and the oven with the thermocouple inserted into the crucible. 144
5.37. Temperature reading of the thermocouple that was inserted into the crucible in the measurements Y1 and Y2. 145
5.38. Temperature measured at the oven cover during the measurements Y1 and Y2 plotted against the oven heating power. 146
5.39. Filament resistance after the temperature stabilized at each power level during the measurements Y1 and Y2. 148
5.40. Evaporation rate (R) and heating power (P) during the ramp up of the oven evaporation in the measurements U1 and U2. 149
5.41. Evaporation rate at different crucible temperatures derived by combining evaporation and temperature measurements at fixed power levels. 150

A.1. Sketch of the low energy beam transport line at Linac3. 156
A.2. Beam current measured by the beam current transformer BCT05 durig a selected time window of the nitrogen test. 157
A.3. Two charge state distributions recorded at Linac3 during the test with nitrogen.158
A.4. Charge state distributions two days after the start of the test. 159
A.5. Charge state distribution recorded one day after the test was terminated. . . 160

B.1. Example for a heat conduction problem. 164

1. Introduction

In the study of basic physics the technology to produce and accelerate ions is a key method for the observation of fundamental particle interactions.

Ionized atoms can be manipulated with electric and magnetic fields which enables experiments where the charged particles are trapped in ion traps or accelerated and then collided.

The European Organization for Nuclear Research, CERN [1], is a research facility where a chain of accelerators allows experiments with different kinds of particles, like high energy proton collisions in the Large Hadron Collider (LHC), but also the cooling and deceleration of antiprotons at the Antiproton Decelerator (AD) and the newly comissioned Extra Low ENergy Antiproton ring (ELENA) [2, 3], or fixed target experiments for Kaon physics, like NA62 [4] that is connected to the Super Proton Synchrotron (SPS).

Several fundamental particles have been discovered at CERN with the Higgs boson being a prominent example [5, 6].

Besides the search for new particles, high energy collisions also allow to study a state of matter that is otherwise not accessible in laboratory conditions, the quark gluon plasma [7]. As quarks are confined by the strong force they are only present as the constituents of another type of particle, the hadrons [8].

During the collisions of heavy ions, which contain many hadrons, the colliding nuclei can become so dense and hot that the quarks within this compressed matter display a quasi free behaviour [9].

This state of matter is believed to have been present during very early stages of the universe and being able to recreate it in a laboratory can allow insights into what happened shortly after the big bang.

In addition to the proton acceleration, CERN also has an infrastructure for the production of heavy ion beams which are used in fixed target experiments at the SPS and during the heavy ion program of the LHC, usually lasting one month per year [10–12]. Figure 1.1 shows a sketch of all accelerators at CERN that are involved in storing and accelerating the heavy ion beam.

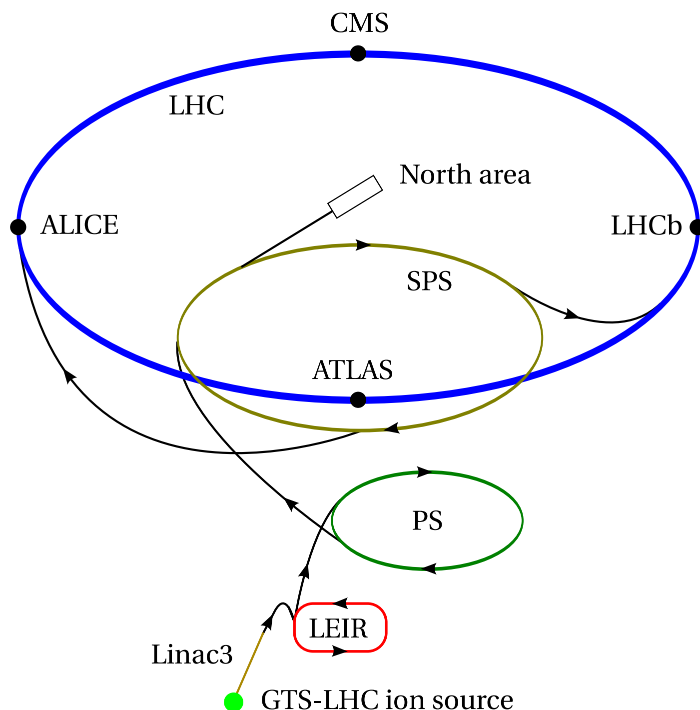

Figure 1.1.: Sketch of the accelerator chain at CERN that is involved in the heavy ion beam acceleration.

The starting point of the heavy ion production at CERN is the GTS-LHC ion source that ionizes neutral gas and then injects the ions into the linear accelerator Linac3. At the end of Linac3 the ions are guided through foils that strip off additional electrons from the ion hulls. The first circular accelerator for the heavy ion beam is the Low Energy Ion Ring (LEIR) which accumulates several pulses, called bunches, coming from Linac3. After their acceleration, the particles are injected into the PS, which besides accelerating also splits each bunch coming from LEIR into two smaller ones. Between the Proton Synchrotron (PS) and the larger SPS additional stripper foils in the transfer line strip the ions off their remaining electrons, leaving a beam only consisting of nuclei. Several fillings from the PS are injected into the SPS before its beam energy is ramped up. The SPS then accelerates the particles to the LHC injection energy [13]. In the LHC two separated beams of the ions are brought to the final energy and collided in the interaction regions. While A Large Ion Collider Experiment (ALICE) is the detector that is dedicated for the investigation of heavy ion collisions, all particle detectors installed at the LHC are involved in the heavy ion program [14].

Figure 1.2 shows a possible scheme for the heavy ion beam production, in this case for lead ions in the run of 2016 [15].

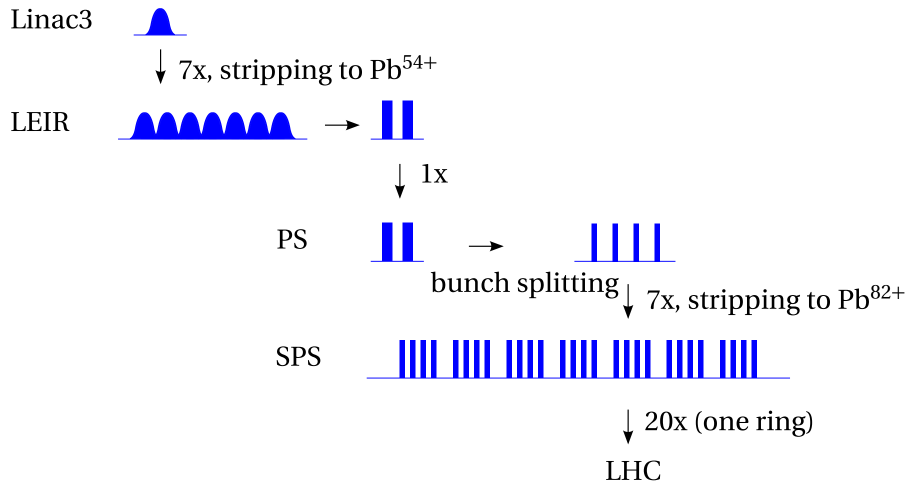

Figure 1.2.: A possible lead ion beam production scheme for the LHC.

Most frequently the LHC collided lead ions during the heavy ion program. For the production of these ions in the ion source a solid lead sample first needs to be evaporated before it can be ionized in the plasma chamber of the ion source. The evaporation takes place in one or both of the two available micro ovens that can be inserted into the GTS-LHC (named after the Grenoble Test Source and the LHC).

The resistively heated ovens are controlled by leveling the heating power supplied by the power supply. The setpoint of the oven power is one of the frequently used tuning parameters at the GTS-LHC ion source and adjusting the oven power is an important part of maintaining a stable ion current from the source.

However so far the underlying mechanisms that make this tuning necessary were not well understood and the tuning decisions are mostly based on operating experience. Additionally to that, the ovens undergo sudden unexpected drops in their evaporation rate, making it necessary to raise the oven power when such a drop is encountered.

The oven operation is routinely ended after two weeks and the crucible is manually exchanged with a newly filled one. After such a two week run the oven crucible often still contains almost half of the initial sample, but continuing a stable operation was so far impossible. The source current would drop and the oven power can not be raised infinitely. 20 W is the usual upper limit as beyond this value damage to the oven is expected.

The refill of the ovens is the main reason for scheduled downtime of the GTS-LHC ion source during the use of lead ions in the heavy ion program of the LHC. As the heavy ion program lasts four weeks an oven configuration that would enable a stable operation over this duration is highly desirable.

In this work a study of the oven in its current setup both experimentally and by simulations is presented. Gas dynamics and thermal simulations were used to get and understanding of the gas jet profile and the thermal distribution inside of the oven. At a test stand the oven was operated in different conditions and with modified configurations to characterize the behavior of the evaporation rate and to find influences on the evaporation stability.

The first chapter introduces the GTS-LHC ion source and the setup of its micro ovens. The following chapter presents the theoretical considerations and simulation models that where developed to understand the oven properties. The third chapter introduces the experimental setup, the test stand, and the principle of the measurements at the test stand together with some basic measurements. In the fourth chapter the results of a series of measurements at the test stand are shown and discussed. The last chapter summarizes the results of the study and gives a short outlook.

2. The GTS-LHC Ion Source, Functionality and Setup

Heavy ions for the CERN accelerator chain up to the LHC are produced by the GTS-LHC ion source connected to the linear accelerator Linac3 [13, 16, 17]. Its design is based on the Grenoble Test Source (hence the name GTS-LHC) which was developed at the Commissariat à l'Énergie atomique (CEA) in Grenoble to study the underlying physics and possible improvements of ECR ion sources [18]. The source is an Electron Cyclotron Resonance Ion Source (ECRIS) and uses microwaves to heat a magnetically confined plasma in which the desired elements are ionized to high charge states [19]. The following chapter introduces the setup and gives an overview of the ion source principle, mainly following the description in [20].

2.1. Ionization principle

The production zone for the ions inside an ECRIS is a plasma, defined as "*a quasineutral gas of charged and neutral particles which exhibits collective behaviour*" ([21]). For an ion source the plasma serves as an environment where electrons, ions and gas atoms can interact by collisions and thereby ionize neutral particles to the desired charge state.

There are several mechanisms where ions, atoms or molecules can lose electrons and thereby become an ion (of a higher charge state), while other mechanisms can reduce the charge state of an ion.

Hence the distribution of charge states in a plasma is a balance between the different processes affecting an ions charge state. This can be described by a balance equation like [22]:

$$\frac{\mathrm{d}n_j}{\mathrm{d}t}(t) = n_\mathrm{e}(t)\big[n_{j-1}(t)\mathrm{IR}_{j-1,j} + n_{j+1}(t)\mathrm{RR}_{j+1,j} \\ - n_j(t)\mathrm{IR}_{j,j+1} - n_j(t)\mathrm{RR}_{j,j-1}\big] - \frac{n_j(t)}{\tau_{\mathrm{ion},j}} \quad . \tag{2.1}$$

Here n_j describes the density of the ions of charge j at the moment t, n_e the electron density in the plasma, $\mathrm{IR}_{i,j}$ is the reaction rate of single electron impact ionization from charge state i to j and $\mathrm{RR}_{i,j}$ the reaction rate of radiative recombination from charge state i to j.

$\frac{n_j(t)}{\tau_{\mathrm{ion},j}}$ is the rate of ions of charge j that are lost from the plasma with the mean ion confinement time $\tau_{\mathrm{ion},j}$.

Equation (2.1) is only true if single electron impact ionization and radiative recombination are the only processes that change the charge state of an ion and if j is neither zero nor the maximum charge state in the plasma.

Electron impact ionization In an ECRIS the dominating process is electron impact ionization [23–25]. A freely moving electron (e^-) collides with an atom or ion (A^{n+}) of charge n and expels another electron from its shell. The result of such an interaction is an increased charge state of the ion and two freely moving electrons:

$$\mathrm{A}^{n+} + \mathrm{e}^- \longrightarrow \mathrm{A}^{(n+1)+} + 2\mathrm{e}^- \quad . \tag{2.2}$$

Charge states higher than A^+ can occur if the ionization process happens multiple times in a stepwise ionization. Also possible but less probable is the double ionization with,

$$\mathrm{A}^{n+} + \mathrm{e}^- \longrightarrow \mathrm{A}^{(n+2)+} + 3\mathrm{e}^- \quad . \tag{2.3}$$

Both processes can only happen if the electron carries enough energy to overcome the respective ionization energy of the involved ion [26], which depends on the element and grows with the initial charge state n [27].

Charge exchange For highly charged ions like the lead ions Pb^{29+} in the GTS-LHC, the ions need to stay in the plasma long enough to be ionized in multiple steps. But competing processes can also lower their charge states again. One interaction leading to lower charge states is a charge exchange between an ion A^{n+} and a neutral particle A or, less probable,

two ions, A^{n+} and A^{f+}, in the plasma:

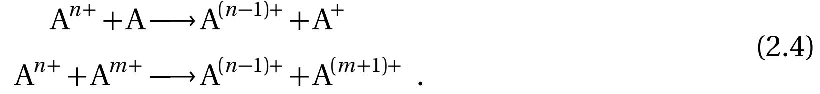

$$\begin{aligned} A^{n+} + A &\longrightarrow A^{(n-1)+} + A^{+} \\ A^{n+} + A^{m+} &\longrightarrow A^{(n-1)+} + A^{(m+1)+} \quad . \end{aligned} \tag{2.4}$$

The charge exchange lowers the amount of high charge states in the plasma but at the same time increases the number of lower charged ions as it is also an ionization process.

Radiative recombination Ions can also recapture electrons from the plasma where the excess energy of the electron is radiated as a photon (γ), called the radiative recombination [28, 29]:

$$A^{n+} + e^{-} \longrightarrow A^{(n-1)+} + \gamma \quad . \tag{2.5}$$

The cross section of this process favours low energy electrons and high charge states and acts more as a limiting factor towards high charge states rather than influencing the amount of less charged ions.

The origin of ionizing electrons is the process itself as each particle being ionized releases new electrons. To keep the ionization running the electrons need to be heated and confined together with the ions.

For the confinement magnetic fields are used, which is described in the next section. Energy to heat the electrons is added to the process by microwaves described in section 2.3. Besides the presented mechanisms also other processes influence the distribution of charges and particles, e.g. loss mechanisms (described by the term $\frac{n_j(t)}{\tau_{\mathrm{ion},j}}$ in equation (2.1)), as an ion source can only produce particle beams if the desired ions are not completely confined.

2.2. Plasma confinement

To create and control a plasma, the charged particles, in this description exemplary the electrons, need to be confined in a certain volume. In the GTS-LHC ion source this is achieved with room-temperature electromagnets creating a magnetic cage for the plasma particles. Working principle of such a cage is the magnetic mirror.

The Lorentz force $\mathbf{F}_{\mathrm{L}}$ on an electron reads [30]:

$$\mathbf{F}_{\mathrm{L}} = -q_{\mathrm{e}} (\mathbf{E} + \mathbf{v}_{\mathrm{e}} \times \mathbf{B}) \quad . \tag{2.6}$$

Here $\mathbf{E}$ and $\mathbf{B}$ are the electric respectively the magnetic field, q_e the charge and $\mathbf{v}_\mathrm{e}$ the velocity vector of the electron.

In the following the Euclidean unit vectors $\mathbf{e}_1$, $\mathbf{e}_2$ and $\mathbf{e}_3$ are used. If the elctron moves through a homogeneous magnetic field ($\mathbf{B} = B\mathbf{e}_2$), its velocity vector can be split into two components, one parallel ($v_\parallel$) and one perpendicular ($v_\perp$) to the magnetic field lines:

$$\mathbf{v}_\mathrm{e} = v_\perp \mathbf{e}_1 + v_\parallel \mathbf{e}_2 \ . \tag{2.7}$$

The force of the magnetic field following from equation (2.6) then reads:

$$\mathbf{F}_B = -q_\mathrm{e}\mathbf{v}_\mathrm{e} \times \mathbf{B} = -q_\mathrm{e} v_\perp B \mathbf{e}_3 \ . \tag{2.8}$$

If the electron is moving perfectly perpendicular to the magnetic field lines, the force following from equation (2.8) will force the electron into a circular motion as it always acts perpendicular to its velocity. An additional parallel component of the velocity brings the electron into a helical trajectory around the field lines.

While moving within the magnetic field the electron generally follows certain conservation laws. Primarily it conserves its energy, E_e, that can be expressed as

$$E_\mathrm{e} = \frac{1}{2} m_\mathrm{e}(v_\perp^2 + v_\parallel^2) \ . \tag{2.9}$$

Here m_e is the electron mass at rest. Another conserved value is the magnetic moment of the gyration μ_e, also called the first adiabatic invariant:

$$\mu_\mathrm{e} = \frac{m_\mathrm{e} v_\perp^2}{2B} \ , \tag{2.10}$$

If an electron moves into a region with a stronger magnetic field (a higher $|\mathbf{B}| = B$), the magnetic moment can only be conserved by increasing the rotational speed $v_\perp$. Equation (2.9) then shows that the kinetic energy can only be kept constant if the speed parallel to the field lines is reduced. An electron is being reflected if the parallel speed component is lowered to zero. From equation (2.10) it can be deduced that this happens at a point in the magnetic field where $E_e = \mu_\mathrm{e} B$. The reflection is only possible if the kinetic energy of the electron is distributed over the two directional components in a way that it can transfer all of its parallel kinetic energy into the rotational energy, which gives the requirement:

$$E_\mathrm{e} \leqq \mu_\mathrm{e} B_\mathrm{max} \ . \tag{2.11}$$

If the parallel component of the velocity vector of an electron is too large compared to the perpendicular one, it traverses the mirror and is lost, even when the total energy is lower than that of others that are being reflected. This parameter combination is called the loss cone [20]. Another way of expressing this can be done using the magnetic mirror ratio R_{mag}:

$$R_{\text{mag}} = \frac{B_{\text{max}}}{B_{\text{min}}} \ , \tag{2.12}$$

where B_{min} is the minimal and B_{max} the maximum field strength of the magnetic bottle. Starting with a particle at speed $|\mathbf{v}| = (v_\perp + v_\parallel)$ in the region with the minimum magnetic field, the requirement for this particle to be kept (see (2.11)) becomes:

$$v_\parallel \leqq v_\perp (R_{\text{mag}} - 1) \ . \tag{2.13}$$

Figure 2.1 visualizes this condition.

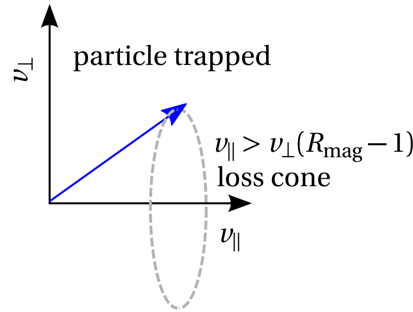

Figure 2.1.: Sketch of the loss cone of a magnetic mirror in velocity space.

In an ECRIS the confinement is done with two magnet sets. On the axis parallel to the beamline, solenoids create a magnetic field whose strength peaks at the ends of the plasma chamber and has a local minimum in its middle. This way the plasma particles are confined in the middle of the chamber. However the plasma confinement in a simple magnetic bottle is unstable and the plasma can escape radially, which is called the magneto hydrodynamic instability (MHD-instablity) [19]. To enhance the radial confinement another set of magnets superposes a radial multipole field (usually a sextupole [20]) that leads to a growth of the field strength with growing radial distance to the symmetry axis of the plasma chamber. Figure 2.2 sketches the field lines of these two magnet setups, while the resulting superposition is a more complex field.

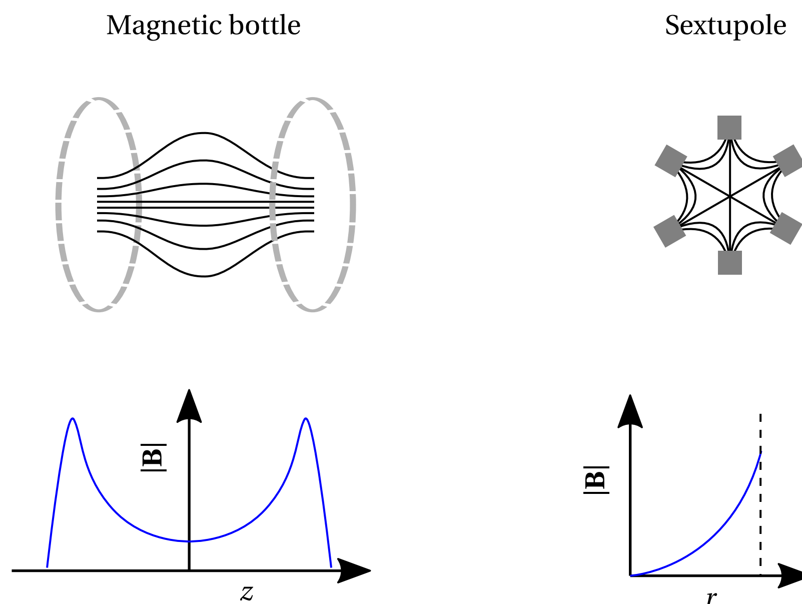

Figure 2.2.: Sketch of the magnetic field lines for the magnetic bottle created by two solenoids and the field lines of a sextupole. The solenoids accomplish longitudinal confinement, while the sextupole magnets stabilize the plasma radially.

2.3. Electron heating

For the plasma to be able to ionize atoms to high charge states, besides the confinement, it also needs to have sufficiently energetic electrons that can interact with the ions as presented in section 2.1. In an ECRIS, this is achieved by injecting microwaves into the plasma chamber which heat the electrons. The heating mechanism is a resonance phenomenon using the gyration of electrons around magnetic field lines. Inside of a magnetic field electrons gyrate around the field lines with the cyclotron frequency ω_C defined by the field strength, B:

$$\omega_C = \frac{q_e B}{m_e} \tag{2.14}$$

When a microwave with a certain frequency ω_{rf} is injected, electrons in the plasma experience a force by the electric field of the microwave. But as this field is oscillating, the electrons do not generally accumulate energy.

In the ECRIS design a zone exists where $\omega_{rf} = \omega_{C,ECR}$ at the magnetic field strength B_{ECR}. Defined by the magnets, this zone usually is an egg shaped closed surface around the centre of the plasma chamber and is called the resonance surface.

Here the electric field of the microwave changes its polarity with the same frequency as

the gyration of the electrons. This way the kinetic energy of the electrons can grow over several turns, depending on the phase relation of the electron and the micro wave. This setup on average heats the plasma electrons. If several microwave frequencies are injected, several resonance surfaces can exist which all heat the electrons.

For the electron heating to work as described it is important that the injected microwaves can reach the ECR surface. As the electrons within a plasma can oscillate with the plasma frequency ω_{p} [31], they are able to adiabatically adapt their position to electric fields that oscillate with a lower frequency than ω_{p}. This leads to the reflection of microwaves with a lower frequency than ω_{p}, hence a critical electron density $n_{\mathrm{e,crit}}$, for every microwave frequency exists where microwaves can not conventionally propagate through the plasma. As the ECR ion sources hold a magnetized plasma, this description is not complete ([32]) and ECR ion sources with frequencies above this cut-off have been demonstrated for certain microwave modes ([33]). The GTS-LHC ion source however is operated below the cut-off frequency.

2.4. Gas mixing

To enhance the amount of high charge state heavy ions in an ECR plasma a usual technique is gas mixing [19]. This means that a second gas that consists of a lighter element (like oxygen, nitrogen or helium) is injected into the plasma chamber besides the gas that delivers the desired heavy ions. It was observed that this can shift the charge state distribution of the heavy ions towards higher charge states [34].

Several explanations for the effect exist: The influence can be explained by a cooling effect on the heavy ions. Within the plasma the heavier ions collide with the lighter ions. This transfers thermal energy to the latter. With the extraction of the lighter ions from the plasma also thermal energy is transported out of the plasma [35].

By cooling the heavier ions their confinement is enhanced and thereby the average time an ion remains in the plasma. This leaves more time for the stepwise ionization to high charge states.

An alternative explanation refers to the plasma potential created by light ions that confines the heavy ions more effectively [36].

It was also suggested that the positive influence on the amount of highly charged ions stems from a combination of several mechanisms including the ones above but also an effect on the electron density and the rate of charge exchange reactions [37].

At the GTS-LHC ion source gas mixing is being applied routinely with oxygen serving as

the buffer gas during the the lead ion production.

2.5. GTS-LHC Ion Source

As a successor of the ECR4 [38] the GTS-LHC ion source is providing heavy ions for CERN accelerators since 2005 as the the old source could not fulfill the needed requirements for the LHC beam [17]. Figure 2.3 shows a sketch of the basic components of the ion source.

The GTS-LHC features a plasma chamber in the shape of a hollow cylinder, whose symmetry axis is parallel to the produced ion beam.

It is surrounded by three room temperature solenoid coils with the same polarity, producing the field for the axial electron confinement. One coil is on each end of the cylinder, defining the maximum magnetic field on the symmetry axis. The third coil is in the middle of the plasma chamber to adjust the minimum field.

The radial plasma confinement is enhanced with a permanent magnet hexapole placed inside of the solenoids around the wall of the plasma chamber.

The extraction of the particle beam is achieved by 3 electrodes at the end of the plasma chamber that are connected to the beamline of Linac3. To extract the positive ions the body of the source is on a positive potential of 18.8 kV compared to the extraction electrode, which is grounded, like the rest of the accelerator beamline.

On the other end of the plasma chamber, the injection side, the injection plug with several functions is facing the inside of the plasma chamber. An additional electrode on negative potential compared to the ion source body is facing the inside of the plasma chamber. This part is called a bias disc and it helps to maximize the ion yield [34]. Besides the magnetic field all remaining "ingredients" for the plasma are brought into the plasma chamber via the injection plug. Here the 14.5 GHz microwaves are coupled into the plasma by one of two rectangular waveguides. The second waveguide is connected to a spare microwave generator and not part of the normal operation. An additional pipe allows to inject gas into the chamber. If several gases shall be inserted, the mixing is done outside of the plasma chamber. Additionally to the gas pipe two micro ovens are inserted through the injection plug. As the micro ovens are the subject of this work their setup is described in more detail in the following section.

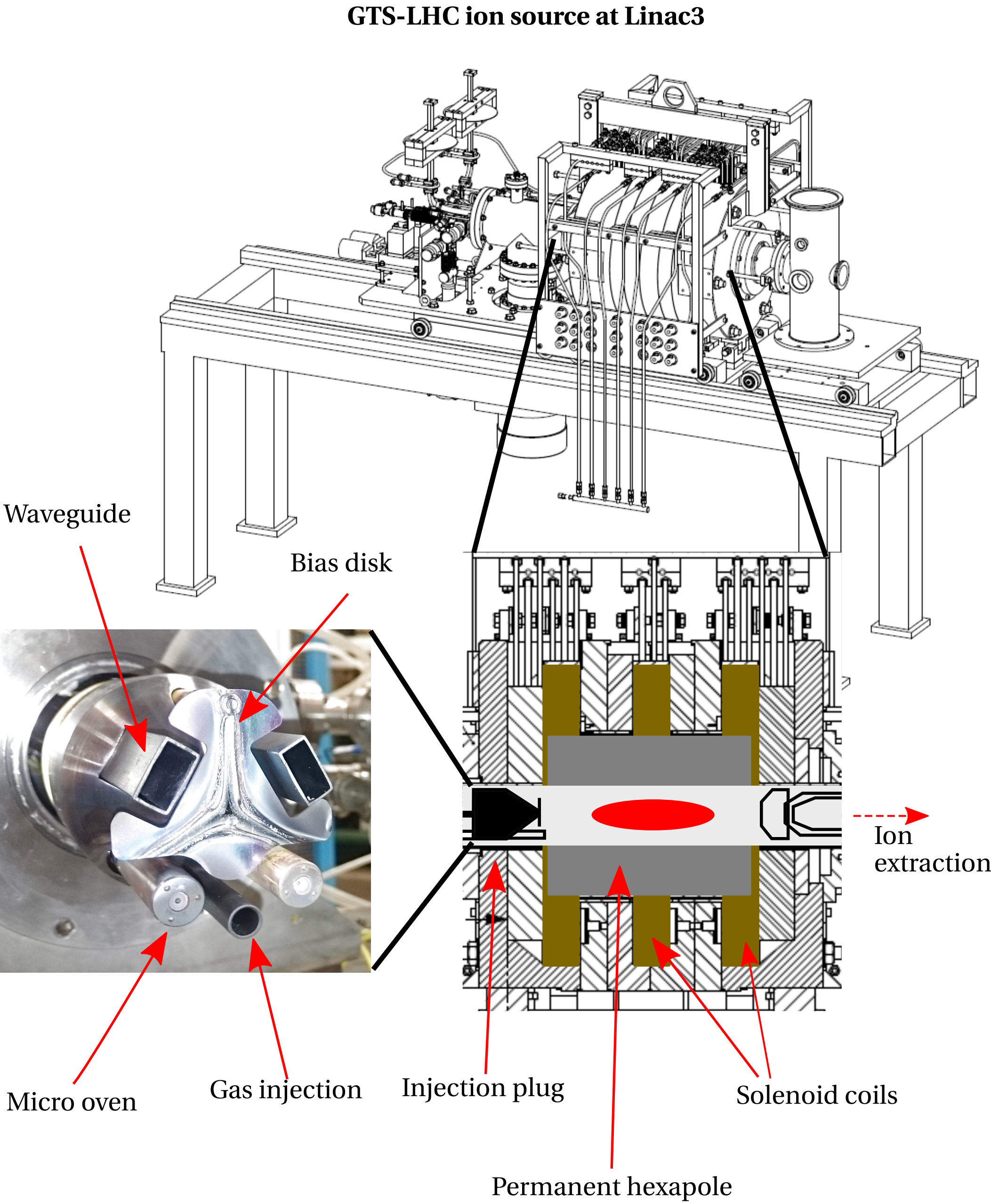

Figure 2.3.: Sketch of the GTS-LHC ion source and its basic components around the plasma chamber. The photo shows the side of the injection plug that is facing the plasma chamber.

2.6. The micro oven

The oven technique is a widely used method to produce vapours from materials that are solid at room temperature and possess relatively high vapour pressures at manageable temperatures like calcium and lead. At the GTS-LHC ion source two ovens are inserted into the vacuum of the plasma chamber via canes. Their setup is optimized to provide sufficient temperatures at a compact design. The achievable temperature range reaches up to 1000 °C in the crucible, which is sufficient for the evaporation of lead. Their operating principle is resistive heating via a filament that is wound around a structure containing the crucible, the filament holder. Outer layers provide thermal insulation to enhance the temperature to power ratio. A sketch of its setup is given in figure 2.4.

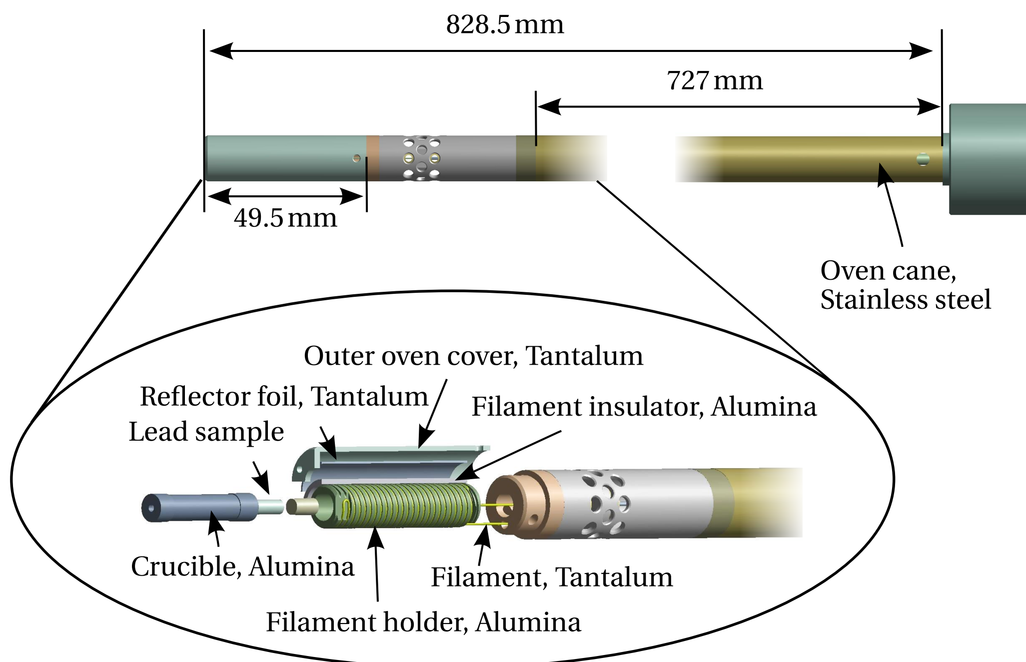

Figure 2.4.: Sketch of the general setup of the micro oven that is used at the GTS-LHC ion source. The upper picture shows the oven on its cane, the lower picture shows an exploded view of the oven.

2.6.1. The crucible

A hollow cylindrical crucible is used to contain the material that is supposed to be evaporated. It is made out of alumina (Al_2O_3) which is able to withstand high temperatures and shows no chemical reactions with hot lead and its vapour. Figure 2.5 shows a photo and the basic dimensions of the crucible.

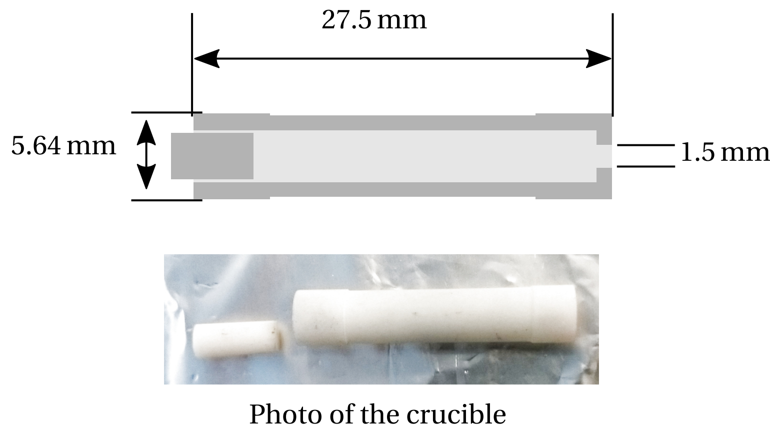

Photo of the crucible

Figure 2.5.: Sketch and photo of the crucible that contains the lead sample for the oven.

In the front, the cylinder is closed with a wall which features the extraction hole for the produced vapour. The back end is closed by a plug that also consists of alumina. The Wall thickness in the middle is thinner compared to the front and the back end, which reduces the area of direct contact to the oven and thereby the possibility of heat conduction.

2.6.2. Filament, filament holder and filament insulator

The heating current is carried by a tantalum filament wound as a double helix that closes at the tip of the oven. In contrast to other possible designs this guides the current back to the end of the oven without the necessity of another electrical conductor, e.g. the outer oven cover. An alumina support structure is holding the filament. This structure is in principle a cylinder which is hollow and open towards the oven tip but closed in the back. On its outside a groove is holding the filament and ensuring that no parts of the wire are electrically short circuited by touching each other. In the back the two ends of the filament are separated so that one end is guided into the middle of the cane while the other end is connected to its outside. Around the filament another alumina part, in the form of a tube, shields it from possible electrical contact with metal parts of the setup. Figure 2.6 shows photos of these parts.

2.6.3. Outer oven layers

Outside of the filament insulator two additional layers are protecting and insulating the oven. A piece of 40 mm x 200 mm tantalum foil with a thickness of 25 µm is wound around the filament protector to enhance the crucibles temperature by reflecting thermal radiation

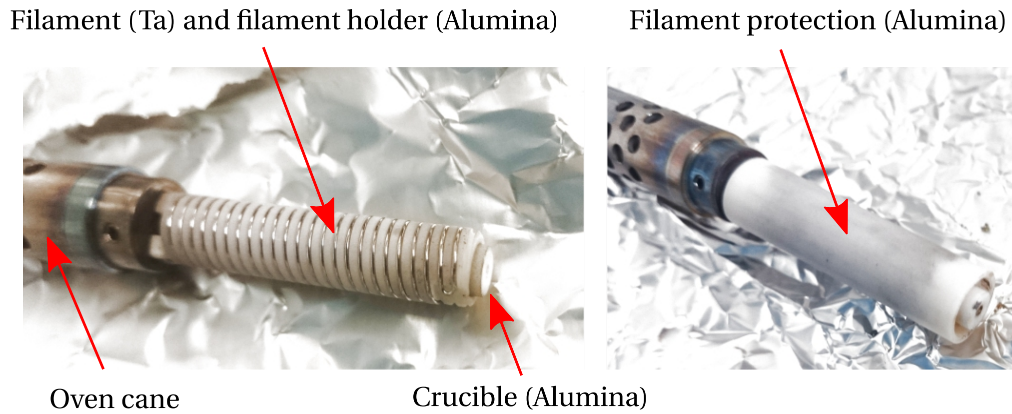

Figure 2.6.: Photo of the filament holder, the filament and the filament protection around it. These parts parts are made out of alumina except the filament, which is a tantalum wire.

back towards the centre of the oven. All oven parts are placed within the outer oven cover which also contributes to the insulation but is mostly physically protecting the oven. This part is also made out of tantalum.

2.6.4. The cane

To insert the oven into the plasma chamber it is mounted on the tip of a long cane. This allows to insert and extract the oven from the plasma chamber without breaking the source vacuum by passing the oven through an airlock during extraction from and insertion into the source plasma. Besides being the oven holder it also serves the purpose of conducting the heating current to and from the oven filament. Figure 2.8 shows a drawing of the electrical connections of the oven and the cane.

Its main body consists of a long stainless steel tube with the same diameter as the outer oven cover. In its middle a long wire that is electrically isolated from the outer metal is guiding the current towards the filament. This wire passes an electrically insulated vacuum feedthrough. One end of the filament is connected to the inner conductors with a connector piece stabilized by an alumina ring inside of the cane. The contact is ensured by two screws whose ends are pressed against the filament. The other end of the filament is in electrical contact with the outer cane, were the current is returned to the cane end. In contrast to the inner conductors the outer cane is on the same potential as its surrounding, i.e. ground potential (during offline experiments, as presented in chapter 4) or the ion source body.

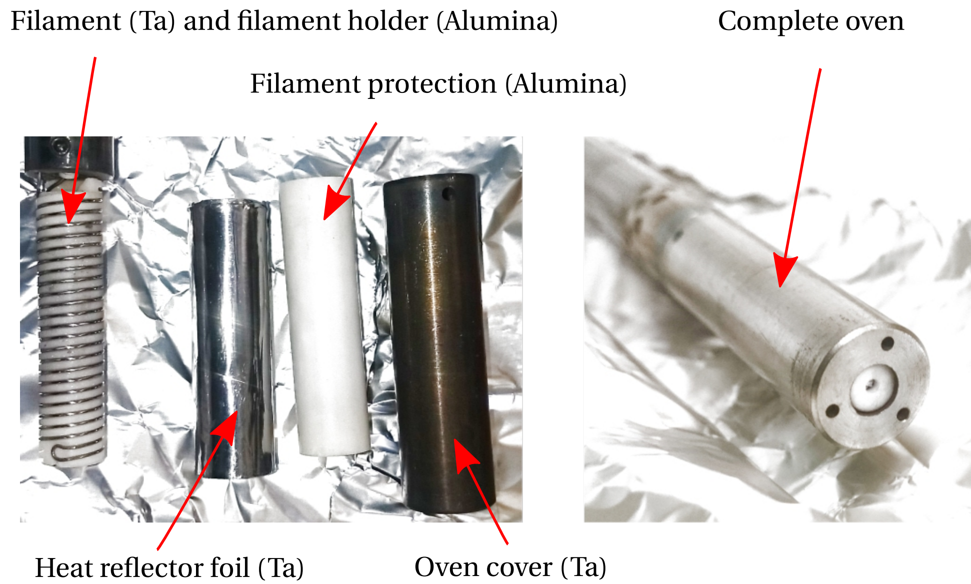

Figure 2.7.: Photo of the layers outside of the filament and a photo of the fully assembled oven.

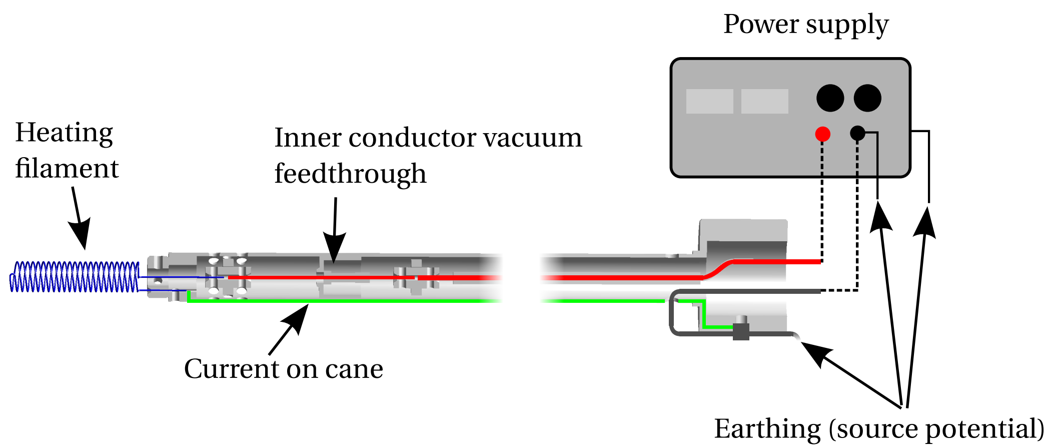

Figure 2.8.: Scheme of the electrical connection of the filament, the cane and the power supply. All earthing points are at the same potential, i.e. either ground or the high voltage potential of the ion source.

2.6.5. Operation cycle at the source

Before being inserted into the source, the crucible is filled with a sample of isotopically pure lead (^{208}Pb), with a mass of approximately 1.5 g. For the high energy particle experiments the involved particles need to be well defined. If a mixture of isotopes comes out of the source a separation in the beamline would be required which would reduce the useful beam current that exits the source.

After the oven is filled it is inserted into the source vacuum. The amount of heating is defined by a power value, which is stabilized by a feedback loop that acts on the power supply of the oven. After around 1 h of bakeout, with a power of 3 W, the power is ramped up until the lead ion output is sufficiently high, which is the case at around 7 W but can vary from run to run. Subsequently the heating power is raised routinely by the operator based on experience and lead ion current at the source. Raising the oven power is part of the common actions taken when the source current is decreasing. The operation cycle is ended when the oven reached 20 W and its power would need to be raised more to maintain a sufficiently intense ion current.

The threshold of 20 W is chosen to not damage the oven with too high temperatures. As this is usually the case after two weeks of operation the refilling is pre-scheduled for the GTS-LHC ion source. This allows to adapt the operation of the CERN accelerator chain to the approximately 10 h of missing beam from the source. However this cycle leaves the oven with roughly half of its lead filling still in the crucible. Attempts to operate the oven significantly longer have not lead to satisfying results.

As the GTS-LHC ion source features two ovens in its plasma chamber the second oven could be used to prolong the operation time, but it is not possible to run this oven for another two weeks in the described cycle. The plasma and the buffer gas that are present in the plasma chamber during the operation of the first oven seem to affect its performance [39].

The choice of when and how much the oven power is being ramped up is based on experience while the link of the oven performance and lifetime and the input parameters has not been studied yet. From the fact that the crucible filling can not be entirely used in one operational cycle it can be deduced that there is room for improvement.

3. Theory and Simulations

To understand and optimize the functionality of the lead oven and to define the optimization strategy it is crucial to understand the underlying physical processes. Two characteristics have been studied, the properties of the lead gas jet coming from the oven and the thermal profile of the oven. The first part of this chapter presents the physics of the gas jet and how it can be modeled by simulations. In the second part the relevant thermal transport mechanisms are presented. In the last part of this chapter thermal simulations are shown which are used to get information about the expected thermal distribution of the oven and its crucible. Several different simulation models are presented and compared with the aim to understand influences on the temperature profile of the oven.

3.1. Vapour pressure and evaporation rate

A characteristic quantity for the evaporation of substances is their vapour pressure. Being kept in an enclosure with a certain range of pressures and temperatures all substances can exist in an equilibrium with both a gas and a condensed phase, so either liquid or solid [40].

Molecules in this case change between those two phases by either evaporation or sublimation from the condensed phase to the gas or condensation from the gas to the condensed phase. The equilibrium is characterized by the same rates of evaporation and condensation. The partial pressure that is exerted by the gas onto the walls of a container in such an equilibrium is called the vapour pressure. It depends on the actual substance and on the temperature in the container.

If the temperature rises, the vapour pressure also rises, which leads to a bigger part of the substance going into the gas phase. In this way the equilibrium could stop existing if the vapour pressure is so high that it requires all molecules of the substance to be part of the gas phase. On the other hand if e.g. a gas liquid equilibrium is kept in a container and one adds more of the respective substance while not changing the temperature of the system, the additional substance would only add to the condensed phase. The described

behaviour can only be observed within a temperature limit. Above this critical temperature a substance will not condense at any pressure and a two phase system is not possible (at very high pressures the liquid and gas phase become indistinguishable). This is for example the case for oxygen or nitrogen at room temperature [41].

3.1.1. The lead vapour pressure

The vapour pressure of a substance depends on its temperature. An approximate way to derive the vapour pressure for different temperatures is the Clausius Clapeyron equation. In its integrated form ([42]) it gives the relation between two parameter combinations of vapour pressure and temperature, $p_{v,1}$ at T_1 and $p_{v,2}$ at T_2, using the enthalpy of vaporization ΔH_{vap} and the gas constant R_{gas}:

$$\ln \frac{p_{v,2}}{p_{v,1}} = \frac{\Delta H_{\text{vap}}}{R_{\text{gas}}} \left(\frac{1}{T_1} - \frac{1}{T_2} \right) \ . \tag{3.1}$$

This equation assumes the gas to be an ideal gas and the substance dependent enthalpy of vaporization to be constant over the temperature range of T_1 to T_2. For the vapour pressure of liquid lead an empirical relation, given in [43] (originally from [44]), can be used:

$$\log_{10}(p_v \ [\text{Pa}]) = 5.006 + A_{\text{Pb}} + \frac{B_{\text{Pb}}}{T[\text{K}]} \ , \tag{3.2}$$

where p_v is the lead vapour pressure in Pa and A_{Pb} and B_{Pb} are measured coefficients. These are: $A_{\text{Pb}} = 4.911$ and $B_{\text{Pb}} = -9701$. The temperature T can be chosen from the melting point of lead at $T = 327.5\,°\text{C}$ to at least $T = 1200\,°\text{C}$ and the results will have a 5 % accuracy or better compared to measured values. Equation (3.2) with different coefficients and if needed also higher order terms, can be used for a large range of metallic elements and substances. Figure 3.1 shows the lead vapour pressure calculated from equation (3.2) together with 3 values from [43] for a large range of temperatures.

3.1.2. Evaporation

Evaporation is the process of particles leaving a condensed phase and becoming part of a vapour. When the same amount of particles condensate back into the liquid or solid, the two phases are in equilibrium. The molecular theory of gases gives a relation between the flux density of ideal gas particles impinging on a surface, J, their average velocity $\bar{v}$ and the density of particles n:

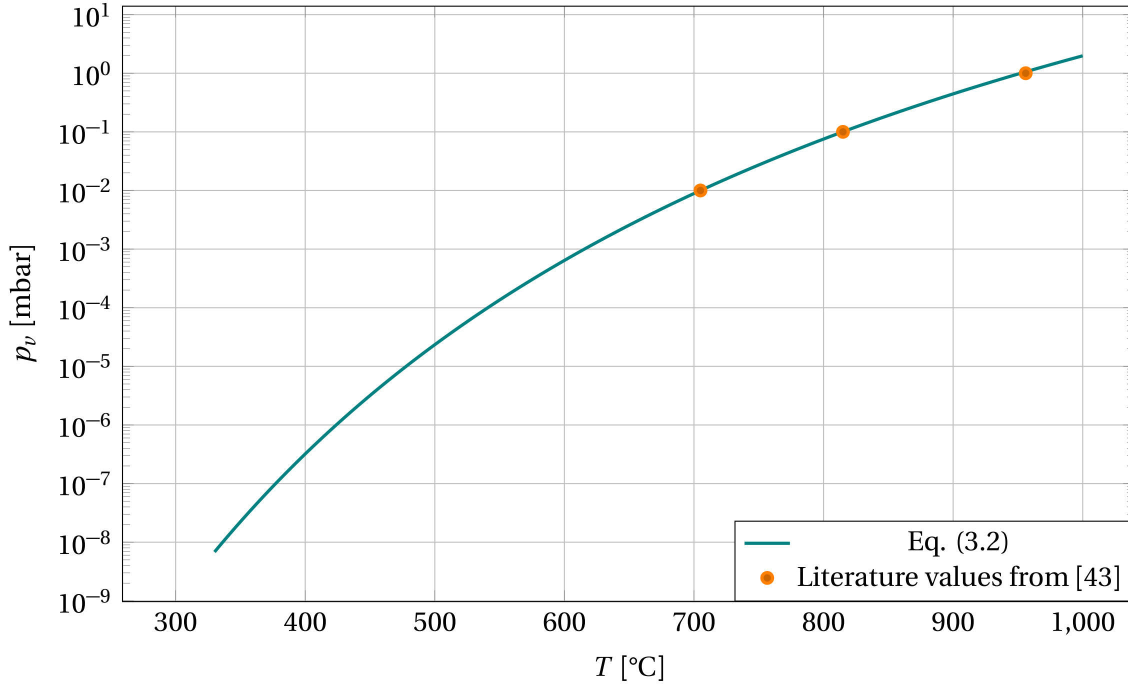

Figure 3.1.: Vapour pressure of lead following from equation (3.2), where the values of Pa where converted to mbar and the temperature K to °C. The plot also shows three literature values from [43].

$$J = \frac{n\bar{v}}{4} \ . \tag{3.3}$$

From the Maxwell-Boltzmann distribution of speeds within the gas at a temperature T it follows:

$$\bar{v} = \sqrt{\frac{8k_\text{B}T}{\pi m}} \ . \tag{3.4}$$

Here m is the mass of the gas particles and k_B the Boltzmann constant. As the gas density can also be linked to the pressure p at temperature T, using:

$$p = nk_\text{B}T \ , \tag{3.5}$$

equation (3.3) can be brought into the form:

$$J = \frac{p}{\sqrt{2\pi m k_\text{B} T}} \ . \tag{3.6}$$

If one considers a liquid in a container that is in equilibrium with its vapour phase

($p = p_v$ at temperature T), equation (3.6) can be used to calculate the amount of particles hitting the surface of the liquid phase. A fraction of these molecules will enter the liquid phase again, making them the condensation flux density J_{cond}:

$$J_{\text{cond}} = \alpha J \quad . \tag{3.7}$$

The coefficient α gives the fraction of particles, that condensate when they are hitting the liquid phase. If the container is closed, the rate of particles exiting the liquid, J_{evap}, and condensing on it is the same, so $J_{\text{evap}} = J_{\text{cond}}$. Now one can assume an opening in the container, reducing the surrounding pressure to $p < p_v$. This leads to a reduction in the flux of particles onto the liquid phase, while the amount of particles evaporating stays the same. Hence the net evaporation rate per surface area $J_{\text{evap,net}}$ becomes:

$$J_{\text{evap,net}} = \frac{\alpha(p_v - p)}{\sqrt{2\pi m k_{\text{B}} T}} \quad . \tag{3.8}$$

This is the Hertz-Knudsen equation for evaporation, that allows calculating the rate of particles evaporating from a liquid substance at a certain temperature, if its vapour pressure and its evaporation coefficient α is known. From the origin of the equation the different values can be resumed:

- $J_{\text{evap,net}}$: The evaporation rate of the substance per surface area in $\text{at}\,\text{s}^{-1}\,\text{m}^{-2}$.
- p_v: Vapour pressure of the concerned substance in Pa at the temperature T.
- α Evaporation coefficient of the substance. A unit less number.
- p: Partial pressure of the vapour from the concerned substance in Pa. The presence of another gas is not considered, i.e. this is not a background pressure from the atmosphere.
- m: The atomic mass in kg.
- T: The temperature of the vapour and of the liquid in K.

It is used for applications where vacuum evaporation takes place and gives usable results for the evaporation of metals when the right evaporation coefficient is chosen [45]. But it needs to be taken into account that it is an interpolation from an assumed equilibrium and does not include a theory of how the evaporation mechanism actually works. To fit the results to measured values the evaporation coefficient is adapted for different substances.

It also does not consider the influence of another gas so the equation does not give the evaporation rate in relation to e.g. the quality of the surrounding vacuum. Yet it is known that another gas present above the evaporating substance will also decrease the evaporation rate. This can be explained as a two step process: The second gases particles can collide with the particles evaporating and thereby increase the fraction of the evaporating particles re-entering the condensed phase. This will however only have an influence if the pressure of the second gas is in the same range or higher as the vapour pressure [46]. In the case of the lead oven it is especially difficult to make assumptions about the background pressure p of the vapour close to the liquid lead inside the crucible. Here the Hertz-Knudsen equation can be used to give an estimate of the maximum achievable evaporation rate by assuming $p = 0\,\mathrm{Pa}$.

To include the atoms re-condensing in the crucible a simulation model is used that is described in the section 3.4. To validate the applicability of the simulation the following section presents an estimation of the flow regime inside the crucible and around the oven.

3.2. Flow regime of the lead gas jet

The flowing characteristics of a gas jet and thereby its divergence and profile depend on the density and the temperature of the gas particles in the jet. Several regimes can be distinguished which lead to different particle distributions and flowing speeds. These differences lie in the number of interactions between the individual gas particles compared to the interactions of particles with surrounding structures like walls.

A common coefficient used to determine the flow regime is the Knudsen number Kn, which is the ratio of the mean free path of a gas particle, λ, to the characteristic length of the system, l [41]:

$$Kn = \frac{\lambda}{l} \quad . \tag{3.9}$$

When the mean free path of the gas particles is long compared to the characteristic length of the system, it is likely that a gas particle traverses from one wall interaction to the next without encountering other particles. In the opposite case, the gas behaves like a continuum with a flowing behaviour closer to that of fluids.

Table 3.1 shows the flow regimes and their respective Knudsen number ranges. However there is no abrupt transition from one regime to another and the Knudsen number is only an orientation. The border between molecular and transitional flow is stated at different Knudsen numbers in different references, e.g. at $Kn = 1$ in [47], or at $Kn = 10$ in [48].

Knudsen number	Gas flow regime
$Kn < 0.01$	Continuum
$0.01 \leq Kn \leq 1.0$	Transitional
$Kn > 1.0$	Molecular

Table 3.1.: Overview of the flow regimes assigned to different Knudsen numbers.

With the different regimes of a gas come different ways of describing and simulating its dynamics, which makes the determination of the respective flow regime an important step. The mean free path of a gas molecule depends on the number density of the particles n and their cross sectional size σ:

$$\lambda = \frac{1}{\sqrt{2}n\sigma} \quad . \tag{3.10}$$

The size σ can be replaced by the molecule or atom diameter d and the number density n can be calculated from the gases temperature T and pressure p using:

$$p = n k_\mathrm{B} T \quad , \tag{3.11}$$

with the Boltzmann constant k_B. With these replacements equation (3.10) becomes:

$$\lambda = \frac{k_\mathrm{B} T}{\sqrt{2}\pi d^2 p} \quad . \tag{3.12}$$

Equation (3.12) shows that besides information about the size of the particles also knowledge about the temperature and the pressure is needed. In case of the lead oven, the species of the particles is lead, whose atoms have a diameter of $d = 360\,\mathrm{pm}$.

As a result of the small size of the crucible and the oven, the pressure is not easily measured and needs to be estimated. Within the oven crucible the vapour pressure p_v can be used as an upper limit. This couples the values $p \approx p_v$ and T in equation (3.12) as the vapour pressure is temperature depended. The other needed quantity for the Knudsen number in equation (3.9) is the characteristic length of the system, l. In a long gas filled pipe this length is usually chosen to be the diameter, as it is a good estimation of the distance a particle needs to overcome to make an interaction with a wall rather than with another particle. For an empty crucible this leads to the length of $l = 3.4\,\mathrm{mm}$, which is used as an estimate because the lead distribution in the crucible is not known.

Figure 3.2 shows the result of the estimation of the Knudsen number in dependence of the temperature T. Until the temperature of 800 °C the flow regime is the molecular flow, above this temperature it is the transitional regime (see table 3.1).

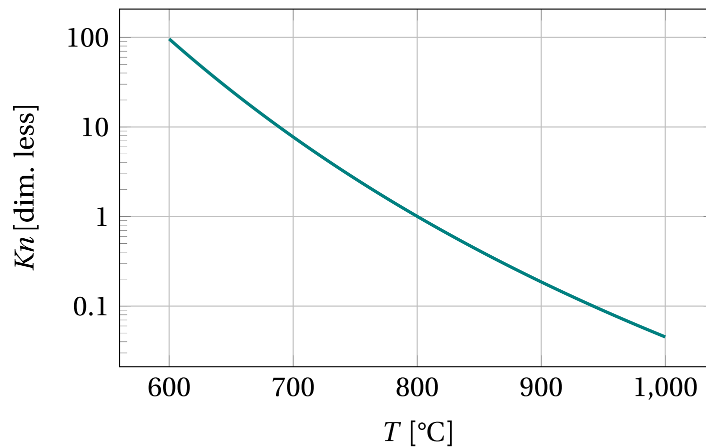

Figure 3.2.: Knudsen number estimation for the flow inside of the oven crucible. For the pressure in equation (3.12) the vapour pressure of lead is assumed and the characteristic length is the diameter of the crucible. The temperatures are chosen to contain the operational regime of the oven (see e.g. figure 3.14)

The big range of numbers comes from the strong temperature dependence of the vapour pressure, which changes the mean free path length over several orders of magnitude within a temperature range that is realistic for the crucible. One can assume that the pressure outside of the crucible and outside of the oven is several orders of magnitude lower than the vapour pressure of lead at the temperature within the crucible.

This leads to longer mean free path length that also overcome the longer characteristic lengths outside of the oven. From these assumptions it is evident that the dynamics of the gas jet coming from the crucible will not behave like a fluid but rather needs to be treated as a molecular flow.

3.3. Knudsen's cosine law

The molecular flow is a flow regime found in systems with high and ultra high vacuum (less than 10^{-4} mbar). Here the particles translate from one wall interaction to the next, without relevant amounts of interactions with each other. An equation emerging in several processes is called Knudsen's or Lambert's cosine law.

It links the measured amount of particles coming from a desorbing or reflecting surface to the cosine of the angle between the observer and the surfaces normal. It is the underlying relation used to model gas particles entering a space through an orifice or their scattering at a wall in the Molflow+ simulations presented in the following section.

The cosine law is also assumed to describe how the directions of the atoms are distributed

that exit the liquid lead surface in the crucible and enter the gas phase. In section 3.4.3 it is discussed how this influences the geometry of the gas jet in the simulation.

From the gas dynamics perspective the law can be deduced from the following consideration, following the explanation in [41]: An enclosure is filled with gas particles moving in all directions. From a small opening in this enclosure they can enter a space, free of gas particles (All particles leaving the enclosure are being pumped).

As the particles are moving in all angles with the same probability inside the enclosure, the rate density of particles emitted from the hole is the same in all directions. But only the particles having the same direction as the surface normal of the hole will see the full size of the hole as their aperture. Particles moving with an angle θ to the surface normal see a reduced aperture, which gets smaller as the angle becomes larger. If a particle is moving parallel to the surface of the hole, i.e. its angle to the normal is $\theta = 90°$, it will not be able to exit the enclosure.

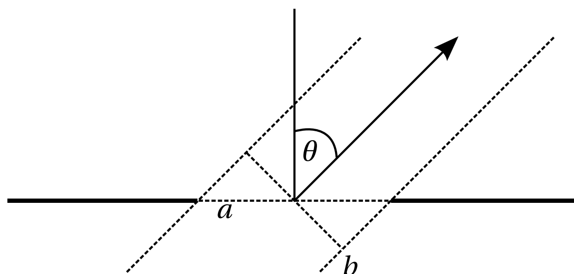

Figure 3.3.: Geometry of Lamberts cosine law in 2D. If particles leave the opening a into the direction of the arrow, they see a reduced aperture b whose size is $a \cos\theta$.

The geometry is sketched in a 2D version in figure 3.3. If the molecular flow regime is assumed, the particles will propagate in straight lines after having passed the opening without interacting with each other. This leads to a flow rate $J(\theta)$ that only depends on the angle θ:

$$J(\theta) = J(0)\cos\theta \quad . \tag{3.13}$$

Here $J(\theta)$ is the number of particles that leave the opening in a certain amount of time into a unit solid angle with the angle θ to the surface normal and $J(0)$ the amount that goes into the unit solid angle directly facing the hole ($\theta = 0$). The law also applies for the behaviour of particles that are being scattered after hitting a wall, which is described in more detail in [41].

3.4. Molflow+ simulation model

Molflow+ is a program to simulate the molecular flow regime using a Monte Carlo algorithm and ray tracing, developed by Roberto Kersevan and Marton Ady at CERN [49, 50]. As particle to particle interactions play no role in this regime the particles can be treated independently and are traced through the geometry from one wall interaction to the next. The system is represented as so called facets, the walls, in the 3 dimensional space. Each facet has several characteristics that need to be defined:

- The desorption rate.
- The sticking factor.
- The opacity.
- The temperature.

The first two characteristics are the particles way of entering and leaving the system. A positive desorption rate on a facet leads to particles streaming into the simulated environment.

The sticking factor is the probability that a particle will be absorbed at the facet during a hit. The opacity defines, whether particles can pass the facet or if they are exclusively either reflected or absorbed. A facets temperature has no effect on the path of a particle but it affects its speed. Following from these characteristics a cycle in the simulation can be described as follows.

A particle is emitted from one of the facets with positive desorption rate. The initial direction is random with a probability based on the cosine law presented in section 3.3. Following its direction it is traced to the next facet to interact with. Here it can either pass, be absorbed or change its direction. The direction changes are again based on the cosine law, which describes the scattering of gas particles on a rough surface. A mirror like reflection only happens when this was specified for the respective surface.

When the particle is finally absorbed the cycle is ended. Only now, the speed evolution of the particle is calculated. Based on the amount of hits and the particle speeds, pressure values on the facets can be calculated. It is evident that only a sufficiently large number of these cycles leads to a realistic density or pressure distribution in the simulation.

3.4.1. The oven geometry in Molflow+

To create a Molflow+ simulation two steps are necessary: Facets, defining the geometry of the system need to be created and their characteristics have to be defined.

As Molfow+ allows the import and transformation of CAD models, the ANSYS DesignModeler, a part of the ANSYS Workbench package [51], could be used to define and prepare the geometry for the gas simulations.

For the simulation of the gas jet coming from the crucible of the lead oven, only the relevant geometry needs to be considered and big parts of its setup, like the cane for the insertion into the vacuum of the source, is not needed.

Used for the simulation geometry are only parts of the oven from the inner back end of its crucible to the oven tip. To make the simulation and the facets produced out of it simpler, the underlying CAD model of the oven was further simplified. The geometry of the filament is rather complex, but it can be expected to have a vanishingly small influence on the behaviour of the lead flow, as it is not in the path of lead atoms leaving the crucible.

For that reason the filament was removed from the geometry. Additionally the grooves that fix the filament inside of the support structure (see subsection 2.6) were filled. As an outer boundary to the simulation a cylinder was chosen. Figure 3.4 shows the resulting CAD geometry.

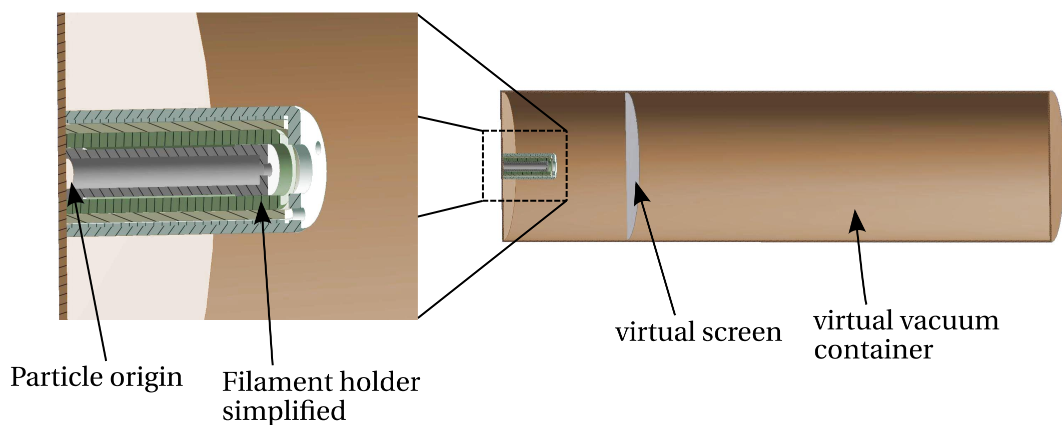

Figure 3.4.: The geometry for a Molflow+ simulation prepared with the ANSYS DesignModeler.

Another step before importing the model to Molflow+ is the inversion of the geometry. This means that the resulting drawing is a single body that represents the gas volume itself and not the surrounding walls.

When the body is then imported into Molflow+, the program creates appropriate facets to enclose it. After the conversion into facets, some of them can be simplified using the

functionalities of Molflow+.

When the systems geometry is defined, the characteristics need to be assigned to the different facets. Figure 3.5 shows the resulting model. In the depicted model the particles are launched from the back of the crucible. Section 3.4.2 presents alternations to this setup. The walls of the crucible are chosen to be repelling and do not absorb any particles, as they should be hot enough to prevent any condensation on them.

For the following evaluation also the outer parts of the oven are assumed to not absorb any particles, which is not true in reality. The outer cylinder is giving the boundary conditions and its properties could establish a surrounding lead gas pressure outside of the oven. In the case of the oven test stand (see chapter 4) its walls are cold and one can assume here that any impinging lead atoms will condensate and leave the gas. So the outer facets are set to absorb 100 % of the impinging atoms.

As it can be seen in Figure 3.5 additional facets were included that are completely transparent to the simulated particles but count them ass they pass, which can be used to depict the lead gas jets geometry.

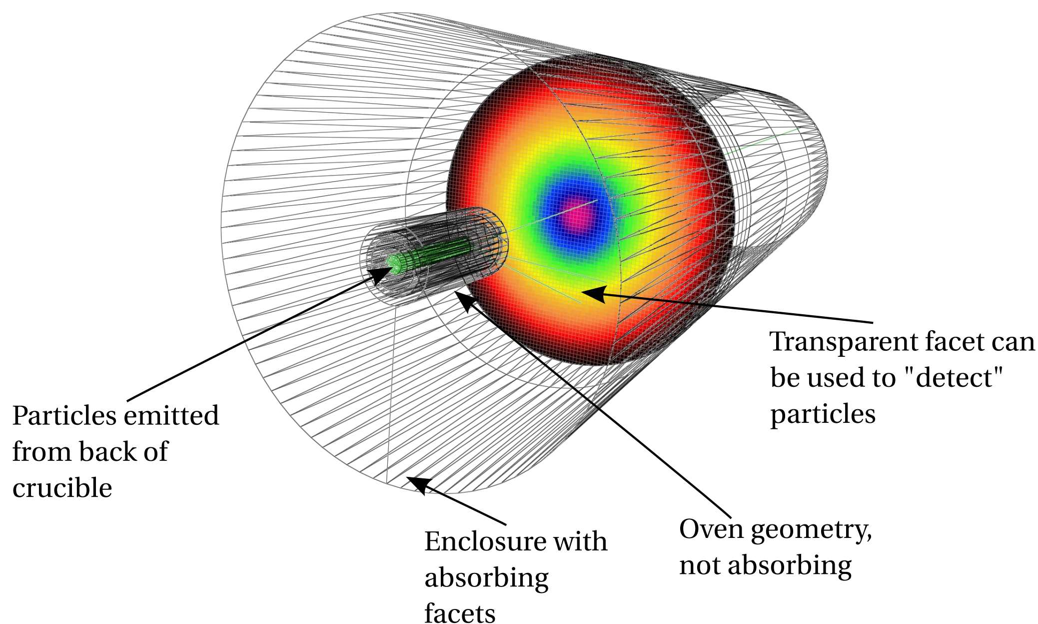

Figure 3.5.: Simulation of the lead gas jet from the oven in Molflow+. The surrounding enclosure is assumed to be completely absorbing. The particles are launched from the back end of the crucible, to create a homogeneous distribution within the crucible. The structure of the oven is not absorbing and reflects the particles according to the cosine law. The profile in front of the oven is a transparent facet that counts the passing particles in a predefined resolution (here 10 cells per cm). These can be used to analyse the beam profile at arbitrary positions.

3.4.2. Lead consumption rates deduced from the Molflow+ model

Molflow+ allows an estimation of the evaporation rates of lead at different temperatures in the oven, assuming that the molecular flow regime is dominating the gas behaviour. The basic principle of the simulation is to establish the lead vapour pressure close to the assumed lead surface in the crucible by choosing the right amount of particles being emitted from the emitting surface.

For the correct pressure values the crucibles temperature also needs to be defined. A simple model is, to assume the crucible to have a homogeneous temperature T where the lead establishes the vapour pressure $p_{v,T}$ according to equation (3.2).

As the molecular flow regime is linear, it is sufficient to start a simulation with the desired crucible temperature and an arbitrary emission rate, e.g. $J_{\text{start},T} = 1.0\,\text{mbar}\,\text{l}\,\text{s}^{-1}\,\text{cm}^{-2}$.

The pressure on the outside of the crucible close to the emitting surface, $p_{\text{start},T}$, is measured for each crucible temperature. The emission rate can then be scaled using:

$$J_{\text{evap,sim},T} = \frac{J_{\text{start},T}}{p_{\text{start},T}} p_{v,T} \quad . \tag{3.14}$$

For this kind of simulation an assumption about the lead distribution within the crucible has to be made.

Lead surface position in the crucible

The real distribution of the lead inside of the crucible is not visible or accessible when the oven is operated. From the remaining lead after the use of the oven, like shown in figure 3.6, one can assume that the lead forms a meniscus and is not spreading over its bottom.

In the Molflow+ simulation the lead distribution is represented by the emitting surface. Different positions of a potential meniscus can be taken into account by moving the emitting surface within the crucible as shown in Figure 3.6.

Results

The results for the different cases are shown in figure 3.7 together with the prediction of the Hertz-Knudsen equation (3.8).

The results presented in figure 3.7 show that the evaporation rate needed to establish the vapour pressure close to the lead surface can differ.

This can be explained by the geometry of the crucible. In the cases A and B the emitting surface is larger than the crucible opening and thereby the crucible reflects particles back

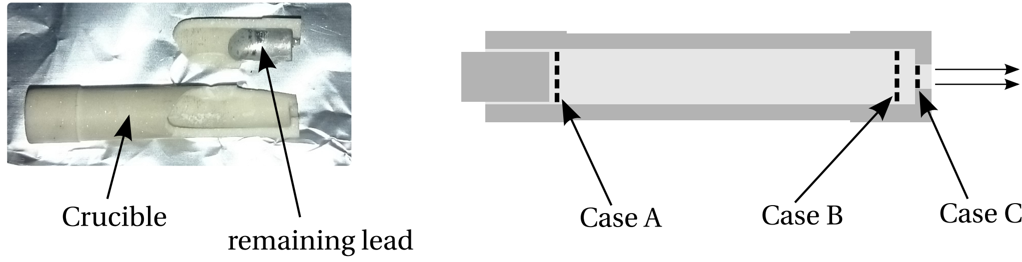

Figure 3.6.: Left: A photo of a crucible that was smashed after a measurement at the oven test stand. Right: Positions of the emitting surface that where used to calculate the evaporation rate from the oven at a range of temperatures.

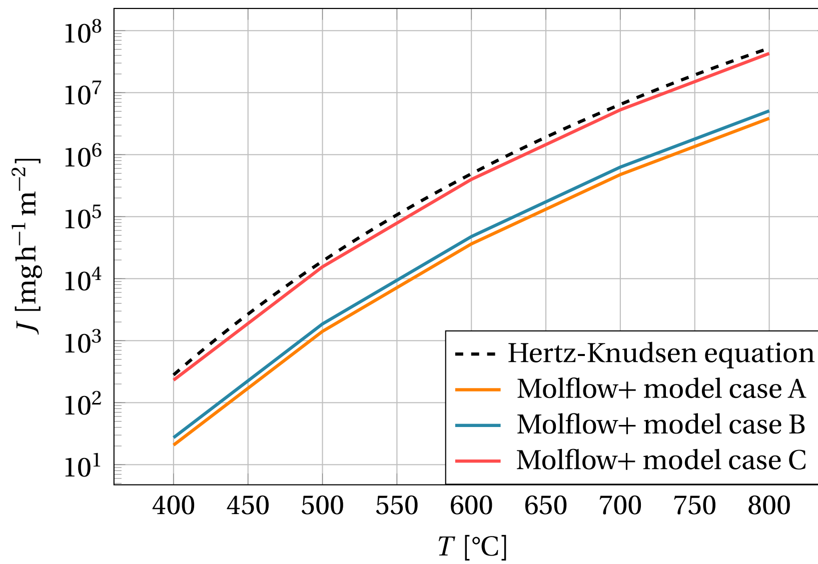

Figure 3.7.: Evaporation rates per surface area for the different positions of the lead surface within the crucible shown in figure 3.6.

to the surface. In case C the emitting surface is directly at the front opening of the crucible, where a big part of the particles leaving the surface will not be reflected back to it.

This is close to the case that can be predicted by the Hertz-Knudsen equation, when the background pressure is assumed to be $p = 0\,\mathrm{Pa}$ and $\alpha = 1$. The prediction of the Molflow+ simulation and the Hertz-Knudsen equation in this case show very similar results.

To calculate a total evaporation rate of the oven, $R_{\mathrm{sim}}[\mathrm{mg\,h^{-1}}]$, i. e. the amount of lead evaporated per time, the rate $J_{\mathrm{evap,sim},T}$ needs to be multiplied with the area of the emitting surface. The surface size for the cases A and B is $a = 9\,\mathrm{mm}^2$ and in the case C it is, $b = 1.7\,\mathrm{mm}^2$. Figure 3.8 shows the resulting total evaporation rates.

The curves show the large range of total evaporation rates coming from realistic lead

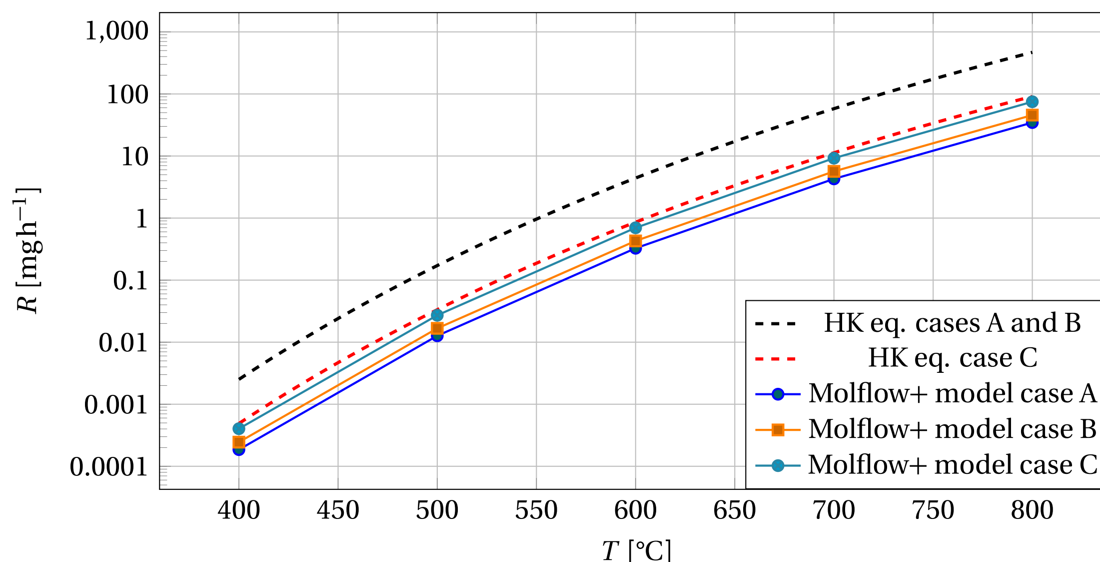

Figure 3.8.: Total evaporation rates of the Linac3 lead oven, from the Molflow+ model and of an estimation using the Hertz-Knudsen equation (3.8) in one case assuming a surface of $a = 9\,\mathrm{mm}^2$ and the other $b = 1.7\,\mathrm{mm}^2$.

temperatures.

The different positions of the lead surface cause differing rates. The closer the lead surface is to the crucible opening the higher is the total evaporation rate and the difference is up to a factor of two between case A and case C.

The Hertz-Knudsen equation only gives a good estimate of the total evaporation when it is assumed that the emitting surface has the size of the crucibles opening.

A comparison with measurements at the oven test stand is given in chapter 5, section 5.5.4 (see figure 5.41).

3.4.3. Transversal profile of the gas jet

Another result from the Molflow+ model is information about the transversal geometry of the lead gas jet coming from the crucible. This information is e.g. helpful to assess the calibration of the deposition detector in the oven test stand (presented in section 4.4). It was also used to study the lead oxide blockage formation process (presented in section 5.2.3.

As shown in figure 3.5 the information about the gas flow in the simulation is analysed using a certain type of facet. Such a facet is set to be transparent to the gas and has a texture defined by its resolution in cells per cm. For transversal information the facet needs to face the oven tip at some distance, as also shown in figure 3.5.

In the case of the lead oven it is more desirable to know the impingement of particles on a certain area, $J_{\mathrm{im.}}$ [at m^{-1}] rather than a pressure profile, where also the impingement angle of each particle plays a role. So the facets were used to record the value $J_{\mathrm{im.}}$ for the different assumed positions of the emitting lead surface that are shown in figure 3.6, at a distance of $d = 50$ mm as as the deposition detector at the oven test stand was usually placed 50 mm away from the oven tip.

The linearity of the molecular flow regime leads to the same $J_{\mathrm{im.}}$-profile at all emission rates, while of course the total amount of impinged particles differs. Figure 3.9 shows the result for the different cases, with normalized impingement rates, $J_{\mathrm{im.,nrm}}$.

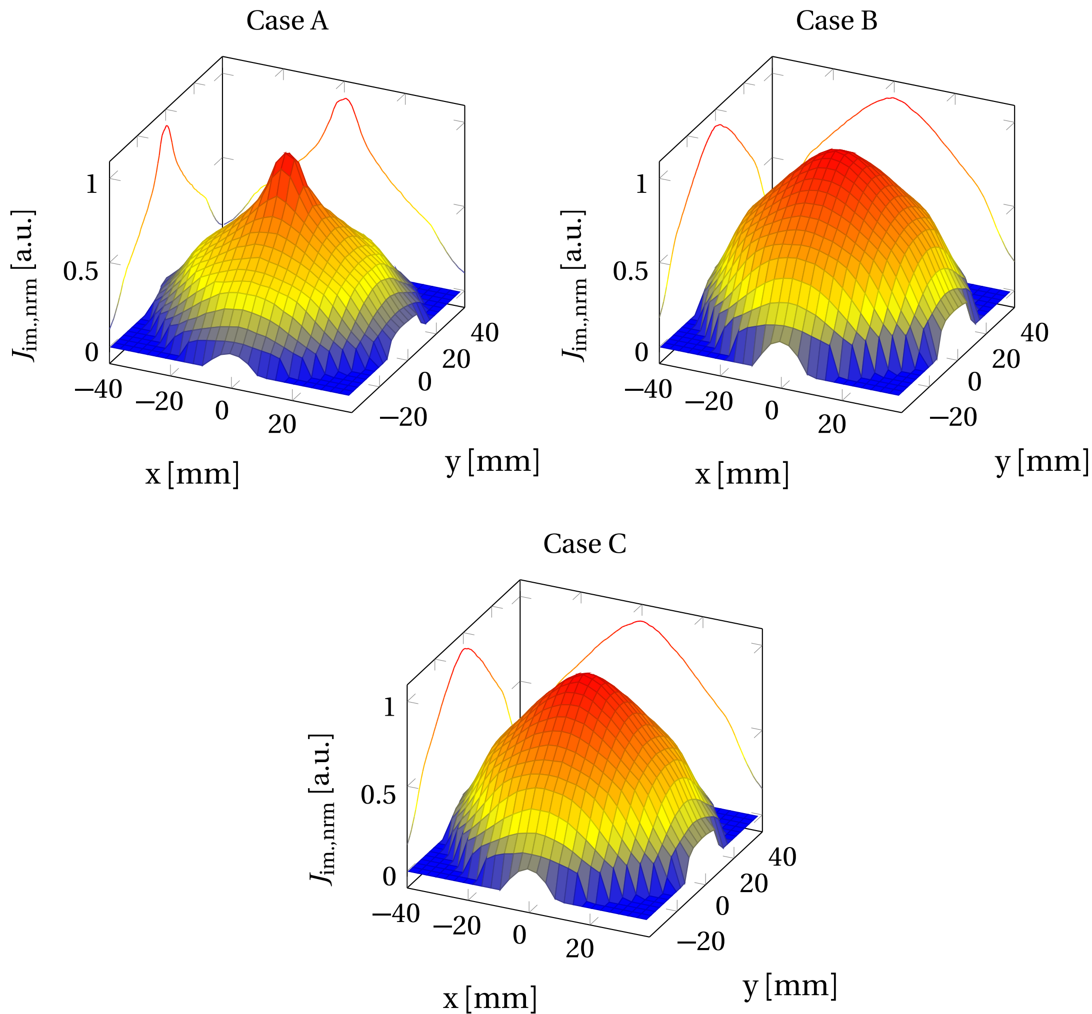

Figure 3.9.: Normalized impingement rate on a facet, placed 5 cm away from the oven for the 3 cases shown in figure 3.6. The lines besides the surface plot show the outline of the projection of the impingement profile.

It can be seen that the evaporation profile is not the same for the different cases. When

the lead surface is further in the back of the crucible, the gas jet gets a distinct peak in the middle while a lead surface at the front of the crucible causes a rounder distribution.

A theoretical distribution for a flat surface in front of an evaporation source can be derived from the cosine law (3.13) that was presented in section 3.3. When assuming that behind the opening hole inside the crucible the gas particles follow the required homogeneous distribution and that the hole itself has no wall thickness, an impingement rate can be calculated by [52]:

$$J_{\mathrm{im.}}(x) = \frac{J_{\mathrm{im.,0}}}{(1+(x/d)^2)^2}\,, \tag{3.15}$$

where $J_{\mathrm{im.}}(x)$ is the impingement rate on a flat surface in front of the emitting one, $J_{\mathrm{im.,0}}$ the impingement at the centre of the surface, d is again the distance from from the emitting surface at which the profile is determined, and x a distance from the centre as shown in figure 3.10.

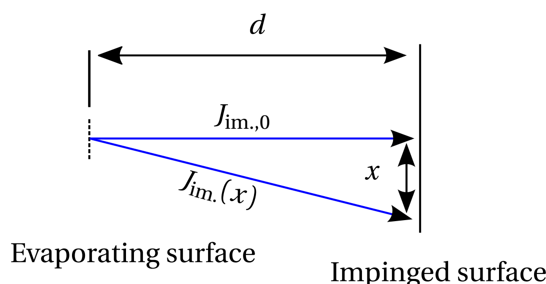

Figure 3.10.: Geometry used to calculate the transversal gas profile of the lead oven with the cosine law in equation (3.15).

To compare the calculated impingement with the simulations, without including information about the total rate, one can set the maximum rate to one. Figure 3.11 shows the resulting profile as a transversal outline.

The cases B and C are in reasonable agreement with the simple cosine law over a wide range, while the peak in the profile of case A can not be described that simple. Especially for the case C this is not surprising as the emitting surface is directly facing the facet used to detect the particles and Molflow+ determines the particles emission according to the cosine law.

3.4.4. Discussion

The simulation of the lead oven, using Molflow+ relies on the assumption that the molecular flow regime is dominating the gas flow behaviour inside and around the oven. The

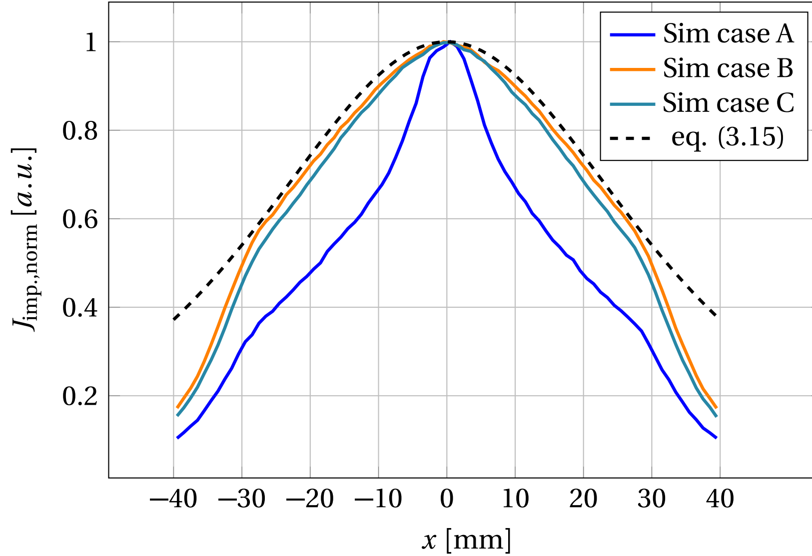

Figure 3.11.: Outline of the transversal profile of the lead gas jet $d = 50$ mm away from the oven tip. The dashed line shows the transversal outline that follows from the cosine law (equation (3.15)).

previous section 3.2 presents the calculation of the Knudsen number, assuming the pressure inside of the crucible is the lead vapour pressure. The Molflow+ model itself can be used to asses if it predicts lead gas pressures outside of the crucible that lead to mean free path lengths that make particle to particle interactions unlikely also on larger scales.

Figure 3.12 shows the mean free path of the gas particles calculated from equation (3.12) using the pressure, given by the Molflow+ model on the symmetry axis around the oven tip for the emitting surface being in the back of the crucible (case A). The pressure in the crucible starts at $p = 7.5 \times 10^{-2}$ mbar, which is the vapour pressure of lead at 800 °C. The starting point of the axis s is arbitrary, within the crucible and growing s values correspond to positions closer to, or exceeding the oven tip. The dashed lines show, starting from the left, the position of the inner front end of the crucible, the crucible exit and the outer oven tip.

In figure 3.2 it can be seen, that at 800 °C the gas inside of the crucible is still in the molecular flow regime. The derived pressure profile then leads to the conclusion that it is consistent to also assume molecular flow everywhere outside of the crucible. Therefore the Molflow+ model is self consistent up to an oven temperature of 800 °C. At higher temperatures the flow inside of the crucible can be influenced by particle to particle collisions which might influence the evaporation rates.

The gas jet outside of the crucible however will still be in the molecular flow regime

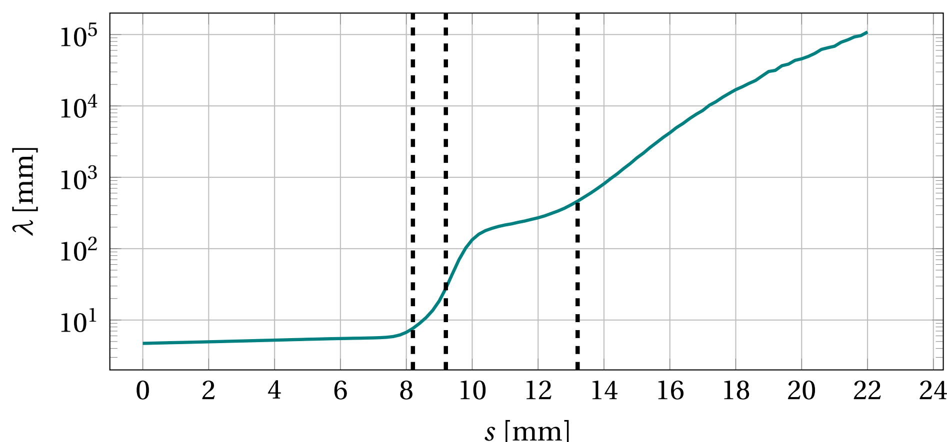

Figure 3.12.: Mean free path of the gas particles calculated from equation (3.12) using the pressure, given by the Molflow+ model on the symmetry axis around the oven tip for the emitting surface being in the back of the crucible (case A, $s = 0$). The dashed lines show, starting from the left, the position of the inner front end of the crucible, the crucible exit and the outer oven tip.

at higher temperatures due to the large drop in pressure outside of the crucible. So the prediction of the shape of the jet coming from the oven and going into a vacuum should be correct for all achievable pressures inside of the crucible. The model was created to get an understanding of the oven gas flow behaviour, the link between its total evaporation rate and the temperature in the crucible and also the geometry of the gas jet coming from the oven.

As it was assumed that the oven is evaporating the lead into a complete vacuum, the transferability to the operation at the oven test stand is higher than to the one at the real ion source. While at the oven test stand the oven evaporates into an enclosure with defined pressure, in the case of the ion source the pressure in front of the oven and the influence of the plasma on the gas jet is not known. Further results of the Molflow+ simulations will be presented in later chapters together with measurements.

3.5. Thermal transport mechanisms

The oven is a device that heats the lead sample to a sufficient temperature to evaporate the lead. It is evident that understanding the functionality of the oven is linked to understanding its thermal characteristics, like the relation of power and temperature and its spacial temperature distribution. This section introduces the basics of thermal transport mechanisms that define the temperature distribution of the oven. A later section then

presents ways to model these processes with thermal simulations.

Thermal transport is the exchange of heat from a hotter to a colder body, which is generally an energy transfer. Three different thermal transport mechanisms are distinguished: Conduction, convection and radiation. The following short description of these phenomena follows the explanations in [53].

3.5.1. Conduction

The process called conduction describes the flow of heat within a body or between two connected bodies that goes from a hotter part to a colder part of the system without the transport of material.

Molecular lattice vibration and temperature are tightly linked. The higher the temperature the more energy is stored in the molecular vibrations. Interactions between particles can transfer this energy within a body and thereby even out temperature differences until an equilibrium is reached. This process is called conduction. The easiest case is an ideal gas, where the temperature is a measure for the average kinetic energy. The conduction happens through collisions between the gas particles, where particles with a higher kinetic energy than average loose energy while particles with lower energy gain it. In solid bodies the nature of the energy transfer depends on the material and involves molecular lattice vibrations and, in electrically conducting materials, mainly the motion of free electrons. As a macroscopic phenomenon, conduction in a body is described by Fouriers law [53]:

$$\mathbf{q} = -k_{\text{therm.}} \nabla T \quad . \tag{3.16}$$

where $\mathbf{q}$ is the heat flux density vector (given in $\mathrm{W\,m^{-2}}$), $k_{\text{therm.}}$ the bodies thermal conductivity in $\mathrm{W\,m^{-1}\,K}$, ∇ the nabla operator and T the scalar temperature field in K. The minus indicates that heat flows from the higher to the lower temperature.

3.5.2. Convection

Convection describes the transport of heat when a moving medium like air or water is involved. The microscopic interactions are similar to conduction but in this case a material transport plays a role. For example a stream of air that is blown against a relatively warmer body will cool this body more efficiently than resting air of the same temperature. Here the heat is not only transported by interactions between particles but also by movements of the material carrying the heat energy. The movement of the material itself can be a

consequence of its temperature (like the rise of hot air within a larger body of cold air in a gravitational field). In this case it is called free or natural convection. If the movement is caused by a mechanism that is not connected to the temperature (like the previous example of a stream of air that is blown against another body) it is called forced convection.

3.5.3. Thermal radiation

Conduction as well as convection can transport heat between bodies that are somehow connected, either touching directly or via a medium. Thermal radiation allows heat transport between bodies even if they are separated and in a perfect vacuum.

It is electromagnetic radiation, usually of wavelengths between 0.1 µm and 100 µm, caused by the thermal movement of charges in a liquid or solid body whose temperature is greater than absolute zero. The radiation emitted by a body cools the emitting body and heats up bodies exposed to it, while it can of course also receive heat radiation of other bodies. This way the thermal radiation is another mechanism that transports heat between bodies.

The Stefan Boltzmann law describes the power P that is emitted by a black body of (absolute) temperature T [54]. In an expanded form for realistic materials it reads:

$$P = A_{\mathrm{surf}} \epsilon \sigma_{\mathrm{B}} T^4 \quad , \tag{3.17}$$

where A_{surf} is the surface of the body, ϵ its emissivity, and σ_{B} the Stefan-Boltzmann constant. When two bodies of temperature T_1 and T_2 are exposed to each others thermal radiation, a heat Q (in W) is transported from the hotter body to the colder one. Assuming body one is hotter, the heat evaluates to:

$$Q = A_{\mathrm{surf},1} \mathfrak{F}_{1-2} \sigma_{\mathrm{B}} \left(T_1^4 - T_2^4 \right) \quad . \tag{3.18}$$

Here $\mathfrak{F}_{1-2}$ is a viewfactor that depends on the geometry of the two body system as well as their emissivities.

For complex bodies the thermal transport and the resulting temperature profile can be arbitrarily complicated or even impossible to solve analytically. Therefore thermal simulations based on the FEM method are being used. In the following section thermal simulations of the micro oven are being presented.

3.6. 2D model of the micro oven in ANSYS

As the setup of the Linac3 micro oven is too compact to record a detailed temperature profile, especially inside of the oven, thermal simulations can be used to extend the knowledge of the oven. The following sections including this one will present simulations of the oven in the commercial multiphysics software ANSYS. A description of the principle of the simulational method is given in appendix B. ANSYS is a commercial multiphysics simulation software that allows a broad range of simulations, like mechanical stress, deformation, temperatures and also fluid dynamics [51]. A thermal two dimensional model of the Linac3 micro oven created by C. Fichera and V. Toivanen, that was not part of this work, was already presented in [55]. As part of this work is based on the existent two dimensional model it is briefly described in the following part.

The first step of a finite element simulation is creating the appropriate geometry. A two dimensional model can only resemble a 3D geometry that has certain symmetries. As the micro oven and its cane is almost axisymmetric, except certain parts, like the filament, the filament holder and several connector pieces within the oven cane, the 2D model is built under the assumption of axis symmetry where the symmetry axis is the middle of the cane. Figure 3.13 shows how the 2D surfaces for the simulation are derived from the 3D drawing of the oven.

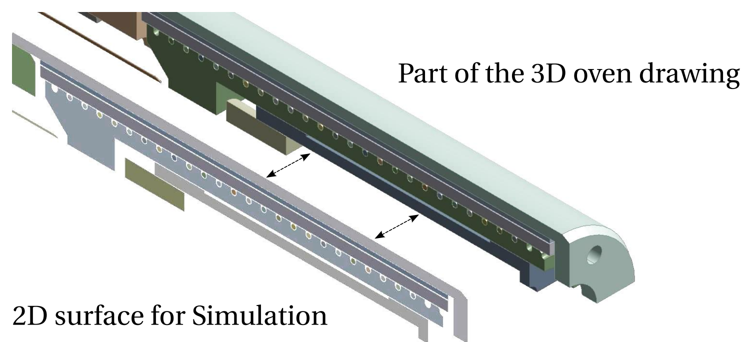

Figure 3.13.: Derivation of the two dimensional geometry for the thermal 2D model of the oven.

As an outer boundary the oven geometry is surrounded by an outer enclosure that completely encloses the oven and its cane.

3.6.1. Materials and connections

In case of the 2D model an individual body is represented by a plane of certain shape. Each body needs an assigned material, that defines its thermal conductivity. In case of

a temperature dependency the conductivity values are given in tabular form for several temperatures and the program will do a linear interpolation between the inserted values (see figure 3.19). As heat conduction might also occur between bodies the connection between bodies needs to be defined. In the case of the oven between most bodies it is assumed that no heat conduction occurs as the touching pressure between the bodies is low due to the construction of the oven. Only where the cane is connected to the oven a conducting boundary is assumed. After the definition of the geometry, the assignment of the materials and the definition of connections, the mesh is created.

3.6.2. Boundary conditions

The next step is to define the boundary conditions of the model, the loads. Several loads are possible:

- Temperature: An edge (1D), a plane / surface (2D), or a body (3D) can have a predefined temperature.
- Convection: A surface or an edge might be exposed to a heat transport due to convection.
- Radiation: Edges or surfaces can emit thermal radiation that will transport heat between the body and other bodies that have a defined radiation boundary.
- Heat flow and heat flux: A defined heat flow or heat flux through an edge or a surface.
- Internal heat generation: A plane or a body generates a defined amount of heat that will be evenly distributed over the body.

Temperature Two regions in the 2D model have a fixed temperature, the end of the cane on the opposing side to the oven and the outside of the outer enclosure. In both cases the temperature here is 22 °C. For the end of the cane this simulates the cooling at the feedthrough, where the cane is inserted into the plasma chamber. The outside of the outer enclosure is the outer boundary of the simulation and in case of the test stand it resembles the test stand walls that are at room temperature and are cooled by the surrounding air.

Convection It is assumed that convection does not play a role for the thermal profile of the oven, as the plasma chamber as well as the test stand are evacuated during its operation. It is however possible that the lead gas jet introduces heat transport by convection that is not modeled in the simulations.

Radiation Radiation is the dominating heat transport mechanism between bodies in the oven assembly, as the setup of the oven insulation is designed to prevent conduction. In the 2D model the radiation happens between the planes representing a body and the radiating parts are the edges of these planes. In ANSYS this means that radiation heat loads are defined on the edges of the planes. Each radiation heat load requires a given emissivity. When the emissivity of the material depends on the temperature it can be given in tabular form, with pairs of an emissivity and a temperature value. The used values are presented in [55]. As they where also used in the 3D model, figure 3.19 in section 3.7.1 shows the emissivity values for the different oven materials.

Internal heat generation The oven is operated at fixed power levels, that are realized by a loop controlling the power supply providing the heating current. A certain power level equals a certain amount of heat being transported into the oven setup by the current. This can be realized as an internal heat generation within the planes or bodies that represent the filament. For the internal heat generation the input value is a heat density in $\mathrm{W\,m^{-2}}$ in 2D or $\mathrm{W\,m^{-3}}$ in 3D. In the 2D model, the resistances of the different conductors that transport the heating current was taken into account, to calculate the fractions of the total power that are lost in each individual conductor. For a given power level the result of this calculation is a total amount of heat that needs to be generated in the planes that represent these conductors. With the area of the plane this can then be evaluated to an internal heat generation value.

3.6.3. Solution and adaption to measurements

The result of a the simulation is a temperature field for every part of the model. Additionally it is possible to derive a field of the total heat that leaves or enters a body at its boundaries. As the dominating heat transfer is radiation, the models behaviour is depending on the input of the emissivity values. It was shown by C. Fichera et al. that the emissivity of tantalum affects the model the most, and the emissivity values of copper, stainless steel and tantalum where adapted to resemble temperature measurements at the test stand [55].

Figure 3.14 shows the resulting temperature for two parts of the oven, a copper pin inside of the crucible and the oven cover, for heating powers between 1 W and 20 W. The copper pin was used to fixate a thermocouple inside of the crucible. As each body in the simulation has a distribution of temperatures, the plot shows the temperature range that is present in the respective distribution at a certain heating power.

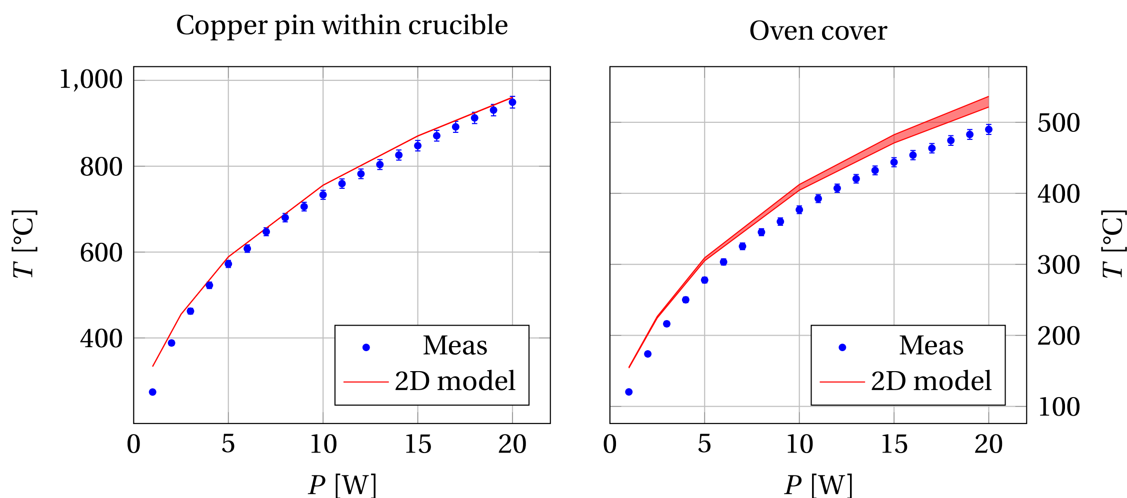

Figure 3.14.: Temperature of the oven cover and a copper pin within the crucible, against heating power. The simulation and the measurement were done before this work and are presented in [55].

The resulting 2D model was used during this work to simulate different aspects of the oven. The following section presents results that where obtained using the 2D model.

3.6.4. Oven tuning needed due to the temperature profile

During the operation of the GTS-LHC ion source the heating power of the oven is one of the frequently adapted tuning parameters. It needs to be raised throughout the run to maintain stable ion beam production. Normally the oven power was raised starting from around 7 W to a final value of 20 W within two weeks of operation at the source.

However when the emitting lead surface within the crucible does not change in size or position, a constant temperature of this surface would lead to a constant evaporation rate (see section 3.4.2). Thus one would not expect that it is necessary to adapt the heating power.

It was studied whether the simulated temperature profile can partly explain the need for the raise in heating power. For this purpose two distributions of lead within the crucible where simulated using the 2D model.

The geometry

In the first case the complete crucible is filled with liquid lead, while in the second case the lead is only occupying a small fraction of the crucibles volume. In both cases it was

assumed that the lead sample, when molten, stays in a cylindrical shape due to surface tension.

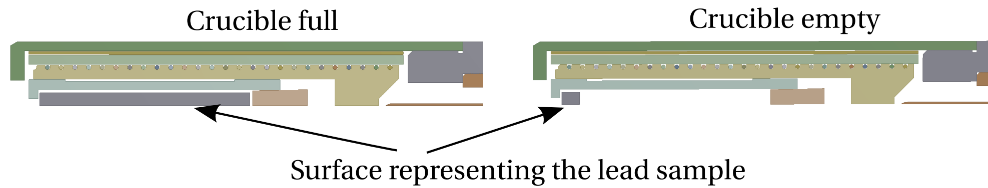

Figure 3.15.: Geometry of the surface representing the cylindrical lead sample in the 2D simulation. On the left: The crucible is newly filled. On the right: The crucible is almost empty with the remaining lead gathered at the tip of the crucible.

The real distribution is not known. At the oven test stand the remaining lead within the crucible, after a run where not all lead was consumed, was always in a cylindrical shape and in most cases in the front of the crucible.

Parameters of the molten lead

For the liquid lead the thermal conductivity and the emissivity needed to be defined. The conductivity was defined with the two values given in table 3.2 [56] [57].

Temperature [°C]	Conductivity [$\mathrm{W\,m^{-1}\,K^{-1}}$]
327.5	15.5
1200	23

Table 3.2.: Conductivity values used in the 2D simulation for the molten lead from [56] and [57].

ANSYS interpolates and extrapolates the conductivity from these values, which is appropriate as the temperature dependence of the conductivity of lead is close to linear.

No published data on the thermal emissivity of molten lead could be found but the simulation showed a low sensitivity on the emission coefficient. Two cases where tested, a constant emissivity value of 0.43 which is published for solid rough or oxidized lead and a value of 0.057 which is published for solid polished lead [58] (Similar in [59]).

Results

Figure 3.16 shows the resulting temperature span of the surface, that represents the lead in the two simulations.

It can be seen that there is a temperature difference between the lead that fully fills the crucible and the lead that is only taking up the tip of the crucible. So, while the oven is

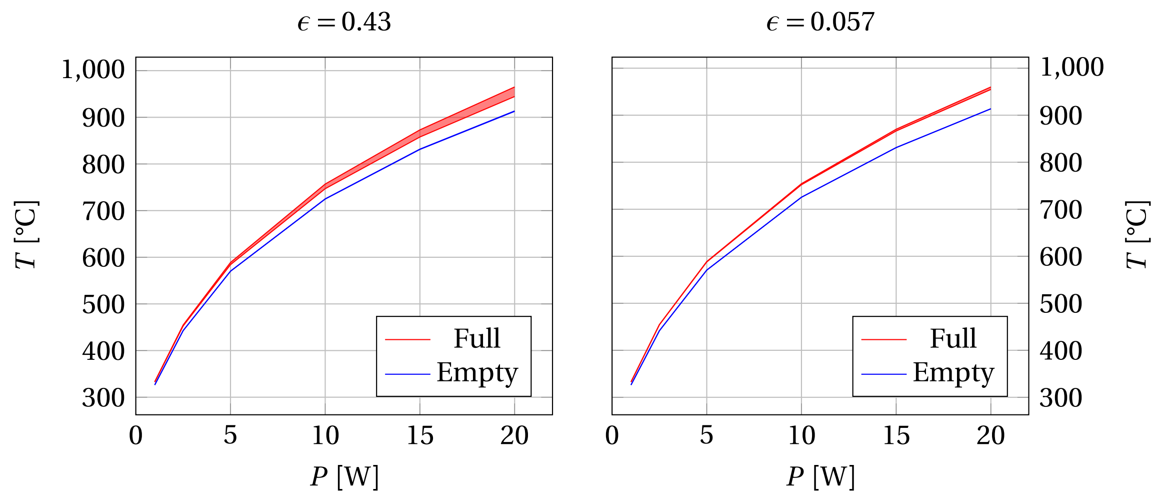

Figure 3.16.: Lead temperature from the thermal 2D simulation for two bodies that resemble a full and an empty crucible. Two different emissivities, ϵ, of the lead where assumed, 0.43 on the left and 0.057 on the right.

operated and the lead sample is consumed it is possible that the overall temperature of the lead changes at a stable power due to redistribution within the crucible.

However it is also evident that the difference in temperature would only need a correction of some watt and does not explain the necessity of raising the oven power e.g. from 8 W to 20 W. This hints that also other mechanisms are involved in reducing the lead gas flow from the crucible like another lead surface position. Other mechanisms that can affect the total evaporation, like blockages and temperature instabilities where found experimentally as presented in chapter 5.

3.7. 3D model in ANSYS

To asses weather the predictions of a 3D model resemble those of the 2D simulation and to be able to simulate non symmetrical structures, in this work, a 3D model of the oven in ANSYS was developed, based on the existing 2D model. It replicates the boundary conditions of the 2D model but with a geometry that resembles the oven in three dimensions. Several versions of the model where created as the level of detail heavily affects the needed computing time.

3.7.1. Detailed model: 3Df

A detailed 3D model, for referral called '3Df', was created including all of the oven parts that also are included in the 2D model and using the same boundary conditions. The basis for the geometry is the CAD model that was used to produce the oven and can be found in the CERN database EDMS [60].

Several adaptions had to be made to allow a proper simulation of the thermal radiation. This mainly consisted of avoiding overlapping geometries, as some bodies in the original CAD model share geometry at the same place in space. The tip of the filament was reshaped to not stick into the surrounding alumina cylinder. Also at the connection of the outer oven cover and the end of the cane some parts of the geometry needed to be cut away to allow heat exchange by radiation.

The mesh which is then created from the geometry is a compromise to the computing time. It was adjusted to be fine enough at certain places to represent the complex geometry from e.g. the filament and the filament holder and is coarser at places with simple geometries like the oven cane. Figure 3.17 depicts the mesh for some of the oven parts.

The ANSYS mesh metric can be used to asses the quality. It is a number between 0 (lowest quality) and 1 (highest quality) that calculates the ratio of the volume of an element and the sum of its edge lengths. Here on average the mesh quality is 0.73. Even with this rather coarse mesh the model is computational heavy and the iterative process can take a long time (For 10 W approximately 13 d of CPU-time on the CERN High Performance Computing (HPC) cluster lxplus and using 48 cores [61]).

The loads

The loads used in the model are the same as in the 2D model. This mainly means that all surfaces are radiating the heat with the respective temperature dependent emission coefficient, for their material. Figure 3.18 shows the material assignments of the 3D model which also determines the assignment of the thermal emissivity that is being used.

Figure 3.19 shows the temperature dependent emissivity values that are assigned to each material and that are also used in the 2D model [55].

Figure 3.20 shows the other loads of the 3D model besides the radiation loads, which are assigned to every surface of the model. In the 2D model the connection between the oven cane and the piece connecting the oven to the cane was evaluated have a thermal conductance coefficient of $14\,500\,\mathrm{W\,m^{-2}\,K^{-1}}$ ([55]). In the 3D model two additional connections with conduction are introduced which are also shown in the figure 3.20. As here the oven

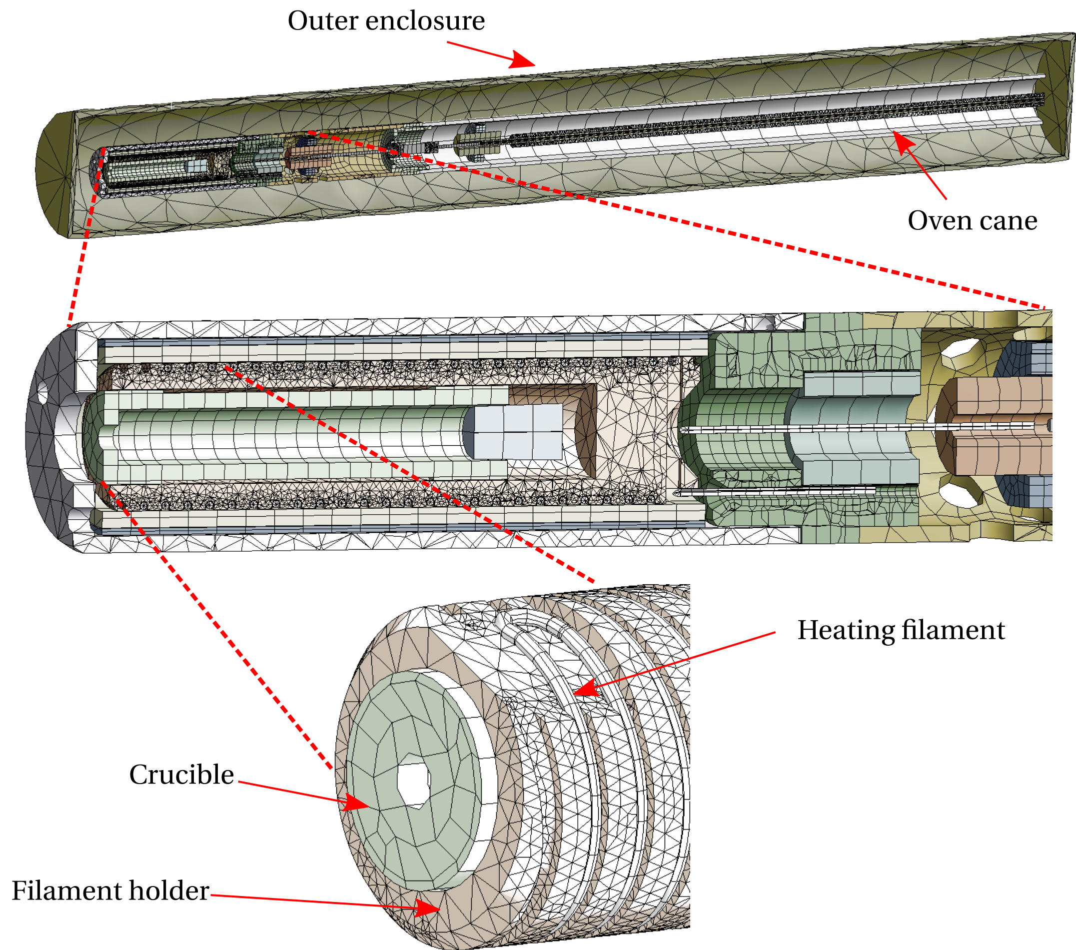

Figure 3.17.: Appearance of the mesh for the three dimensional oven model in ANSYS. The mesh is a compromise between representing the geometry correctly and not introducing too many nodes.

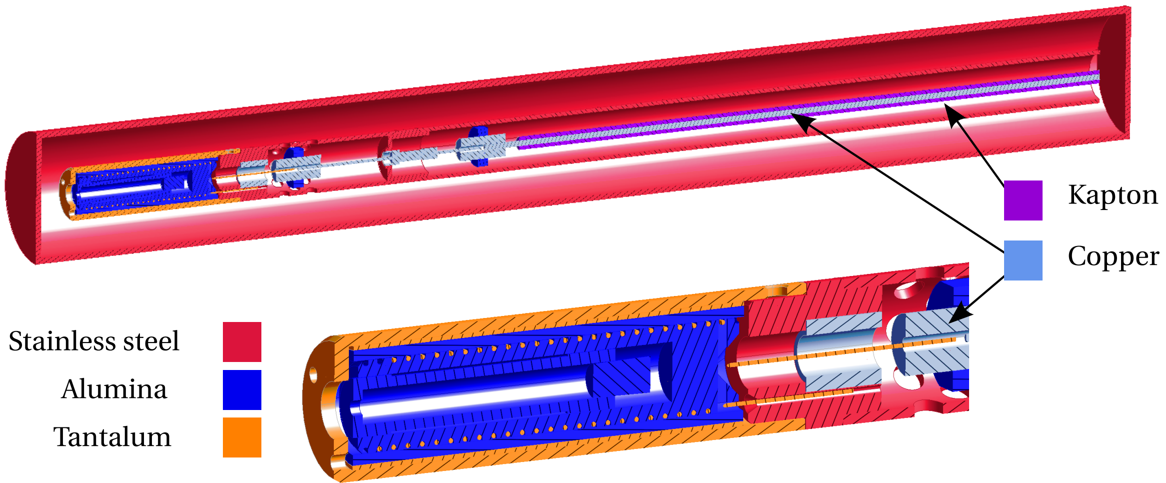

Figure 3.18.: The material assignments at the 3D model of the oven.

is welded the connections are assumed to be perfectly conducting, i.e. the temperature of both bodies at the connection needs to be the same.

While the radiation boundaries can be directly transferred from the 2D model, the internal heat generation has to be adapted. For a scheme of the current carrying parts of the oven see figure 2.8.

In the 2D model the bodies are represented by planes. But if these planes are revolved around the symmetry axis the resulting shape is not the same as in the 3D model. For example the 3D model features the real shape of the filament, which is a single long body and the volume of this body can be a different one than the theoretical ring shaped filaments from the symmetrical 2D model.

When the heat generation is given as a density, e.g. in $[\mathrm{W\,m^{-3}}]$ the total heat generated depends on the volume of the body. Therefore the heat density input in the 3D model needs to be adapted. To convert the internal heat generation from the 2D model ($h_{2D}/[\mathrm{W\,m^{-3}}]$) to a corresponding heat generation for the 3D body ($h_{3D}/[\mathrm{W\,m^{-3}}]$), the volume $V_{\mathrm{cond.2D}}$ of the theoretical symmetrical conductors from the 2D simulation is needed. This can be calculated from the respective surface area $a_{\mathrm{cond.2D}}$ of the conductors in 2D:

$$V_{\mathrm{cond.2D}} = 2\pi r_{\mathrm{rot.}} a_{\mathrm{cond.2D}} \quad , \tag{3.19}$$

where $r_{\mathrm{rot.}}$ is the distance of the surface centre to the symmetry axis. Using this volume the internal heat generation can be adapted:

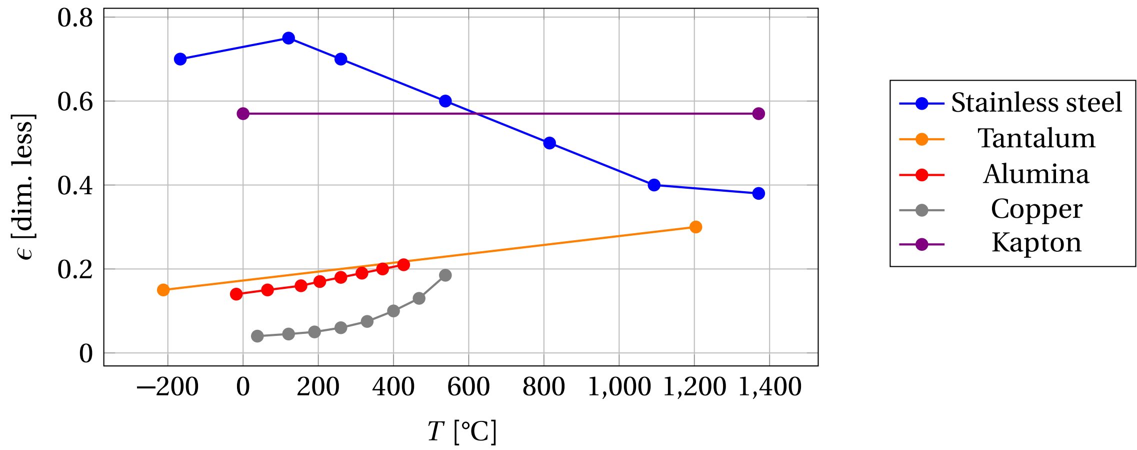

Figure 3.19.: Thermal emissivities of the materials that are used in the 3D model. The values at temperatures below 20 °C are used for ANSYS to make the correct interpolation.

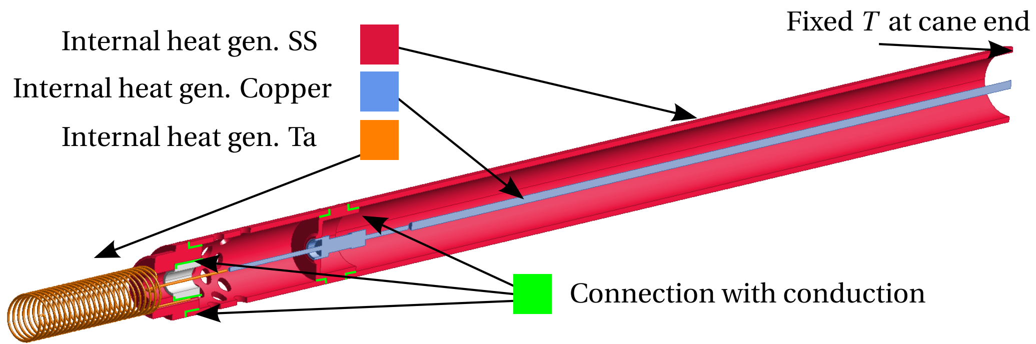

Figure 3.20.: Loads and contacts of the 3D oven model, apart from the radiation. The heat generation happens in all parts that transport the heating current, weighted with their respective resistances.

$$h_{3D} = h_{2D} \frac{V_{fil.2D}}{V_{fil.3D}} \quad . \tag{3.20}$$

Table 3.3 shows the heat generation values of the 2D conductors and the derived heat generation for the 3D model.

The difference in volume for the copper conductor in 2D and 3D stems from the different representation of this body in 3D. In the 2D model the cane is simplified and does not feature the vacuum feedthrough of the inner conductors. As described in appendix B, simulations containing temperature dependent values like conduction or emissivity (and generally radiation) are not linear and need to be solved by using an iterative process. It helps to apply the loads like heat generation stepwise. For the heating power of only 10 W the simulation of the detailed 3D model was run with 100 sub steps.

Material	Power fraction	h_{2D} [W mm^{-3}]	$V_{cond.2D}/V_{cond.3D}$	h_{3D} [W mm^{-3}]
Tantalum	0.95	8.47 10^{-3}	1.04	8.81 10^{-3}
Stainless steel	0.027	2.00 10^{-6}	0.9957	1.99 10^{-6}
Copper	0.021	9.9 10^{-5}	1.621	1.6 10^{-4}

Table 3.3.: Heat generation values of the 2D conductors (h_{2D}), the conversion factor $\frac{V_{fil.2D}}{V_{fil.3D}}$ and the derived heat generation for the 3D model h_{3D} for the different conductors.

3.7.2. Comparison of the results to the 2D model

One purpose of the 3D model was to study whether the differences of the body geometries between 2D and 3D change the predicted thermal profile. In this section the thermal profile derived from the 2D model and the 3D model are presented.

Due to the long computation times the 3D model was only simulated up to a maximum heating power of 10 W. Figure 3.21 compares the temperatures of two different oven parts for a range of heating powers up to 10 W. As each oven part has a distribution of temperatures, the plot again shows all temperatures that are present in the respective distribution at a certain heating power.

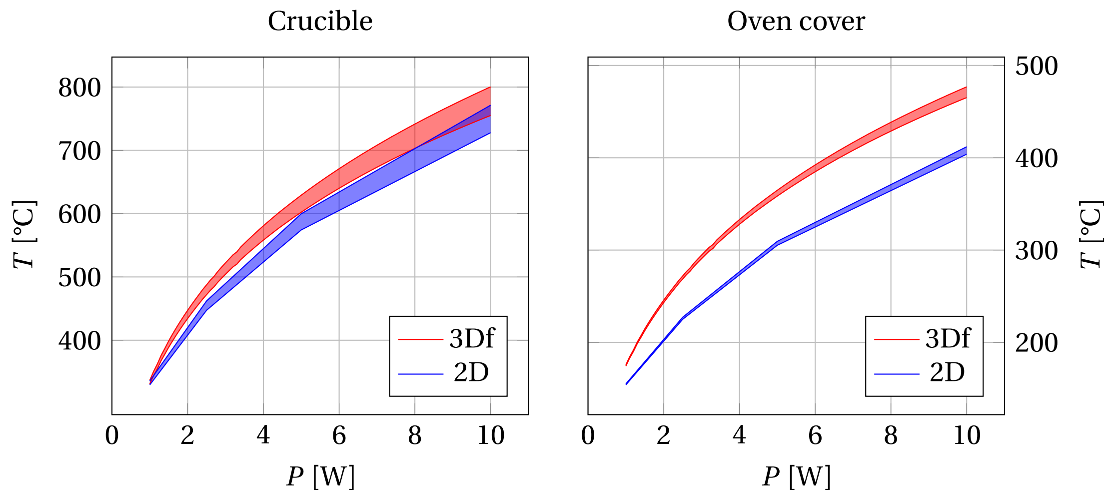

Figure 3.21.: Temperature span of the crucible and the oven cover in the 3D model compared to the 2D model for the same heating power in the filament.

It can be seen that the temperature in the 3D simulation displays a similar power dependency as the one of the 2D simulation. However the simulations show a systematic difference in the predicted temperature for the individual bodies.

While for the crucible the difference in temperature lies within the temperature span of the body itself, the difference in the predicted temperature grows with distance to the

oven center. The right plot of figure 3.21 shows that the temperatures of the oven cover differ significantly between the 2D and the 3D simulation.

Figure 3.22 shows the temperature at a heating power of 10 W along a path within the crucibles wall, that has the same coordinates in the 2D and the 3D simulation.

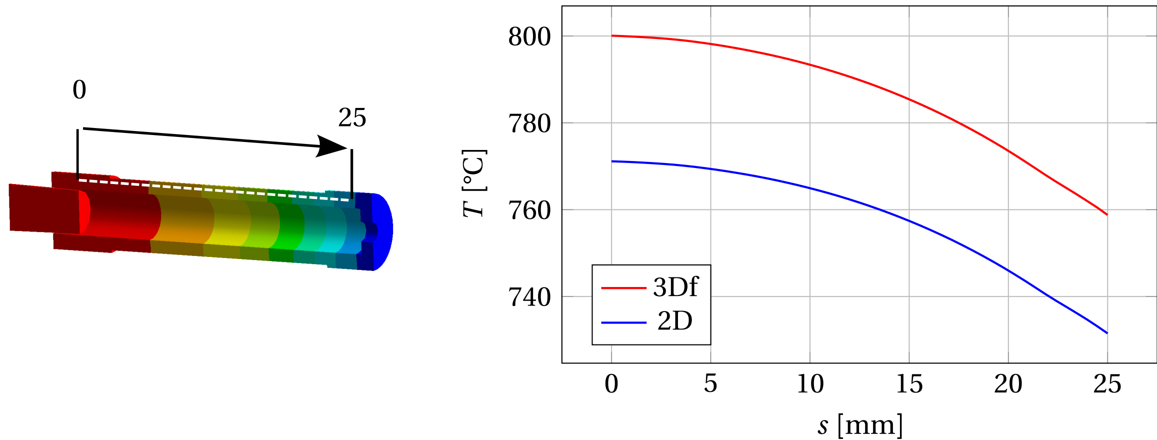

Figure 3.22.: Temperature on a path within the crucible derived from the 3D and the 2D simulation both at a heating power of 10 W.

Both simulations predict a decrease of the temperature towards the tip of the crucible and the decrease shows the same dependency of the position. The only difference seems to be the total temperature. Figure 3.23 shows the general temperature distribution of the micro oven at 10 W as it is predicted by the two models.

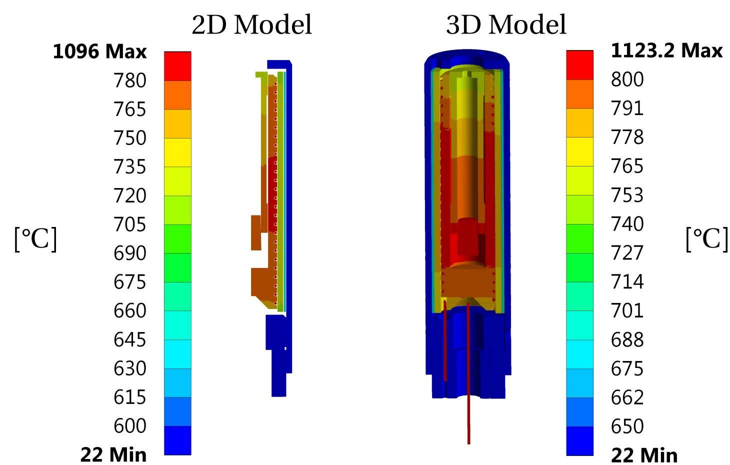

Figure 3.23.: Comparison of the thermal distribution of the micro oven at 10 W predicted by the two models in ANSYS.

Generally the resulting temperature distribution for individual oven parts is similar in the 3D and the 2D simulation, however the total value differs, with the oven cover showing the biggest difference. To asses whether this difference is due to the difference in the geometry or has another reason a second 3D model was developed, that has the same geometry as the 2D model.

3.7.3. Symmetrical 3D model: 3Dy

To analyse the influence of the geometry on the difference of the temperature between the models, simulations of a 3D geometry where performed that resemble the one of the two dimensional oven model, here called '3Dy'.

In a first step the 2D model was simplified by removing parts that do not have a big impact on the thermal distribution of the oven itself. This was done to reduce the computational effort especially for the three dimensional simulation. The simplified 2D geometry was then recreated in 3D by revolving the 2D plane around its symmetry axis. This way the difference in the results of the simulation in 2D and 3D are not caused by different geometries. The connections between the different bodies of the 2D and the 3D model are the same, as well as the boundary conditions like thermal radiation coefficients, fixed temperatures and heat generation.

A difference that can not be overcome easily is again the mesh density. As a 3D model leads to much greater numbers of nodes and also the interaction between different nodes, especially when it comes to radiation, the computation of the 3D model is more complex. While the mesh of the 2D model can be chosen to be as dense as necessary, the finest possible mesh of the 3D model is limited by computational resources. Figure 3.24 shows a comparison of the 2D and the 3D simulation for a heating power of 1 W.

Even for supposedly identical geometries there are differences in the resulting thermal distribution. This shows that also in the more detailed 3D models the differences to the 2D model do not necessarily come from a difference in geometry but e.g. from the way the heat is transported through the model.

Basic geometries

To further assess the different results in 2D and 3D, a series of equal 2D and axisymmetric 3D simulations with simple shapes was performed. Starting from a slice of the 3Dy model that only contains one "filament ring" the shape was simplified until 2D and 3D showed equal results.

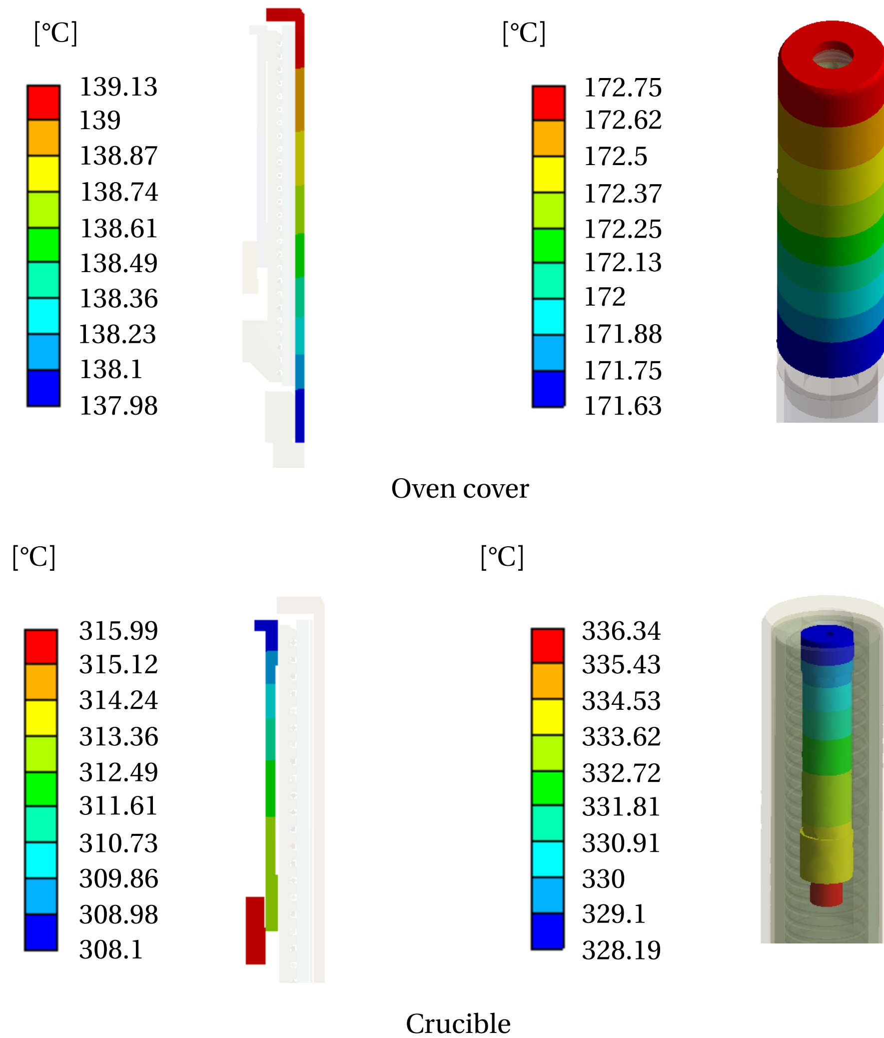

Figure 3.24.: Comparison of a reduced 2D model of the oven with a 3D model that was derived by rotating the 2D model around its symmetry axis, 3Dy. In both cases the heating power is 1 W.

Simulational models All geometries are encapsulated by a stainless steel container whose outside has a fixed temperature of 22 °C. Inside of this container three different geometries were simulated, as shown in figure 3.25.

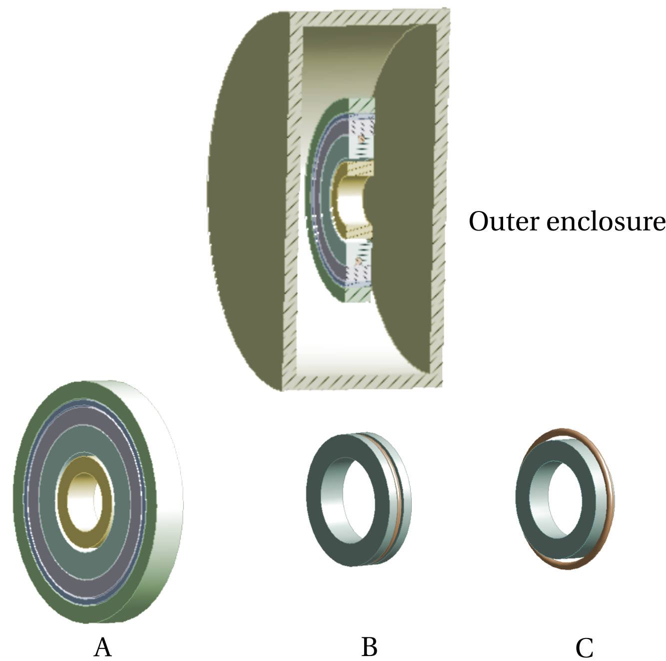

Figure 3.25.: Geometry used for a 3D and 2D comparison of simpler structures. The upper picture shows the outer enclosure that was present in all cases. A: A slice from the 3Dy model that contains one filament ring. B: only the filament holder and the filament. C: Filament holder and filament but simplified.

The case 'A' is a slice from the 3Dy model, that contains one filament ring. The used materials are the same as in the complete model. This time the filament was set on a fixed temperature of 1200 °C instead of a fixed heating power.

In case 'B' only the filament holder and the filament are inside of the container.

In the case 'C' the same bodies are present, but the filament was scaled up with a factor of 1.2 and the groove of the filament holder was evened out.

Results The results for the filament holder that was present in all six simulations is shown in figure 3.26.

For case A the 3D model shows a temperature of around 390 °C while in the 2D model the filament holder has 380 °C. In the case B the temperature in the 3D model is 337 °C while in 2D it is 325 °C. In the case C the 3D model shows 310 °C while in 2D the temperature

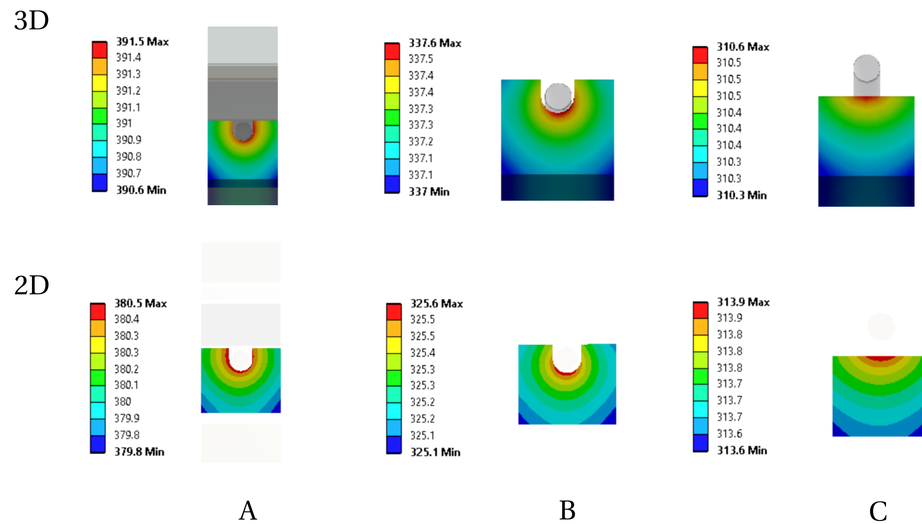

Figure 3.26.: Thermal distribution of the filament holder in all six simulations.

is 313 °C. The oven cover that is only present in case A has a temperature of 221 °C in 3D while the 2D simulation resulted in 208 °C.

Discussion Also for a reduced geometry like case A, the thermal simulations show a difference between 3D and 2D. Case B shows a similar temperature difference as case A and only in case C this difference is significantly reduced. The filament in case C is not embedded in a groove within the filament holder.

This is a hint that the heat transport between filament and filament holder is a problematic part in the simulation. However a modification of the filament or the groove in the filament holder would be a strong deviation from the real geometry of the oven.

3.7.4. Simplified model: 3Ds

As the detailed 3D model in ANSYS is too computational heavy to actively use it to e.g. test modifications of the setup, the geometry was further simplified to reduce its complexity. For this model in a first step some structures, like the conductors inside of the oven cane where removed, as it is assumed that they do not have a big impact on the temperature profile of the crucible. Additionally to that the shape of several parts of the oven was modified. Here a list of the modifications:

- The shape of the filament holder was simplified. At the tip the unused grooves where evened out and the end has less detail.

- The crucible and its plug are united into one object.
- No inner conductor within the cane is included.
- Additionally the conductor connections within the cane are removed.
- The details of the cane are heavily reduced, rendering the cane a simple pipe.

Another change in this model is to abandon the outer structure that was resembling the oven test stand walls, to get rid of the necessity of meshing this structure. As the enclosures wall temperature in the 2D model is set to 22 °C the radiation from the oven was absorbed here while almost no thermal radiation from these walls is emitted back to the oven.

In the simplified 3D model the surrounding is open with no additional structure around the oven. This requires a setting within the program that allows thermal radiation to leave the model. Figure 3.27 depicts the simplified geometry.

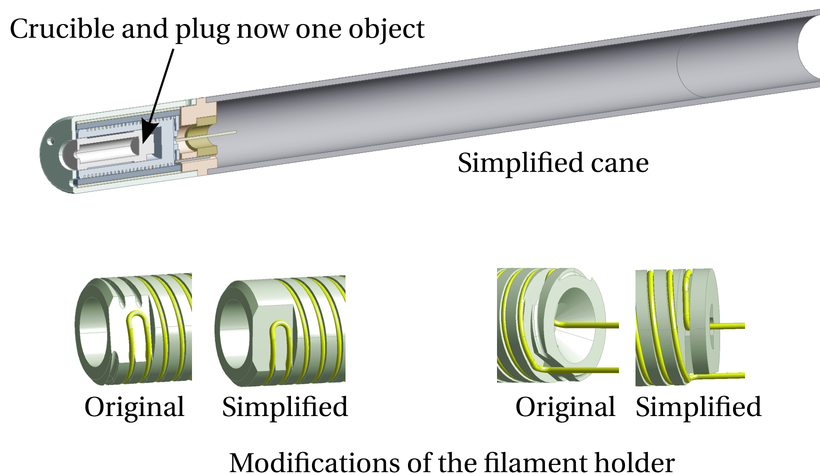

Figure 3.27.: Geometry of the simplified oven model in 3D. The modifications of the filament holder are shown in more detail.

A consequence of the simplifications is that also the loads of the model change. The internal heat generation within the copper conductors inside the cane is not present any more leaving the crucible and the cane as the only bodies that produce heat.

Comparison of the simplified model to the full 3D model

While the number of mesh nodes was only reduced by 17 % (from 368000 to 304000 nodes) the necessary computing time changed an order of magnitude. For the power of 10 W the

CPU-time reduced from 13 d to 22 h. This reduced computing time also made it possible to simulate the model up to 20 W.

Figure 3.28 shows similar plots like 3.21, this time comparing the detailed "full" 3D model with the simplified model.

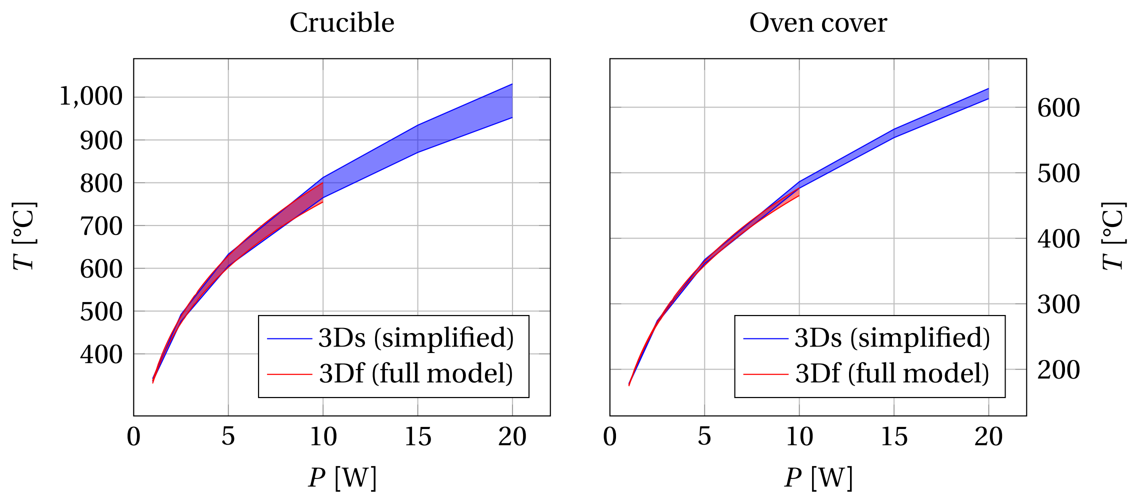

Figure 3.28.: Temperature span of the crucible and the oven cover from the simplified 3D model compared to the full 3D model. Only the simplified model could be simulated with a power of 20 W.

The resulting temperatures in the crucible and in the oven cover do not differ significantly, making the simplified model a feasible tool for further studies of the 3D geometry in ANSYS.

Realistic tantalum reflector foil: 3Ds2

In the 2D model as well as the so far presented 3D models the heat reflective tantalum foil within the oven is represented by a hollow tantalum cylinder. In 3D here a body can be used that models the tantalum foil more realistic. This was done using the simplified 3D model.

A body, depicted in figure 3.29, was created that spirals outwards like the wound foil does. However, while roughly reproducing the real foils volume, the modelled foil is thicker and shorter: In reality the foils dimensions are 40 mm x 200 mm with a thickness of 25 µm. The simulated body has the dimensions of 40 mm x 108 mm and a thickness of 50 µm.

This is a concession to the mesh size (a thinner and longer foil needs more mesh elements) and to keep a sufficient distance between the windings to allow the simulation of thermal radiation.

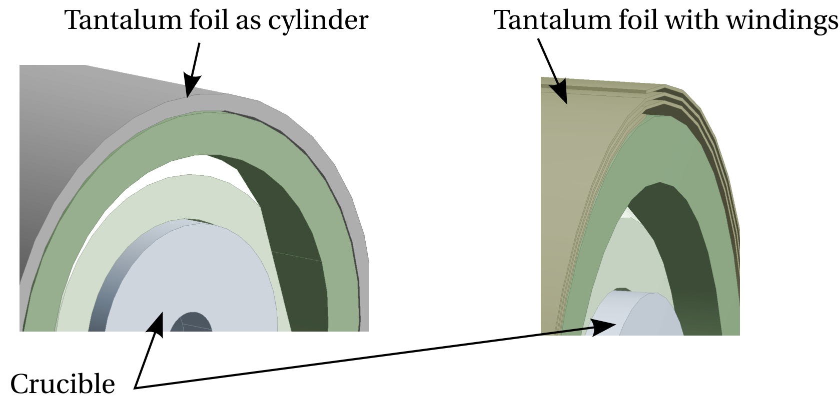

Figure 3.29.: The body representing the reflective tantalum foil as a cylinder and the new body where the foil is thin and has windings

Figure 3.30 shows the temperature distribution of the tantalum foil for a heating power of 5 W in the two different 3D representations.

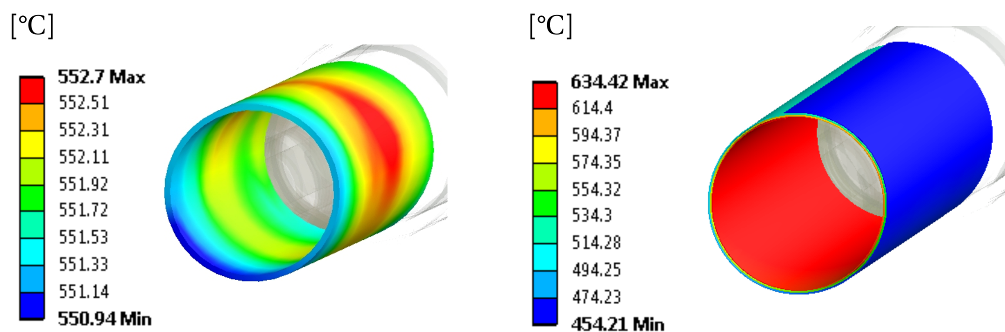

Figure 3.30.: Temperature profile of the tantalum foil for a heating power of 5 W. On the left the foil is represented as a thick cylinder and on the right with several windings.

It is noticeable that the realistic shape predicts a much higher temperature gradient from inside to outside than the cylinder that shows no difference between the inner and outer faces (like one would expect), indicating that the spiral indeed has a different insulation behaviour. While the simple cylindrical representation of the foil shows more temperature fluctuations along the cylinders symmetry axis and generally only has a span over 2 K the temperature of the spiral shaped foil shows a large gradient of 180 K from inside to outside.

This affects the temperature distribution of the complete oven, at the crucible as well as on the outer oven cover. The plots in figure 3.31 show the temperature span, so all temperatures between the minimum and maximum within the distribution, for the crucible and the oven cover from three different models including the model 3Ds2.

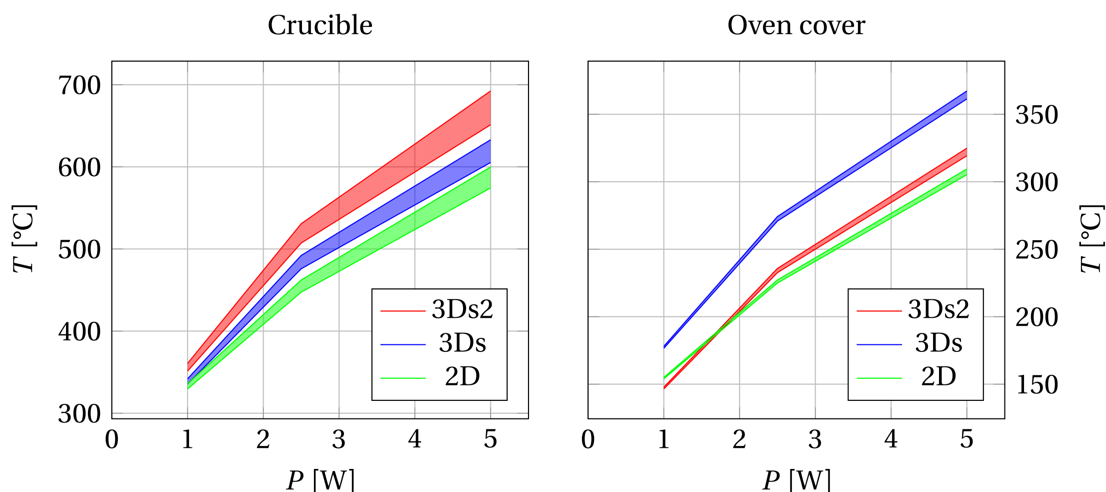

Figure 3.31.: All temperature values within the thermal distribution of the crucible (left plot) and the oven cover (right plot) at a certain heating power level. 3Ds is the simplified 3D model with the hollow cylinder as tantalum foil while 3Ds2 is the same model but with the wound foil shape. 2D indicates the 2D model.

It can be seen that the realistic foil shape changes both the crucibles temperature and also the oven cover temperature. While the crucible becomes hotter compared to the original simple 3D model, the outer oven cover is colder at the same heating power. This demonstrates that a hollow cylinder is an oversimplification of the tantalum foil behaviour.

The plots also show that with the realistic foil shape the resulting temperature of the outer oven cover is closer to the one of the 2D model, which itself is close to measurements as presented in [55].

Crucible temperature profile Figure 3.32 shows the temperature profile of the crucible on the same path as seen in figure 3.22 for three simulations, 3Ds, 2D and the model with the spiral foil, 3Ds2 with a heating power of 5 W.

The predicted temperature profile of the crucible in all simulations is similar disregarding the total temperature. The spiral foil however creates a slightly steeper temperature drop at the tip of the crucible. But also the more realistic shaped tantalum foil does not display a temperature drop that could explain the need to raise the heating power of the oven in the range that is experienced.

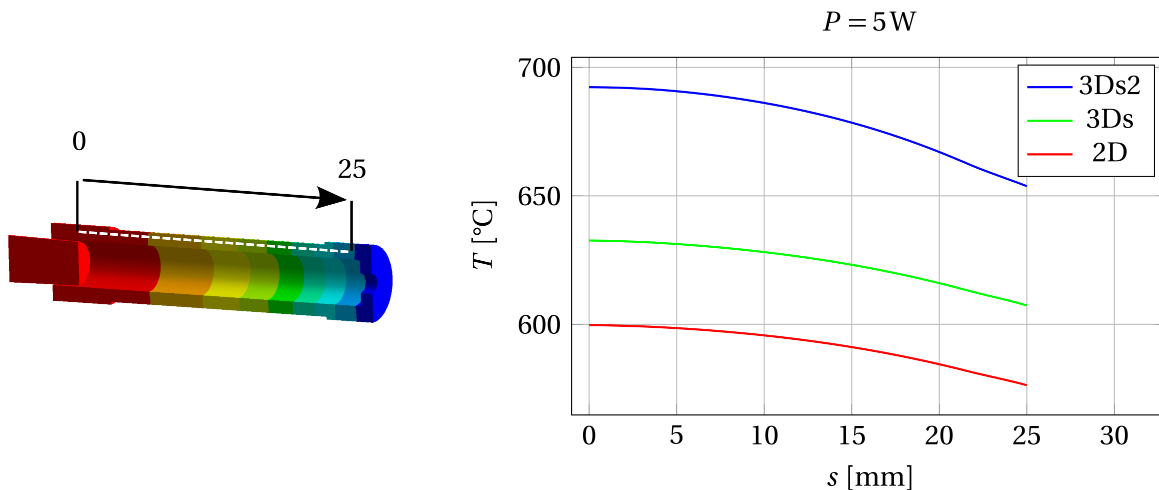

Figure 3.32.: Temperature on a path along the crucible for three different simulation models at 5W.

3.7.5. Influence of the injection plug: 3DsT and 3Dsp

As the oven is part of the source setup efforts were made to understand the influence of the direct environment of the oven on its thermal distribution, i.e. the injection plug. To be able to simulate realistically high heating powers, a further simplification to the oven model, presented in section 3.7.4 had to be made, called '3DsT'. In the so far presented simulations the oven power was a direct input parameter. For an easier converging simulation as a new input parameter the filament was simulated with fixed temperature. The net power irradiated by the filament in the simulation corresponds to the former input power. This method does not allow to establish the power ratios shown in table 3.3 so it assumes that all power is lost at the filament. However this simplification seems to be more stable as the model only converged this way.

figure 3.33 shows a comparison of the model presented in section 3.7.4, 3Ds, with power as direct input value and the same geometry with a fixed temperature, 3DsT, where the power is only determined after the simulation.

The differences are low enough to assume that the additional simplification does not heavily impact the accuracy of this 3D model.

The injection plug model

Here the simulational model including the injection plug is called '3Dsp'. The body representing the injection plug is a simplification of the real setup. it is shown in figure 3.34.

The thermal profile of the plug or its temperature were not yet assessed and in the

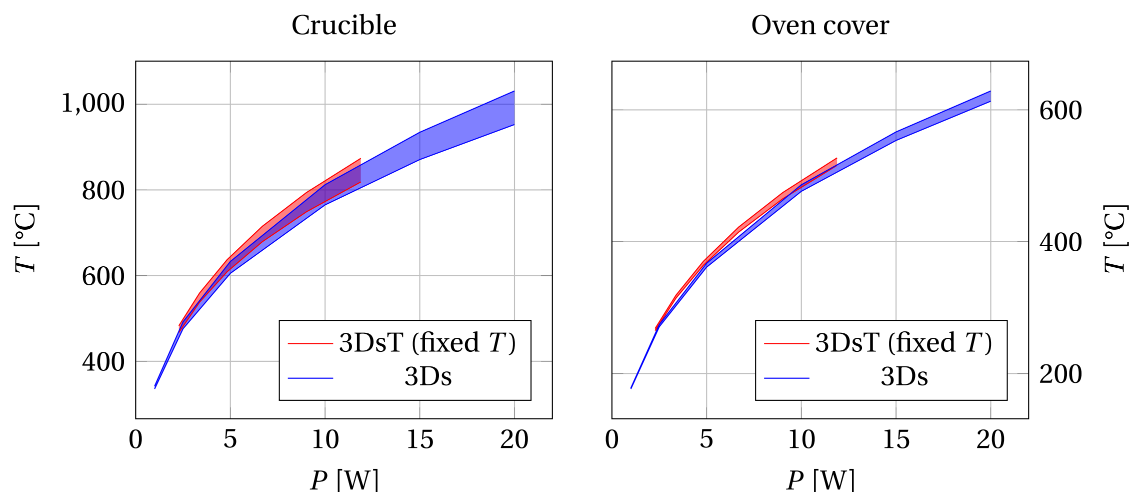

Figure 3.33.: Temperature span from two 3D simulations. In one the filament was set on a fixed temperature while the other used the heat generation.

presented simulation it is simplified to a two body model. The plug geometry is represented by a body shaped like the injection plug itself, however with only the hole for one oven, and none of the other holes, like the second oven, the gas injection or the two wave guides. Also the bias disc electrode that is placed at its front is not included. The plug is connected to a stainless steel rod of the length of 210 mm, whose end is set to the fixed temperature of 20 °C.

Also the real plug at the source is connected to such a rod, which is connected to a bigger part of the ion source body at a length of 390 mm. In the simulation the cane was cut to 210 mm to reduce the computational effort.

The presented model is an extreme case, where thermal conduction is assumed to happen only between the plug and the rod.

The thermal emissivity for cobalt that was used for the thermal radiation is shown in table 3.4 [58].

Temperature [°C]	emissivity ϵ[dim. less.]
0	0.13
500	0.13
1000	0.23

Table 3.4.: Thermal emissivity values of cobalt used for the simulation.

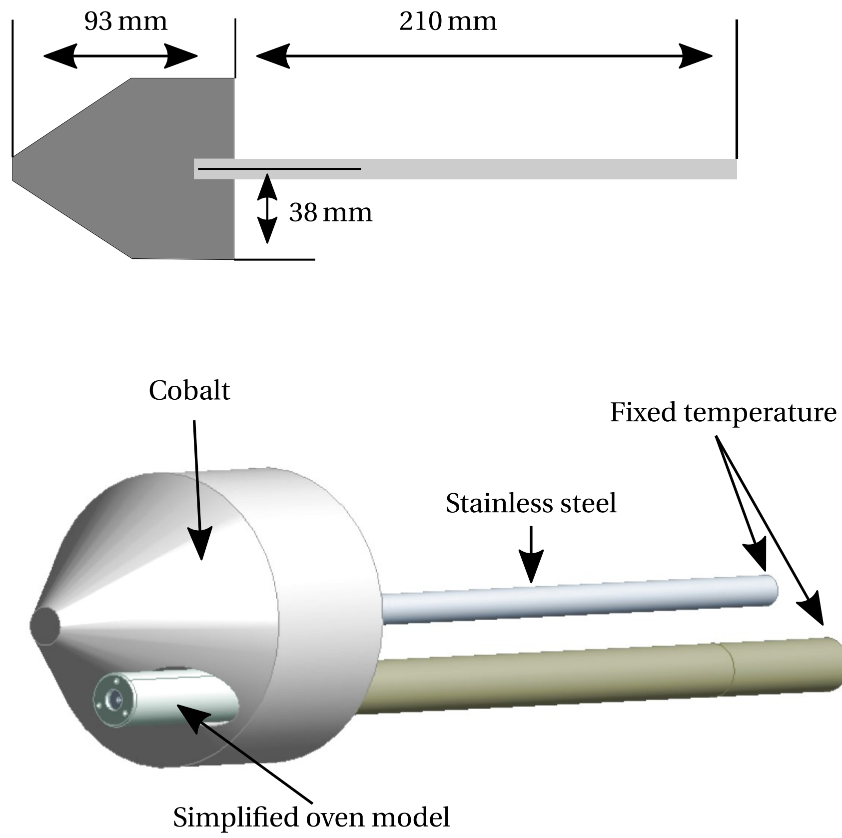

Figure 3.34.: Simple model of the injection plug at the GTS-LHC ion source.

Results of the simulation 3Dsp

Figure 3.35 shows the temperature of the crucible and the oven cover in comparison with the simplified model presented in section 3.7.4.

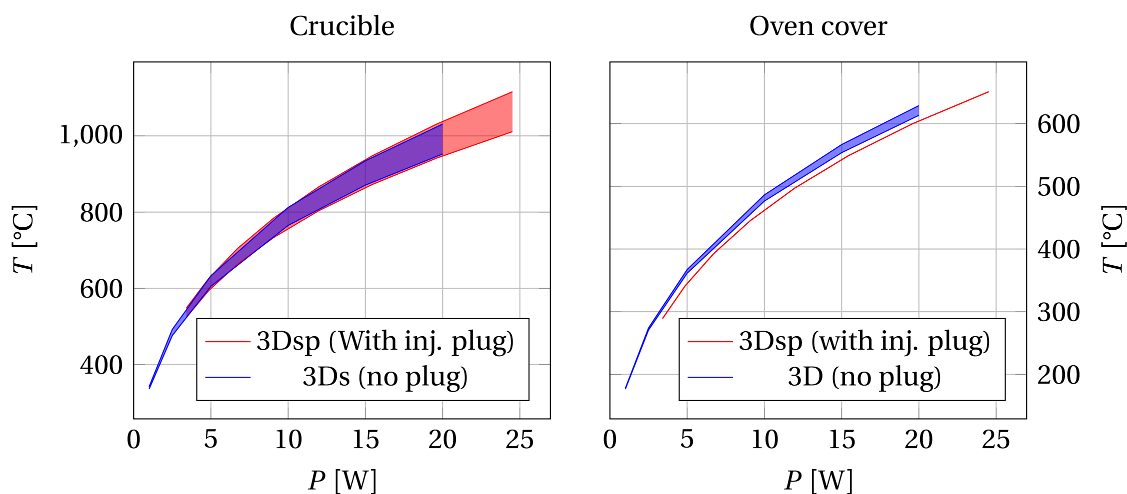

Figure 3.35.: Temperature span of the crucible and the oven cover with and without the injection plug.

It can be seen that the presence of the injection plug did not affect the crucible temperature, while the temperature of the oven cover changed slightly. Figure 3.36 shows the temperature span of the injection plug.

The injection plug is significantly colder than the oven cover. At 24.5 W (the highest simulated heating power) the plug has a temperature of 200 °C, while the oven cover has more than 600 °C. In the plot of figure 3.36 it can also be seen that the temperature span of the plug is small compared to its total temperature, only showing differences of less then 4 K between different parts of the body.

Discussion This simulation is an extreme case, with a simplified geometry of the injection plug and its connection to the source. It can be assumed that the real injection plug will have more connections that transport heat away by thermal conduction. Its body might be colder than the one in the simulation. When this is the case it will affect the oven temperature even less, as the thermal heat radiated back onto the oven will be reduced.

Therefore this simulation hints that the oven temperature at the GTS-LHC ion source is not affected by the presence of the injection plug, as long as the oven is the only source of heat. The presence of the plasma in the plasma chamber however might have an influence.

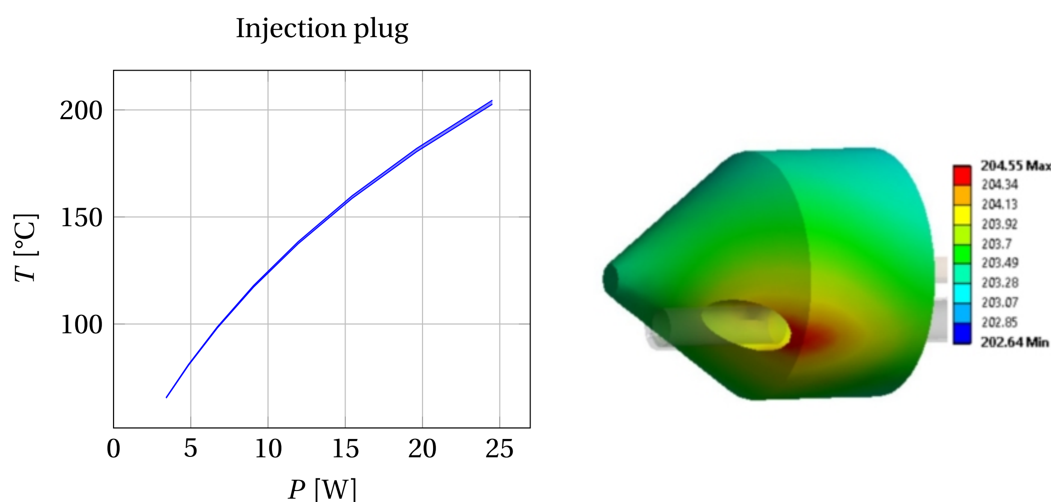

Figure 3.36.: The left plot shows the temperature span of the injection plug plotted against the heating power of the oven. The right picture shows the temperature profile of the plug.

3.8. Conclusion from the thermal simulations

Thermal simulations of the oven consistently showed that the crucible within the oven has a temperature profile where the tip is colder than the body of the crucible. This can be a cause of changing evaporation rates at a constant heating power. However simulations presented in section 3.6.4 hint that this temperature loss towards the tip is not enough to explain the need for the steep rise in heating power that is experienced during the oven operation at the GTS-LHC ion source.

Also the 3D simulation revealed no explanation for this behaviour. In the 3D simulations a difference in the resulting absolute temperatures especially at the outer oven cover was observed that can not be explained by geometrical differences.

3D simulations in ANSYS are computational heavy, but with simplified models it was possible to test different geometries with reasonable simulation times (less than one week). This way a more realistic model of the thermal insulation within the oven could be created. Additionally the influence of the GTS-LHC ion source injection plug was assessed.

These simulations show that changes of the geometry only slightly affect the predicted temperature profile of the crucible compared to the existing 2D simulation. While a realistically shaped tantalum reflector foil showed a slightly steeper temperature drop at the tip, the injection plug geometry did not affect the crucible profile at all. The total temperature however differed between the different models.

4. Oven Characterization at the Test Stand

Experiments at the oven test stand were conducted to characterize the oven in different operational conditions as the ion source itself provides only very limited possibilities for diagnosing the oven behaviour in terms of temperature and evaporation rate.

This chapter presents the setup of the oven test stand and the principle of the different measurements that where used to characterize the oven performance. It will start with a description of the general setup and then give more detail on the two types of sensors used: The thermocouples and the deposition sensor. The data analysis of the oven test stand data was exclusively done with Wolfram Mathematica [62].

4.1. Setup of the oven test stand

The design and the assembly of the oven test stand (OTS) was not part of this work and the setup was already presented in [55]. During this study several modifications of the test stand where made to the setup to allow the presented measurements, most prominently the gas injection system and the motorized movable feedthrough were added.

Also the automation of the deposition rate measurements with a periodically opening and closing shutter was developed during the presented work. Purpose of the test stand is to provide an environment for the oven that resembles the source, in terms of the water cooled feedthrough, a vacuum with low enough rest gas pressures (down to 5.0×10^{-8} mbar), the power supply for the heating power and also the presence of an injected gas at a desired pressure, which allows to diagnose the oven performance in realistic conditions.

Besides the operational parameters that come from the power supply of the oven, like the heating current and following from the applied voltage and the current, the filament resistance, the oven test stand allows to measure temperatures via thermocouples and features a deposition sensor. Figure 4.1 shows a sketch of the oven test stand and the position of the different sensors.

The basic setup is a vacuum chamber with different feedthroughs for the oven cane and several sensors. The evacuation of the test stand is done with a row of pumps for the

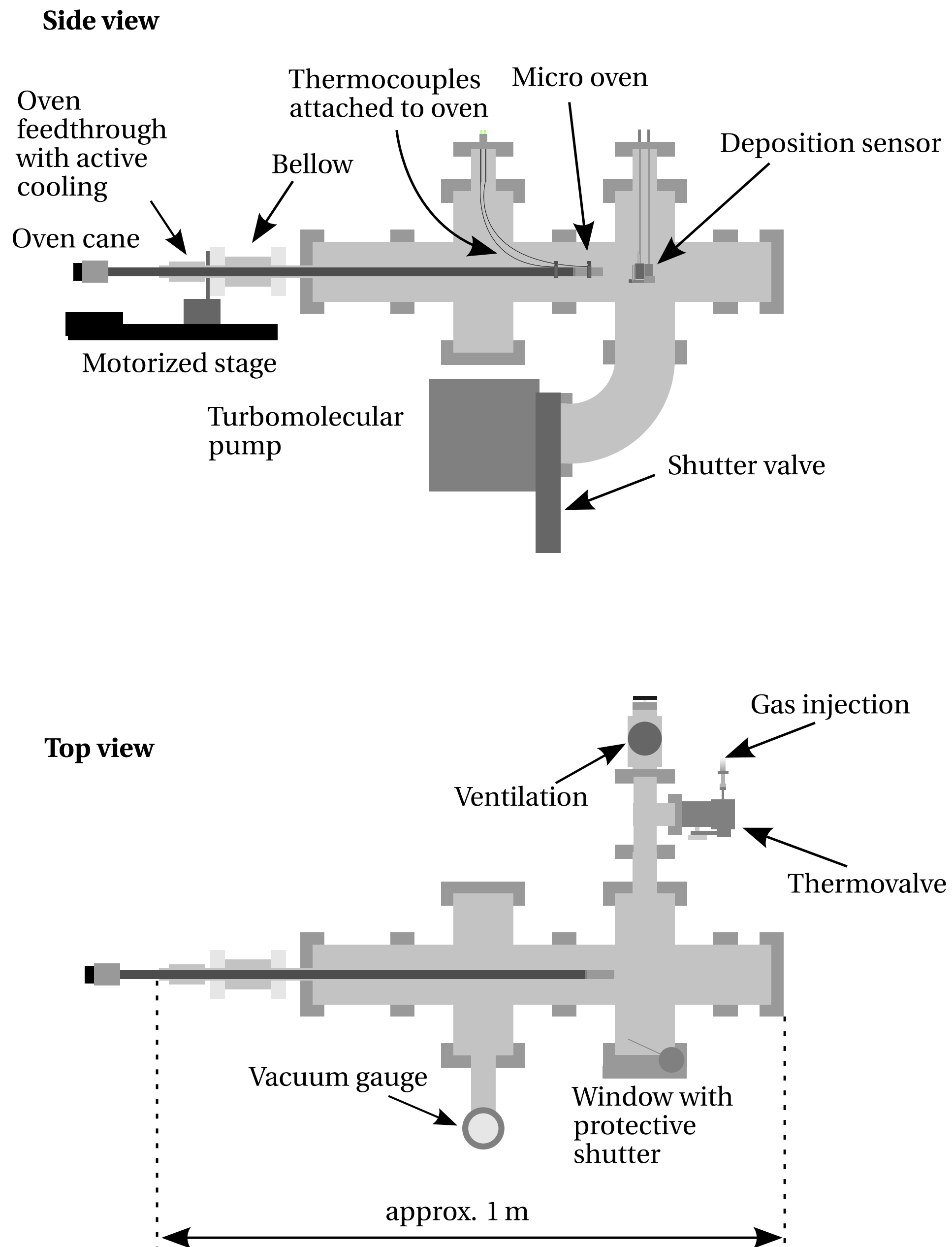

Figure 4.1.: Sketch of the inside of the oven test stand vacuum chamber as seen from the side and from the top.

different pressure regimes with turbomolecular pump that is protected with a shutter valve for the lowest pressures.

During the study presented in this work also a gas injection system was added to the setup that allows to simulate the background pressure created by the buffer gas in the GTS-LHC ion source. A vacuum gauge measures the pressure inside the enclosure of the test stand.

4.1.1. Test stand control and power supply

Almost all parameters of the oven, the oven test stand and the sensors pass a SIMATIC S7-300 programmable logic controller (PLC) from Siemens [63]. Figure 4.2 shows a sketch of the OTS interfaces and connections.

The functions of the PLC can be controlled by a WinCC application on a PC next to the oven test stand. In the application the input parameters for the oven can be chosen and also some functionalities of the sensors and the motorized movable stage are controllable.

The heating current of the oven comes from a Delta Elektronika power supply. In the WinCC application the usual input parameter for the oven heating is the desired power, which is then realized by a feedback loop running on the PLC that defines the current setpoint for the power supply.

Apart from controlling the test stand, the PLC also transfers a number of values to the CERN Acelerator Logging Service (CALS) with its interface Timber and thereby makes them accessible for the data analysis [64, 65].

4.1.2. Oven feedthrough

Like at the GTS-LHC ion source the oven is inserted and mounted via a approximately 1 m long cane that also transports the heating current into the vacuum chamber. The feedthrough for the oven cane actively cools the cane end with water. During the course of the study the feedthrough was extended with an additional bellow. This way, in combination with a motorized movable stage, the oven can be remotely moved back and forth on the axis of the cane. Figure 4.3 shows a photo of this setup.

The cooling at the feedthrough, the motor and the bellow are identical to the setup at the GTS-LHC ion source. A purpose of this extension that is outside of the scope of the presented study was the development of a new control software of the motorized stage at the GTS-LHC ion source.

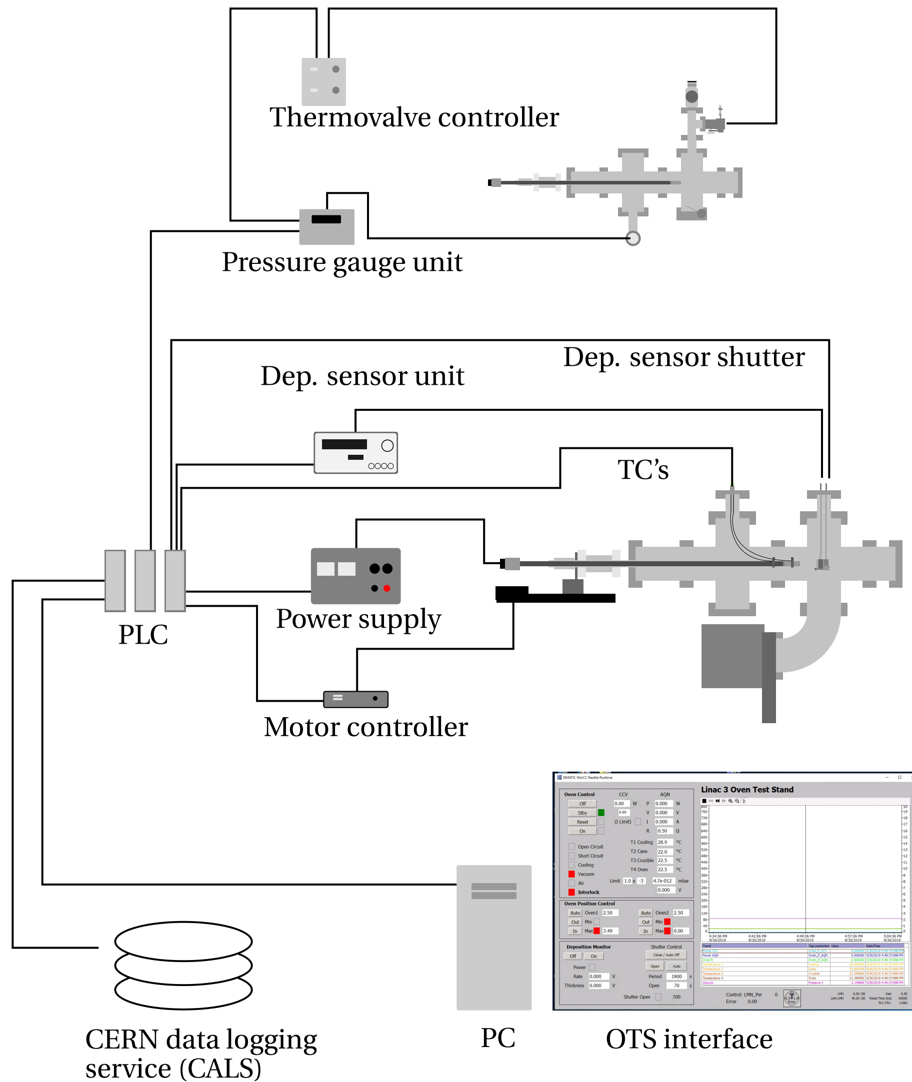

Figure 4.2.: Sketch of the connections outside of the oven test stand.

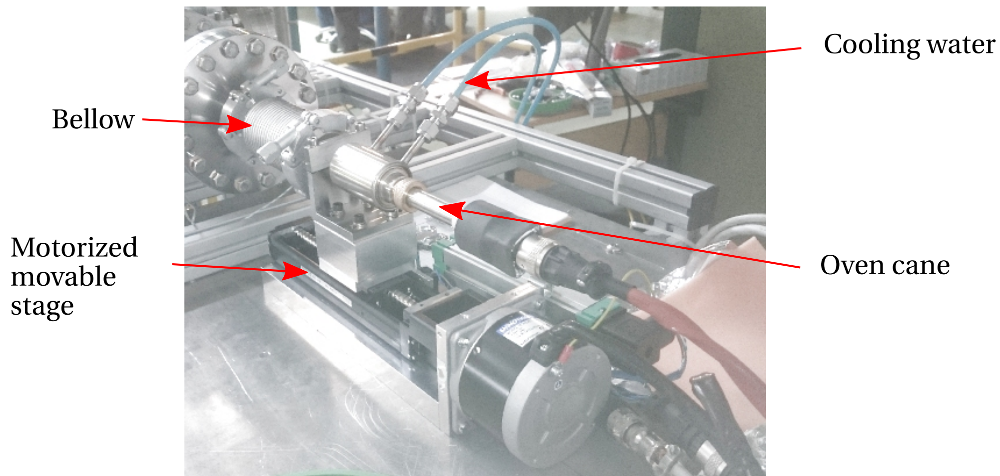

Figure 4.3.: Photos of the oven feedthrough with the cooling, the bellow and the motorized stage that allows to move the oven.

4.1.3. Gas injection

To feed a certain gas into the OTS a pressure reducer connected to the gas bottle stabilizes the pressure in the injection system in front of the thermovalve at 1.5 bar. The thermovalve then injects the gas into the vacuum chamber of the oven test stand. Figure 4.4 shows two photos of this setup. The thermovalve can be controlled manually or via a feedback loop which stabilizes the pressure measured by the vacuum gauge.

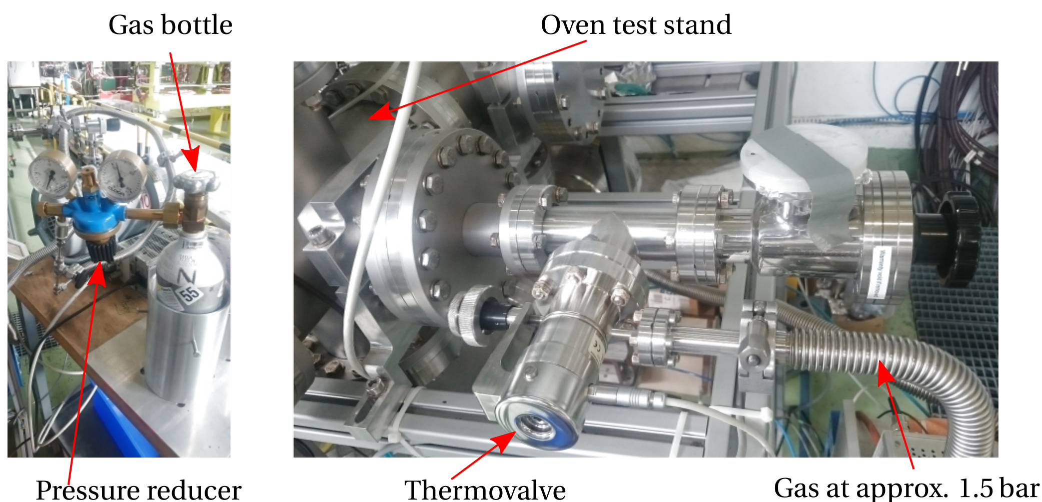

Figure 4.4.: Photos of the gas injection at the test stand. The left photo shows the gas bottle and the pressure reducer, the right one the thermovalve that injects the gas into the vacuum enclosure of the OTS.

4.1.4. Thermocouples

Thermocouples allow temperature measurements at different positions as they are flexible and can handle a wide range of temperatures. Their principle is the Seebeck effect [66]. If a conductor of a certain material has a temperature difference between its two ends, a voltage between these ends will arise. A thermocouple consists of two wires of different materials that are only electrically connected at the tip of the thermocouple. A temperature difference between the point of junction, the thermocouple tip, and the end of the thermocouple will then create a measurable voltage. If the two wires would consist of the same material the path to and back from the point of measurement would create opposing voltages in each wire that equal each other out, creating no measurable voltage at the thermocouple end. Figure 4.5 gives a sketch of this setup. As only temperature differences are measured with the thermocouple itself, the temperature at the end of the thermocouple ($T_{\text{Comp.}}$ in figure 4.5) needs to be known, i.e. measured with an additional device.

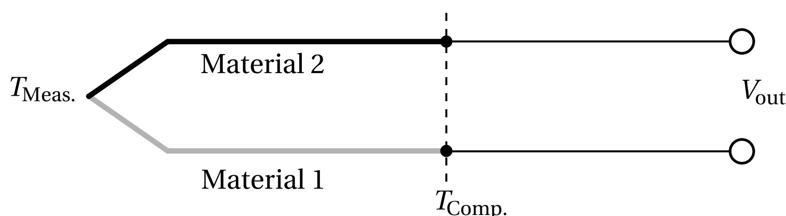

Figure 4.5.: Principle of a thermocouple. The tip measures $T_{\text{Meas.}}$ as the voltage V_{out} arises from the difference to the temperature $T_{\text{Comp.}}$ at the end of the thermocouple.

Thermocouples at the test stand

For the measurements at the test stand the K-type was chosen as they offer a wide temperature range. Table 4.1 shows some specifications of this type of thermocouple [67].

Type	Material	T range [°C]	Uncertainty σ_{TC} [% of °C reading]
K	NiCr-Ni	-270 to 1300	0.75

Table 4.1.: Characteristics of the used thermocouples in the oven test stand.

A dedicated feedthrough connects two thermocouples to the outside of the test stand, while insulating them from electrical contact to the test stand at the position of the feedthrough. Figure 4.6 shows the two thermocouples inside the test stand.

As always one end of a thermocouple needs to be grounded, the end is chosen depending on the measurement: For measurements on the (conducting) outer oven cover the

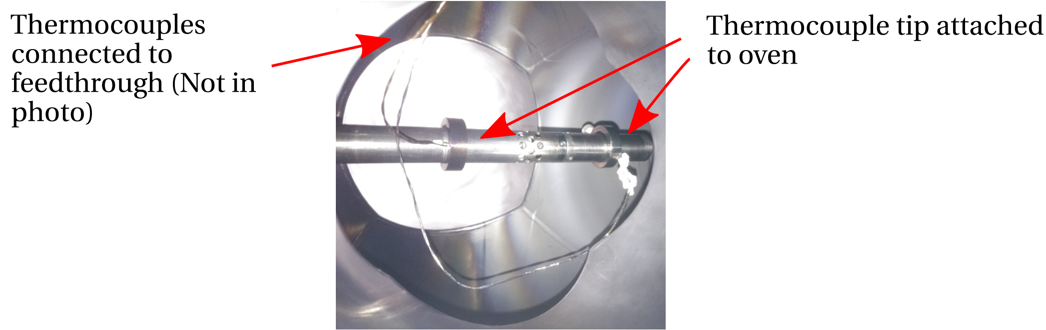

Figure 4.6.: Photo of the thermocouples inside the oven test stand. One end of each thermocouple is connected to the feedthrough at the oven test stand and each tip is clamped to the outside of the oven.

thermocouples are electrically floating on their end outside of the test stand, while the tip, that touches the oven directly is grounded, as the oven cover is grounded. As end is floating the thermocouples themselves are not conducting and the oven current should not interfere with the measurement. When the thermocouple tip can not be brought in contact with a grounded part, its outer end is adjusted to be grounded, while the tip is floating. In this case however it has to be ensured that the part inside of the test stand is electrically insulated from making contact to the ground potential. The outer parts of the thermocouples are connected to the PLC unit, which handles the calibration, grounding, and data acquisition. The PLC logs the thermocouple reading as values in degree Celsius in the database CALS.

For temperature measurements on the outer oven cover, thermal contact is ensured by clamping the thermocouple under a ring that embraces the oven. Figure 4.7 gives an example of a measurement with two thermocouples attached to the oven.

To enhance the comparability of measurements, throughout the study a reference position was introduced. At this position, which corresponds to the middle of the outer oven cover, the front side of the clamping ring is 22 mm away from the front tip of the oven.

Temperature uncertainty

Different factors contribute to the uncertainty of the measured temperature. The uncertainty for the K-type thermocouple is $\sigma_{\mathrm{TC}} = 0.75\,\%$ of the measured temperature, unless the error then yields a value lower than 2.2 K [68]. In that case the uncertainty is capped down at 2.2 K. Also the PLC units accuracy in reading the thermocouple voltage adds to the uncertainty with $\sigma_{\mathrm{PLC1}} = 0.7\,\%$ [63]. Another contribution is the internal compensation of the

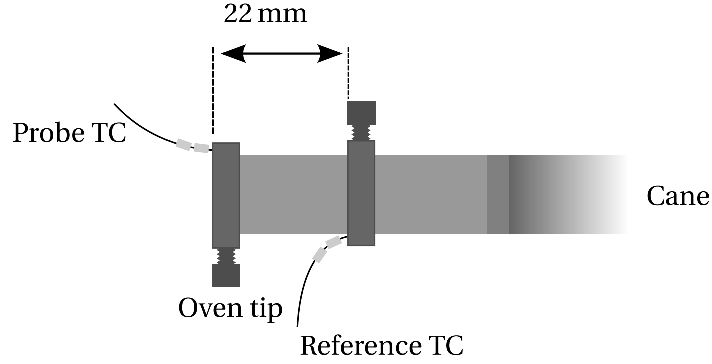

Figure 4.7.: Example for the setup of a temperature measurement. One thermocouple (TC) is placed in the middle of the oven cover and is used as a reference throughout the study. In the presented case the probe-thermocouple is on the height of the oven tip.

PLC for the cold end of the thermocouple, which is estimated to be $\sigma_{\text{PLC2}} = 1\,\%$ [63]. A third contribution from the PLC is the resolution of the stored digital value with $\sigma_{\text{PLC3}} = 0.5\,\text{K}$. As independent values, these uncertainties can be combined to a total uncertainty of a logged temperature value, σ_{T1}:

$$\sigma_{\text{T1}} = \sqrt{\sigma_{\text{TC}}^2 + \sigma_{\text{PLC1}}^2 + \sigma_{\text{PLC2}}^2 + \sigma_{\text{PLC3}}^2} \ . \tag{4.1}$$

As these values can be calculated directly for different readings, table 4.2 gives some examples of the resulting uncertainty.

Signal of TC [°C]	σ_{TC} [K]	σ_{PLC1} [K]	σ_{PLC2} [K]	σ_{PLC3} [K]	σ_{T1} [K]
100	2.2	0.7	1	0.5	2.6
500	3.75	3.5	5	0.5	7.2
1000	7.5	7	10	0.5	14.3

Table 4.2.: Calculated temperature uncertainty of the thermocouple reading for different temperatures using equation (4.1).

Positional precision

The width of the clamping rings, used to fasten the thermocouples, is 5 mm (along the longitudinal oven axis). Ceramic beads on the thermocouple were used to prevent contact with the oven on other parts than its tip. Therefore a positional precision of 5 mm is assumed when using a combination of temperature and positional values (e.g. in figure 4.19).

Influence of the TC holder ring on the thermal distribution

As the thermocouples are fastened with a stainless steel holder ring, the ANSYS simulations were used to assess the influence of this holder ring on the thermal distribution of the oven. A geometry representing one holder ring on the center of the oven was added to the simplified ANSYS model 3Ds (described in section 3.7.4 of chapter 3). Figure 4.8 shows the oven together with the geometry representing the ring.

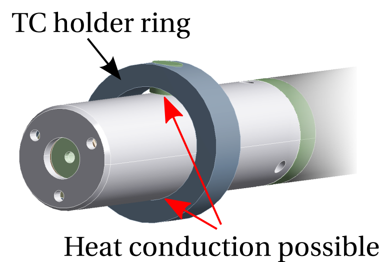

Figure 4.8.: Geometry of the holder ring for ANSYS thermal simulations.

The ring diameter is slightly bigger than that of the oven, therefore it touches the oven only at the fastening screw and on the opposite side of the screw. Here also thermal conduction is possible because of the touching pressure. This is also indicated in figure 4.8.

As the amount of conduction happening here, especially on the side of the ring opposite to the fastening screw, is not known, two extremes were simulated. One simulation did not include any conduction between the ring and the oven cover, while a second one assumed a perfectly conducting bond at the screw and the opposing side. For both cases the oven heating power in the simulation was 10 W.

results The two simulations showed differing results. Figure 4.9 depicts the thermal distribution of the outer oven cover together with the holder ring for the two simulations.

Without conduction between ring and oven cover the holder ring has a lower temperature than the oven cover (around 270 °C while the cover is at 489 °C). With a perfect conducting bond, evidently the ring and the oven cover share the same temperature at the touching parts. Here the oven cover is cooler than in the first simulation, only ranging from around 450 to 462 °C.

Figure 4.10 shows the temperature along a path in the oven cover for three simulations, the two described here, and one without any ring present.

The path leads from the front of the oven cover to its back (towards the cane) and in case a ring is present, it is directly under the fastening screw of the holder ring.

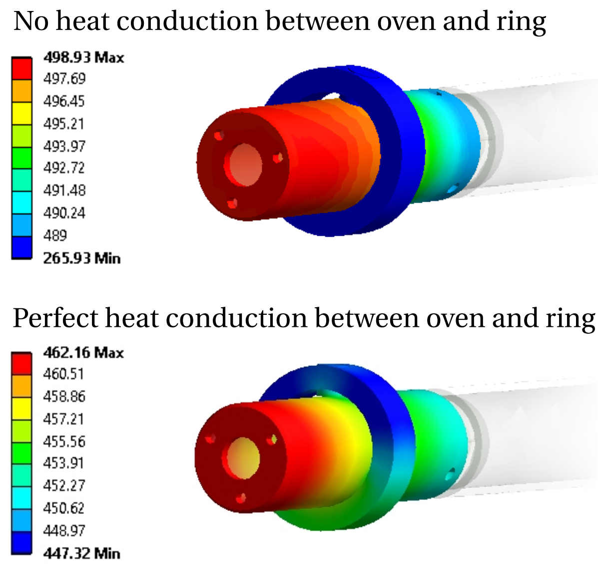

Figure 4.9.: Temperature distribution of the oven cover and the holder ring for two different simulations at 10 W.

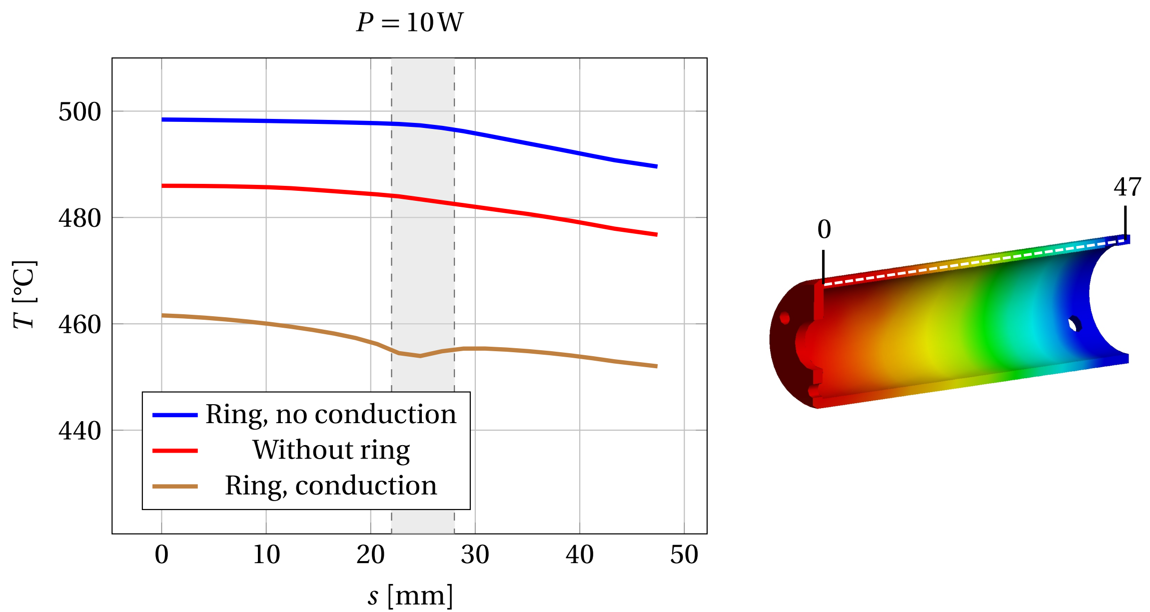

Figure 4.10.: Temperature along a path in the oven cover, shown on the right, for ANSYS simulations at 10 W of heating power, including a thermocouple holder ring. The grey area shows the position of the holder ring.

It shows that the two cases with ring have an opposing effect on the overall temperature of the oven cover, without conduction it is elevated (by around 13 K), with conduction it is reduced by approximately 24 K.

Additionally the conduction can influence the temperature profile locally, by creating a local temperature minimum, where the ring and the oven cover are in contact. Here the temperature difference between the model with ring and without is 30 K. Besides from that, in both cases the overall temperature profile is not changed significantly and in all three cases the temperature of the cover drops from the front to the back by 8.9 respective 9.6 K (no conduction, with conduction) and in the case of no present ring by 9.2 K.

The temperature of the crucible is slightly increased in both cases with a holder ring. With conduction the increase is around 2 K, without conduction 11 K.

discussion As the two models show opposing directions in the resulting temperature change of the oven cover, it is difficult to estimate the effect for the real oven. Most probably the conduction is less than perfect and thereby the real effect on the temperature is lying somewhere between the two extremes. However if the conduction dominates the influence of the ring, the measurement of the thermocouple happens within the local temperature minimum and will measure a temperature that is lower than without a ring.

The temperature change of the crucible is low enough to conclude that the evaporation behaviour should not be different whether a holder ring is installed or not.

4.1.5. Deposition detector

To detect the evaporation rate coming from the oven a commercial thin film deposition sensor from INFICON is installed at the test stand [69]. These sensors are routinely used to monitor the thickness of a deposited film in processes like physical vapour deposition [70].

The short description of its principle follows the description given in the sensor manual [71]. The functionality of the sensor is based on using the piezoelectricity of a quartz crystal. If a voltage is applied to the crystal it deforms and in return deformation also creates a voltage. The crystal can mechanically oscillate, when an alternating voltage is applied and then acts as a frequency filter, favouring its resonance frequency. If integrated in an oscillator circuit the crystal can define the circuits frequency: Starting from electrical noise that is filtered by the crystal, the frequency coming from the crystal is amplified and then fed back to the crystal. This way the circuit will start to oscillate in the resonance frequency of the crystal if the gain of the amplifier compensates for the power losses at the crystal. Figure 4.11 shows the principle of this circuit.

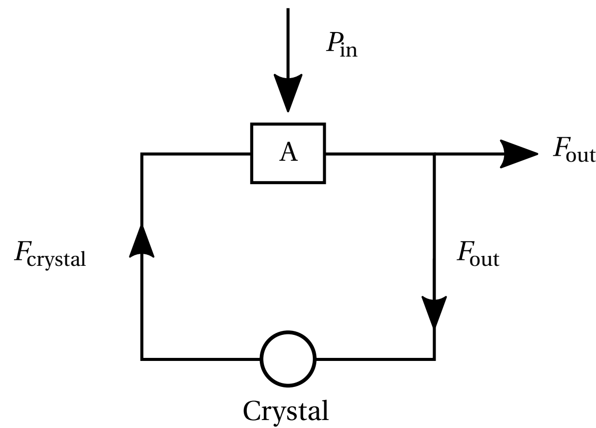

Figure 4.11.: Sketch of the oscillator circuit that lets the crystal oscillate at its resonance frequency. The frequency F_{out} is fed to the crystal. The crystal attenuates frequencies outside of its resonance frequency. What passes the crystal, $F_{crystal}$, is amplified and fed back to the crystal as well as coupled out and used for the analysis. The power P_{in} is providing the energy for the process.

The oscillation modes of the crystal depend on its shape and mass. If the crystal changes its mass by deposition of a material, the resonance frequency shifts, which affects the oscillator circuit. The frequency is then analyzed in the detector control unit, whose output is a thickness growth rate derived from the frequency shift and an internal calibration.

Setup of the sensor at the oven test stand

The setup at the test stand has several components: The detector containing the quartz crystal sensor, a shutter that protects the crystal, a feedthrough and a control unit, called SQM-160 [71]. Additionally, the control unit is connected to the test stand PLC via its analogue output cable. More detail on the connections is given in the next section. Like the thermocouples, the deposition detector has a dedicated feedthrough, which connects several of the detector parts to the outside: The frequency reading coming from the sensor is passed to the control unit. Cooling tubes are bringing a coolant to the detector, which at the oven test stand is air. Additionally to the signals and the cooling air, the sensor feedthrough also features additional air tubes for a shutter in front of the sensor, that is opened and closed by pressurized air.

Figure 4.12 shows several photos of the deposition sensor, its crystal and the feedthrough.

Additionally figure 4.13 shows a sketch of the sensor in front of the oven. The control of the shutter is done via the winCC application for the oven test stand, which can also turn

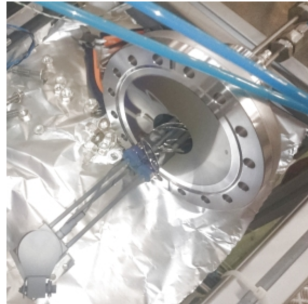
Detector and feedthrough

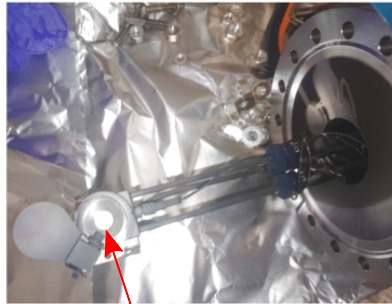
Sensor crystal (unused)

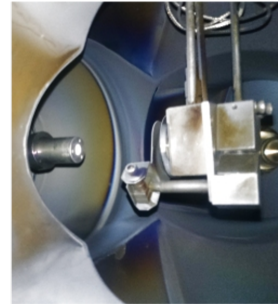
Detector inside test stand

Figure 4.12.: Photos of the deposition sensor and its feedthrough.

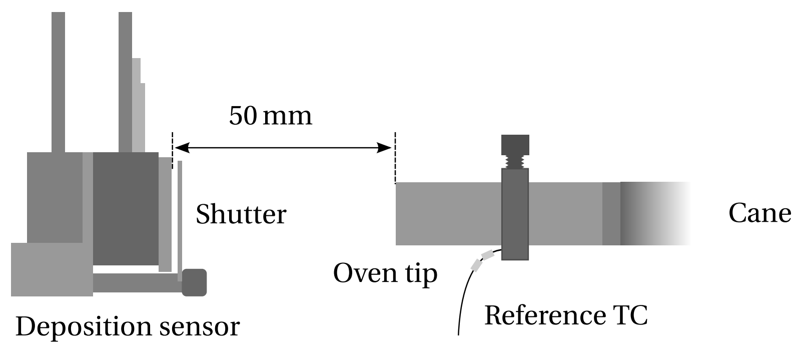

Figure 4.13.: Setup of the deposition sensor in front of the oven.

the sensor on and off.

Signal processing

A sketch of the deposition sensor connections is given in figure 4.14.

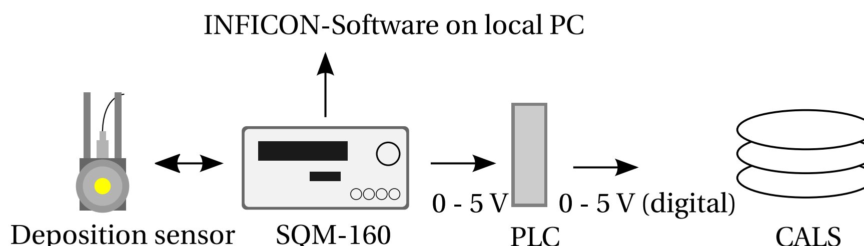

Figure 4.14.: Visualization of how the deposition data after the SQM-160 is distributed.

The sensor itself is controlled by the monitor unit SQM-160. It is turned on during the complete measurement and the deposition sensor measures the deposition rate permanently. The oscillation frequency of the sensor is read out by the SQM-160. The module uses its own software to analyze the data and return a thickness growth rate in Å s^{-1} for a given material, which in this case is lead.

A local PC can be connected to the SQM-160 via USB and a software provided by INFICON then allows recording of the deposition data. Additionally, the SQM-160 converts its reading into an analogue output signal ranging from 0 V to 5 V corresponding to a chosen deposition rate span. At the OTS the analogue reading is being digitalized by the test stand PLC and fed into the CERN logging database CALS. In the CALS also the status of the shutter is logged.

Operation with periodically opening and closing shutter

As the deposition sensor accumulates all material that is deposited onto it, its life time in the test stand is limited. To protect the sensor from unnecessary exposure to heat and lead vapour, the shutter in front of it only opens during selected moments.

In most measurements the shutter opens for 70 s every 30 min, which is a setting that proved to sample the time structure of the evaporation rate changes of the oven well enough in most cases. It is evident that in some cases a sudden change of the evaporation rate can happen while the shutter is closed (as e.g. can be seen in figure 5.26 in chapter 5). When the oven is evaporating lead at a sufficient rate and the shutter opens, the crystal is

deposited with lead vapour which changes the resonance frequency of the quartz crystal. This frequency change is measured and processed by the SQM-160.

As also the heat exposure of the sensor changes, by thermal radiation and the hot vapour, it thermally expands after the opening of the shutter. This causes the resonance-frequency to rise, leading to a sudden negative deposition rate reading after opening the shutter.

Only after some seconds the sensor temperature is stable and the reading turns into a positive stable value. After the shutter closes, the thermal exposure is decreased and the cooling makes the sensor contract. This causes a drop in the resonance frequency and thereby a positively peaking deposition rate (described in [72]).

The spiking deposition rates at the beginning and the end of an interval with an open shutter can be seen in the upper plot of figure 4.15.

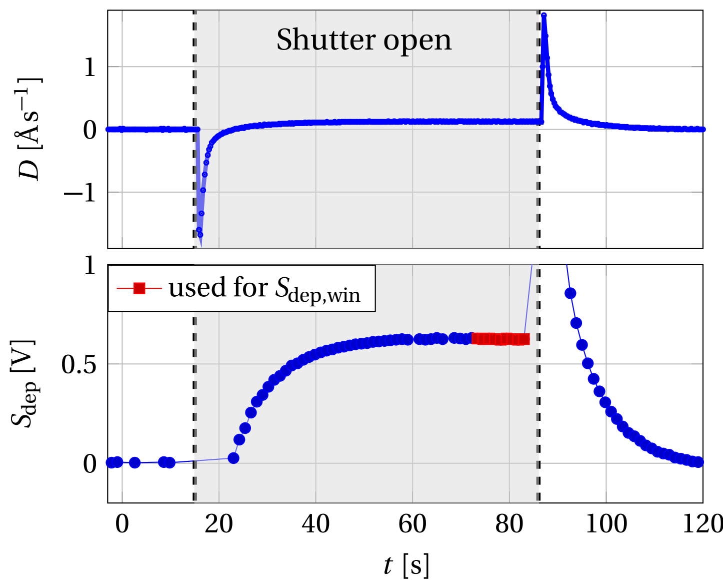

Figure 4.15.: Reading of the deposition sensor in a time window where the shutter opens for 70 s and then closes again, while the oven is running. The upper plot shows the data recorded with the INFICON-software on a local PC. The lower plot shows the reading as it is stored in the CALS during the same time window. In the CALS the rate is represented as a voltage and the initial peak is not visible as negative deposition rates are cut off. The data that is used as the actual deposition rate is shown in red in the lower plot.

For each time window with an open shutter only one deposition rate value, $S_{dep,win}$, is derived by averaging the last 10 recorded values within the interval, as shown in the lower plot of figure 4.15. The corresponding timestamp for that value is chosen to be the moment when the shutter closes.

As the reading D that is saved in the CALS, is given in V it needs to be reconverted to a

deposition rate:

$$D\,[\text{Å}\,\text{s}^{-1}] = \frac{u-l}{5}\,[\text{Å}\,\text{s}^{-1}\,\text{V}^{-1}]\,S_{\text{dep}}\,[\text{V}] + l\,[\text{Å}\,\text{s}^{-1}]\ , \tag{4.2}$$

where u is the rate that corresponds to 5 V and l the rate corresponding to 0 V.

To get the best possible resolution of low deposition rates, the values are set to $u = 1\,\text{Å}\,\text{s}^{-1}$ and $l = 0\,\text{Å}\,\text{s}^{-1}$, which is the smallest rate span possible on the SQM-160. A consequence of setting l to zero is, that the negative deposition rate peak after the shutter opens is not visible in the data which is saved in CALS (As it can be seen in figure 4.15).

Uncertainty of the measured deposition rate

The deposition rate resolution of the SQM-160 monitor is stated to be $\sigma_{\text{SQM}} = 0.037\,\text{Å}\,\text{s}^{-1}$ [71]. As the analogue signal is treated by the analogue digital converter (ADC) of the PLC, its conversion resolution can contribute to the uncertainty. The ADC has a resolution of approximately $\sigma_{\text{ADC1}} = 0.003\,\text{V}$ [63]. With equation (4.2) this converts to $\sigma_{\text{ADC1}} = 6\times10^{-4}\,\text{Å}\,\text{s}^{-1}$.

Besides the resolution, an accuracy of $\sigma_{\text{ADC2,rel.}} = 0.8\,\%$ for the analogue to digital conversion is stated in the manual of the PLC [63]. Depending on the deposition rate this can lead to a maximum value of $\sigma_{\text{ADC2,max}} = 0.003\,\text{Å}\,\text{s}^{-1}$ for a deposition rate of $0.4\,\text{Å}\,\text{s}^{-1}$. The mentioned deposition rate is an upper limit for the usually measured values.

When the shutter is opened for a short time window as shown in figure 4.15, the deposition rate can show noise, which is taken into account by introducing the standard error of the mean of each averaged value, σ_{noise}. All contributions can be added to get the total uncertainty of the deposition rate, σ_{D}.

In the following section basic measurements at the OTS are presented that help to get an understanding of the oven. In the first section the outer temperature profile of the oven was derived and the result is compared to the thermal simulations presented in chapter 3.

4.2. Outer thermal profile at stable power levels

A first thermal analysis of the oven was already presented in [55]. Additional measurements were conducted to measure the outer temperature profile of the oven and compare it to the thermal simulation models.

This section presents the results of five consecutive scans, where two thermocouples were attached to the outside of the oven and its cane, as shown in figure 4.7. One thermocouple always remained at the reference position while the position of the second

thermocouple was changed between individual scans. During these scans a crucible was inserted into the oven but it remained empty.

For each step the heating power was raised to a certain set-point and remained there until the temperature had stabilized. The plot in figure 4.16 shows the thermocouple reading in the beginning of such a stepwise power ramp up.

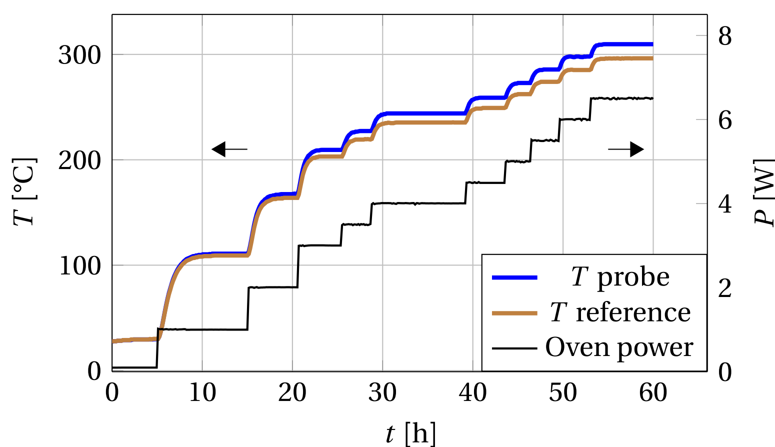

Figure 4.16.: Example of a temperature scan with different oven powers over time. The reference is in the middle of the oven cover while the probe is installed at its tip.

The resulting stable temperature can be retrieved by averaging the values from the end of a power step. Due to the long time it takes for the oven to stabilize its temperature, a scan took up to 14 days. For the analysis the temperature values corresponding to a time window of 20 min in the stable plateau were averaged.

4.2.1. Results

The outer thermal profile of the oven was measured by changing the position of the probe thermocouple for each scan, while the reference thermocouple remained at a fixed position. Figure 4.17 shows the stable temperature on the reference position at the outer oven cover for the different scans.

The individual measurements show differences exceeding the estimated uncertainty. One possible influence is the second thermocouple ring, that affects the thermal distribution of the oven cover and has a different position for each scan. Possibly also different clamping forces of the ring that attaches the thermocouple to the oven can influence the temperature measurement. As an estimation of the temperature at the middle of the oven cover the temperature of the different scans is averaged. Figure 4.18 shows the resulting averaged reference reading. The plot also includes the measurement of the outer oven

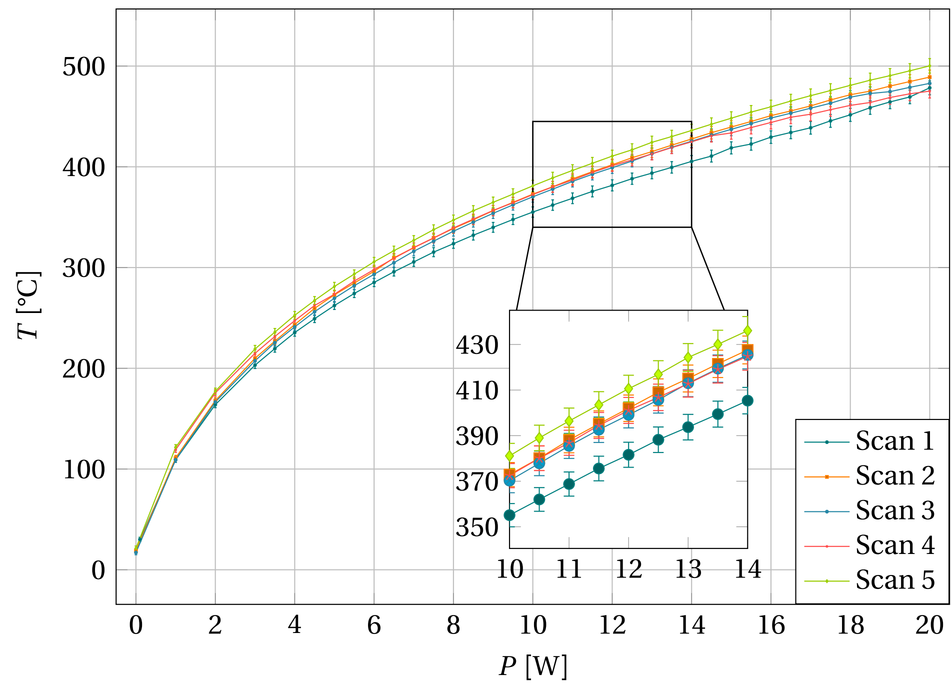

Figure 4.17.: Temperature at the reference position shown in figure 4.7 for the full power range of the oven at several scans. The shown error bars are calculated according to the uncertainties presented in section 4.1.4. A zoom shows the differences and the errors in more detail for a small power range.

cover that was presented by Fichera et al. in [55] as a comparison. As there is no big difference it can be deduced that the second attached thermocouple did not have a big influence on the overall temperature of the oven.

The plot shows the general power to temperature relation of the oven. A fit model can be deduced from the Stefan-Boltzmann law (already shown and described as equation (3.17)):

$$P = A_{\text{surf}}\epsilon\sigma_{\text{B}}T^4 \ . \tag{4.3}$$

If the radiated power is equal to the power leaving the filament, the bodies temperature, in this case the oven cover, should follow:

$$T_{\text{fit}}\,[°\text{C}] = a_{\text{fit}}\,[\text{K}\,\text{W}^{-\frac{1}{4}}]\,(P_{\text{oven}}\,[\text{W}])^{\frac{1}{4}} - 273.15\,[\text{K}] \ . \tag{4.4}$$

Here the temperature unit of T_{fit} is °C. Figure 4.18 shows the fit function (4.4) with a derived value of $a_{\text{fit}} = 360 \pm 20\,[\text{K}\,\text{W}^{-\frac{1}{4}}]$.

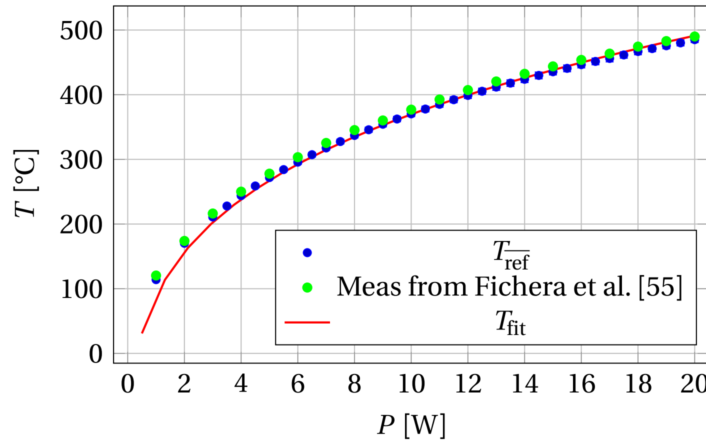

Figure 4.18.: Averaged stable reading of the thermocouple positioned at the reference position during all presented scans, $T_{\overline{\text{ref}}}$. The red line shows the fit function (4.4) for a value of $a_{\text{fit}} = 361.5\,[\text{K}\,\text{W}^{-\frac{1}{4}}]$.

The fit shows a good agreement with the power dependency of the outer oven temperature. This shows that the governing thermal transport mechanism at the oven tip is indeed thermal radiation (Already discussed by Fichera et al. in [55]).

To make the individual scans comparable and compensate for possible total temperature differences between individual scans, the probe thermocouples are only used to derive the difference to the reference measurement ($\Delta T_{\text{p-ref},P,n}$):

$$\Delta T_{\mathrm{p-ref},P,n} = T_{\mathrm{probe},P,n} - T_{\mathrm{ref},P,n} \quad . \tag{4.5}$$

Where $T_{\mathrm{probe},P,n}$ is the stable probe thermocouple reading from scan n at the power P. The outer temperature profile of the oven can then be derived by adding the averaged reference temperature to the individual difference between reference and probe:

$$T_{\mathrm{probe,corr},P,n} = \Delta T_{\mathrm{p-ref},P,n} + T_{\mathrm{ref},P} \quad . \tag{4.6}$$

As for each scan the probe thermocouple was placed at a different position on the cover, the scan number n in equation (4.6) can be replaced with the corresponding position s along the oven. Figure 4.19 shows the resulting measured thermal distribution of the outer oven cover for heating powers up to 20 W.

It can be seen that the hottest part of the oven cover is at the front tip of the oven. As the cane is inserted into the test stand through a feedthrough featuring an active water cooling it is logical that the temperature then falls towards the cane end. In the following the result of the measurements is compared to thermal simulations.

Comparison to ANSYS simulations

Figure 4.20 displays the measured outer temperature profile together with the result of thermal simulations. For the simulation result a path within the oven, starting at the oven tip and leading down the cane for 100 mm was used.

The comparison shows that while both simulation models overestimate the temperature of the oven cover, the 2D model is closer to the measurement. This behavior was expected from the results presented in section 3.7.2 as the 3D model showed a higher temperature on the oven cover compared to the 2D model (which was adapted to the measurements). Both the simulations and the measurement show the highest temperature at the tip of the oven cover, so the general trend is described correctly in the simulations. Additionally both models are close to the measurement at the cane which demonstrates that the assumption of a fixed temperature at the cane end is sufficiently describing its thermal behaviour.

A big difference however is the temperature gap between the oven cover and the cane. The simulations predict a higher temperature difference than what was measured.

One possible explanation is the influence of the holder rings, as discussed in section 4.1.4. Thermal conduction between ring and oven cover can lower the overall temperature of the oven cover and possibly also create a local minimum at the position of the thermocouple. Especially with two holder rings on the oven cover this effect could be even enhanced.

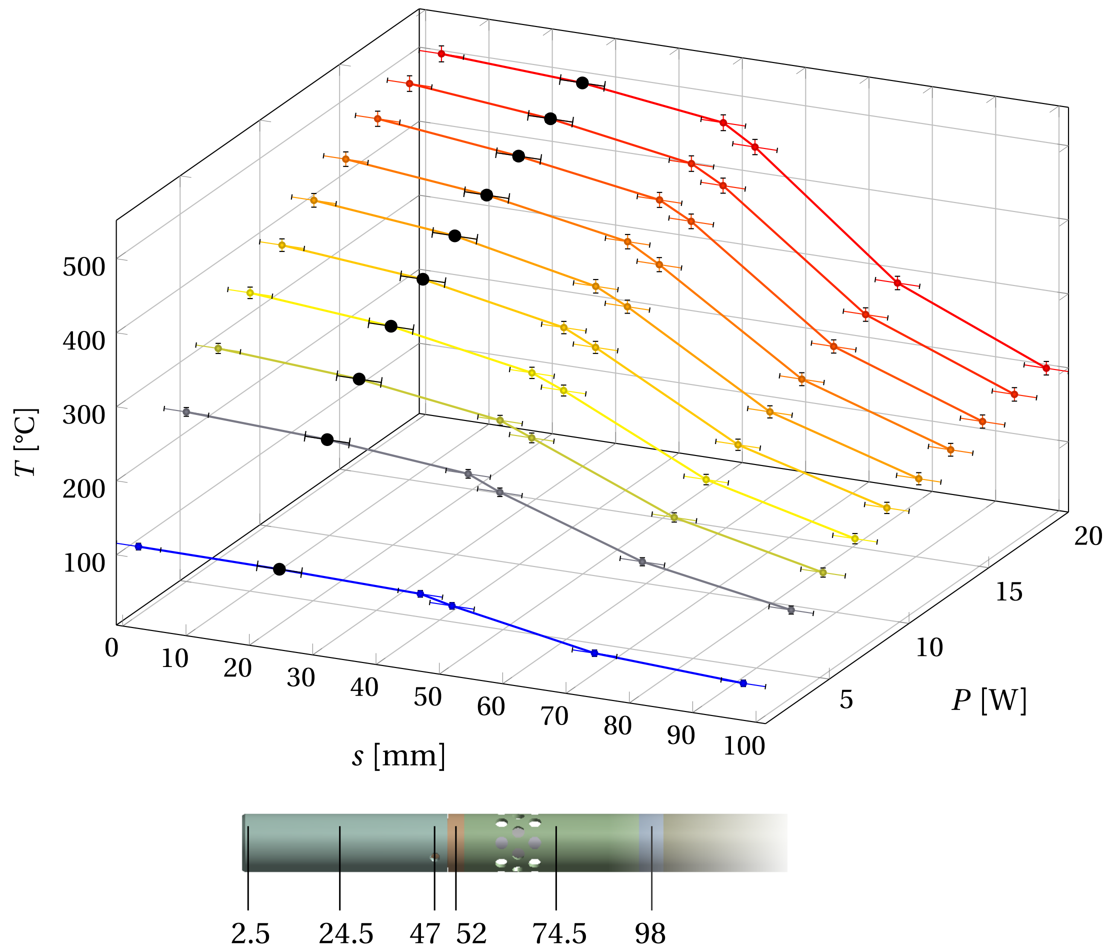

Figure 4.19.: Thermal profile of the Linac3 oven resulting from equation (4.6). The black marks indicate the reading at the reference position. The coordinate s is the position of the thermal measurement as indicated in the drawing.

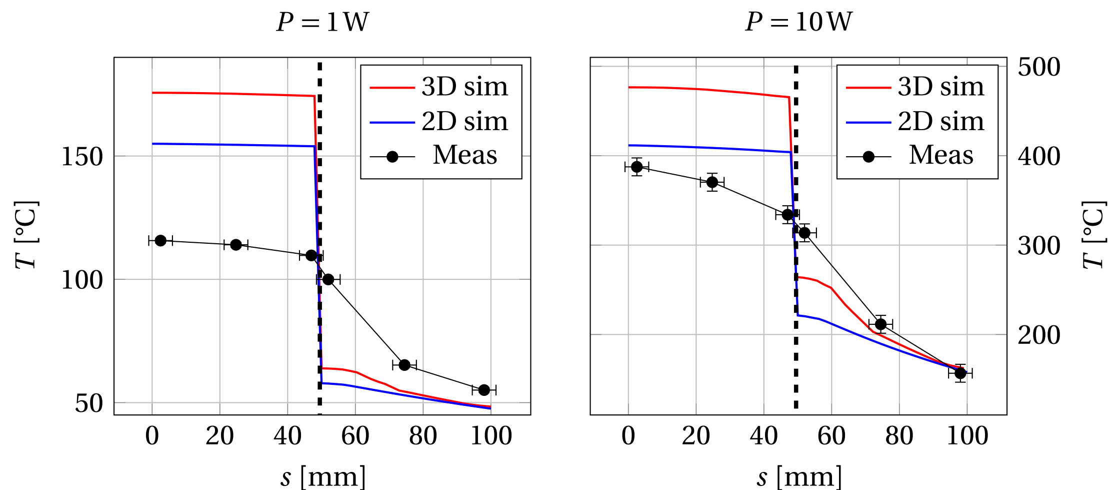

Figure 4.20.: The measured outer thermal profile of the oven together with the result of the 2D and the detailled 3D simulation for the heating power P of 1 W (left) and 10 W (right). The black dashed line shows the border between the oven cover ($s < 49,5$) and the oven cane.

Another possibility is that the assumption of having no conduction between the oven cover and the cane is not correct.

Figure 4.21 shows a similar plot with 2D simulations where the oven cover and the cane have a perfectly conducting connection.

It can be seen that the temperature predicted by the model changes mainly by reducing the difference in temperature between the cane and the oven cover. The resulting outer temperature of the oven cover is now closer to the measurement, while the temperature of the cane is being overestimated by the simulation.

The property of the connection between the two parts obviously influences the outer thermal profile of the oven. Figure 4.22 shows the temperature along a path within the crucible for two 2D simulations with a heating power of 10 W, one without the conducting connection and one with the perfect connection.

Both simulations show a similar temperature profile for the crucible but with a constant temperature offset of approximately 12 K. The difference in the crucible temperature between the 2D model and the measurements (as presented in [55]) at 10 W is 23 K.

Hence the difference in the crucible temperature of the two 2D models is below the general precision of the 2D simulation model and thereby also clearly below the one of the 3D model that shows larger differences to the measurements.

It can be concluded that the predicted temperature profile of the crucible in the ANSYS simulations is rather robust to changes at the outer oven layers and to possible improve-

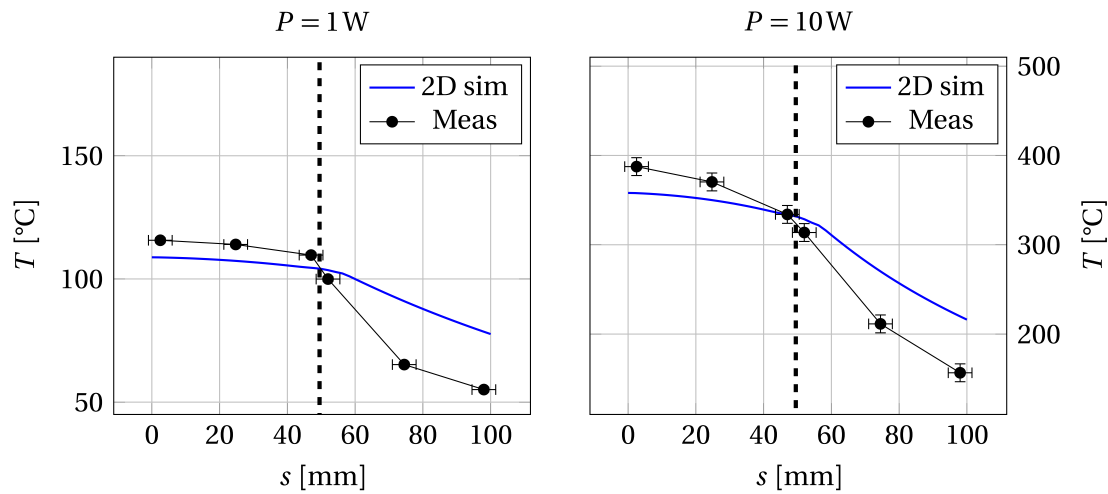

Figure 4.21.: Outer thermal profile derived from the measurement and from 2D simulations, where the oven cover and the cane share a conducting connection. The black dashed line shows the border between the oven cover ($s < 49,5$) and the oven cane.

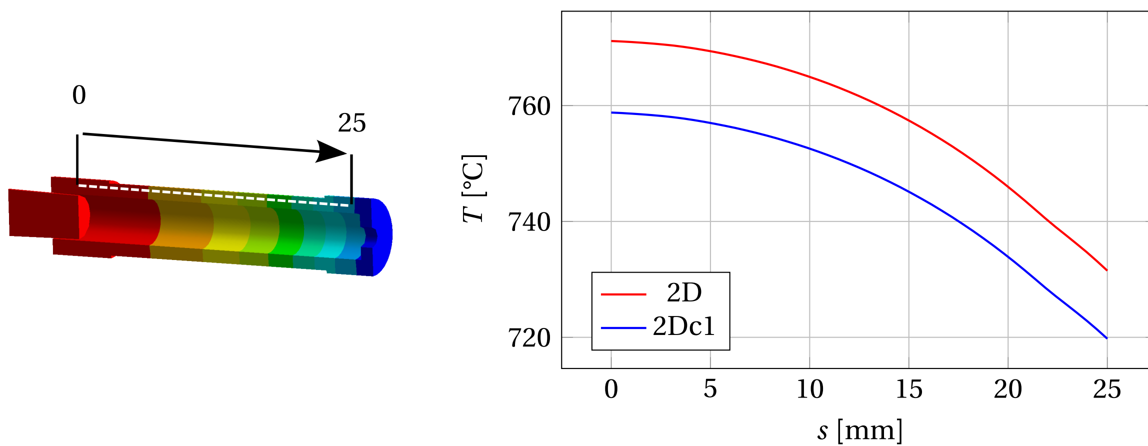

Figure 4.22.: Temperature along a path within the crucible, for two thermal simulations: "2D" is the already presented 2D model of the oven, "2Dc1" a modified version of the model, where the oven cover and the cane are connected via conduction.

ments of the simulation regarding the outer thermal profile. This behaviour was also observed in section 3.7.5.

The next section presents basic measurements with the deposition sensor and the calibration method that was used to derive evaporation rates instead of deposition rates, which are presented in the following chapter (chapter 5).

4.3. Divergence of the lead gas jet

As the motorized stage at the oven test stand allowed to change the distance between the oven and the deposition detector without interrupting the oven operation, it was tested how the change of the deposition reading is comparing to predictions.

Using the motor, the distance between the oven tip and the sensor can be changed during a running experiment. Starting with 50 mm at a fully compressed bellow the distance can be raised to 69 mm. This allows to measure the reduction of the deposition rate with growing distance of the oven tip to the sensor as a consequence of the gas jet divergence.

A scan was performed where the oven was moved away from the deposition sensor stepwise and a deposition rate measurement was taken at every step by opening the sensor shutter for 70 s. After the scan the motor was moved back to its initial position without sub-steps and an additional measurement of the deposition rate was taken.

Figure 4.23 shows the resulting deposition rate against time during this scan. The rate started with approx. $3.6\,\text{Å}\,\text{s}^{-1}$ and then linearly decreased to $2.3\,\text{Å}\,\text{s}^{-1}$ over the duration of the scan (approximately 30 min). The last value is at around $4\,\text{Å}\,\text{s}^{-1}$.

As the evaporation rate of the lead coming from the oven can drift over time, the sensor reading at the beginning and the end of the scan was used to calculate a corrected deposition rate that represents a stable evaporation rate:

$$D_{\text{corr},i} = D_i - \frac{\Delta D_{\text{scan}}}{\Delta t_{\text{scan}}} t_i \ , \tag{4.7}$$

where $D_{\text{corr},i}$ is the corrected deposition rate D_i at the time t_i. ΔD_{scan} is the difference between the deposition rate at the beginning and after the motor scan at the same motor position and Δt_{scan} the time that passed between taking these two values. Here the drift of the evaporation rate was assumed to be linear.

The corrected reading, using equation (4.7) can also be seen in figure 4.23. Its decrease is a bit steeper than the originally measured values, with $2\,\text{Å}\,\text{s}^{-1}$ as the lowest value. The decrease of the corrected reading should only depend on the growing distance between

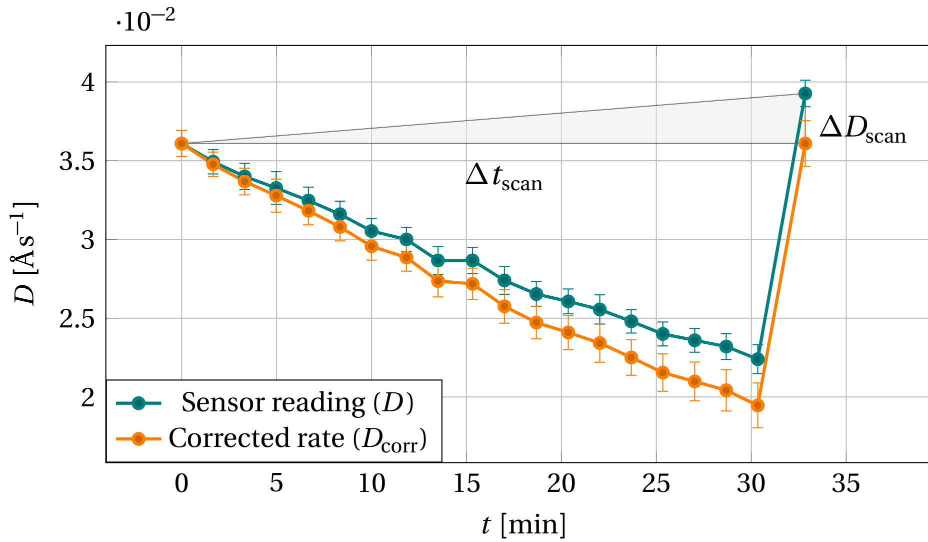

Figure 4.23.: Reading of the deposition sensor over time when the distance of the oven to the detector is increased. The triangle demonstrates equation (4.7) and the orange values show the outcome of applying the equation to the measured values.

the sensor and the oven.

To make the deposition decrease comparable to predictions, without taking the actual evaporation rate into account, the measured values, D_i, were normalized to the deposition value at the starting point of the scan:

$$D_{\text{norm},i} = D_i / D_1 \quad . \tag{4.8}$$

Here $D_{\text{norm},i}$ is the normalized deposition rate, and D_1 the rate measured when the oven was 50 mm away from the detector at the start of the scan.

A simple geometrical prediction

A simple geometrical approach can be used to make a prediction for the reduction of the gas flow on the detector by assuming the gas particles are being emitted by a pointlike source in every direction. When this source is moved away from the detector the deposition rate on the detector reduces by the same amount as the solid angle of the detector seen by the pointlike source. The geometry for this assumption is shown in figure 4.24.

In this model the fraction of the gas jet that hits the detector, $f_{\text{geom.}}$, is:

$$f_{\text{geom.}} = \frac{1}{2}\left(1 - \frac{d}{r}\right) = \frac{1}{2}\left(1 - \frac{d}{\sqrt{a^2 + d^2}}\right) \quad , \tag{4.9}$$

where a is the radius of the detector, d the distance of the source and the detector and r

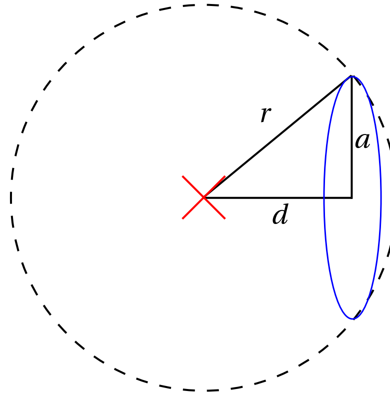

Figure 4.24.: Geometry of the solid angle taken up by the deposition detector. The red cross shows the position of the pointlike source. The detector with radius a is positioned at a distance d.

the radius of the sphere that has its origin at the pointlike source and is just completely including the detector. When using the detector radius $a = 4.1\,\text{mm}$ the fraction $f_{\text{geom.}}$ can be calculated for different values of d. To derive only the reduction of the deposition values the values can be normalized:

$$D_{\text{geom.,norm}} = \frac{f_{\text{geom.}}(d)}{f_{\text{geom.}}(d = 50\,\text{mm})} \quad . \tag{4.10}$$

The result of the calculation is shown together with Molflow+ simulations and the measured values in the following section.

Result and comparison to the Molflow+ simulation

As in the molecular flow regime interactions between gas particles are negligible and only interactions of particles with walls define the gas flow, the gas jet geometry prediction is independent of the actual pressures in the crucible or in the volume around it. The measured deposition rate is linear to the number of particles that hit the sensor area in a certain amount of time. In the simulation this can be modeled as the rate of particles that fall onto a surface whose position and diameter resemble the deposition detector. The rate of particles per time is then again normalized to the one at a distance of 50 mm. Figure 4.25 shows the measured normalized deposition rate together with the Molflow+ simulation for two different lead surfaces (case A and C as seen in figure 3.6) against the distance of the oven tip and the detector. Additionally the prediction of equation (4.10) is included.

Both the measured and the simulated curve start at $D_{\text{norm}} = 1.[a.u.]$ as they are normal-

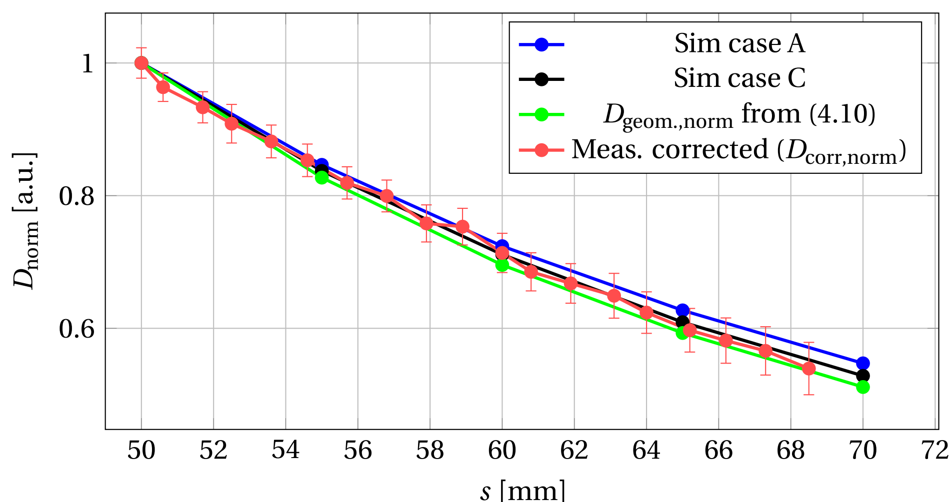

Figure 4.25.: The measured normalized deposition sensor reading (D_{norm}) at different distances (s) between the oven tip and the detector together with theoretical values. Two simulation geometries where used: A and C as shown in figure 3.6. The green line shows results from equation (4.10).

ized. The rate then falls of to approximately 55 % of its original value at a distance above 69 mm. The Molflow+ model predicts the reduction of the deposition rate due to growing detector distance correctly, especially when the drift of the evaporation rate over time is taken into account.

However the reduction is also correctly described by the simple assumptions of equation (4.10), showing that the method is limited in making predictions about the real shape of the gas jet coming from the oven. For this purpose the detector is too far away from the oven. Measurements with the oven closer to the detector have not yet been attempted to prevent heat damage to the detector crystal.

In section 4.4.4 it can be seen that the Molflow+ simulation makes a clearly more precise prediction of the calibration factor than one that is derived with the help of equation (4.9).

4.4. Calibration: From the deposition to an evaporation rate

The deposition monitor is used to get a measure for how much lead the oven is evaporating in a certain amount of time. To get a transformation from the deposition to an evaporation rate, a calibration is needed. As shown, the dominant flow regime is the molecular flow (see e.g. subsection 4.3). Hence the geometry of the lead gas jet outside of the oven is independent of the actual pressures and temperatures in the setup. From this follows that there is a linear relation between the amount of lead deposited onto the deposition sensor

and the one evaporated from the oven crucible, for all relevant temperatures, as long as the structure or the lead surface does not change:

$$R(t) = AD(t) \ , \tag{4.11}$$

where t is a moment in time, $R(t)$ the oven evaporation rate and $D(t)$ the deposition rate on the sensor. A is the relation between the two rates. The term evaporation rate has a certain ambiguity, as lead can be evaporated from the crucible but then re-condensate on other parts of the oven tip. When in this section the evaporation rate is used, it is meant synonymous to the consumption rate of lead in the crucible, when evaporation is the only way that lead exits the crucible. This section presents the method and results of the sensor calibration and compares the results with Molflow+ simulations.

4.4.1. Integration of the measured deposition rates

At the oven test stand it is not possible to measure the mass loss of the crucible during an evaporation measurement. But the weight difference of the crucible before and after a certain time of evaporation at the oven test stand can be measured.

If the shape of the gas jet did not change during the measurement, e.g. due to movement of the oven or changes of the lead surface, the complete amount of deposited material onto the deposition sensor and the amount of lead evaporated from the crucible should have the same relation as in equation (4.11):

$$\int_{t_1}^{t_2} R(t)\,\mathrm{d}t = \Delta M = A \int_{t_1}^{t_2} D(t)\,\mathrm{d}t \ . \tag{4.12}$$

Here t_1 and t_2 are the start and the end point of the measurement in time and ΔM the weight change of the crucible over the measurement. From the equation follows a way to measure the calibration factor A:

$$A = \frac{\Delta M}{\int_{t_1}^{t_2} D(t)\,\mathrm{d}t} = \frac{\Delta M}{I} \ . \tag{4.13}$$

The integral, I, in equation (4.13) can be calculated by using an interpolating fit function through the individual deposition rate measurements over the time in which the oven was operated inside the oven test stand. This is done under the assumption that the sampling rate, i.e. the time between two separated deposition rate measurements as shown in figure 4.15 is resolving all relevant changes of the evaporation rate.

The crucible weight change ΔM is measured using a laboratory-scale for the crucibles weight before and after the run at the oven test stand.

As several changes on the oven test stand were made throughout the study and also other factors like changes in the sensitivity of the crystal might affect the calibration, the described procedure is repeated for each measurement. For each run of the oven at the oven test stand the calibration factor from that run is then used to calibrate the deposition reading.

4.4.2. Uncertainty of the measured calibration factor

The presented method to derive an absolute value for the evaporation rates via integrating the signal and measuring the weight change of the crucible relies on several assumptions. The gas jet geometry needs to be constant over the measurement. For different pressures this is true but simulations show that different positions of the emitting lead surface within the crucible can lead to changing jet profiles. The effect of these geometry changes on the calibration is analyzed in the following section.

Additionally to this the geometry seen by the lead gas atoms can change by condensation droplets or lead oxide formations (presented in section 5.2.3). Another possible flaw of the procedure is the possibility of droplets of lead flowing out of the crucible and thereby changing its weight by another process than evaporation. The effect of this is not easily estimated but the test stand and the oven is checked for visible droplets after each measurement to evaluate whether lead was ejected from the crucible.

Besides the discussed issues with the procedure itself, the uncertainty of the measured values contributes to the uncertainty of the calibration factor. This contribution can be analysed by propagating the uncertainty to the value calculated with equation (4.13).

The uncertainty of the integral, I, in equation (4.13) comes from the uncertainty of the measured deposition values.

I corresponds to a total thickness of deposited material over the time of the integration. However the uncertainty of the measured total thickness is larger than the contribution of I to the uncertainty of the calibration: If the detector systematically over or underestimates the actual deposition rate by a fixed value, the calibration factor A will not be less precise as it only needs the deposition reading of the sensor to be linear to the actual evaporation rate and an offset to the actual amount would be included in the calibration factor.

However independent uncertainties as discussed in subsection 4.1.5 contribute to the total uncertainty of the derived calibration factor as they lower the precision of the integral reading. To estimate their effect on the integral, the functional approach of uncertainty

propagation is used [73]. Here the numerical calculated integral is seen as a function $I(D_1, D_2, D_3, ..)$ where the D_i are the deposition measurement values used to calculate the integral. The contribution $\sigma_{I,i}$ of each independent uncertainty $\sigma_{D,i}$ is then calculated using:

$$\sigma_{I,i} = I(D_1, D_2, .., D_i + \sigma_{D,i}, ..) - I(D_1, D_2, .., D_i, ..) \ . \tag{4.14}$$

All uncertainties can be summed to a total value σ_I with:

$$\sigma_I = \sqrt{\sum_i \sigma_{I,i}^2} \ . \tag{4.15}$$

The uncertainty of the measured weight loss of the crucible due to evaporation comes from the used scale and from the fact that some lead droplets may have been ejected from the crucible. The uncertainty given in the scales manual is $\sigma_{\Delta M,\mathrm{manual}} = 1\,\mathrm{mg}$ [74].

In most measurements of the uncertainty of the crucible weight change was estimated to be $\sigma_{\Delta M} = 10\,\mathrm{mg}$ as an upper limit but when larger droplets are found after a measurement the value was adapted based on the weight of that droplet. The two uncertainties can then be propagated to the uncertainty of A, σ_A:

$$\sigma_A = \sqrt{\left(\frac{\Delta M}{I^2}\sigma_I\right)^2 + \left(\frac{1}{I}\sigma_{\Delta M}\right)^2} \ . \tag{4.16}$$

4.4.3. Calibration factor from Molflow+ simulations

The Molflow+ model can be used to derive a calibration factor. This allows to investigate the influence of the lead surface position within the crucible on the calibration factor.

The deposition rate on the detector is proportional to the fraction f of the lead gas jet that is incident on the detector. Therefore the calibration factor A will be inversely proportional to the value of this fraction:

$$A \propto \frac{1}{f} \ . \tag{4.17}$$

Molflow+ can be used to derive the fraction f for different lead surface positions in the crucible. For these simulations the lead surface positions shown in figure 3.6 from section 3.4.2 were used. Case A is in the back of the crucible, case B in the front but within the crucible and case C is a lead surface that coincides with the inner opening hole of the crucible. The results are shown in the table 4.3.

The simulations predict that a different position of the emitting lead surface in the crucible can cause a difference in the calibration factor of up to up to 35 %.

Additionally the simulated gas jet fraction can also be used to derive a theoretical calibration factor A_{sim} based on the correct internal calibration of the deposition sensor. As the output of the SQM-160 is already a thickness growth rate, these values need to be converted back to a mass deposition rate. This is done with the density of lead ρ_{Pb} and the detector surface area c. The resulting calibration factor A_{sim} can then be calculated, using:

$$A_{sim} = \frac{C\rho_{Pb}}{f} \quad . \tag{4.18}$$

As discussed, the different gas jet fractions f lead to different expected calibration factors, which are also shown in table 4.3.

Derived from	f [%]	A_{sim} [mgÅ^{-1}] $\times 10^{-3}$
Sim case A	1.76	3.4
Sim case B	1.17	5.2
Sim case C	1.27	4.8
Equation (4.9)	0.17	35.56

Table 4.3.: Fraction f hitting the detector together with the calibration factor A_{sim} based on the simulated gas jet profile for the three different lead surface positions shown in figure 3.6. As a comparison also the simple approach with equation (4.9) is shown.

The simulations show that a changing lead surface position can influence the deposition rate measurements significantly. During a measurement it can not be seen if this is the reason of an observed change in the rate. However the connection between the evaporation rate and other parameters still allowed to identify fluctuations of the measured deposition rate that are most likely not caused by simple redistribution of the lead in the crucible.

4.4.4. Comparison of the measured and the predicted calibration factors.

As the calibration of the deposition sensor depends on the geometry of the lead gas jet and the setup was varied over time, for each longterm measurement presented in chapter 5 a new calibration factor was calculated after the measurement. Table 4.4 gives an overview of the measured calibration factors, A_{meas} and the gas jet fraction hitting the detector, f_{meas}, for selected measurements with comparable setups. The measurements have designated names that assign them to the presented measurements in chapter 5.

The measured gas jet fractions are in the same order of magnitude as the ones derived with the Molflow+ model that are presented in table 4.3. On the other hand simply assum-

Measurement name	A_{meas} [mgÅ^{-1}] $\times 10^{-3}$	f_{meas} [%]
S1	3.1 ±0.05	1.95 ±0.03
S2	6.8 ±0.18	0.89 ±0.02
S3	5.7 ±0.2	1.06 ±0.04
N1	6.87 ±0.97	0.88 ±0.04
N2	5.02 ±0.05	1.2 ±0.01
I1	5.7 ±0.1	1.06 ±0.02
I2	5.63 ±0.06	1.07 ±0.01
T1	6.75 ±0.1	0.9 ±0.01
T2	5.66 ±0.1	1.07 ±0.02
U1	4.78 ±0.62	1.26 ±0.16
U2	5.04 ±0.1	1.2 ±0.02

Table 4.4.: Calibration factor A_{meas} and gas jet fraction f_{meas} that hits the detector for selected measurements. The measurement names refer to measurements presented in chapter 5.

ing a point like source that emits into all directions as it is done with equation (4.9) would lead to a significant overestimation of the calibration factor. This demonstrates that the basic understanding of the lead gas profile and the measurements agree. However from table 4.4 it can also be seen that the measured calibration factor varies from run to run, while the setup was not changed. These fluctuations, which are larger than the estimated uncertainties, are not understood.

5. Temporal Evaporation Behaviour

The previous chapter presented the principle of measurements at the oven test stand. The main focus of the study is the temporal behaviour of the evaporation rate. It is mandatory for the GTS-LHC ion source to run for comparably long times, i.e. 2 weeks, to continuously provide the heavy ion beam for the CERN accelerator chain. During the heavy ion program at the LHC, the refill of the oven is the main reason for scheduled downtime of the GTS-LHC ion source. Understanding the influences affecting its stability and endurance is crucial to find methods to improve the oven usage at the GTS-LHC ion source. Two characteristics need to be investigated, the stability of the evaporation and the failure modes, i.e. reasons why the evaporation stops.

This chapter presents a series of measurements that where conducted to understand the temporal evolution of the evaporation rate during continuous oven operation. In the final part of the chapter also alternations to the oven setup are presented that showed promising results to enhance the oven stability and lifetime.

To conveniently identify individual measurements they are referred to with simple names like 'S1' or 'N1'.

5.1. Operation simulation at the test stand

The evaporation rate at the ion source can not be measured with the current setup of the GTS-LHC. But as the applied power is recorded at the source, the oven test stand can be used to replicate the oven operation while using the deposition sensor to measure its evaporation rate and also monitor the outer temperature of the oven with thermocouples. For this goal the oven power data of all runs of 2016 were collected to derive a simple model that resembles a typical tuning of the oven at the source, which can then be applied at the test stand.

5.1.1. Typical power time curve at the GTS-LHC ion source

Figure 5.1 shows the oven power plotted against time for all oven runs at the GTS-LHC ion source in 2016.

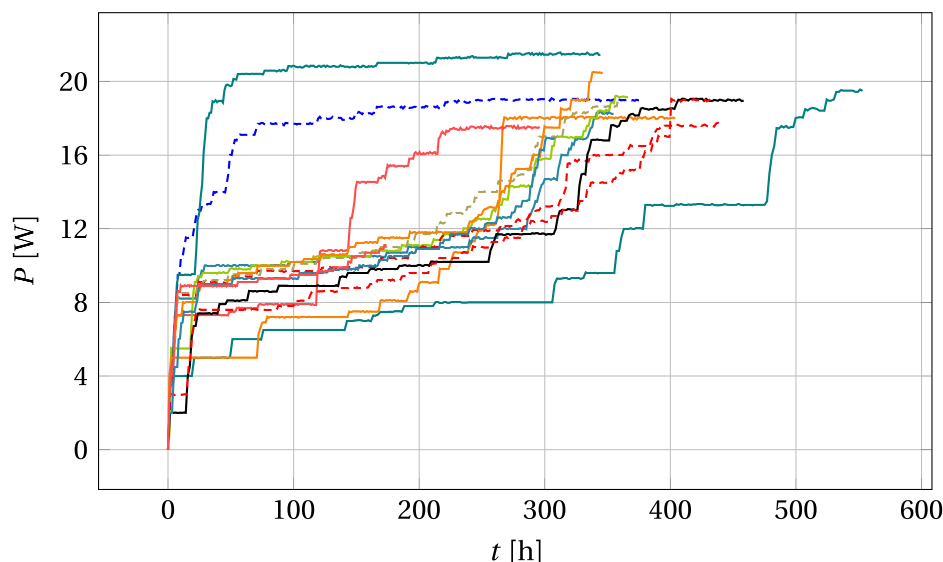

Figure 5.1.: Power values of different oven runs at the GTS-LHC ion source in 2016, set to a common starting time.

It can be seen that at the beginning of an individual run the power was ramped up to start the evaporation. From then on it was adapted by the operator as part of the source tuning to maintain a sufficient source current. From figure 5.1 it is evident that the tuning decisions varied from run to run.

Creating a model for the oven operation

A subset from these curves, shown in figure 5.2, was chosen and manipulated with the goal to derive a model for a typical run. Some of the curves that looked too atypical where excluded, only leaving similar shaped power-time curves.

To not include singular events that happened at the source, the power of the individual oven runs was then manually "cleaned" of sudden drops. Here the oven power dropped to zero for a short time and was then restored after some kind of event cut the oven power. An example of this procedure is given in the left plot of figure 5.3.

Also any long pauses of the ramp up at powers below 6 W were reduced, as this occurred when the oven ramp up was stopped at the evening to be continued on the next morning. To remove these pauses the respective data was dropped and the time values of the power-

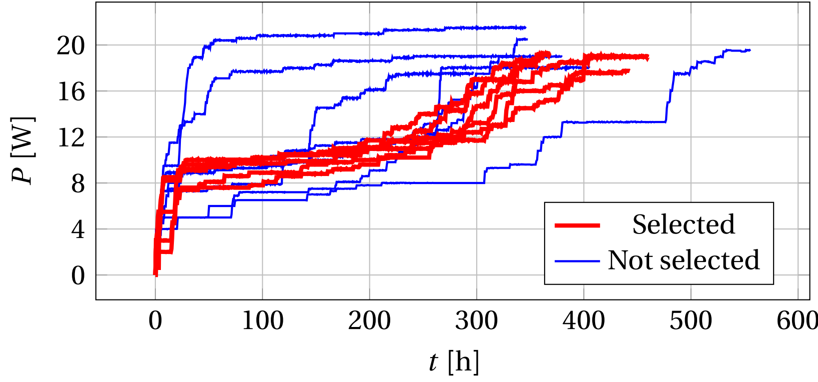

Figure 5.2.: Subset of the power-time curves that was used to derive the model for the typical oven operation at the source.

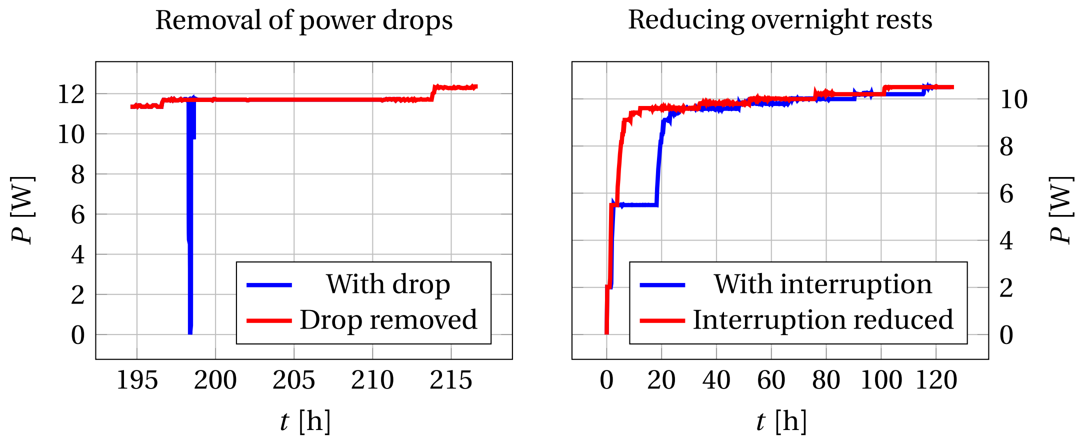

Figure 5.3.: Two examples for manipulation of the power-time curves. Left: Removal of sudden power drops. Right: Reduction of resting time during the power ramp up.

time value pairs after the pause were corrected by subtracting the duration of the pause. The right hand plot of figure 5.3 gives an example for this. The selected curves where cut off at a duration of 360 h into the run.

A simple fit model was then applied to the resulting oven power curves, shown in Figure 5.4 together with the selected and adapted power time curves from the GTS-LHC ion source.

The model consists of a piecewise linear function with 3 different slopes.

$$P_{\text{model}}(t) = \begin{cases} a_1 t & t < t_1 \\ a_2 t + b_2 = \left(a_1 - \frac{b_2}{t_1}\right) t + b_2 & t_1 \leq t < t_2 \\ a_3 t + b_3 = \left(a_1 - \frac{b_2}{t_1} + \frac{b_2 - b_3}{t_2}\right) t + b_3 & t_2 \leq t\ . \end{cases} \tag{5.1}$$

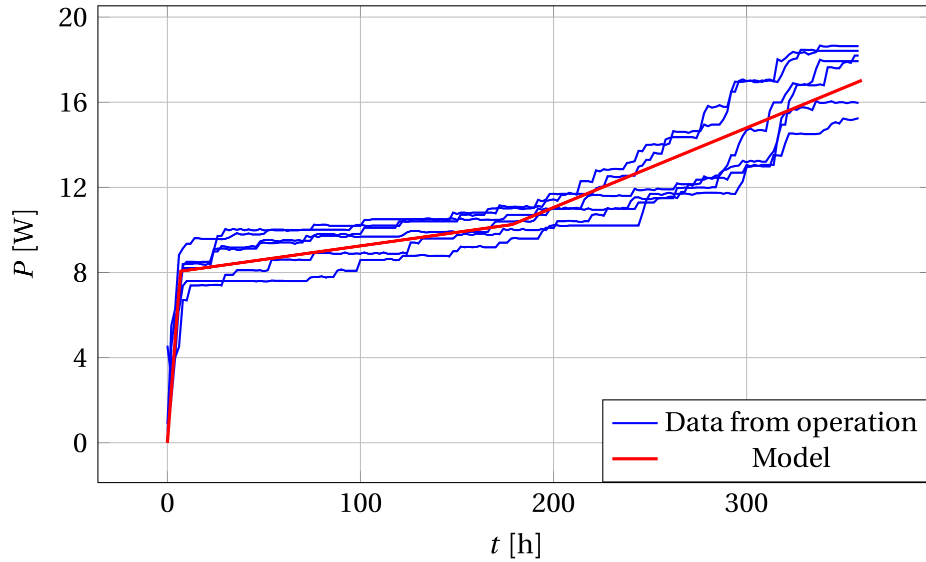

Figure 5.4.: Selected power-time curves where the longer interruptions at below 6 W where cut out. The red line shows a fit model that was applied with the goal to get a representative power-time curve that can be used at the oven test stand.

By fitting the parameters a_1, b_2, b_3, t_1 and t_2, the resulting function reads:

$$P_{\text{model}}(t)[\text{W}] = \begin{cases} 1.19\,[\text{W}\,\text{h}^{-1}]\,t & t < 6.7\,[\text{h}] \\ 0.3\,[\text{W}\,\text{d}^{-1}]\,t + 8\,[\text{W}] & 6.7\,[\text{h}] \leq t < 7.4\,[\text{d}] \\ 0.89\,[\text{W}\,\text{d}^{-1}]\,t + 3.6[\text{W}] & 7.4\,[\text{d}] \leq t\ . \end{cases} \quad (5.2)$$

Following from this fit model a plan for the oven power tuning is derived: A first quick ramp up brings the power to 8 W within a day, then the oven power is only increased approximately 0.3 W a day for 5 consecutive days. In the last part the ramp up is steeper with 1 W per day. This ramp up is kept for another 10 days until the final power is 20 W.

5.1.2. Measurements S1-S3: Applying the power time curve at the test stand

The derived time dependency of the power was applied to the oven at the test stand for several measurements with the goal of recording a characteristic time dependency of the evaporation rate at the oven during operation at the GTS-LHC ion source.

During these measurements the test stand was under vacuum with a pressure of around 5.0×10^{-8} mbar. The deposition sensor shutter opened for 70 s every 30 min and the signal was processed as discussed is section 4.1.5.

As the evaporation behavior of isotopically pure lead should not be different from natural lead, in this study no isotopically purified lead was used. The first measurements were done with unspecified natural lead and the lead samples in the presented tests also displayed visible passivation on their surfaces. In the measurements O3-O4, I1-I2, T1-T2 and U1 samples of chemically pure lead were used to exclude any effects due to lead impurities. Possible influences of the lead quality were studied in measurement U2 in section 5.5.

Table 5.1 gives details about the three measurements like the evaporated amount of lead and the calibration factor.

Measurement	S1	S2	S3
Purpose	Measure typical evaporation rate for GTS-LHC Ion Source		
Setup	2 thermocouples attached to outer oven Oven tip 50 mm from Detector Use derived $P-t$ relation as power input		
Atmosphere	vacuum		
ΔM [g]	0.96 ± 0.01	0.51 ± 0.01	0.37 ± 0.01
$A\,[\mathrm{mg\AA^{-1}}] \times 10^{-3}$	3.1 ± 0.05	6.88 ± 0.18	5.7 ± 0.2

Table 5.1.: Measurements at the OTS where the derived power-time curve was applied to the oven.

Result of run S1

Figure 5.5 shows the resulting evaporation rate of the first measurement together with the applied power.

After the initial ramp up an evaporation rate of approximately 1.2 $\mathrm{mg\,h^{-1}}$ was measured. During the second part of the ramp, the rate then unsteadily grew to 7 $\mathrm{mg\,h^{-1}}$ after 150 h and at a power of 10 W. At $t = 150$ h the rate suddenly dropped to around 2 $\mathrm{mg\,h^{-1}}$ and then rose again with the increasing power.

After 200 h the rate was fluctuating around 7 $\mathrm{mg\,h^{-1}}$ and then suddenly dropped to less then 1 $\mathrm{mg\,h^{-1}}$ at $t = 230$ h. After the drop the evaporation rate again rose to a value of almost 6 $\mathrm{mg\,h^{-1}}$ and then dropped to almost zero after 300 h.

The oven showed heavy fluctuations of the evaporation rate throughout the run. Besides the fluctuations, also the evaporation rate grew much higher than what was expected as average evaporation rate at the GTS-LHC ion source.

As the usual consumption at the source is around 0.75 g of lead in two weeks the average evaporation rate is about 2 $\mathrm{mg\,h^{-1}}$.

To test the reproducibility of this behaviour, the measurement, where the oven power is following the curve shown in figure 5.4, was repeated two additional times.

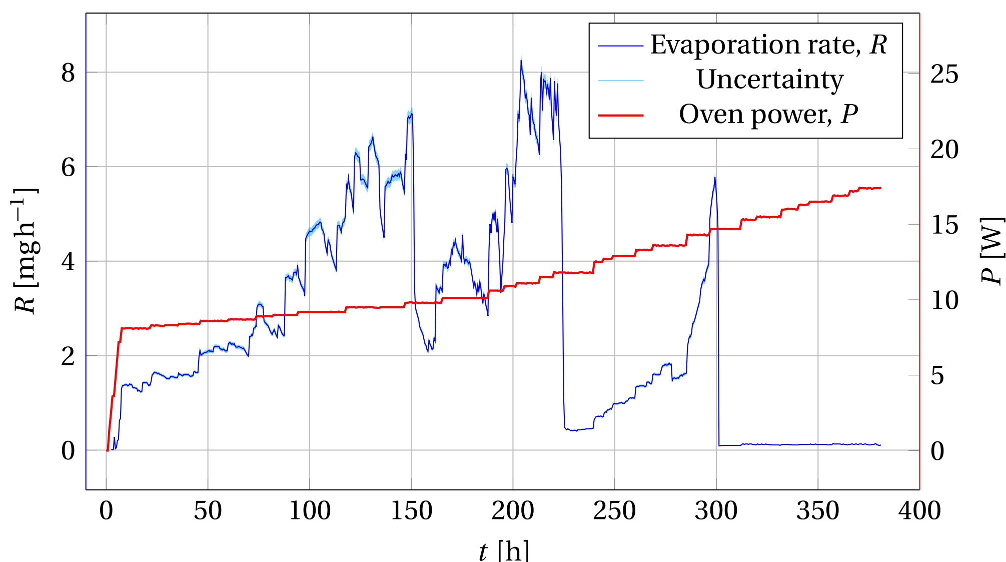

Figure 5.5.: Evaporation rate during the oven operation replication S1 at the oven test stand.

Results of run S2 and S3

Figure 5.6 shows the resulting deposition and evaporation rates for all three consecutive measurements.

The resulting evaporation rate over time is different for every individual measurement. The second run (S2) showed a steep rise of the evaporation rate to a value of 6 $\mathrm{mg\,h^{-1}}$ in the beginning of the measurement. The rate then dropped and after 30 h it was below 1 $\mathrm{mg\,h^{-1}}$. It then slowly rose to a rate slightly below 6 $\mathrm{mg\,h^{-1}}$ over a duration of 120 h with increasing power. After 160 h it suddenly dropped and did not rise above 0.5 $\mathrm{mg\,h^{-1}}$. The run was then stopped after 210 h.

The third measurement showed a very slow rise of the evaporation rate. It reached 2 $\mathrm{mg\,h^{-1}}$ after more than 250 h. After 320 h The evaporation rate started to fluctuate and also reached values above 7 $\mathrm{mg\,h^{-1}}$ before the rate dropped after 350 h.

Calibration

The evaporation rate was measured using the calibration method described in subsection 4.4. The uncertainty of the derived evaporation rate σ_R comes from the uncertainty of the individual measurements σ_D described in section 4.1.5 together with the uncertainty of the calibration σ_A described in subsection 4.4.2. The calibration factor A measured for the individual runs shows differences of more than a factor of two as shown in table 5.1.

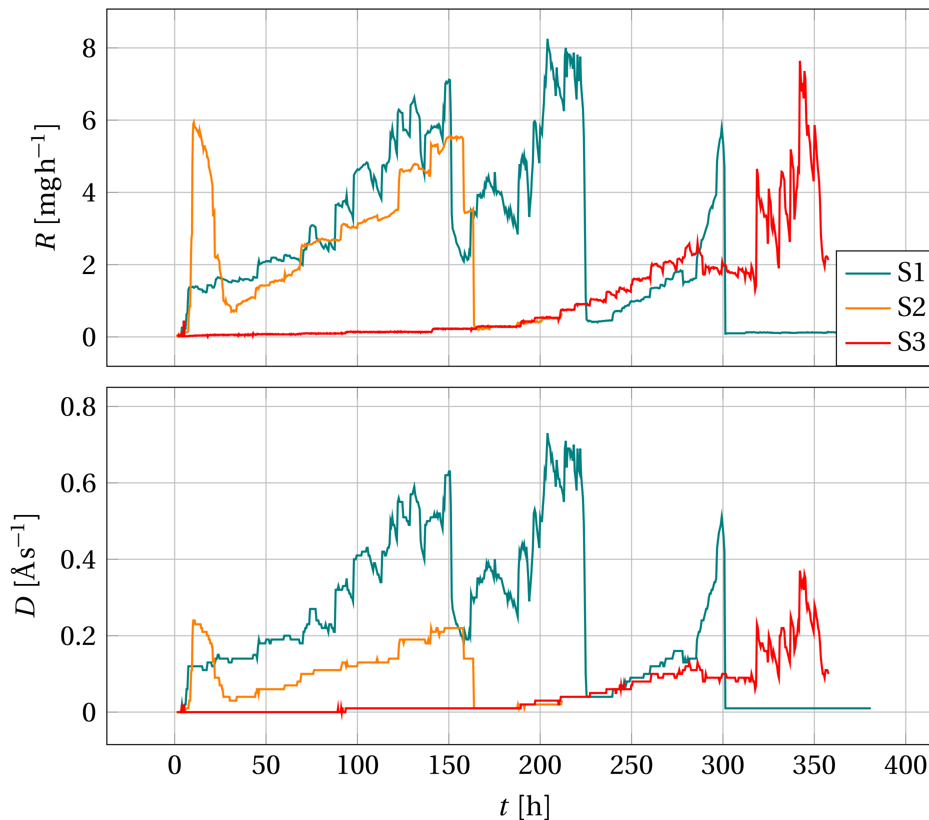

Figure 5.6.: Resulting evaporation rate R and the uncalibrated deposition rate D of the operation replications S1-S3 at the test stand. The two values are shown as the calibration factor A derived from the different runs varies strongly as shown in table 5.1. Run S2 was stopped before reaching the maximum power (after 212 h at 11.5 W) as the evaporation rate did not seem to recover.

Evaporation rate per power

The measurements S1-S3 can also be used to get a basic understanding of the power to evaporation relation of the oven. For this purpose the recorded evaporation rate of each measurement was sorted by the respective heating power that was applied.

Figure 5.7 gives an example for this, where the first 120 h of the evaporation rate measurement of the run S1 are shown in different colors.

Each color in this plot represents all evaporation rate values that where recorded during a fixed power level. To get a single evaporation rate per power it was decided to use the last evaporation rate that was measured during a time step of fixed power. The fluctuations during these steps where too high to make averaging over them reasonable.

Figure 5.8 shows the resulting power to evaporation rate relation for the measurements S1-S3.

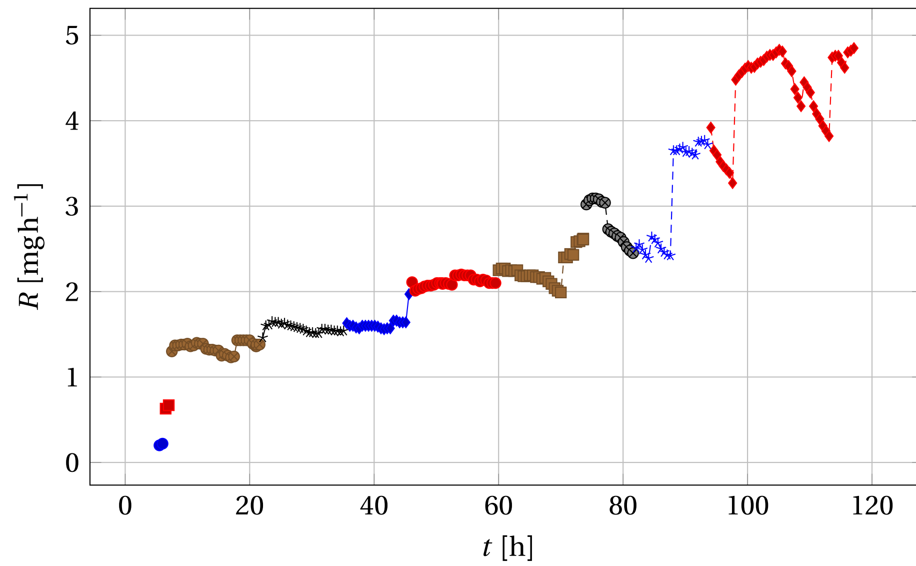

Figure 5.7.: First 120 h of the evaporation rate measurement S1. The different colors represent fixed heating power levels.

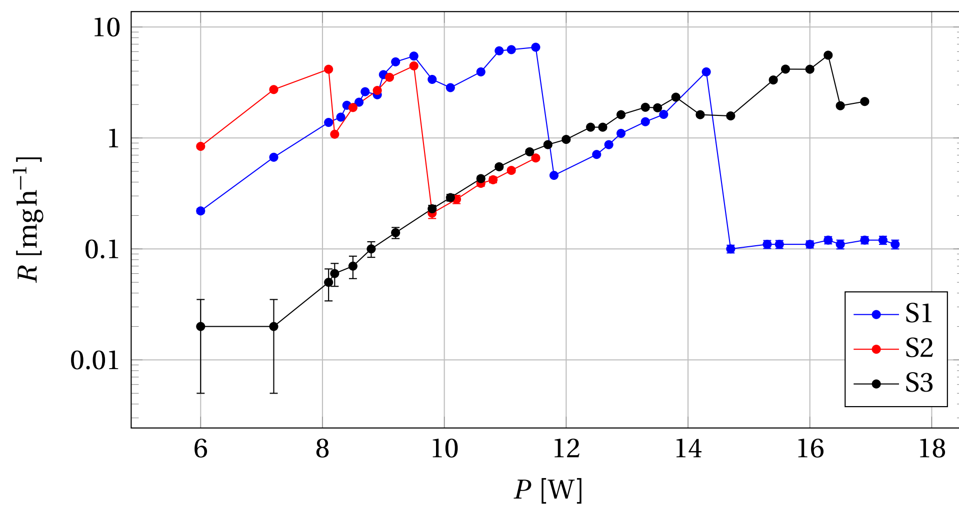

Figure 5.8.: Power to evaporation rate relation for the measurements S1-S3.

It can be seen that measurement S1 shows two distinctive phases. Between the powers of 6 W to 11.5 W the evaporation rate grew almost exponentially with the rising power level. At powers above 12 W the power to evaporation rate relation seems to be another one, corresponding to the steep drop also seen in the time resolved plot in figure 5.5.

At powers above 14.3 W the evaporation rate did not rise with power probably due to an empty crucible in run S1. Run S2 seems to have followed three different relations. At powers between 6 W to 8 W the evaporation rate is higher than during run S1. Then the evaporation rate follows the same relation as S1. At 9.5 W it drops to follow what appears to be a third power evaporation rate relationship.

The run S3 shows a rather consistent rise of the evaporation rate with power without sudden changes. It is noticeable that the final power to evaporation rate relations of the runs S1 and S2 seem to roughly match with the one of the run S3.

Discussion

The setup of the oven test stand was not changed during the three presented measurements. A possible reason for differences in the calibration factor might be a changing crucible position inside the oven between the individual runs as a result of movement during the insertion into the oven test stand. This can not easily be avoided and also happens at the GTS-LHC ion source. Following the predefined power time curve at the oven test stand leads to a measured evaporation rate that is fluctuating and also different for each individual run.

A strong hint that the fluctuations and drops of the deposition rate are indeed not a default of the deposition sensor is, that the evaporation rate could be stabilized by oven modifications (See e.g. figure 5.35). This is presented in the measurements T2 and U1-U2 in later sections of this chapter.

Looking at the power to evaporation rate relation shown in figure 5.8 the oven and the crucible seem to have gone through changes during the run that affect the evaporation rate of the rest of the complete run and possibly even of later runs. This can be seen as hints of changes in the power to temperature relation of the crucible, which was seen and further studied in additional measurements as presented in section 5.3.

The recorded evaporation rates emphasize one aspect of the oven behaviour: In terms of evaporation rate it is not easily reproducible by just strictly following a predefined power-time curve.

At the GTS-LHC ion source the oven power is raised by the operator, who often does this as a reaction to a decrease of the ion current. As the current can undergo sudden

drops in its intensity it is likely that the observed fluctuations partially also happen at the GTS-LHC ion source. Figure 5.1 shows the power time curves at the source, demonstrating that individual runs led to different tuning decisions of the operator.

On the other hand there are aspects of the temporal behaviour of the oven at the GTS-LHC ion source that were not recreated in the presented measurements. Inside of the GTS-LHC plasma chamber oxygen is used as a buffer gas, so the oven does not operate in complete vacuum but is surrounded by gas at a higher pressure. The effects of the buffer gas on the oven were studied in additional measurements at the oven test stand that are presented in the following section.

Possible reasons for the observed fluctuations and the low reproducibility are discussed in the section 5.3 with supplemental measurements but also with additional data from the already presented ones.

5.2. Active gas injection

As the plasma chamber is usually filled with a buffer gas besides the gas jet coming from the lead oven (described in section 2.4), it is important to also assess the effect of different gases on the oven performance. Especially as a frequent observation after a run at the ion source is a built-up of oxidized lead on the tip of the outer oven cover. After the measurements presented so far the only visible formation at the oven cover tip, were small droplets of condensed lead.

To allow experiments with different gases, a gas injection system with a thermovalve was installed at the oven test stand (presented in section 4.1.3). The following measurements were performed to asses the effect of two different gases at different pressures on the oven.

Table 5.2 presents the measurements with an active nitrogen injection.

Measurement	N1	N2
Purpose	Effect of nitrogen	General oven stability in nitrogen
Setup	Same as S1-3	
	P follows predefined $P-t$-curve	P set according to evap. rate
Atmosphere	Nitrogen with 1×10^{-5} mbar	Nitrogen with 1×10^{-5} mbar
ΔM [g]	1.4 ± 0.2	1.51 ± 0.01
A [mgÅ^{-1}] $\times 10^{-3}$	6.87 ± 0.97	5.02 ± 0.05

Table 5.2.: Measurements that were conducted with a nitrogen atmosphere.

5.2.1. Measurement N1: Operation simulation in nitrogen

Measurements using nitrogen were performed to test if a change of the oven evaporation behaviour could be noticed in the presence of a non reactive gas in the test stand. A first measurement repeated the method previously presented, following a preset power time curve (measurements S1-3) for the heating power. With the gas injection a nitrogen a pressure of 1×10^{-5} mbar was set inside of the OTS.

Results

The evaporation rate and the applied power of measurement N1 is shown in figure 5.9.

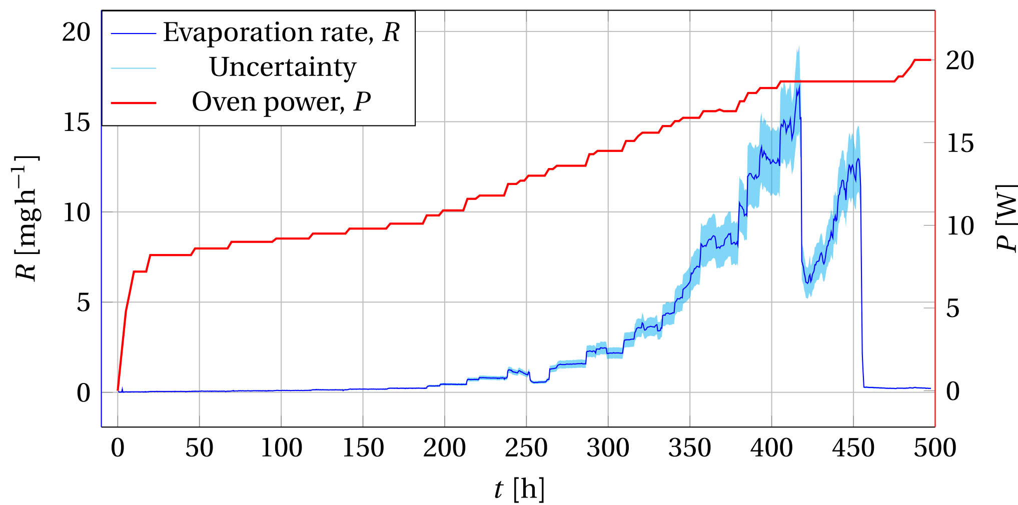

Figure 5.9.: Measured evaporation rate of the oven with a nitrogen atmosphere at a pressure of 1×10^{-5} mbar during run N1. The calibration factor was calculated to be $A = 6.87 \pm 0.97$ [10^{-3} $\mathrm{mg\AA^{-1}}$] with $\Delta M = 1.42 \pm 0.2$ [g]. The comparably large uncertainty for ΔM comes from observing a droplet of lead under the oven in the test stand. This could be a sign of lead flowing out of the crucible without evaporating.

The evaporation rate grew very slowly and only after 250 h it started to rise to a value of $1\,\mathrm{mg\,h^{-1}}$. It then grew with the increasing oven power until it reached a value of $15\,\mathrm{mg\,h^{-1}}$ after 400 h. After a drop to approximately $6\,\mathrm{mg\,h^{-1}}$ the evaporation rate rose again to $13\,\mathrm{mg\,h^{-1}}$ and then dropped to almost zero after 450 h, which was before the power was raised to its final value, 20 W.

The same procedure to derive a power to evaporation rate relation as presented for the measureents S1-3 was applied to the data of this measurement. The results are presented in figure 5.10 together with measurement S3 as a comparison.

It appears that during the measurement N1 the oven followed approximately the same

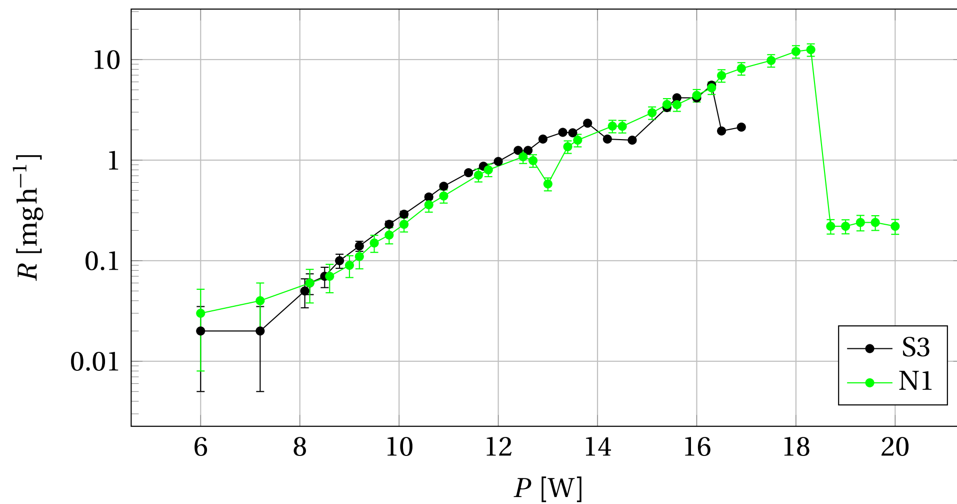

Figure 5.10.: Power to evaporation rate relation for the measurements S3 and N1.

evaporation rate to power relation as during the measurement S3 but this time the rise continued further to higher rates before the evaporation stopped.

Discussion

As discussed before, a difficulty is the anyway poor reproducibility of the evaporation behaviour in this kind of measurement. The measurement this time showed a higher final evaporation rate compared to what was observed before. However it is not unrealistic that the evaporation rate can grow steeply when the oven temperature rises as the temperature dependence of the the vapour pressure is exponential (see equation 3.2). The evaporation rate to power relation seems not to have changed compared to the previous measurement that had no nitrogen injection.

5.2.2. Measurement N2: Can the oven run stable when operated accordingly within nitrogen ?

A second measurement was conducted where the oven power was adjusted to achieve a sufficient deposition signal from the start of the run and was then only raised if the signal dropped. It should test how stable the oven can be operated when the operator actively reacts on the evaporation rate. Also it should asses if the evaporation stops before the crucible is empty. Another purpose was to asses how the injected nitrogen would affect the lead condensation at the tip of the oven. This requires a sufficient amount of lead condensate at the oven tip.

Results

The results are shown in figure 5.11.

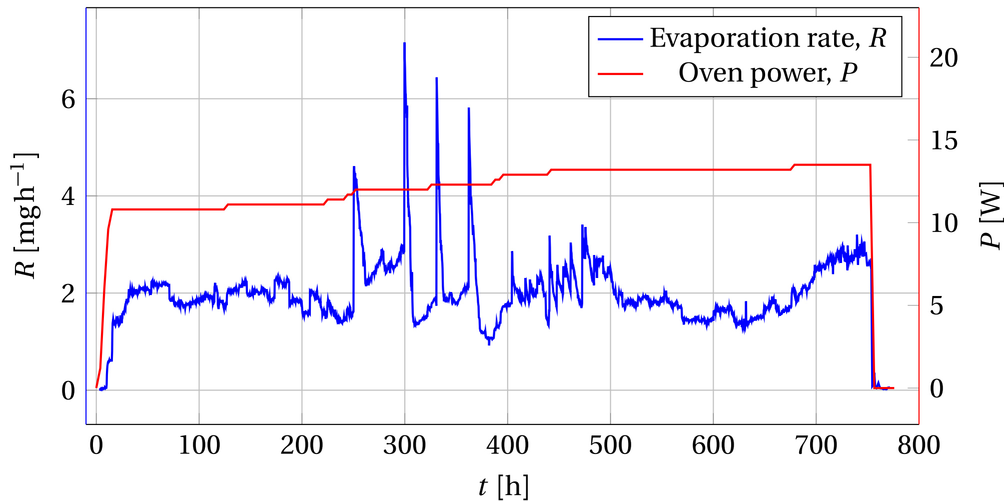

Figure 5.11.: Evaporation rate and power during run N2, in a nitrogen atmosphere where the power was adjusted to keep the evaporation stable. The lead consumed in total was $\Delta M = 1.51 \pm 0.01$g and the resulting calibration factor is $A = 5.02 \pm 0.05\,[10^{-3}\,\mathrm{mg\AA^{-1}}]$.

The power was ramped up to a value of 11 W in the beginning of the measurement and then only raised slowly to a maximum value of 14 W after 690 h. During the measurement the evaporation rate fluctuated around a mean value of around 2 $\mathrm{mg\,h^{-1}}$. After 250 h the evaporation rate displayed four peaks where it grew to a rate between 4 and 6 $\mathrm{mg\,h^{-1}}$ and then returned to a value similar to what it had before the rise. After 400 h no further peaks occurred but the evaporation rate still fluctuated and drifted. The run was stopped after 755 h and the crucible was examined. It appeared empty and no remaining lead could be seen or measured.

The power to evaporation rate relation derived for measurement N2, shown in figure 5.12 shows higher evaporation rates then the ones measured during run N1.

Also the curve shows no clear exponential rise of the evaporation rate with heating power. This however is not surprising, as the power was only raised as a reaction to a dropping evaporation rate during the run and the oven was resting at constant power for much longer time than in the previously presented measurements. Hence the final evaporation rate at each power step was similar.

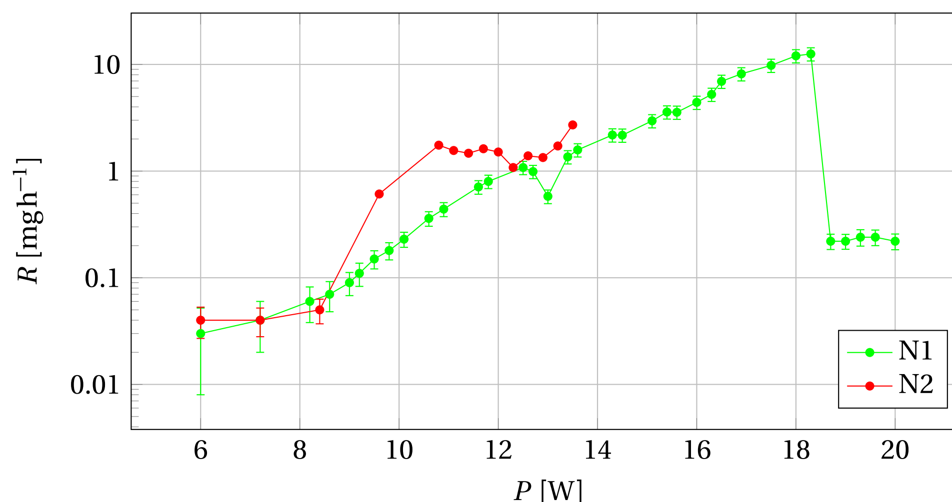

Figure 5.12.: Power to evaporation rate relation for the measurements N1 and N2.

Discussion

The measurement shows that it is possible to run the oven over a long time (more than 30 d) with an evaporation rate that is fluctuating around a median of $2\,\mathrm{mg\,h^{-1}}$ and practically consume all of the lead in the oven crucible. But the evaporation rate remained unpredictable, making the oven tuning unplannable. Also the evaporation rate to power relation differs from the one measured in measurement N1, again demonstrating the poor reproducibility of the oven operation.

The reason for the sudden rises and following drops of the evaporation rate are not understood. The oven tip after the run showed no significant material built-up exceeding the condensate droplets that have been seen before, which was expected as nitrogen is not oxidizing.

5.2.3. Oven operation in an oxygen atmosphere

The GTS-LHC ion source is using oxygen (see section 2.4) as a buffer gas and the oven tip after a run at the source frequently shows formations of lead oxide that can be big enough to block the complete oven. Two examples of the oven appearance after running at the GTS-LHC ion source are shown in figure 5.13.

The test stand was used to asses whether an oxygen atmosphere without a present plasma is enough to reproduce this behaviour.

A first test with oxygen in the test stand demonstrated that indeed the oven tip showed a formation of lead oxide. As the following measurement demonstrates the same behaviour

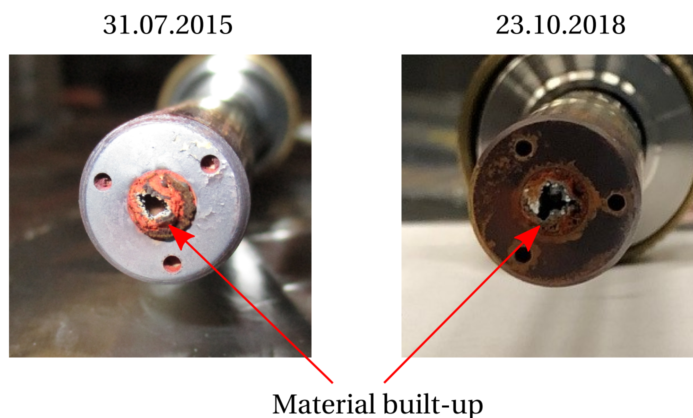

Figure 5.13.: Appearance of the oven tip at the given dates after two individual runs at the GTS-LHC ion source. The oven tip shows a built-up of material that is composed of lead and lead oxide.

in more detail, the first test will not be presented.

The test stand was then modified to study the oxide formation in more detail: A window was installed besides the deposition detector, that allows to observe the oven tip while the oven is running. Additionally a feedback loop controlling the thermovalve was put in place, which allows to more precisely stabilize lower pressures (down to 1×10^{-6} mbar) in the test stand. Without the loop this was prevented by drifting. Table 5.3 presents some details of the measurements, used to asses the effect of oxygen on the oven.

5.2.4. Measurement O1: Formation of a lead oxide blockage

At a pressure of 1×10^{-5} mbar the oven was operated in a similar way as during measurement N2, presented in figure 5.11. The power was ramped up until a sufficient deposition rate was seen and then only increased when the rate seemed too low. Photos were taken to document the changes in the oven tip appearance, i.e. the formation process of the blockage.

Results

Figure 5.14 shows the resulting measurement of the evaporation rate together with selected photos of the oven tip.

The evaporation rate rose steeply and then fluctuated around a value of around 3.5 $\mathrm{mg\,h^{-1}}$ until it dropped to nearly zero after 440 h. The photos show a material built up at the oven tip that grows into a complete blockage. After around 14 days the oven was completely

Measurement	O1	O2	O3
Purpose	Effect of oxygen Document lead oxide blockage formation	Effect of oxygen at lower pressure	Influence of lead quality
Setup	No changes on oven Thermocouples attached Power set according to evaporation rate	Same as O1	Same as O1 Chemically pure lead
Atmosphere	Oxygen with 1×10^{-5} mbar	Oxygen with 1×10^{-6} mbar	Oxygen with 1×10^{-5} mbar
ΔM [g]	1.62 ± 0.01	1.49 ± 0.2	0.71 ± 0.01
$A\,[\mathrm{mg\AA^{-1}}] \times 10^{-3}$	7.4 ± 0.18	4.66 ± 0.6	6.07 ± 0.6

Table 5.3.: Experiments at the OTS used to asses the formation process of a lead oxide blockage at the oven tip.

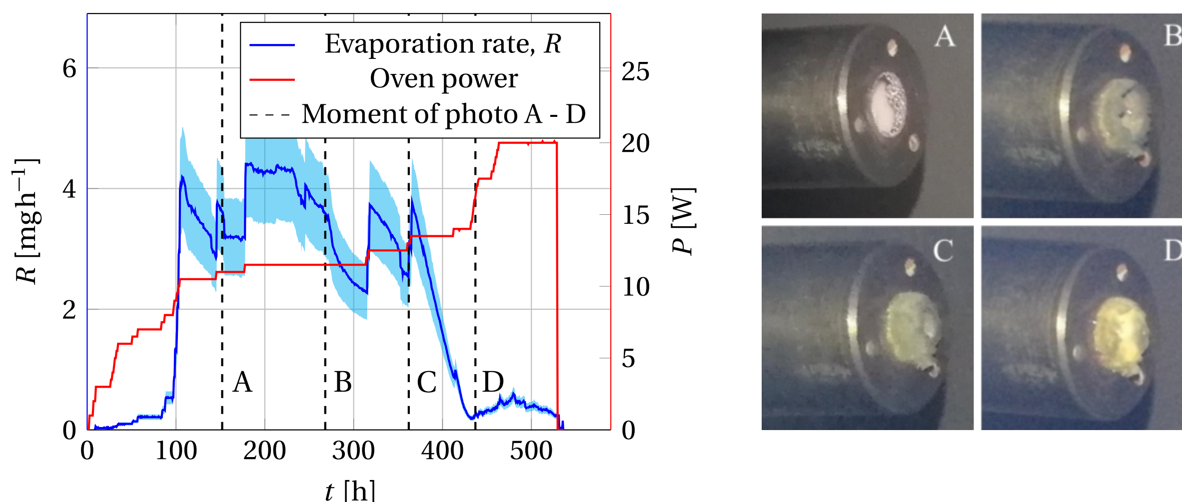

Figure 5.14.: Effect of the oxygen atmosphere of 1×10^{-5} mbar on the oven. The plot shows the evaporation rate and the oven power during the measurement O1. The dashed lines within the plot depict the moments at which the photos on the right where taken.

blocked. It was tested if the blockage can be removed by heating the oven with 20 W but that was not the case.

Calibration

The usual calibration from a deposition to an evaporation rate via the weight change of the crucible would lead to a calibration factor of $A = 7.4[10 \times 10^{-3}\,\mathrm{mg\,Å^{-1}}]$. However after the oven was blocked the evaporation continued depositing the lead onto the inner part of the blockage. Hence the deposition sensor showed no signal, while the evaporation was still ongoing, making the integral of the detector readout an underestimation.

To still get an estimation of the evaporation rate during the run, the calibration factor of a former run, N2, was used (shown in table 5.2). The scattering of the measured calibration factors for different runs however shows, that this estimation has an uncertainty that exceeds the calculated uncertainties of the individual calibration factors for the respective run.

To take this into account, the standard deviation of all individual calibration factors throughout the study, which were assessed to not be flawed by blockages or larger lead spillage, was calculated and used as the uncertainty of the calibration in this case: $\sigma_{A,\mathrm{comb.}} = 1.4\,[10^{-3}\,\mathrm{mg\,Å^{-1}}]$.

Blockage formation process

The photos in figure 5.14 give insight into the formation process of the lead oxide blockage. It is not growing from the crucible but, as it can be seen in photo 'A', the starting point is a formation at the outer oven cover. This shows that the lead forming the blockage is oxidizing, after a fraction of the gas jet re-condenses on the front of the cover. By oxidizing the condensate becomes solid and the blockage can grow, as more lead is being deposited onto the already existing formation. For this to happen several factors play a role:

A significant amount of lead coming from the crucible is deposited onto the oven cover. Secondly the oven cover is cold compared to the crucible and lowers the local vapour pressure of lead on the covers surface enough to form a condensate. As a third factor the oxygen pressure needs to be high enough to have a sufficient amount of reactions to form the blockage.

The fraction of gas being deposited onto the oven cover can be estimated using Molflow+ simulations (see section 3.4). For this purpose the properties of the facets that represent the inner oven cover are adapted to count and absorb all particles impinging on them. The simulation was performed for different positions of the lead surface within the crucible (the same as presented in figure 3.6) and also for two crucible positions.

At the GTS-LHC the crucible is usually placed as far in front within the oven cover as possible. To asses if this is already a countermeasure for the deposition onto the oven cover, the Molflow+ simulations were performed for one case were the crucible is further within the oven and another one, where it is almost touching the oven cover in its front. The two crucible positions are depicted in figure 5.15.

In the photo 'A' of figure 5.14 it can be seen that the initial area of growth for the lead oxide blockage is the inner part of the oven cover opening. To distinguish, where the lead is actually deposited, two fractions of the lead gas jet were calculated, $f_{\text{compl.}}$ is the one that hits the inside of the oven cover anywhere (the red area in figure 5.15) and the fraction, f_{opening}, that is hitting the cover exclusively at its opening (shown as cyan in figure 5.15).

Table 5.4 presents the results of the simulations. The position of the emitting lead surface within the crucible is not changing the results significantly, so the presented table shows only the outcome of the simulations for the lead surface at the front of the crucible (case C in figure 3.6) and states an uncertainty that takes into account the result from the other surface positions.

The simulated fractions show that if the crucible is placed deep inside the oven more than half of the emitted lead is interacting with the oven cover. This does not imply that also half of the lead is re-condensed, as the gas atoms may be reflected off the walls of the

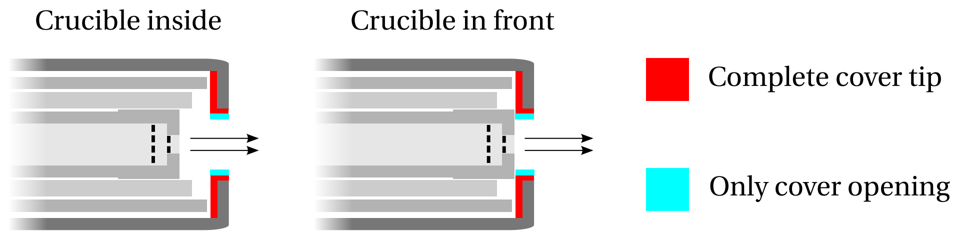

Figure 5.15.: The two crucible positions that were simulated with Molflow+ to derive the fractions of the gas jet that hit the inner walls of the oven cover. Fraction $f_{\text{compl.}}$ is impinging the cover anywhere in the red region, f_{opening} is the fraction that impinges the opening of the oven cover, depicted in cyan.

Crucible position	$f_{\text{compl.}}$ [%]	f_{opening} [%]
Inside	54 ±2	28 ±1
In front	18 ±1	18 ±1

Table 5.4.: Simulated fractions of the lead gas jet that hit the oven cover. $f_{\text{compl.}}$ is the part that impinges the cover anywhere, while f_{opening} is the fraction hitting the oven cover opening.

oven cover but it shows that the deposition is a significant fraction of the gas jet. When the crucible is moved to the front this value drops to around 20 %.

But the simulations also show that while the total value drops significantly the impingement on the inside of the cover opening is only reduced from 28 % to 18 % by moving the crucible to the front. So in both cases it can be expected that enough lead is deposited onto the part of the cover that was identified as the starting point of the blockage.

5.2.5. Measurement O2: Does the blockage form at a lower oxygen pressure ?

To asses the range of oxygen pressures in which the oxide blockage forms the oven was operated within an oxygen pressure of 1×10^{-6} mbar. The power was chosen to ensure a comparably high evaporation rate.

Results

The evaporation rate during the measurement with an oxygen pressure of 1×10^{-6} mbar is shown in figure 5.16 together with a photo of the oven tip taken directly after the run.

The evaporation rate throughout the measurement was around $3\,\text{mg}\,\text{h}^{-1}$ with some fluctuations leading to a rate as high as $15\,\text{mg}\,\text{h}^{-1}$. This ensured a sufficient deposition of

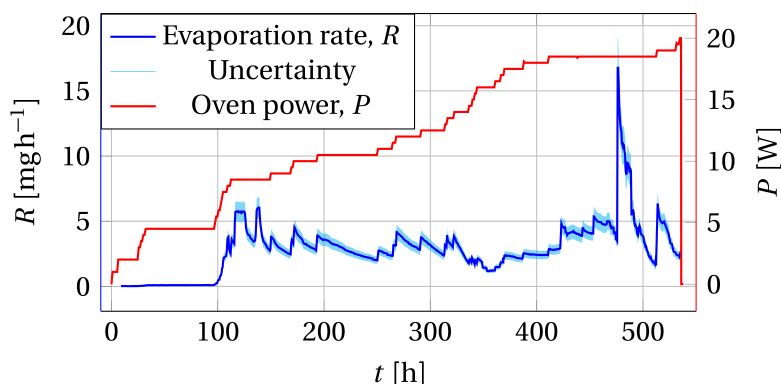

Figure 5.16.: Oven run in 1×10^{-6} mbar of oxygen during run O2. The evaporation rate was kept comparably high throughout the run to observe the blockage formation. At this pressure little to no visible lead oxide is forming apart from a brown colouring of the oven cover and comparably much lead condensate as well as a bigger lead droplet within the oven cover. The photo shows the oven tip after the measurement.

lead onto the outer oven cover and with engough oxygen this would have led to a blockage.

In contrast to the measurement in 1×10^{-5} mbar of oxygen, a lower pressure of 1×10^{-6} mbar led to a picture more similar to the condensate that was also observed without gas injection or with nitrogen and the oven was not fully blocked.

Calibration

A big lead droplet in the front of the oven that can be seen in the photo of figure 5.16 might have been ejected from the crucible. Therefore the weight of this droplet is added to the uncertainty of the measured crucible weight difference, which increases the uncertainty of the calibration factor. The calibration then yields $A = 4.7 \pm 0.6\,[10^{-3}\,\mathrm{mg\text{Å}^{-1}}]$.

Discussion

The local oxygen pressure at the oven within the plasma chamber of the GTS-LHC ion source is not known. From the presented measurements it can be deduced that the lead oxide formation is depending on the pressure and when no plasma is present, a stable blockage only forms at oxygen pressures above 1×10^{-6} mbar.

The difference in appearance of the photos in figure 5.13 and the blockage in figure 5.14 demonstrates that the blockage formation in the test stand is not fully identical to the one in the plasma chamber. A possible factor is the presence of a plasma at the GTS-LHC ion source and thereby also oxygen ions.

5.2.6. Measurement O3: Blockage formation with chemically clean lead

The two photos in figure 5.13 demonstrate that the appearance of the material formation at the oven tip can vary after different runs. The picture of 2015 shows a more extensive formation than the left one from 2018. While it was usual routine in 2015 to recycle the lead that was left in the crucible and reuse it for later runs, this procedure was not continued in 2018.

The lead samples at the GTS-LHC ion source of 2018 all consisted of lead that was not used in the oven before. Generally the experience is that the blockage formation at the GTS-LHC ion source is less severe with the new practice of not recycling.

Therefore it was tested if the influence of the lead quality also affects the blockage formation at the oven test stand. The samples from the measurements presented so far were produced out of unspecified lead that already showed clear signs of passivation from oxidation in air. In a series of measurements, including the one in this section, the samples were made from chemically clean (99.999 %) lead purchased from Nova Elements [75].

Result

Figure 5.17 presents the evaporation rate and photos of the oven tip at different times. The oxygen pressure was 1×10^{-5} mbar (like in run O1). To calibrate the evaporation rate, again the calibration factor from run N2 was used, together with an uncertainty representing the scattering of the calibration factors, as discussed for measurement O1.

After ramping up the heating power to 8.2 W the power was not changed for almost 100 h as the evaporation rate did not drop. Contrary the evaporation rose, which led to the decision to reduce the heating power to 8.0 W. A buildup of lead oxide appeared and after approximately 150 h the oven appeared blocked. The evaporation rate could not be held stable and also a rise in the heating power could only recover the rate for short times. After 273 h having reached a heating power of 19.5 W it was decided to stop the run.

Discussion

The formation of the lead oxide blockage is the same as in measurement O1, showing that the blockage can not be mitigated by using chemically pure lead. The pictures also demonstrate what was discussed in a previous paragraph about the blockage formation process: The crucible is placed as far in the front as possible within the oven cover, but the blockage formation is not reduced compared to the one of measurement O1 shown in figure 5.14.

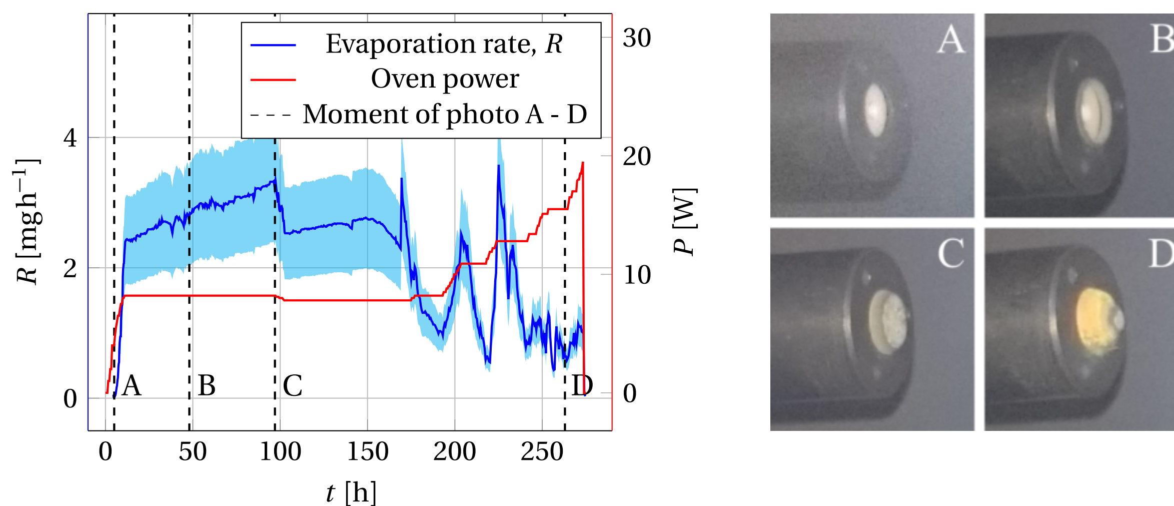

Figure 5.17.: Measurement O3 at the oven test stand, using chemically clean lead at an oxygen pressure of 1×10^{-5} mbar. The photos show the oven tip at different times during the measurement.

The experiment could not reproduce the experience of a reduced blockage formation when only using not recycled and thereby cleaner lead at the GTS-LHC ion source.

5.2.7. Measurement O4: Crucible with a beak

Based on the discussion of the blockage formation one can develop strategies to prevent the blockage and enhance the oven endurance. One possible way is to modify the crucible tip in a way that no lead is being deposited onto the colder oven cover. Figure 5.18 shows a crucible design where the crucible tip is extended out of the oven cover with a 'beak'.

From the molecular flow of the gas follows that no lead gas should get behind the beak, as there are no straight trajectories from the crucibles opening to the oven cover. This can be seen in the Molflow+ simulation of the gas jet coming from the modified crucible, which is also shown in figure 5.18.

A crucible with the presented design, made of the same material (alumina) as the usually used crucibles, was produced and tested at the test stand. Table 5.5 summarizes this measurement.

An oxygen pressure of 1×10^{-5} mbar was maintained throughout the run. Again the heating power was raised until a sufficient reading on the deposition sensor was seen. Then the power was only adapted when the evaporation rate would decrease significantly.

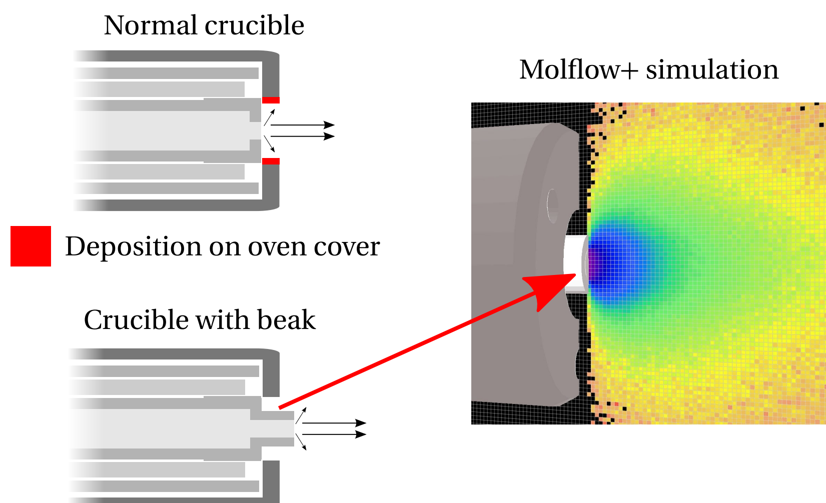

Figure 5.18.: Crucible modification with the goal to prevent lead deposition on the outer oven cover. Right: A Molflow+ simulation showing a gas density plane in a logarithmic color map using the modified crucible shape.

Measurement	O4
Purpose	Can a modified crucible prevent the oxide blockage
Setup	Modified crucible with beak Crucible completely in front Unused tantalum reflector foil
Atmosphere	Oxygen with 1×10^{-5} mbar
ΔM [g]	0.61 ± 0.01
A [mgÅ^{-1}] $\times 10^{-3}$	2.92 ± 0.5

Table 5.5.: Measurement O4 at the OTS.

Results

The measured evaporation rate together with the applied power is depicted in the plot of figure 5.19. The photo on the right hand side of figure 5.19 shows the tip of the oven inside the oven test stand after the measurement.

The oven power was raised until 9.3 W within the first 35 h of the measurement. As the deposition signal then remained stable and did not decrease, the power was not increased any more throughout the run. The evaporation rate fluctuated around a mean value of 1.7 mg h^{-1}. After 390 h the measurement was stopped.

No traces of lead oxide could be seen on the oven tip during or after the run. Additionally no lead was inside the crucible beak, all of the remaining lead was still in the usual 'reservoir'

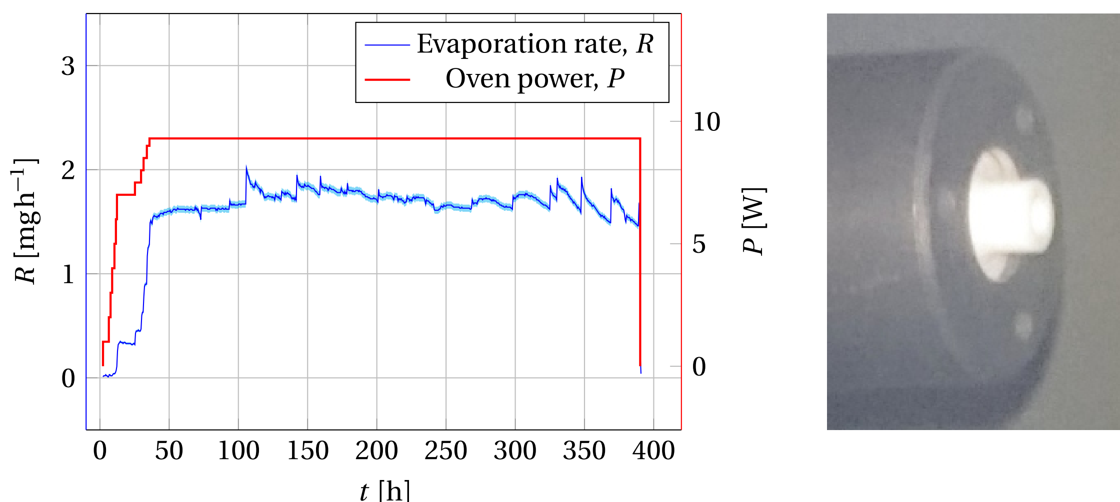

Figure 5.19.: Evaporation rate and power during measurement O4 at the oven test stand. The photo shows the appearance of the oven tip after the run.

of the crucible.

Discussion

The run demonstrates that it is possible to use this type of crucible without damage to the beak like falling of due to thermal stress. Additionally no lead or lead oxide blocked the crucible beak, which shows that the lead did not flow into the beak and that the beak itself was hot enough to not cause any condensation of the lead vapour. Throughout the run the oven could be operated in an oxidizing atmosphere without any trace of lead oxide forming at its tip.

However the evaporation rate that was achieved so far is below the average lead consumption rate of the oven at the GTS-LHC ion source. This measurement was a first test with an unknown calibration factor. It is believed that by choosing an appropriate heating power, a higher evaporation rate should be possible.

5.2.8. Discussion of the blockage formation

Measurements at the test stand demonstrate that the presence of an oxygen atmosphere with a pressure of 1×10^{-5} mbar leads to the formation of a blockage that can not be removed by higher heating powers.

Molflow+ simulations show that a significant fraction of the lead gas jet is incident on the colder oven cover and that this can not be mitigated by adjusting the crucible position

within the oven. The lead condensates at the oven cover and then oxidizes, which allows the growth of a lead oxide cone. While a chemically purer lead sample showed no effect on the formation process, a lower oxygen pressure of 1×10^{-6} mbar caused no blockage formation.

The formation of the blockage is a failure mechanism of the evaporation and also an (at least partial) explanation of the need to raise the oven power throughout operation at the GTS-LHC ion source: The shrinking aperture requires higher evaporation rates for the same amount of lead gas exiting the oven into the plasma chamber.

The measurement O4 demonstrates one possible way to prevent the blockage buildup by using a modified crucible tip that prevents the lead deposition on the oven cover. Another way to operate the oven within 1×10^{-5} mbar without clogging is demonstrated with the measurements U1 and U2.

5.3. Unstable evaporation rates

From the presented measurements it can be seen that the evaporation rate over a longer period of time is not always constant but can display sudden changes both growing or dropping as well as drifting over periods of time.

The absolute evaporation rate of a sample of lead does not depend on the amount of lead but on its temperature, the position and the size of the emitting surface (see section 3.4.2).

Different processes can be considered to affect the stability of the measured deposition rate.

- Impurities of the used lead samples affect the evaporation rate.
- The lead surface changes its position inside of the crucible, which influences both the evaporation rate and the measured deposition rate.
- The temperature in the crucible is not homogeneous and when the lead relocates when being consumed it is exposed to different temperatures.
- The overall oven temperature is temporally not stable.
- The environmental conditions change, like the pressure around the oven or the outer temperature.
- The oven or the test stand is exposed to vibrations.

The environmental influences do not qualify as an explanation for the observed changes. When the test stand is used without active gas injection the pressure is not changing rapidly and is so low that one would expect no influence on the evaporation rate. During measurements with active gas injection the thermovalve stabilized the pressure.

A series of measurements was conducted to find influences on the temporal stability of the evaporation rate. Table 5.6 shows the measurements presented in this section and which focused on the oven stability.

Measurement	I1	I2
Purpose	Understand unstable evaporation	test r-leveling
Setup	No thermocouples Power controlled	Thermocouples installed Resistance controlled
	Pure lead New filament Ta-foil had to be reduced	
Atmosphere	Vacuum	
ΔM [g]	0.94 ± 0.01	1.59 ± 0.01
$A\,[\mathrm{mg\AA^{-1}}] \times 10^{-3}$	5.7 ± 0.1	5.63 ± 0.06

Table 5.6.: Measurements at the OTS that focused on the evaporation rate stability of the oven.

5.3.1. Measurement I1: Minimizing interfering influences

To rule out as many interfering influences as possible, a measurement was performed with an unused filament and a new crucible filled with chemically clean lead. Additionally no thermocouples were attached.

While assembling the oven, the heat reflective tantalum foil that is part of its setup had to be shortened by cutting off a piece of approximately 1 cm as it was damaged and would not fit into the assembly otherwise. The power was adjusted manually to keep a stable evaporation rate. When the rate dropped notably it was raised until the evaporation rate recovered.

Results

The measured evaporation rate together with the power is presented in figure 5.20.

At a power of 9 W the evaporation rate rose to a value of around $5\,\mathrm{mg\,h^{-1}}$ and stayed stable for more than 60 h at a constant power value. Then it dropped suddenly, which led

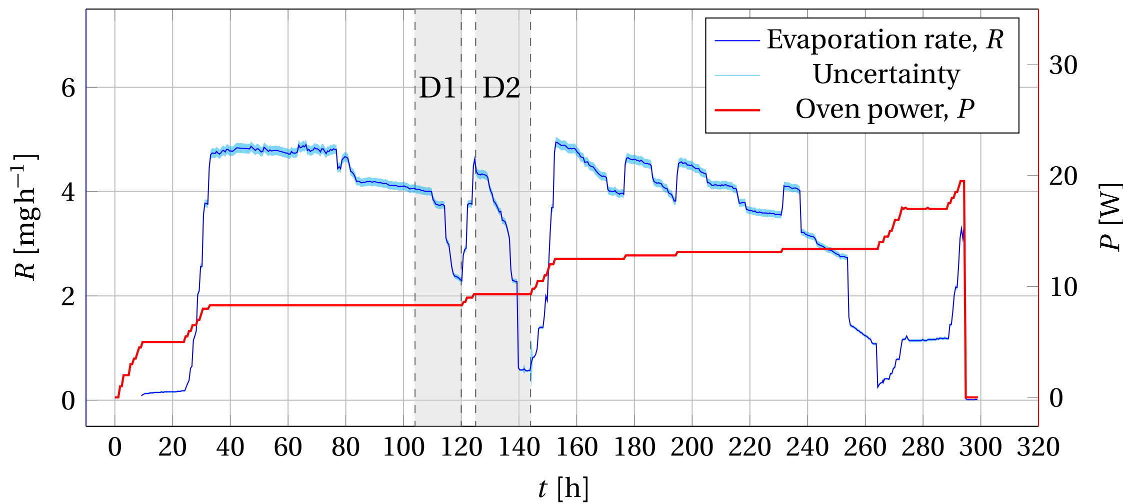

Figure 5.20.: Evaporation rate and power during measurement I1, with chemically clean lead, a reduced tantalum foil and without external thermocouples. Two time windows, D1 and D2 are further discussed, see figure 5.21.

to the decision to raise the oven power. A second drop of the evaporation rate followed and made an additional raise of the power necessary.

In the second half the evaporation rate decreased over time when the power stayed constant. By raising the oven power several times the evaporation rate could be stopped from dropping below 3 $mg h^{-1}$ for around 80 h. Then it dropped further and it was decided to stop the measurement. During this measurement the evaporation rate was stable over longer times than what was observed before.

Evaporation and resistance changes

Two distinctive drops of the evaporation rate can be seen and only an increase of the oven power could restore a comparable rate as before. The time frames of the drops are marked in grey in figure 5.20, calling them 'D1' and 'D2'.

It was observed that during the evaporation decrease the oven filament resistance, r, displayed a similar decrease over time as the evaporation rate. Figure 5.21 shows the evaporation rate during these time frames, together with the filament resistance.

In both time frames the evaporation is not changing more than 1 $mg h^{-1}$ over a time of approximately 10 h and then suddenly drops, in the frame D1 1.5 $mg h^{-1}$ in 4 h and in frame D2 2.5 $mg h^{-1}$ in less than 4 h. In the two time frames the resistance of the oven filament showed a similar temporal profile as the evaporation rate.

The visible fluctuation of the filament resistance is due to the numerical precision of the

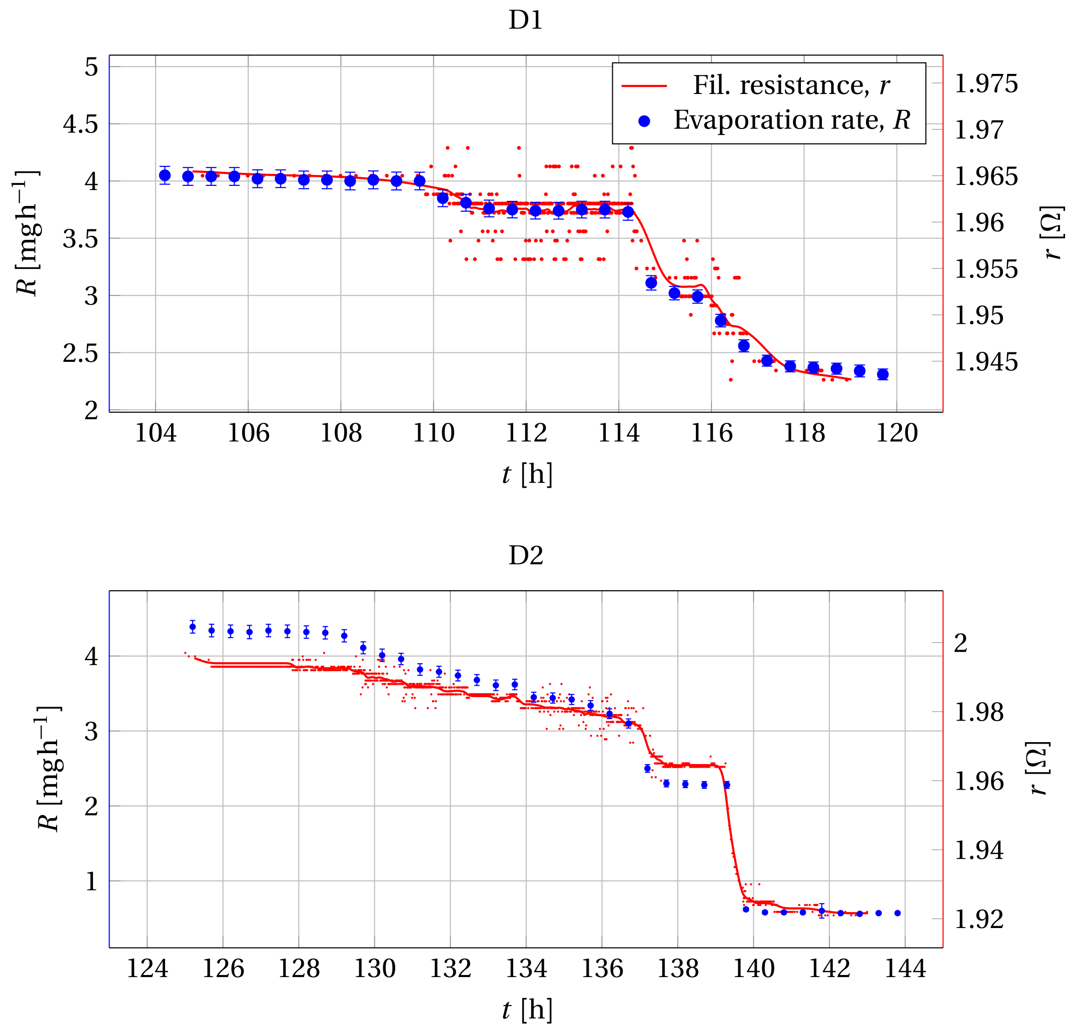

Figure 5.21.: Evaporation rate and filament resistance r plotted for the two time windows D1 and D2 as shown in figure 5.20. Both drops of the evaporation rate happened while the oven power was constant.

PLC that calculates the resistance from the current and voltage values of the power supply.

The change of the resistance especially in the first case (D1) is more easily visible by smoothing the data, as the change is within the range of the noise fluctuation. For this purpose the resistance data was smoothed using a Gaussian filter.

In both graphs of figure 5.21 the measured resistance is convoluted with a Gaussian function in the time domain, whose width is $\sigma = 20\,\text{min}$. The smoothed values are shown as a solid line while the raw resistance data is included as unconnected marks.

Resistance derivation

Plotting the resistance together with the evaporation rate for the complete run in a similar way as done with the oven power in figure 5.20 makes it difficult to see any drops in the resistance, as e.g. the change during the time window D1 is smaller than the resistance increase during a typical power increase.

To still get an overview of the local resistance behaviour in comparison to the evaporation rate, a time derivation of the resistance values can be used. In the two presented cases the resistance is decreasing together with the evaporation. To focus on such events one can look at a value representing the negative derivation:

$$|r'_{\text{neg}}| = H\left(-\frac{\partial r}{\partial t}\right)\left|\frac{\partial r}{\partial t}\right| \quad , \tag{5.3}$$

where H is the Heaviside step function in this case setting positive results to zero and $\frac{\partial r}{\partial t}$ the derivative of the resistance r with respect to time t. Equation 5.3 gives a value that is positive if the resistance drops and zero if it does not change or if it grows.

Figure 5.22 shows the value of $|r'_{\text{neg}}|$ calculated from the smoothed resistance data together with the evaporation rate. The values were normalized, becoming $|r'_{\text{neg,norm}}|$. Additionally the resistance data were cut off before the power was set to zero, as the resulting peak of $|r'_{\text{neg}}|$ would otherwise overshadow all other resistance drops. As a last step all values of $|r'_{\text{neg,norm}}|$ smaller than 0.05 were set to zero simply to make the resulting plot clearer.

The result shows that several times the resistance drops over the duration of the measurement and in the time of the three largest decreases of the resistance also the evaporation rate dropped, which is visible as peaks of the $|r'_{\text{neg,norm}}|$ value.

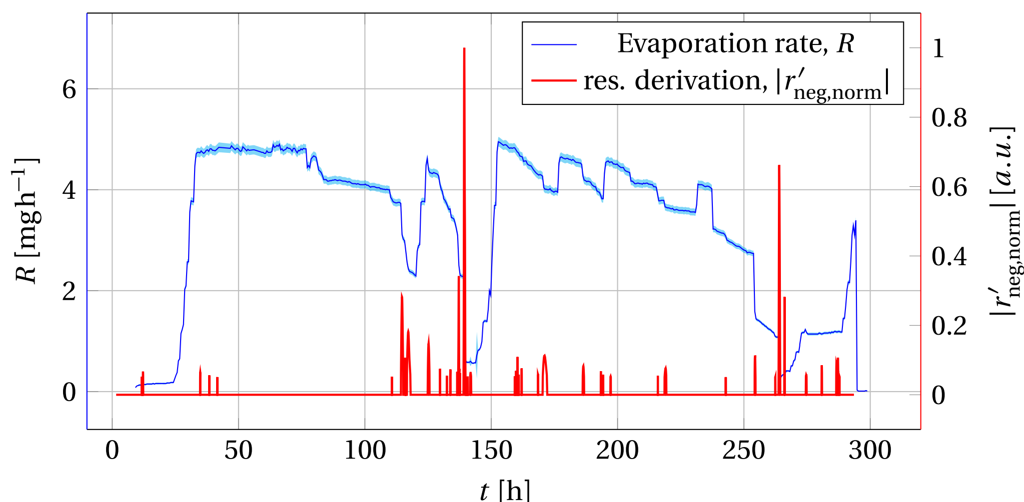

Figure 5.22.: The evaporation rate together with $|r'_{\text{neg,norm}}|$ which indicates a negative derivation of the filaments resistance.

5.3.2. Similar events in other measurements

With the presented method the evaporation rate in other measurements was compared to the filament resistance behaviour. Figure 5.23 shows the resistance decreases for the measurement S1, first presented in figure 5.5.

Again the largest resistance decrease (without turning off the power) fell into a time window where the evaporation rate dropped significantly, although the sampling rate of the evaporation measurement was too low to resolve if the correlation is as direct as in the cases in figure 5.21.

At this time also the two thermocouples (TC1 is placed 22 mm and TC2 98 mm from the oven tip) attached to the outside of the oven displayed a change in their reading, which is shown in the lower plots of figure 5.23.

The plot also shows that not all encountered sudden evaporation rate changes are accompanied by resistance changes.

5.3.3. Discussion of the resistance changes

To explain the correlation between the evaporation rate and the filament resistance one can look at the possible influences on the evaporation rate. From the ones listed in the introduction to this section only the crucible temperature qualifies as a possible connection.

This means that the observed behaviour is a strong hint that the inner temperature of the oven can be unstable at constant power levels. So at least in the presented cases parts

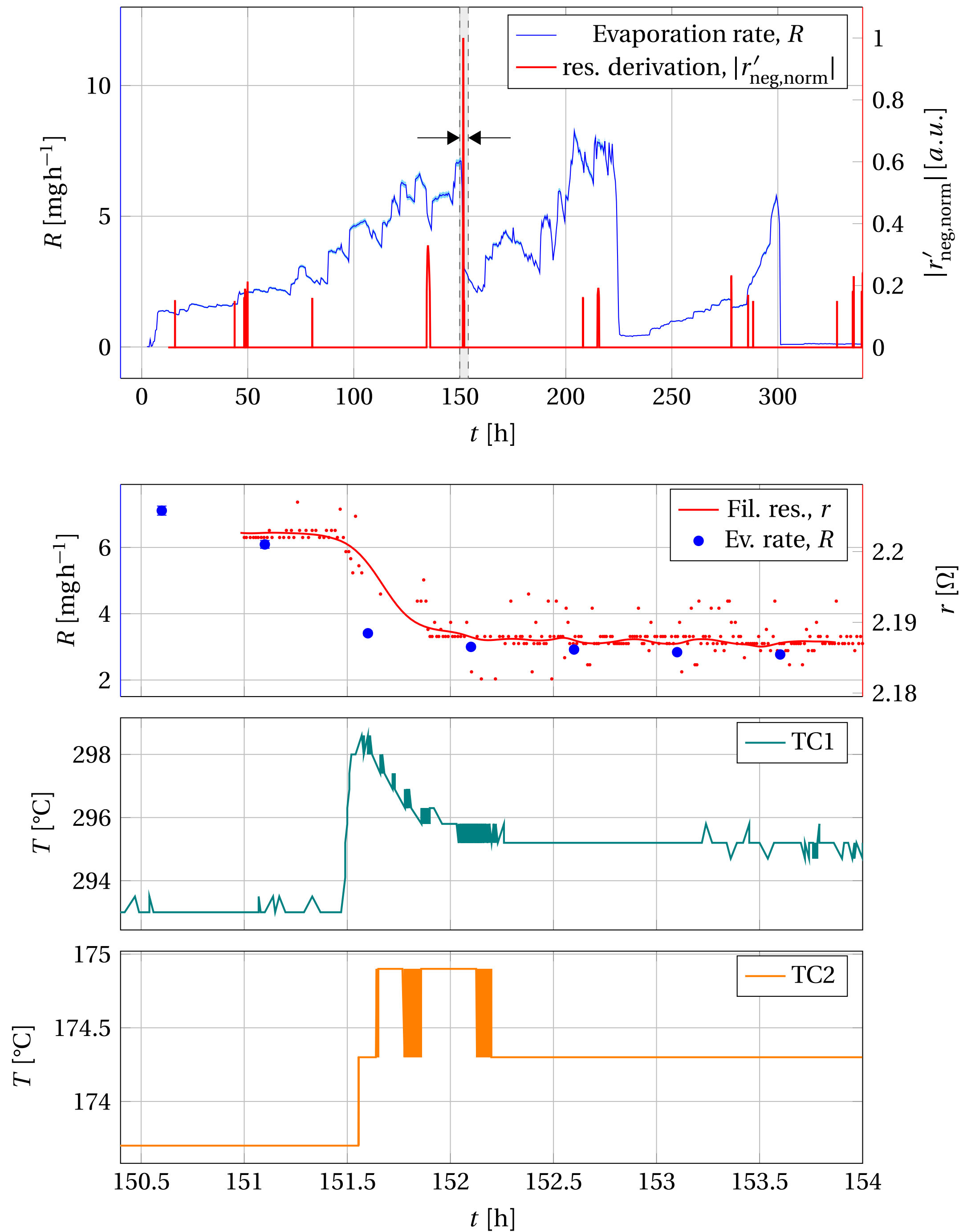

Figure 5.23.: The upper plot shows the evaporation rate together with peaks indicating negative resistance changes during measurement S1. The grey area, also marked by arrows, in the upper plot shows the time window of the three lower plots. In this time frame the evaporation and the resistance dropped while the thermocouples showed a slight increase.

of the evaporation rate instabilities can be explained by a changing temperature of the oven itself. Also the change in the thermocouple reading at the same time as the resistance changes during measurement S1, shown in figure 5.23, is a hint that the complete oven is affected by some kind of process changing its thermal distribution at a constant power.

The behaviour of the evaporation rate and the resistance can both be explained as a reaction to a changed thermal distribution within the oven. When the temperature drops, the evaporation rate drops. As the resistance of the tantalum filament is almost linear to the filament temperature the resistance also drops when the filament temperature drops.

A possible cause for the change of the thermal distribution are changes in the insulation properties of one or several of the layers around the filament, possibly due to thermal stress.

Besides being desirable for the operation in the source, stabilizing the oven temperature would allow to asses further influences on the evaporation rate. The following section presents a "non invasive" test at the test stand to cushion the instabilities by automatically leveling the filament resistance with a feedback loop that controls the current. A bigger impact on the stability was however seen by changing the oven insulation, which will be presented in a later section.

5.3.4. Measurement I2: Can instabilities be reduced with a stabilized filament resistance ?

In measurement I2 it was tested if a feedback loop acting on resistance changes can stabilize the evaporation rate. In an ideal case a feedback loop would stabilize the crucible temperature. But as no direct reading of the crucible temperature exists during the oven operation, the filament resistance serves as an alternative way to measure the temperature inside of the oven.

If during a change of temperature inside of the oven the crucible and the filament change their temperature at the same time, the resistance also changes. So when the feedback loop acts on a resistance change, it indirectly reacts on a temperature change inside of the oven.

During the previously presented measurements the heating power was leveled by a feedback loop that changes the current in the filament with the aim to achieve a certain heating power, as presented in section 4.1.1. This control loop was modified to instead level the filament resistance. After the change, the loop changed the current of the oven power supply until a desired resistance value, within a tolerance of 30 mΩ, was reached.

During measurement I2 the oven was operated by manually changing the resistance setpoint, until a desired evaporation rate was measured. When the evaporation rate dropped during the measurement, the setpoint was manually raised, which increased the heating current until the evaporation rate recovered. The measurement was done in a similar setup to the measurement I1, with chemically clean lead and the reduced heat reflective tantalum foil inside the oven.

Results

Figure 5.24 shows the resulting evaporation rate during measurement I2.

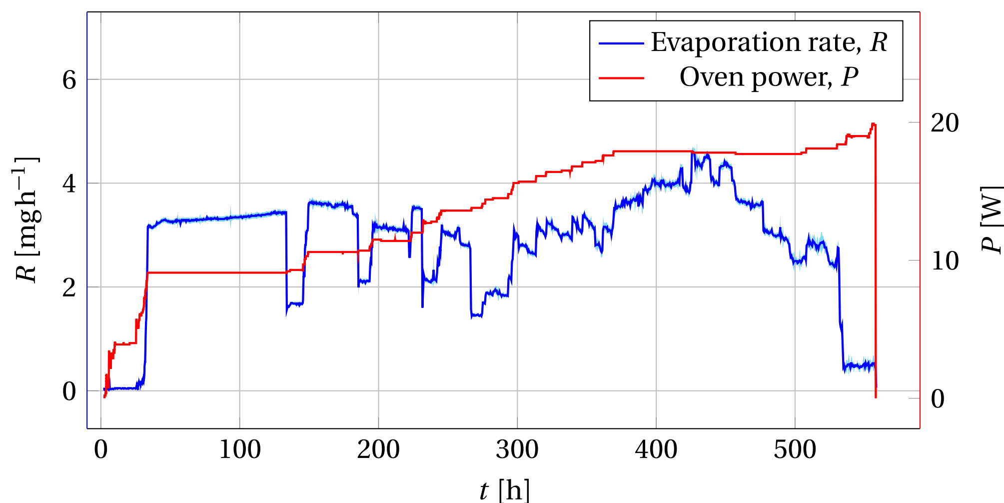

Figure 5.24.: Evaporation rate and power of measurement I2, where the filament current is automatically adjusted to keep the filament resistance at a desired value. The oven was operated by manually changing the resistance setpoint.

At the beginning of the measurement the evaporation rate stayed almost constant at a value of 3 mg h^{-1} for more then 100 h. Then it dropped below 2 mg h^{-1} in less than 1 h. As the evaporation rate stayed at that value it was decided to raise the resistance setpoint which led to a higher filament current and a higher power in the oven. This happened several times and in the second half the evaporation rate underwent more fluctuations than in the beginning.

Figure 5.25 shows the evaporation rate over the time of the complete measurement together with the value given by equation 5.3. Even though the resistance was controlled by the feedback loop it underwent sudden drops, that the feedback loop reacted on by raising the heating current.

It is evident that the first significant evaporation rate drops correlate with negative

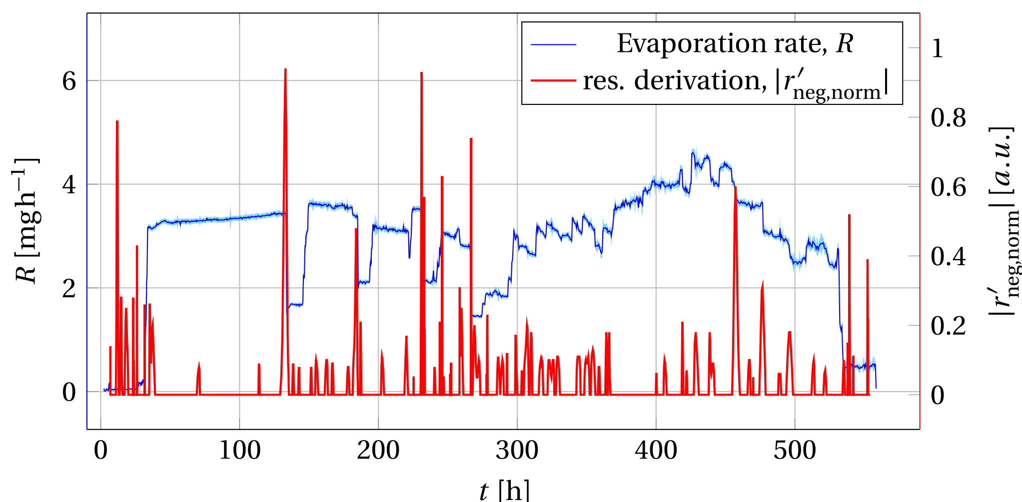

Figure 5.25.: Evaporation rate of the oven together with drops of the resistance during measurement I2.

changes of the oven resistance. As the feedback loop acted on these changes the filament resistance was brought back to an allowed value by raising the current in the filament and thereby the power. Figure 5.26 shows this reaction for the first drop of the evaporation rate.

The resistance suddenly decreased and when its value dropped below the allowed difference of 30 mΩ to the setpoint, the feedback loop reacted and raised the current in the filament. With the higher current the power increased by approximately 0.2 W. This higher power also needed to be maintained to keep the filament resistance close to the setpoint value after the drop. The evaporation rate however stayed below 2 mg h^{-1} after the drop, even when the resistance was brought back into the allowed range by the feedback loop. Figure 5.27 depicts the resistance setpoint with its tolerance as a colored region, together with the measured resistance and the evaporation rate during a selected time window.

Only a manual increase of the resistance setpoint for the feedback loop, resulting in a significantly higher heating power, could restore an evaporation rate similar to the one before the drop.

Discussion

This behaviour again demonstrates that parts of the evaporation rate instabilities come from temperature instabilities of the oven itself. A feedback loop reacted in a desired way, changing the oven power at the right time and into the right direction when the evaporation rate dropped.

But while the loop reacted on the evaporation rate instabilities, only stabilizing the

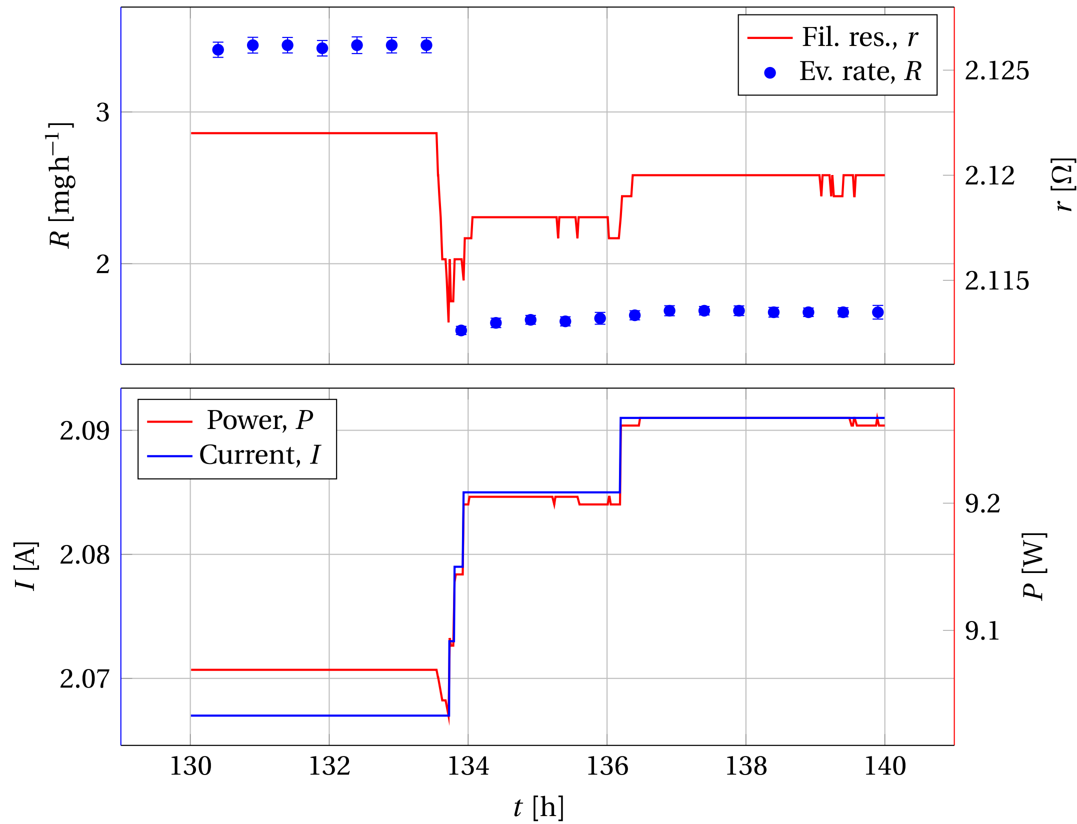

Figure 5.26.: Filament resistance, oven current and oven power together with the evaporation rate in the time frame of the first evaporation rate drop.

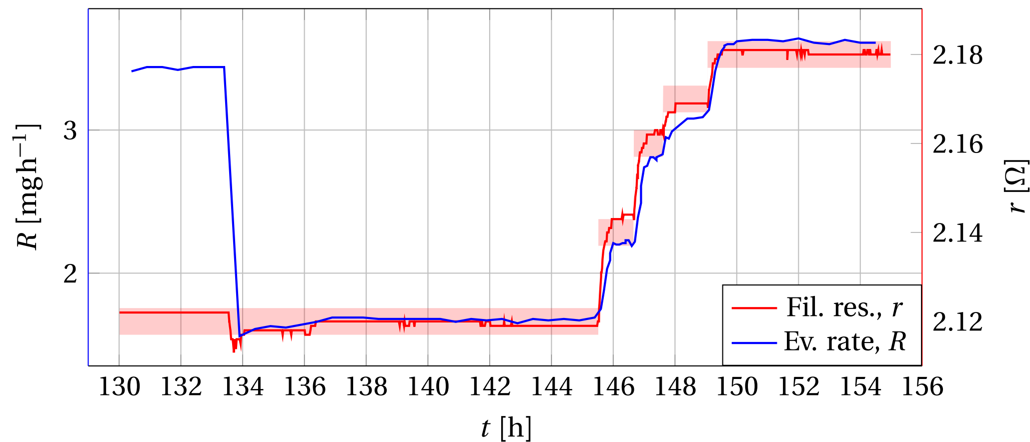

Figure 5.27.: Resistance setpoint together with the measured resistance and the evaporation rate during a time window where the evaporation rate dropped. Only by manually choosing a new setpoint the evaporation rate could be restored.

resistance was not sufficient to keep the evaporation rate stable. This can be interpreted as such that the process in the oven, that changes the thermal distribution within it, affects the crucible stronger than the filament temperature and thereby its resistance.

It is not understood why this measurement showed more resistance changes than the measurement before (5.22 compared to 5.25). It is possible that structural changes of the oven, like aging of the heat reflective foil, or difference in the tightness of the screws holding the oven cover caused this behaviour.

5.4. Oven insulation modifications

The previously presented results show that some of the evaporation rate instabilities seen at the oven test stand come from processes changing the ovens thermal distribution and thereby the temperature of the crucible. To understand the role of the oven insulation in these processes the heat reflection foil was modified in several measurements. Additional front insulation as well as removing the reflective foil was tested. Table 5.7 shows the measurements whose results are being presented in the following section.

Measurement	T1	T2
Purpose	Is stability affected ?	Is stability affected ?
Setup	3 Ta insulation rings in front inner diameter: $d_{\mathrm{ta}} = 3.6\,\mathrm{mm}$ Feedback loop on resistance	Ta foil removed Crucible completely in front Feedback loop on resistance
Atmosphere	vacuum	vacuum
ΔM [g]	0.99 ± 0.01	0.85 ± 0.01
$A\,[\mathrm{mg\AA^{-1}}] \times 10^{-3}$	6.75 ± 0.12	5.66 ± 0.10

Table 5.7.: Measurements where the effect of insulation changes on the stability was tested.

5.4.1. Measurement T1: Additional insulation at the front

In another laboratory with comparable ovens, the GSI in Darmstadt [76], the used ovens feature additional heat reflective foil pieces in their front as it was measured that they have a positive effect on the homogeneity of the oven temperature [77].

The setup of the Linac3 micro oven does not include any foil pieces that reflect heat radiation going towards its front opening.

Measurements at the oven test stand should test whether the insertion of tantalum foil pieces in the shape of rings in the front of the oven have a positive influence on the

stability of the lead evaporation by making the temperature profile of the crucible more homogeneous.

Following the results presented in section 5.2 it has to be considered that additional parts exposed to the lead gas jet can create more condensate and thereby also lead oxide formations.

The presented measurement was conducted with rings of the inner opening radius $r_{\mathrm{Ta}} = 3.6\,\mathrm{mm}$ which are shown in figure 5.28.

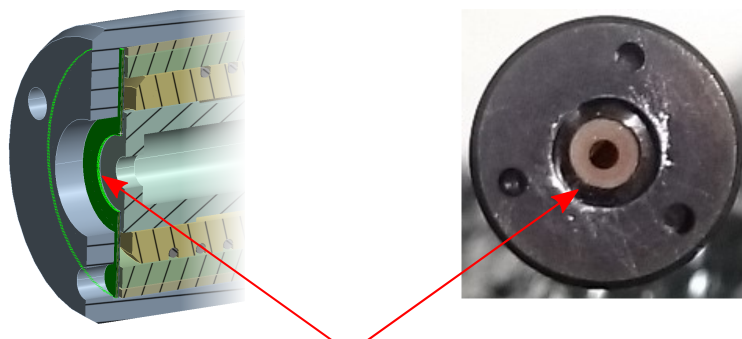

Figure 5.28.: Tantalum insulation rings at the front of the oven to enhance the heat reflection at the oven tip. The rings outer diameter is adapted to the oven covers inner size so that their central opening hole is in the middle of the ovens front face without the need of any attachment. In measurement T1 three of these rings were inserted into the oven.

During this measurement the oven was again controlled via a setpoint for the filament resistance which was then realized by a feedback loop that changes the filament current. This decision was made as the feedback loop showed no negative effect on the stability of the oven in the previous tests. Like in the measurement I2 the setpoint was manually controlled with the aim of reaching a sufficiently high evaporation rate and keeping it over a time comparable to the oven operation at the GTS-LHC ion source.

Results

The evaporation rate over the complete run together with the applied power are shown in figure 5.29.

At the beginning of the run the setpoint of the filament resistance was corrected downwards as the evaporation rate grew larger than intended. The evaporation rate could then be held around a median of approximately $3\,\mathrm{mg\,h^{-1}}$ over the duration of the complete run, which lasted 350 h. Initially the evaporation rate stayed comparably stable for around 24 h

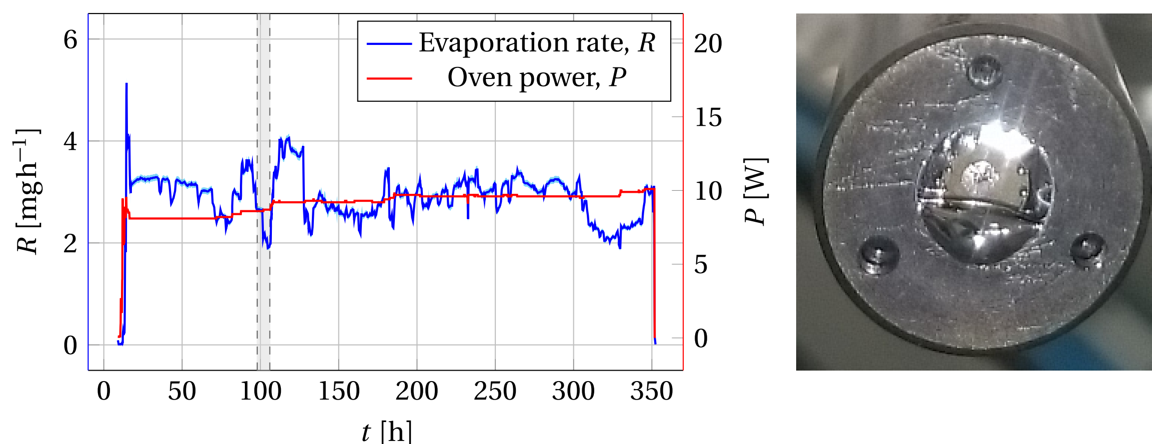

Figure 5.29.: Evaporation rate and oven power over the time of the measurement T1. The power is not actively controlled but a result of the feedback loop changing the current in the filament to achieve a preset filament resistance. The photo shows the oven tip after the measurement.

and then started to show fluctuations.

In its first change the evaporation rate dropped around 0.5 mg h^{-1} and then recovered to its previous value again several times. This happened without any outer changes, and might be due to redistribution of lead within the crucible. After around 90 h of evaporation also drops occurred that would not recover. Like in the measurement I2 the feedback loop here reacted and raised the filament current as a reaction of a decreasing filament resistance.

Again the evaporation rate only recovered after the resistance setpoint was raised manually. In comparison to e.g. measurement I2 the evaporation rate underwent smaller drops but fluctuations happened more frequent. It is notably how the oven power throughout the run only had to be raised in a rather small range from 8 W to 10 W. The photo in figure 5.29 shows the oven tip after the run. A big droplet of lead has gathered in the opening of the oven cover. Smaller droplets can be seen on the tantalum foil rings.

Figure 5.30 shows several parameters during a selected drop of the evaporation rate. In the upper plot the evaporation rate and the filament resistance are depicted. To emphasize the resistances behaviour a line, showing the resistance where a Gaussian filter was applied, is included. In the presented time window the evaporation rate started stable at around 2.6 mg h^{-1} and then dropped to 2.1 mg h^{-1} in less than an hour. At the same time the resistance dropped too from initially 2.119 Ω to 2.116 Ω. After dropping the resistance rose again as the control loop reacted on the drop and raised the current. The current and the power are shown in the second plot from above. The two lower plots show the signals

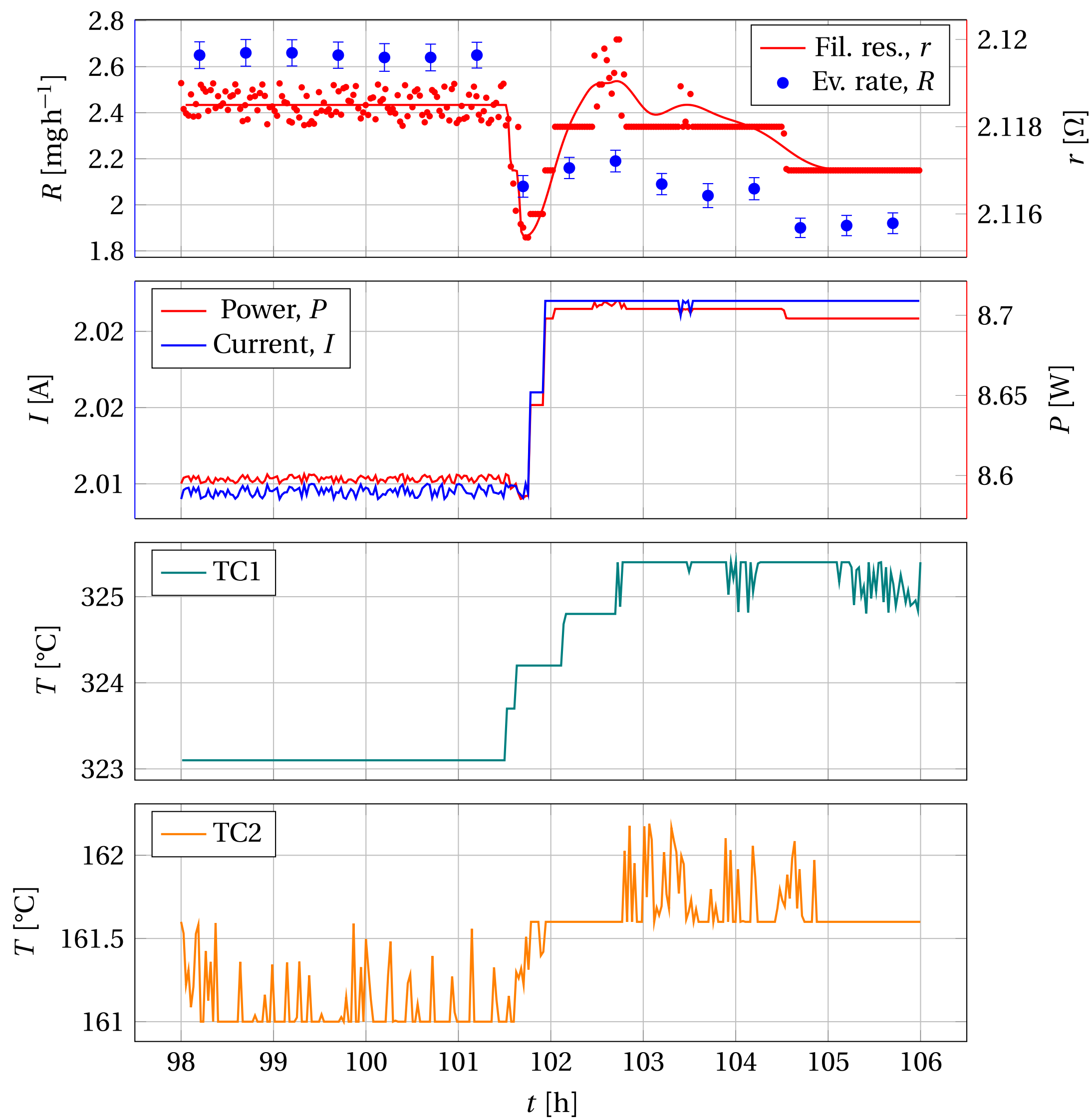

Figure 5.30.: Several parameters during an evaporation rate drop that where recorded in measurement T1.

of the two thermocouples, TC1 and TC2, that where attached to the outside of the oven during the measurement. Both thermocouples showed a slight increase in temperature at the time of the evaporation rate drop.

Discussion

Without oxygen injection the oven could be operated for two weeks, without raising the oven power over 10.5 W. But the evaporation rate showed unpredictable fluctuations and even in combination with the feedback loop reacting on the filaments resistance, the oven needed active tuning to maintain its output. From the formation of condensate at the tantalum foil rings it can be deduced that they would be a new starting point for a lead oxide blockage in an oxygen atmosphere. From this behaviour it can not be deduced that the additional shielding increases the oven stability. Even if the rings might even out the crucible temperature distribution this is overshadowed by the instabilities that where seen before and seem to affect the overall crucible temperature.

5.4.2. Measurement T2: Heat reflective tantalum foil removed

The standard setup of the oven features a heat reflective tantalum foil of approximately 20 cm, equating to approximately 6 layers of foil, that is wound around the alumina cylinder containing the filament holder and the crucible.

As it has a big effect on the ovens thermal behaviour but is not fixed other than being clamped between the outer oven cover and the alumina cylinder it is a candidate for creating changes of the thermal distribution by moving within the oven. A test was conducted where the oven was run without including the foil in the setup.

Assembling the oven in this way required to insert several alumina beads behind the crucible to let the crucibles front end slightly touch the outer oven cover to fixate the crucible. In principle this is already in practice at the GTS-LHC ion source to define the position of the crucible, but it is not needed for the same reason: In this case it was necessary, as otherwise the missing foil left enough space for the inner oven parts to sink down instead of staying centered within the cover. Figure 5.31 sketches the alignment via ceramic beads.

Another change to the operation of the oven was the allowed oven power. To get a sufficient deposition signal on the detector 20 W were not sufficient as the missing insulation leads to a colder crucible for the same power. Therefore the oven power interlock was raised to allow oven powers above 20 W. Again the feedback loop reacting on the filament

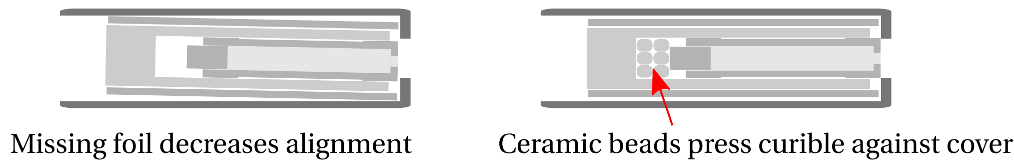

Figure 5.31.: Removing the tantalum foil can cause a misalignment of the inner oven parts. This can be countered by pressing the tip of the crucible against the oven cover.

resistance was active instead of choosing the oven power.

Results

The evaporation rate and the oven power during this measurement are shown in figure 5.32

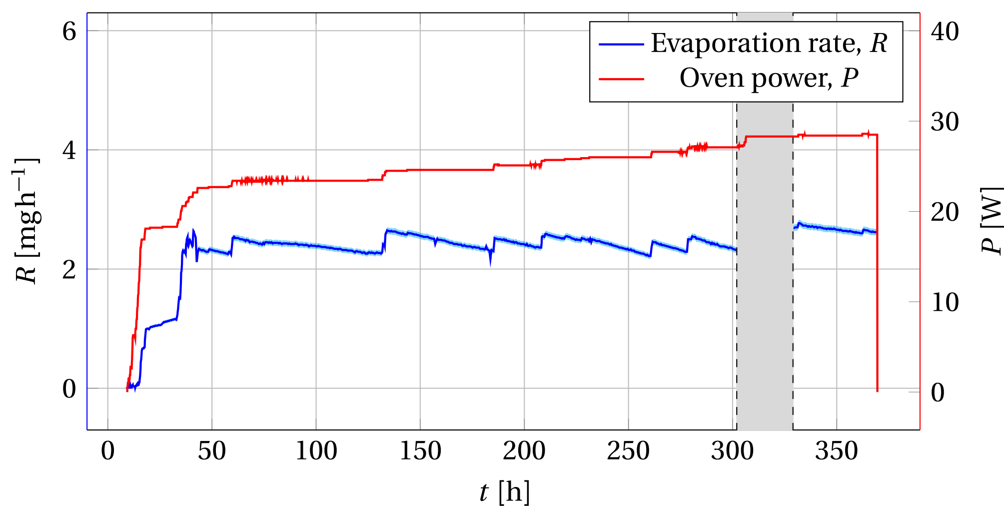

Figure 5.32.: Evaporation rate and oven power during the measurement T2. The grey area indicates a time window in which the shutter of the deposition sensor malfunctioned. Here no deposition data was recorded.

The oven power had to be increased to 23 W to get an evaporation rate that was stable at approximately 2.5 $\mathrm{mg\,h^{-1}}$. Over the course of the measurement the power was then increased several times to a final value of 28.5 W.

The evaporation rate stabilized after around 50 h and was then slowly decreasing. When the power was raised the evaporation rate increased and then slowly decreased again. Over the duration of the measurement no sudden drops or unexpected fluctuations of the evaporation rate occurred. 300 h into the run a malfunction of the shutter protecting the deposition sensor stopped the evaporation rate measurements. The defect was repaired

after 30 h and the measurement recorded a stable evaporation rate again. As in this time the oven power was manually increased reacting on a misinterpretation of the missing evaporation rate measurement the evaporation rate most likely rose shortly after the defect occured. The raising of the oven power (by adjusting the resistance setpoint) allowed to prevent the evaporation rate from dropping below 2 $mg\,h^{-1}$ over the time of 300 h without any unexpected changes.

Discussion

Measurement T2 showed an evaporation rate that was stable and predictable. This demonstrates that the previously observed fluctuations where to a great extend caused by the oven setup and its general temperature stability and not any processes within the crucible. It also reinforces the assumption that what was measured before where indeed fluctuations of the evaporation rate and not a faulty behaviour of the deposition sensor.

5.4.3. Discussion of the insulation modifications

The measurements T1 and T2 demonstrate the great impact of the heat reflective foils on the overall temperature of the crucible as well as the stability of the evaporation rate.

To achieve a comparable evaporation rate without the tantalum foil (setup T2) the oven power had to be increased by a factor of two compared to the one where the oven was additionally insulated (T1). But while the evaporation rate fluctuated during measurement T1 it showed an increased stability during measurement T2. A possible explanation for this behaviour are changes of the insulation properties of these foils during operation.

It was observed several times that while the resistance of the filament and the evaporation rate dropped, the thermocouples showed a slight increase in temperature on the oven cover. This hints that a redistribution of the heat being transported into the oven took place. It is possible that by decreasing its heat insulating property e.g. by creating new contact points for thermal conduction, the foil allows more heat to radiate out of the oven without reaching the crucible. This way the outer cover temperature increases while the crucible temperature decreases at the same power. And the comparison of the measurements T1 and T2 also shows that the insulation affects the crucible temperature significantly. The change of the insulation property might be caused by thermal stress that leads to deformation and thereby a repositioning of the heat reflective foil.

Measurement T2 also shows a way to operate the oven with a stable temperature, which allows to study further impacts on the ovens stability and endurance. The next section

presents two additional measurements taken without the heat reflective foil.

5.5. Stable oven operation

The previous section showed a measurement that presents a way to operate the oven with a stable evaporation rate in vacuum (T2). The measurement U1 tested if this also opens the way to operate the oven in oxygen without forming a lead oxide blockage. Measurement U2 was conducted to test if the lead quality can visibly affect the stability when no temperature instabilities are present. Table 5.8 shows some characteristics of the two measurements presented in this section.

Measurement	U1	U2
Purpose	Mitigate oxide blockage	Test effect of lead quality
Setup	Ta foil removed Crucible completely in front Controlled by power setpoint Lead: Chemically clean	Ta foil removed Crucible completely in front Controlled by power setpoint Lead: Visibly passivated
Atmosphere	Oxygen 1×10^{-5} mbar	Oxygen 1×10^{-5} mbar
ΔM [g]	1.51 ± 0.01	0.75 ± 0.01
A [mgÅ^{-1}] $\times 10^{-3}$	4.78 ± 0.62	5.04 ± 0.10

Table 5.8.: Measurements that where done without the tantalum foil. U1 should test the effect of a hotter oven cover and U2 the influence of the lead quality.

5.5.1. Measurement U1: Can a hot oven cover prevent the oxide blockage ?

When the oven has a reduced insulation for the same crucible temperature the oven needs to be run with a higher power, which leads to a different temperature distribution at a certain evaporation rate. Without the foil the oven cover is generally hotter while evaporating sufficient amounts of lead.

Therefore it was tested whether the hotter oven cover has an effect on the formation of the previously observed lead oxide blockage in an oxygen atmosphere. In this measurement the oven again was run without the foil and this time in an oxygen atmosphere of 1×10^{-5} mbar. At this pressure of oxygen the formation of a lead oxide blockage occurred reproducibly (As in the measurements O1 and O3).

Results

A photo of the oven tip after the measurement as well as the measured evaporation rate and the applied power during the run are shown in figure 5.33.

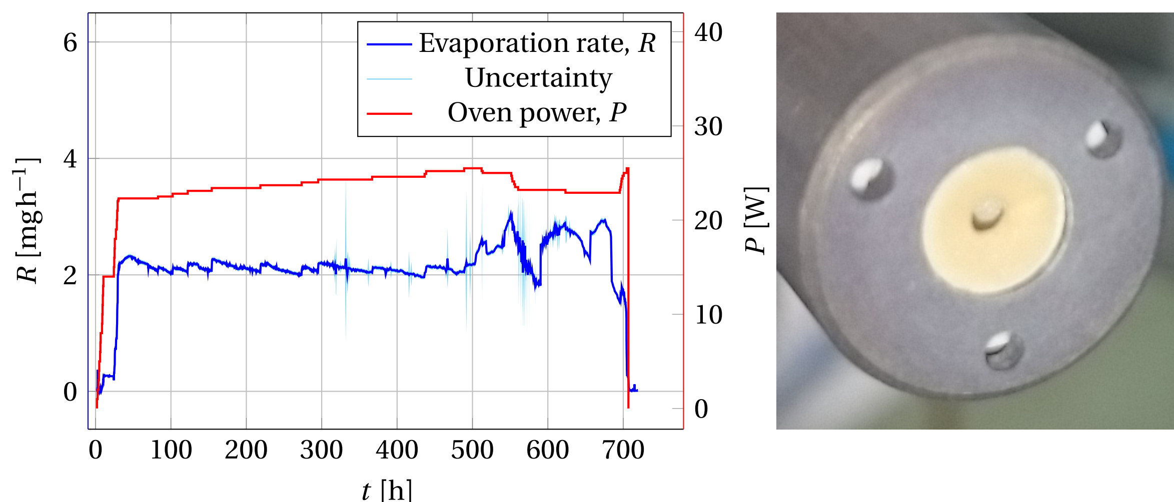

Figure 5.33.: Evaporation rate and applied oven oven power during measurement U1. The photo shows the tip of the oven after the run.

The evaporation rate could again only be ramped up sufficiently by applying a power above 20 W. To keep the evaporation rate at a stable level the oven power was increased several times until a maximum value of 25.5 W. For a time of 500 h the evaporation rate stayed stable and showed no sudden fluctuations. In the last third of the run the evaporation rate then started to increase and it was decided to decrease the oven power several times. After 750 h the evaporation rate finally dropped to zero and could not be recovered.

The photo in figure 5.33 shows the oven tip after the run. No traces of lead oxide could be observed neither at the oven tip nor in the crucible, which was completely empty after the measurement. The test stand window allowed observation of the oven tip during the measurement and no lead condensate or lead oxide was present on the oven tip at any time. The final drop of the evaporation rate is most likely due to a complete consumption of the lead sample as the crucible was empty after the run.

Fluctuations at the end of the run Around 500 h after the measurement started the evaporation rate began to fluctuate and showed sudden changes, which it had not done before. Figure 5.34 shows 3 plots in which the evaporation rate is shown together with the filament resistance for the time where the oven power was kept constant.

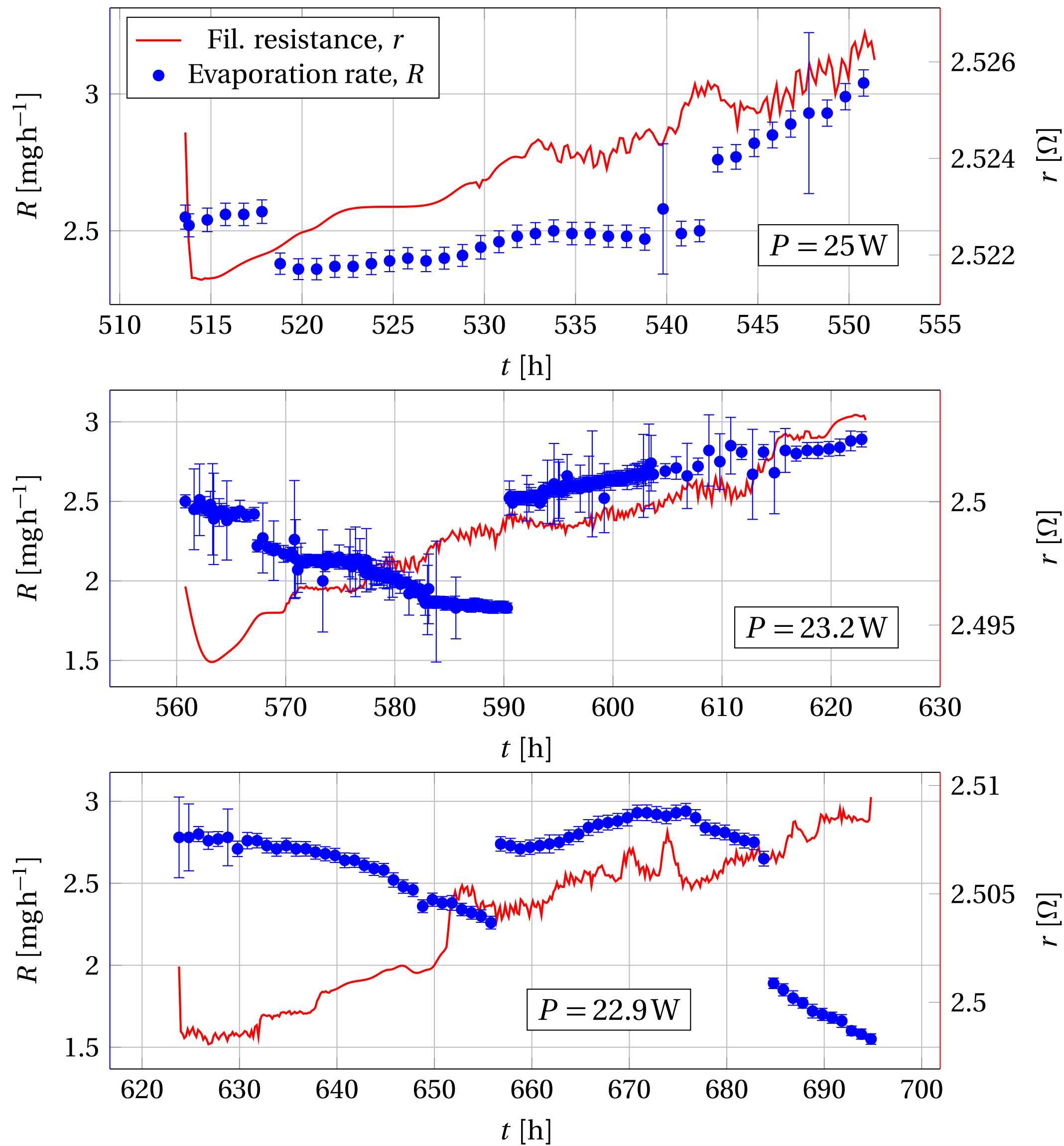

Figure 5.34.: Evaporation rate and the filament resistance for time windows of stable power at the end of measurement U1.

It was previously observed that the evaporation rate changes sometimes correlated with changes of the filament resistance. The plots show events where the evaporation rate decreased (the upper and the lower plot) and events where it suddenly increased (all three plots). To plot the filaments resistance again a Gaussian filter was applied to the resistance data to even out the noise. During the evaporation rate changes the filaments resistance did not show any changes that have the same temporal profile as the evaporation rate. However the filament resistance still displays a drift over time. This data hints that the fluctuations of the evaporation rate might have another cause than a temperature change of the crucible. A possible explanation for this behaviour is the redistribution of the shrunken lead sample. The temperature in the crucible is most likely not entirely homogenous. If a lead droplet moves within the crucible it can be exposed to a different temperature and thereby evaporate at a different rate.

Discussion

This measurement allows to draw several conclusions about the oven behaviour. First it demonstrates a way to avoid the blockage of the oven in an oxidizing atmosphere without changing the geometry of the oven tip: By increasing the temperature of the outer oven cover. As no lead condensate gathered at the oven cover there was no formation of lead oxide and no blockage.

Additionally the measurements shows that the oxygen does not stop the lead within the crucible from being used up completely. The oxidation of the lead sample within the crucible did not form a further blockage or notable amounts of lead oxide that stayed within the crucible.

It is a demonstration of the possibility to run the oven with around 4 weeks of continuous evaporation within an oxidizing atmosphere, until the crucible runs completely empty. As the run stopped with using up all of the lead sample the lifetime in this case can potentially be increased by increasing the amount of lead (e.g. with a larger crucible capacity).

Additionally the measurement is a new demonstration of the ovens stability without the reflective tantalum foil. The fluctuations of the evaporation rate at the end of the run could be caused by redistribution of the remaining lead within the crucible.

5.5.2. Measurement U2: Is the oven stable with old lead ?

The ability to operate the oven more stable also allows to asses the influence of the lead quality on the stability. The previous measurements without the tantalum foil all used

chemically clean lead to exclude any possible influences from the lead quality. Measurement U2 repeated the operation of the oven without the tantalum foil and in oxygen atmosphere, but this time the crucible was filled with a lead sample made out of lead that was already visibly oxidized in air (The same used in the measurements S1-S3, N1-N2 and O1-O2).

Results

In this measurement the oven power had to be ramped up to 29.3 W to achieve a sufficient deposition signal. Throughout the measurement the power was then increased several times reaching 30.8 W after 360 h. The measurement was stopped after 380 h. Figure 5.35 shows the oven power and the measured evaporation rate.

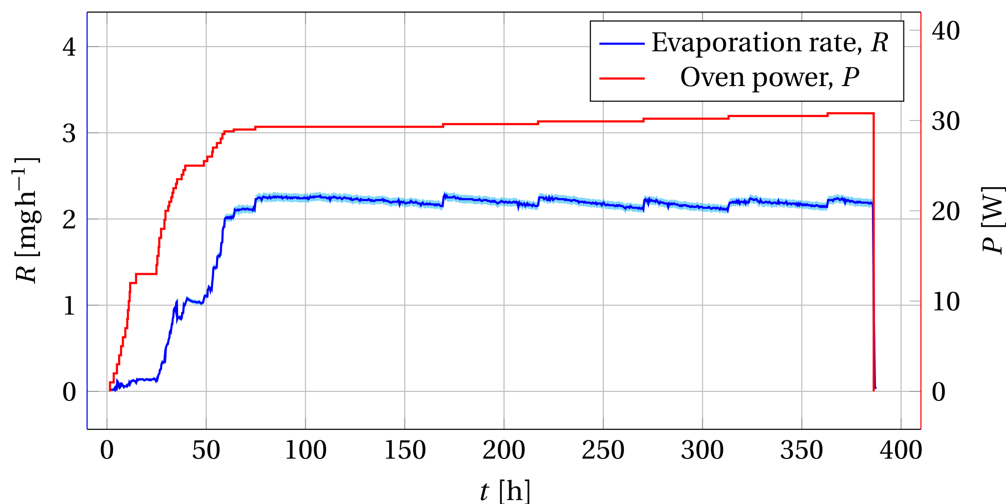

Figure 5.35.: Evaporation rate and power during measurement U2.

No fluctuations of the evaporation rate were observed, after each increase of the power it increased and then slowly started to decrease again. Like in the measurement U1 the oven tip showed no formation of lead oxide despite an oxygen pressure of 1×10^{-5} mbar in the test stand. It is notable that the oven power in this run had to be higher than in the measurements T2 and U1.

Discussion

This measurement hints that most of the fluctuations that have been seen before are not caused by processes linked to the lead quality. Even with a sample of unspecified and passivized lead the evaporation rate stayed stable when the tantalum foil was not present.

However the measurement hints that the absolute evaporation rate of the oven is also linked to the chemical composition of the lead sample. As the vapour pressure of a liquid can be reduced if other solvents are present. This is also stated in the Raoults law [78] (Translation in [79]):

$$p_{v,\text{sol.}} = x_{\text{sol.}} p_v \quad . \tag{5.4}$$

Here $p_{v,n,\text{sol.}}$ is the vapour pressure of the solvent in the solution, $x_{\text{sol.}}$ the molar fraction of the respective solvent and p_v the vapour pressure of the pure substance. Thereby the presence of impurities can reduce the partial vapour pressure of the lead in the sample.

This effect was however not further studied in this work.

5.5.3. Measurements Y1 and Y2: Thermal assessment of the oven operation without the heat reflective foil

To assess the possibility of operating the oven without the heat reflective tantalum foil the temperature inside of the crucible was measured, with and without the heat reflective tantalum foil. For this purpose one of the two thermocouples of the test stand was clamped into a small copper pin that fits into the crucible. To increase the accessibility of the crucible it was decided to turn the crucible around with its open end facing the front of the oven. This way the copper pin could be easily inserted into the front of the oven, while the oven was already installed in the test stand. Figure 5.36 shows the setup of the measurements Y1 and Y2.

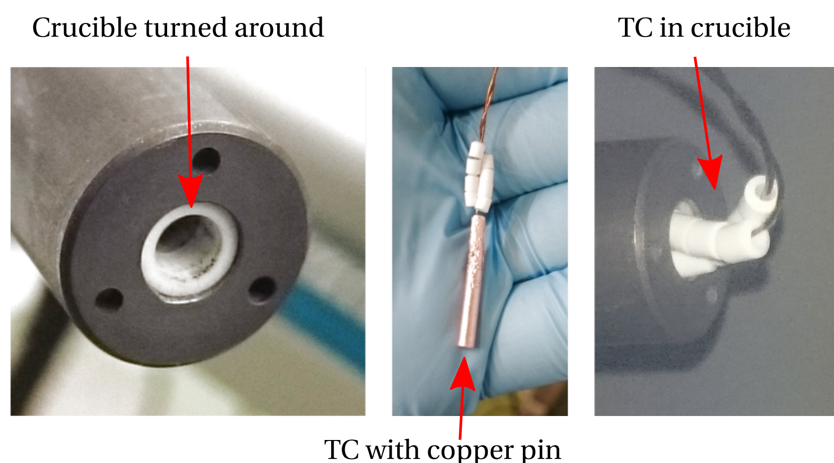

Figure 5.36.: Photos of the oven with an empty and turned crucible, the thermocouple with a copper pin and the oven with the thermocouple inserted into the crucible.

This decision was made as the extended oven feedthrough, with the bellow, made it too difficult to insert the oven with the thermocouple already installed (the method used in [55]).

Table 5.9 gives an overview of the two measurements.

Measurement	Y1	Y2
Purpose	Measure crucible temperature	
Setup	No ta foil	With Ta foil
	TC1 in crucible	
	TC2 on middle of oven cover	
Atmosphere	Vacuum	

Table 5.9.: The measurements Y1 and Y2.

The oven power was then ramped up similar to the already presented temperature scans in section 4.2.

Crucible temperature

Figure 5.37 shows the resulting temperatures from the measurement Y1 (without the foil) and Y2 (with the foil) and the temperature measurement of the crucible published in [55].

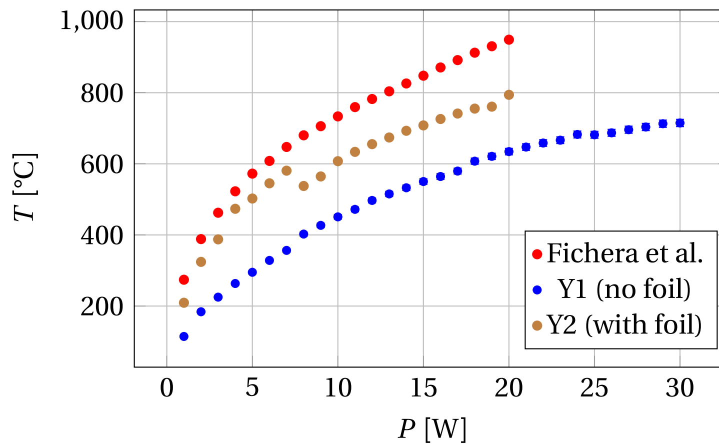

Figure 5.37.: Temperature reading of the thermocouple that was inserted into the crucible in the measurements Y1 and Y2.

It can be seen that also with the foil installed the measurement Y2 does not reproduce the previous temperature measurement. The difference per power in the range from 1 W to 7 W is up to 75 K at a fixed power level. The temperature reading during measurement Y2 then underwent a drop. The temperatures above 8 W show a difference of up to 155 K.

Both measurements with the usual oven setup still show a clear difference in temperature compared to measurement Y1 without the heat reflective foil.

The maximum temperature during Y1 was measured to be 714 °C at 30 W while during the measurement of Fichera et al. this temperature was already surpassed at 10 W. In measurement Y2 the thermocouple showed a reading of 726 °C at 14 W.

Discussion The differences between the values from Fichera et al. and measurement Y2 can have several reasons. For example the oven filament and the heat reflective tantalum foil were exchanged between the two measurements hence the oven might have shown differences in its thermal profile.

Then the method to record the temperature was different, as the measurements Y1 and Y2 were done with a turned around crucible.

The drop of temperature reading in measurement Y2 is propably due to a change in contact pressure between the thermocouple and the copper pin inside the crucible.

Nevertheless the measurements show the reduced temperature in the crucible when the heat reflective tantalum foil is removed. To achieve a sufficient lead vapour pressure in the crucible the heating power needs to be higher than the usual limit of 20 W.

Temperature of the oven cover

Figure 5.38 shows the stable temperature reading of the thermocouple that was clamped on the outside of the oven cover in the measurements Y1 and Y2. As a comparison also the measurement from Fichera et al. is included.

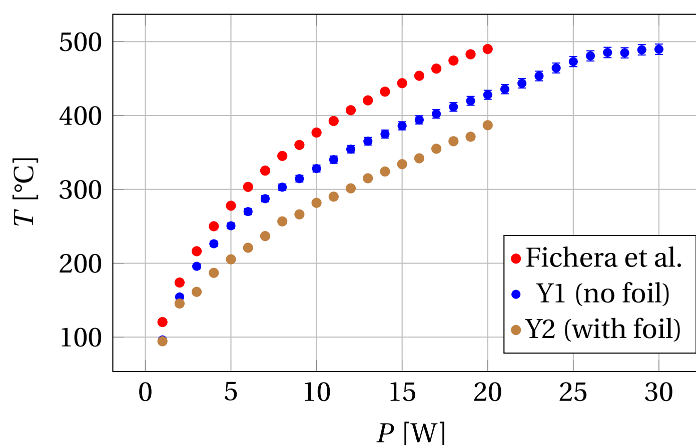

Figure 5.38.: Temperature measured at the oven cover during the measurements Y1 and Y2 plotted against the oven heating power.

It can be seen that the temperatures measured during Y1, without the heat reflective foil, are higher at all power levels compared to measurement Y2, where the foil was inserted. At 20 W the temperature reading of Y1 is 428 °C and at Y2 386 °C. The maximum temperature measured at the oven cover in Y1 is 490 °C at 30 W.

The comparison to the measurement from Fichera et al. shows a reading of 490 °C at 20 W.

Discussion It was already shown that the higher temperature of the oven cover during a run with the reduced heat insulation can have a beneficial effect by preventing the blockage formation in an oxygen atmosphere. However a hotter oven could have implications for the GTS-LHC ion source, as the oven is radiating its heat directly onto the injection plug of the source.

The comparison to the measurements from Fichera et al. which also are very similar to thermal measurements presented in section 4.2 (see figure 4.18) shows that the oven cover during both measurements Y1 and Y2 was colder at all power levels. This is not fully understood and shows that the oven might have gone through some kind of permanent structural change during the series of measurements at the oven test stand.

Temperature of the filament

The temperature of the filament can not be measured directly. However it is of interest to compare the filament temperatures of Y1 and Y2 as it can give insight into whether the filament takes damage during the higher powers that are needed when the oven is operated without the reflective tantalum foil.

As the resistance of the tantalum filament is rising linear with the filament temperature, figure 5.39 displays the filament resistance at stable temperatures for the individual heating powers during the runs Y1 and Y2.

During both measurements the resistance rose with the heating power. Measurement Y2 was stopped at 20 W and at this power the resistance of the filament was 2.7 Ω. The resistance of the filament during measurement Y1 was lower at all power levels, reaching a final resistance of 2.5 Ω at 30 W.

Discussion Comparing the filament resistance during the two measurements hints that, while the foil is installed, the filament at 20 W is hotter than at 30 W, when the heat reflective foil was removed. So in the runs without the foil the filament temperature does not exceed the temperature it also encounters in the normal operation.

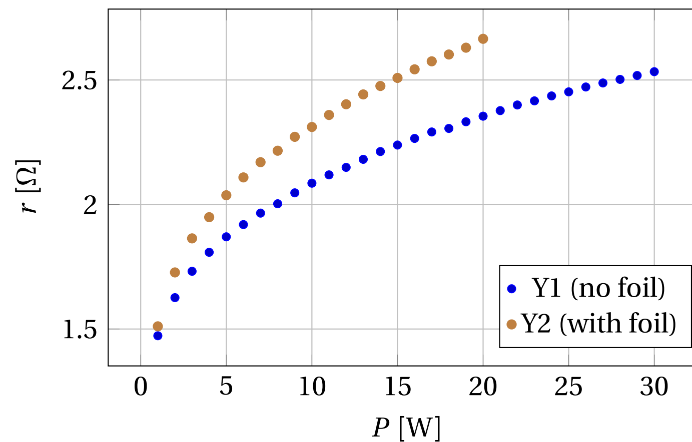

Figure 5.39.: Filament resistance after the temperature stabilized at each power level during the measurements Y1 and Y2.

It is however likely that the average temperature load on the filament during a run without the tantalum foil is higher than during a similar measurement in the original setup as the filament still needs to be hotter to achieve a sufficient crucible temperature.

From this one could expect a faster wear of the filament until it needs to be replaced when the oven is operated without the foil.

5.5.4. Evaporation rate against crucible temperature

The evaporation rates that were recorded in the measurements U1 and U2 displayed a relatively stable growth with growing heating power during the initial ramp up. Therefore the evaporation rates from these measurements were used to derive evaporation rates for a certain crucible temperature to compare them with the predictions of the Molflow+ simulations.

In both measurements only the evaporation rate that was recorded in the beginning of the measurement was used. Figure 5.40 shows the heating power and the evaporation rate in the concerned time window of each run.

These values were then sorted in a similar way as presented in section 5.1.2. For each power step only the last recorded evaporation rate is then used.

The resulting evaporation rate values can then be combined with the stable crucible temperature that was measured at the same heating power in measurement Y1 (see figure 5.37). The result is a relation of measured crucible temperature and measured evaporation rate.

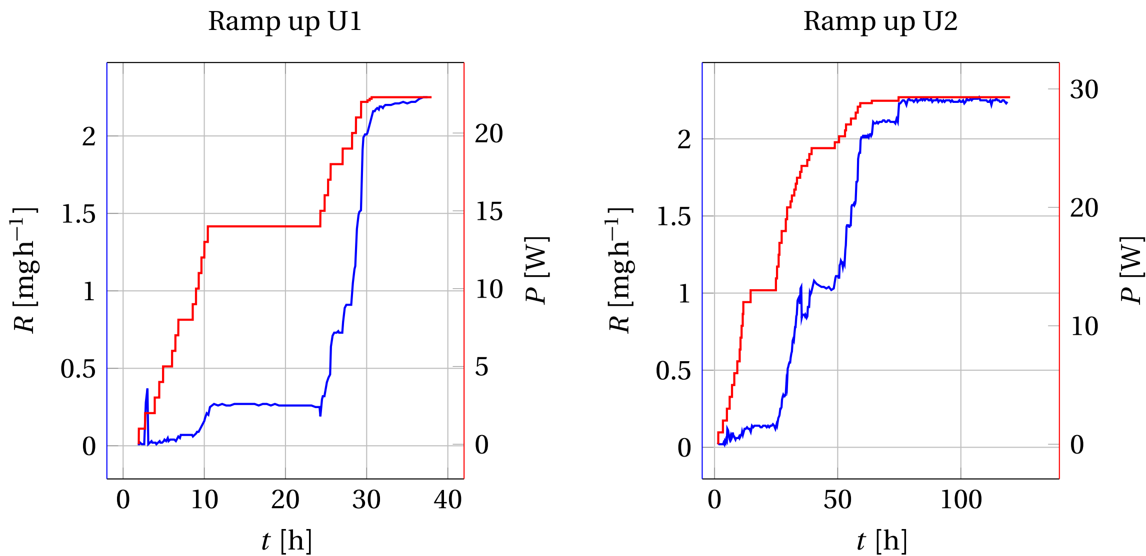

Figure 5.40.: Evaporation rate (R) and heating power (P) during the ramp up of the oven evaporation in the measurements U1 and U2.

Result

Figure 5.41 shows the resulting evaporation rate to temperature relation, together with the predictions of the Molflow+ simulations and the Hertz Knudsen equation.

It can be seen that the curves resulting from measurement U1 and U2 show a rather big difference in the temperature to evaporation rate relation. This result was expected as the evaporation rate of approximately 2 $\mathrm{mg\,h^{-1}}$ in measurement U2 could only be achieved with a much higher heating power.

While the evaporation to temperature relation above 580 °C of measurement U1 is within the predicted range of the simulations, measurement U2 leads to a significantly lower evaporation rate than predicted. It can also be seen that both measurements show a different temperature to evaporation rate behavior than the prediction at temperatures below 600 °C.

Discussion

The difference between the two measurements might be explained by the type of lead that was used in measurement U2. As the main purpose of the measurement was to test if passivated lead can cause instable evaporation rates, the lead sample was not chemically pure. This could cause a lower evaporation rate. It is however also possible that the temperature of the oven in the two experiments was a different one at the same power.

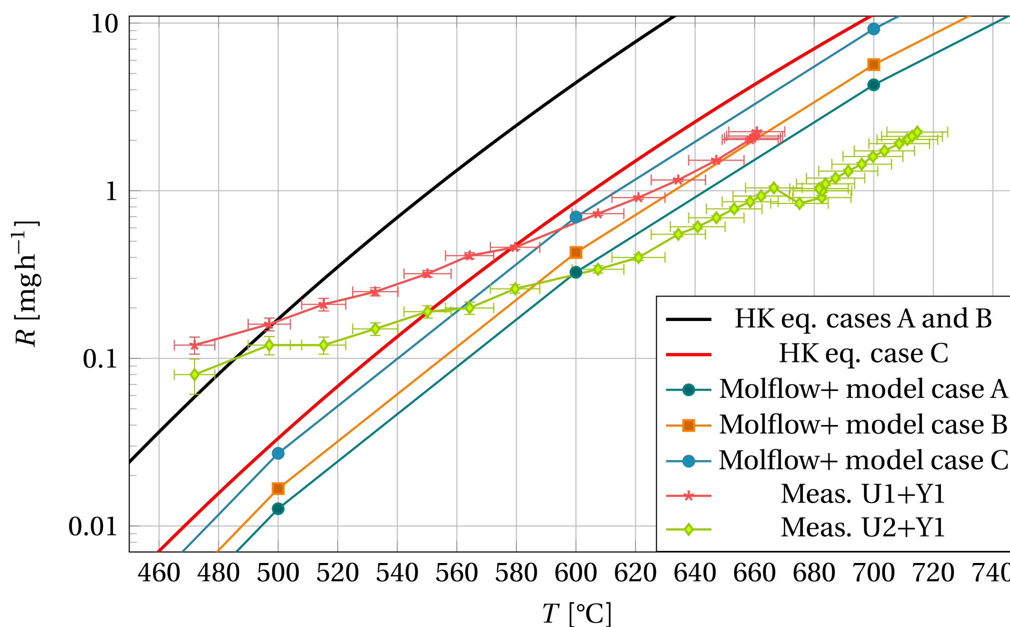

Figure 5.41.: Evaporation rate at different crucible temperatures derived by combining evaporation and temperature measurements at fixed power levels.

The comparison of the measurement and the model show that the evaporation rate for temperatures lower than around 580 °C can not be described by the Molflow+ model and the underlying assumptions. Above 580 °C the measured evaporation rate of the combined measurement U1 and Y1 match well with the simulated values. This is not the case for the rates measured during U2. As discussed a possible reason could be the lower lead quality of the lead sample in measurement U2.

5.6. Conclusion of the measurement series

The following lists gives an overview of the main results of the measurements series.

- Several occasions of unstable evaporation rates at stable heating power were recorded.
- The formation of a lead oxide blockage that was also observed at the GTS-LHC ion source could be recreated in the test stand when an oxygen pressure of at least 1×10^{-5} mbar was present.
- It was found out that the main factor for evaporation rate instabilities of the oven are thermal instabilities.
- When the oven is operated without a foil it shows a much more stable behaviour.

- Additionally, when the foil is taken out, the oven can be operated in an oxygen atmosphere that otherwise leads to the formation of an oxide blockage. This way the oven could be operated at the test stand until its crucible was completely empty, rendering the size of the lead sample the limiting factor for the oven lifetime.
- The thermal assessment shows that the crucible temperature is clearly reduced without the heat reflective foil, which might become a problem when higher evaporation rates or materials with a lower vapour pressure are requested.
- To enhance the oven lifetime and stabilize its evaporation during the lead evaporation the following modifications to the setup can be recommended for tests at the GTS-LHC ion source. Its heat reflected foil should be removed. To enhance the stability of the rest of the setup the filament protection should then be modified in a way that it touches the oven cover at some parts, to stabilize the oven crucible on the symmetry axis of the oven.
- If the insulation of the oven is kept or a more stable setup is found, a crucible design should be chosen that prevents the deposition of gas onto the oven cover. It could be shown that this is possible by using an extension at the front of the crucible.

6. Conclusion and Outlook

This work presents a study that was performed to characterize the micro oven of the GTS-LHC ion source, to understand its evaporation behaviour and to find means of improving the oven operation in terms of stability and endurance.

The study included gas flow as well as thermal simulations and a series of measurements at a dedicated offline test stand.

A Molflow+ model was used to understand the geometry of the gas jet from the oven, which could be used to benchmark the deposition to evaporation rate calibration at the test stand.

Thermal simulations in ANSYS were performed to gain insight into the connection of the thermal profile of the oven and its performance. Besides the use of an already existing 2D model, a 3D model was developed to further study the influence of the shape of the individual oven parts and also the surrounding structure at the GTS-LHC ion source.

Both models predict a thermal profile in which the crucible temperature is falling towards its tip. However the temperature differences within the crucible predicted by the simulations are not high enough to explain the amount of power tuning that is necessary to maintain a stable output current of the GTS-LHC ion source.

A series of experiments at the offline test stand could give further insight into the need for increasing the heating power over time. It could be demonstrated that the presence of oxygen at a pressure of 1×10^{-5} mbar leads to the formation of a lead oxide blockage, an occurrence that is also observed at the GTS-LHC ion source. The closing aperture of the oven due to the blockage creates the need for a higher evaporation rate to maintain a constant lead gas output. The blockage is also a limiting factor for the oven endurance. By using a changed crucible design the blockage formation at the same oxygen pressure could be prevented.

It was found out that the majority of fluctuations of the evaporation rate happen due to an unstable crucible temperature at stable power levels. The correlation of changes of the evaporation rate with outer parameters like the filament resistance show that the overall thermal profile of the oven can change during operation. Possibly due to changes in the

thermal insulation.

A feedback loop that stabilizes the filament resistance by adjusting the heating current reacted at drops of the evaporation rate but did not increase the current enough to have an effect on the evaporation rate.

The evaporation could be stabilized by removing the heat reflective tantalum foil from the oven setup. However a sufficient evaporation rate then requires heating powers above 20 W. Removing the tantalum foil also demonstrates another possible way to operate the oven in an oxidizing atmosphere: The higher heating powers cause a hotter outer oven cover, which prevents the accumulation of lead condensate on the cover. And without the condensate also no lead oxide is forming at the oven tip. This way the oven could be operated within an oxygen atmosphere until its crucible was empty.

The results of the study show that is possible to improve the stability and the endurance of the oven with a modified design. Therefore it can be recommended to test the following modifications at the GTS-LHC ion source:

For the stability of the lead evaporation it would be beneficial to use an oven design without the usually present heat reflective tantalum foil. The formation of the lead oxide blockage can be prevented with two modifications, a changed crucible design or a hotter oven cover, which again can be achieved with the reduced insulation.

A. Nitrogen Test at the GTS-LHC Ion Source

It was mentioned previously that oxygen is the usual choice as buffer gas for the lead ion production at the GTS-LHC ion source.

As the experiments at the oven test stand clearly show the connection between the presence of oxygen and the formation of a lead oxide blockage at the oven tip, a test at the GTS-LHC ion source should show whether oxygen could be replaced as a buffer gas. For this test nitrogen was chosen. Its atoms have a similar atomic weight as oxygen so the ion-cooling effect in the plasma (see 2.4) could be expected to be similar. Additionally it was already shown at the OTS that nitrogen does not cause the formation of any blockage at the oven tip or affects the oven operation negatively.

To be able to compare the stable operation of the source between oxygen and nitrogen it was decided to ramp up the oven in the usual oxygen atmosphere and then switch the buffer gas injection to nitrogen. Subsequently the ion source was operated and tuned to maintain a stable ion beam current in a similar way as during the normal operation.

A.1. Low energy beam transfer line and instrumentation

Figure A.1 shows a sketch of the low energy beam transfer line behind the GTS-LHC ion source (Similar in [80]).

Behind the source the extracted ion beam traverses two dipoles that bend the beam 135° serving as a spectrometer for the different ion species that are extracted from the source. In the usual operation the dipoles filter out the selected ion species that is supposed to be accelerated further, which in this case is $^{208}Pb^{29+}$.

Downstream of the spectrometer the beam current transformer 'ITL.BCT05', here for simplicity 'BCT05', can be used to measure the beam current non destructively. Additionally the Faraday cup 'ITL.MFC02M', here called 'FC2', can be moved into the beam directly behind the spectrometer [10]. When FC2 is moved into the beam, the spectrometer current

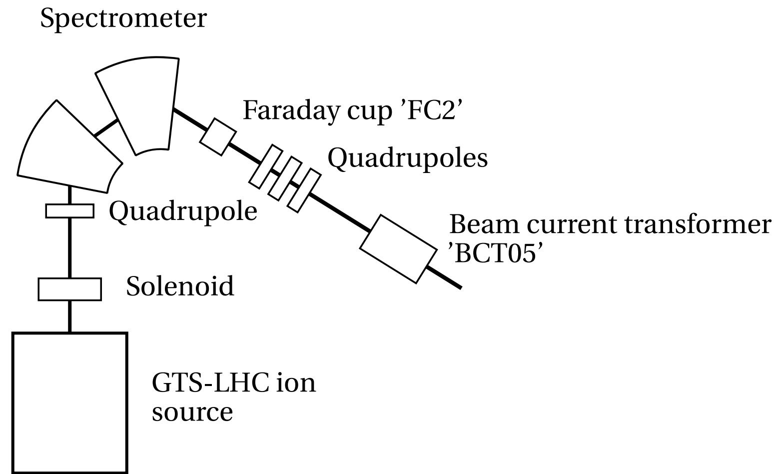

Figure A.1.: Sketch of the low energy beam transport line at Linac3. The sketch only contains the instrumentation that is used in the following section.

I_{mag}, can be scanned, to measure a charge state distribution of the ions that are extracted from the GTS-LHC ion source.

In the following section measurements from BCT05 and charge state distributions recorded with FC2 are presented.

A.2. Measurements

After switching to nitrogen as the buffer gas, the source could soon be brought back to a state where it delivered a similar ion current as before the gas change. However it was experienced that after the appropriate tuning the source current would only remain stable for a duration of approximately 1-2 hour and then become more erratic and require a retuning of the source parameters.

Figure A.2 shows the beam current that was measured in the beam transformer BCT05 in a selected time window of around 8 h after the start of the test. At the beginning of this time window source was tuned to deliver a stable output.

It can be seen that the beam current remained stable at around 170 eμA for 1 h and then started to decrease. At the same time also the shot to shot stability decreased. This behaviour occurred several times during the test and throughout the complete run the beam current could not be held stable for longer periods than 3 h.

Additionally the extraction voltage of the source tripped several times and required a

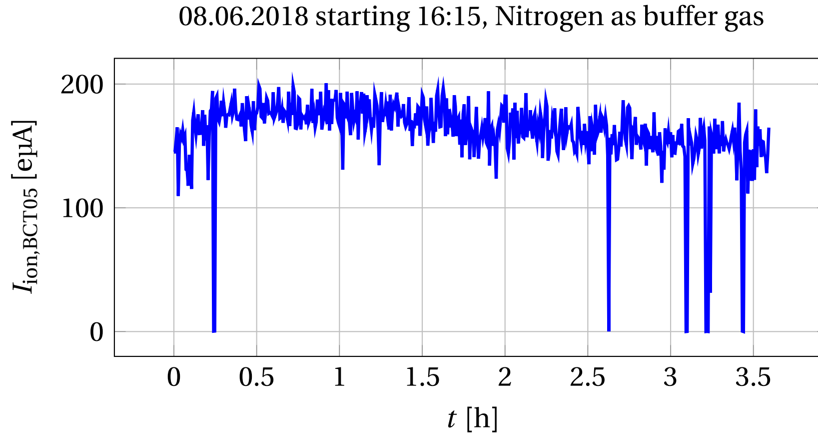

Figure A.2.: Beam current measured by the beam current transformer BCT05 durig a selected time window of the nitrogen test.

reset by the operator. This prevented over night recording of the beam transformer reading.

Several charge state distributions (CSDs) where recorded during the run to get some insight into the processes within the ion source. The recorded beam current in FC2, $I_{\text{ion,FC}}$, corresponds to a certain mass to charge ratio. Hence some peaks overlap, e.g. those of $^{208}Pb^{26+}$ and $^{16}O^{2+}$, as both have a very similar mass to charge ratio.

The recorded CSDs show the occurrence of several negative peaks that hint towards some kind of obstacle in the accelerator beamline that scattered electrons into the Faraday cup, when it was scraped by the ion beam. In the presented ion currents ($I_{\text{ion,FC}}$) the negative values were set to zero.

Figure A.3 shows two CSDs that where recorded during the test run with nitrogen.

The upper plot shows the charge state distribution 5 h after the start of the nitrogen injection. The majority of visible peaks are the different charge states of Lead. Next to the $^{208}Pb^{29+}$ peak a $^{14}N^{2+}$ peak was identified. Also a $^{14}N^{3+}$ peak could be clearly identified. Additionally the distribution shows that oxygen was still present in the source plasma, as $^{16}O^{3+}$ and $^{16}O^{2+}$ are visible in the spectrum. The $^{208}Pb^{30+}$ peak is not visible as it overlaps with a negative peak coming from electrons that where probably ejected by the $^{14}N^{2+}$ beam, while scraping the aforementioned obstacle.

The lower plot shows a CSD that was recorded approximately 23 h after the start of the nitrogen injection. While the $^{14}N^{3+}$ peak has become more prominent the peak of $^{208}Pb^{26+}$ and $^{16}O^{2+}$ is reduced. It can also be seen that between the peaks of $^{14}N^{3+}$ and $^{16}O^{3+}$ new peaks appeared. These peaks grew, as seen in a CSD that was recorded 24 h later, which is shown in the upper plot of figure A.4.

These peaks where identified as charge states of iron and cobalt. This is a strong hint

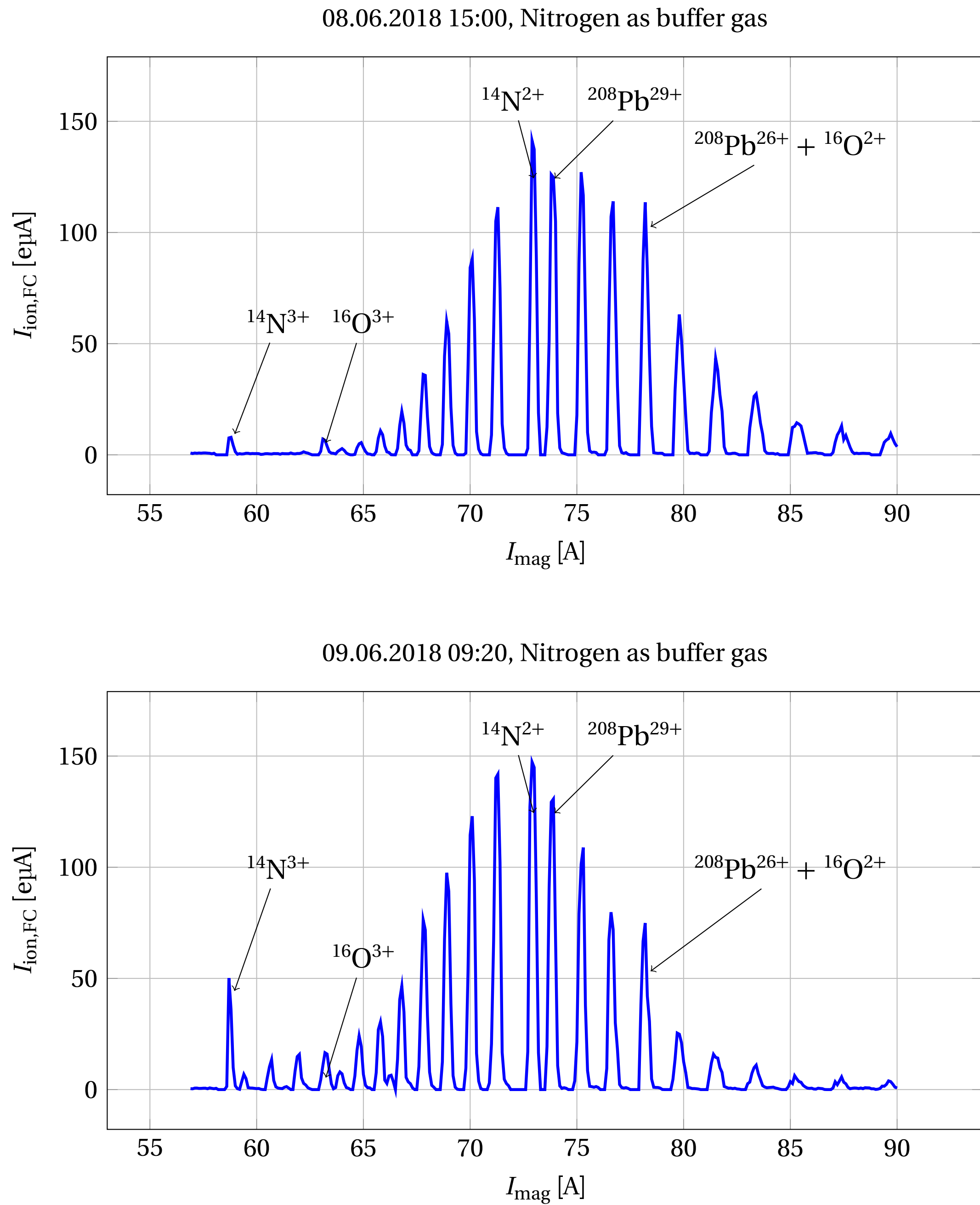

Figure A.3.: Two charge state distributions recorded at Linac3 during the test with nitrogen. Upper plot: 5 h after the start of the nitrogen injection. Lower plot: 23 h after the start of the test.

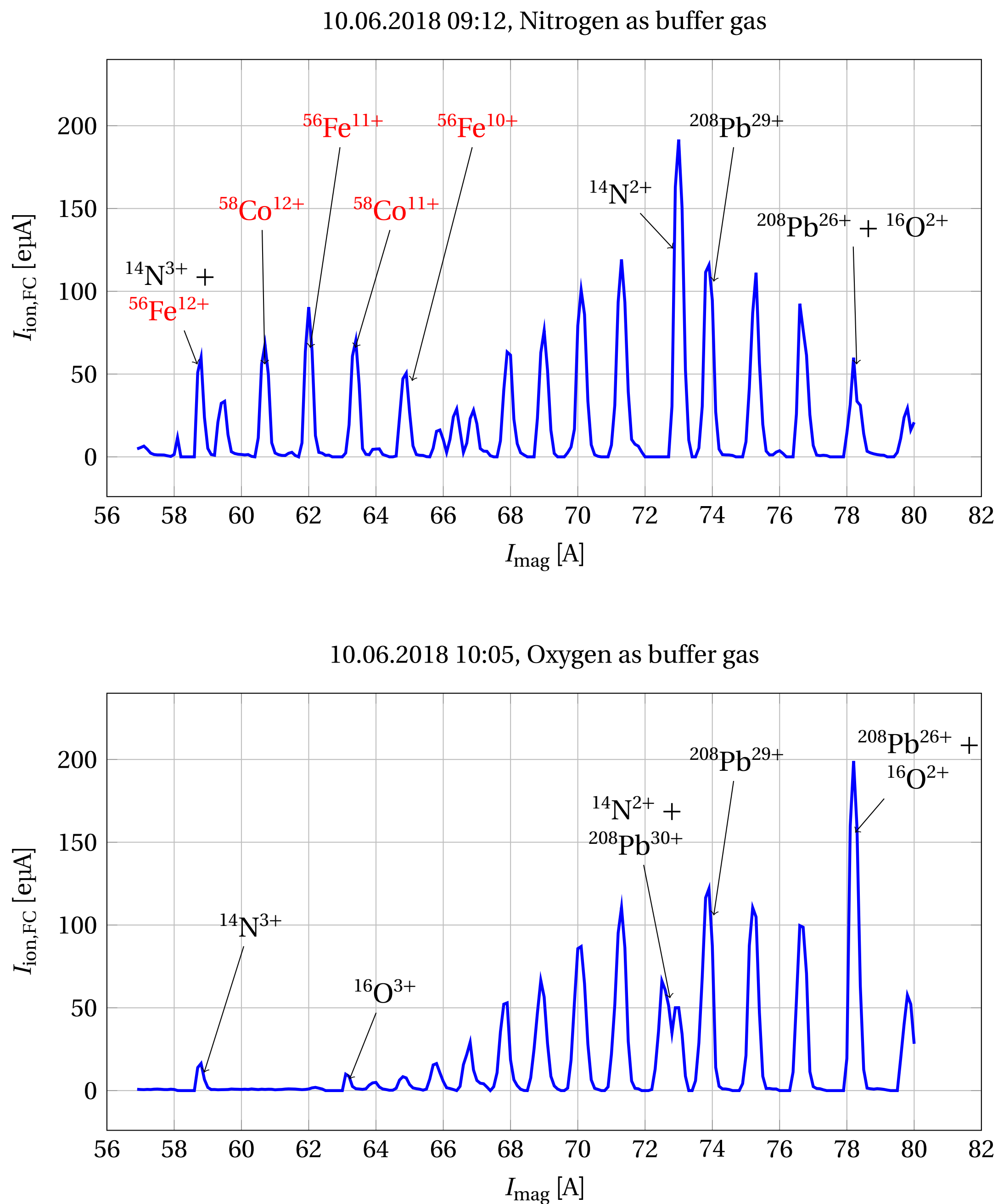

Figure A.4.: Charge state distributions two days after the start of the test. The upper plot shows peaks of cobalt and iron ions. The lower plot shows the CSD after the injection was switched back to oxygen.

that the plasma chamber was sputtered and taking damages. It was therefore decided to abort the nitrogen injection and return to oxygen as a buffer gas. A new charge state distribution recorded less than one hour later, already with oxygen injection, showed that the iron and cobalt peaks had disappeared.

The CSD that is shown in figure A.5 was recorded on the following day, after around 24 h of source operation with oxygen as buffer gas.

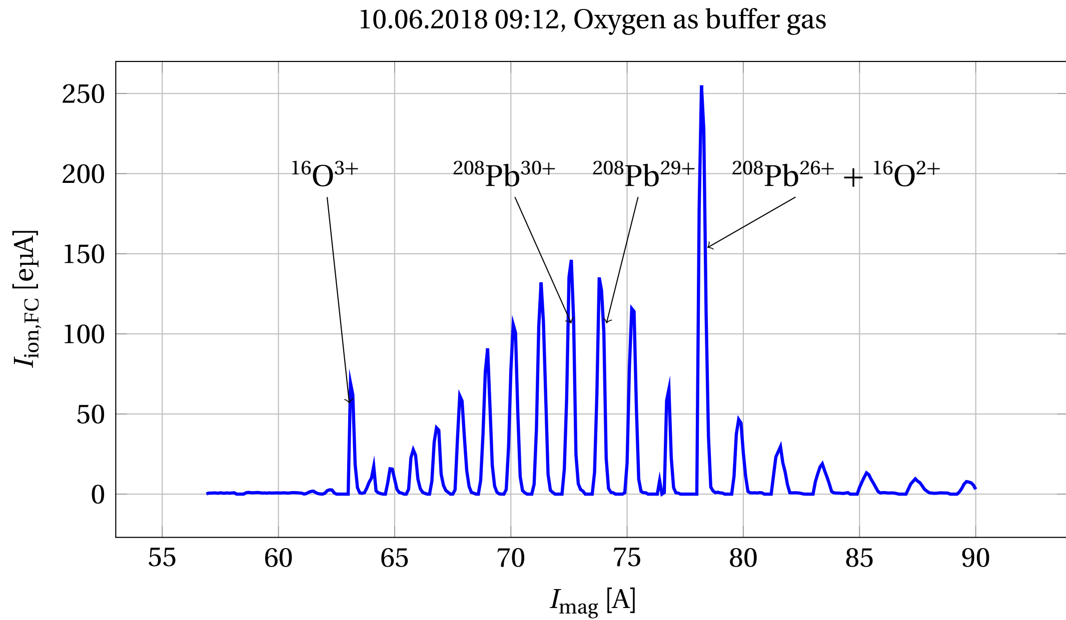

Figure A.5.: Charge state distribution recorded one day after the test was terminated.

No traces of iron, cobalt or nitrogen ions can be seen.

A.3. Discussion

The test demonstrates that oxygen as a buffer gas can not easily be replaced at the GTS-LHC ion source. Even though a plasma could be upheld with nitrogen injection, the source required more tuning and a reliable longterm operation could not be achieved. Additionally the recorded charge state distributions hint that during the nitrogen operation material from the plasma chamber and the ion source injection plug was sputtered into the source plasma.

The difference to the operation with oxygen might be explained by the chemical reactivity of oxygen. When oxygen forms an oxide layer inside the plasma chamber this layer might protect the chamber and possibly even have a positive effect on the plasma formation

itself.

These observations do not exclude the possibility of operating the GTS-LHC with nitrogen but to find the appropriate mode of operation (e.g. a gas mixture) would require a dedicated study that also accepts possible damage to the source.

B. Finite Elements Method

A typical task for a thermal analysis is to derive the temperature profile of several bodies with certain shapes and certain materials that transfer heat within them and between different bodies. The boundary conditions can dictate heat flux to these bodies through their surfaces or even heat production inside of them. This type of problem is a field problem, where the solution to a given differential equation is a scalar field. Here the field value is the temperature which depends on the position in space. The method of finite elements offers a way to find an approximate solution to the field problem by breaking down the geometry into simpler elements. Within each of these elements a linear combination of known approach functions can be used to describe the field approximately. The boundary conditions dictate the coefficients of the linear combination of these functions. They depend on the nodes of the element which are connection points to the surrounding elements or to the boundary of the system.

B.1. Example for the FEM

In the following a simple example shall sketch some aspects of the FEM method and its different steps. It is oriented on examples given in [81].

The problem A simple heat flow problem is used to show the different steps of an FEM analysis. The geometry shall be a long rod of length L and constant cross sectional area A consisting of two parts of individual material (with individual thermal conductivities k_1 and k_2), each part of length l. The contact between the two materials is assumed to be perfectly conducting, i.e. no sudden temperature step exists between these two parts. The rod is assumed to be perfectly thermally insulated on the walls, except at its two ends, which allows heat flux only in the longitudinal direction. Also assuming that the temperature at its ends is homogenous over the cross section, the equilibrium temperature $T(x)$ along its longitudinal axis $0 < x < L$ shall be calculated, based on the boundary conditions, like temperature at one end $T_{x=0}$ and heat flux at the other end $q_{x=L}$. The upper part of figure

B.1 shows the geometry of the rod.

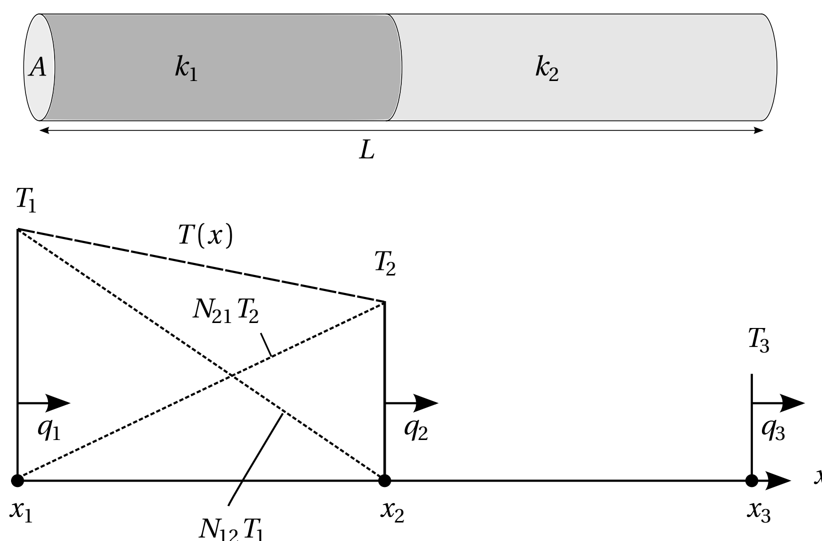

Figure B.1.: Example for a heat conduction problem. The upper part shows the geometry while the lower part demonstrates the discretization into two elements for the FEM-Method.

Only looking at heat conduction from one side ($x = 0$) to the other ($x = L$) and assuming that no heat enters the rod by any internal process, the one dimensional heat equation reads [81]:

$$\frac{\mathrm{d}}{\mathrm{dx}}\left(Ak\frac{\mathrm{d}T}{\mathrm{dx}}\right) = 0 \ . \tag{B.1}$$

Step 1: Weak formulation of the differential equation The first step of the FEM is to reformulate the governing differential equation, here equation (B.1), into its weak form. The solutions to the weak formulation can be approximations of the functions that solve the strong formulation (B.1). To derive the weak formulation, test functions v are introduced such that:

$$\int_0^L v\left(\frac{\mathrm{d}}{\mathrm{dx}}\left(Ak\frac{\mathrm{d}T}{\mathrm{dx}}\right)\right)\mathrm{d}x = 0 \ . \tag{B.2}$$

This is a new differential equation and a solution $T(x)$ to this equation will not solve equation (B.1) (the term in the brackets is not always 0) but approximate it. This step is described in more detail in [81]. Integration by parts of equation (B.2) then yields the weak formulation of equation (B.1):

$$\int_0^L \frac{\mathrm{d}v}{\mathrm{dx}}Ak\frac{\mathrm{d}T}{\mathrm{dx}}\mathrm{d}x = \left[vAk\frac{\mathrm{d}T}{\mathrm{dx}}\right]_0^L \ . \tag{B.3}$$

The square brackets around the right hand term here indicate that the term inside the brackets is used to calculate the difference between inserting $x = L$ and $x = 0$.

The weak form (equation (B.3)) does not include the second derivative of T and additionally the requirements for the solutions are less strict, which allows discontinuous solutions. This makes the following discretization of the solution possible.

Step 2: Discretization In this step the geometry is broken down into several elements, connected with nodes. Each element is a subsystem of the larger geometry and the nodes are the connection points that define the boundary conditions for the field inside of the element.

In the described case the elements are one dimensional in space and enclosed by a node at each endpoint of the element. The elements in the example case are chosen to span over the areas with constant thermal conductivity, so two elements are needed. On the nodes the element has certain degrees of freedom, here temperature values T_i. The field within each element is then described by a superposition of shape functions (here N) multiplied with its nodal values. In the described case a possible shape function is a linear slope between the two nodes. For an element enclosed by the values x_i and x_j the two shape functions then read:

$$N(x)_{ij} = \frac{x - x_i}{x_j - x_i} \quad \text{and} \quad N(x)_{ji} = -\frac{x_j - x}{x_j - x_i} \quad . \tag{B.4}$$

The temperature field of the one dimensional element can be expressed as a superposition of these functions:

$$T(x) = \frac{x - x_i}{x_j - x_i} T_j + \frac{x_j - x}{x_j - x_i} T_i \quad . \tag{B.5}$$

In a more general form the temperature field is the product of the shape function vector $\mathbf{N}$ and a vector containing the nodal values $\mathbf{a}$, making it $T(x) = \mathbf{Na}$. Formulating the temperature field as a vector product of the shape functions and the nodal values and inserting it into the weak formulation of the governing differential equation (equation (B.3)), it is possible to transform the problem into an algebraic form.

$$\mathbf{Ka} = \mathbf{f} \quad , \tag{B.6}$$

where $\mathbf{K}$ is called the stiffness matrix, $\mathbf{a}$ a vector containing all nodal values, and $\mathbf{f}$ a vector containing the boundary conditions and loads, like heat flow and inner heat generation. To

find the matrix **K** that follows from the weak form of the differential equation like equation (B.3) together with the chosen shape functions and the nodes and element geometries, several methods exist, where the most frequently used ones are the Garlerkin method and the variation method (Both described by G. Comini in [81]). In this description the step will be skipped and only the result for the given shape functions is presented. The matrix form can also be formulated for a single element, in the example case it is:

$$\frac{Ak_e}{x_j - x_i}\begin{bmatrix} 1 & -1 \\ -1 & 1 \end{bmatrix}\begin{bmatrix} T_i \\ T_j \end{bmatrix} = -A\begin{bmatrix} q_i \\ -q_j \end{bmatrix}. \tag{B.7}$$

Here q_i are the nodal heat fluxes, with $q = -k\frac{\mathrm{d}T}{\mathrm{d}x}$ at the position of the nodes. In the example case the stiffness matrix reads the same for both elements, but this is not generally the case. The stiffness matrix **K** of the complete problem can then be assembled from the single element matrices. Here one needs to take into account that the elements share nodes and hence the nodal values are the same. When assuming that both elements have the same length $x_2 - x_1 = x_3 - x_2 = l$, the same section A but individual thermal conductivity, k_1 and k_2 the resulting equation reads:

$$\frac{A}{l}\begin{bmatrix} k_1 & -k_1 & 0 \\ -k_1 & k_1 + k_2 & -k_2 \\ 0 & -k_2 & k_2 \end{bmatrix}\begin{bmatrix} T_1 \\ T_2 \\ T_3 \end{bmatrix} = -A\begin{bmatrix} q_1 \\ 0 \\ q_3 \end{bmatrix}. \tag{B.8}$$

Step 3: Solving the equation Now the boundary conditions can be inserted to make it a solvable system of equations. In the example at least two additional boundary conditions are needed, e.g. $T_1 = T_{x=0}$ and $q_3 = k_2 \left.\frac{\mathrm{d}T}{\mathrm{d}x}\right|_{x=L}$. If all T_i are calculated they can be used in equation (B.5) to calculate the temperature at every value of x and following from the temperature also the heat flow.

B.2. Non linear systems

As described above the FEM relies on discretizing a field problem by introducing a stiffness matrix that describes the reaction of the system to the boundary conditions. A simple and linear example for such a matrix was given above. However in realistic thermal systems in many cases the heat transport depends on the temperature of the bodies themselves. This leads to a non linear stiffness matrix that depends on the temperature values, $\mathbf{K}(\mathbf{a})$. For example heat conductivities may depend on the temperature and also the heat transport

via radiation is heavily depending on the body temperature. A strategy to solve these kind of problems is an iterative process based on the Newton Rhapson method [82]:

- Calculate the stiffness matrix, $\mathbf{K}_1$, with a given starting temperature field, $\mathbf{a}_{\text{start}}$: $\mathbf{K}_1 = \mathbf{K}(\mathbf{a}_{\text{start}})$.
- Apply the loads, like defined temperatures, heat generation and heat flows , $\mathbf{f}_{\text{des}}$, and derive the temperature field, $\mathbf{a}_1$: $\mathbf{f}_{\text{des}} = \mathbf{K}_1\mathbf{a}_1$.
- Use the temperature field $\mathbf{a}_1$ to create a new stiffness matrix, $\mathbf{K}(\mathbf{a}_1)$, and calculate all loads, $\mathbf{f}_1$, from it: $\mathbf{f}_1 = \mathbf{K}(\mathbf{a}_1)\mathbf{a}_1$.
- If $\mathbf{f}_{\text{des}} - \mathbf{f}_1 >$ Limit, then use $\mathbf{K}(\mathbf{a}_1)$ with the desired loads $\mathbf{f}_{\text{des}}$ to derive a new temperature field, $\mathbf{a}_2$, for the next iteration.

The chance to achieve convergence enhances when the starting temperature field is not too different from the one resulting from the applied loads. Therefore it helps the convergence to apply loads like heat generation stepwise and use the results from the previous analysis as a basis for a new iteration.

List of Symbols and Abbreviations

Symbols

Chapter 1	
n	A density value
$\mathrm{IR}_{i,j}$	The reaction rate of single electron impact ionization
$\mathrm{RR}_{i,j}$	the reaction rate of radiative recombination
$\tau_{\mathrm{ion},j}$	Ion confinement time in a plasma
e^-	Symbol for an electron
A^{n+}	Atom or ion of charge n
γ	Symbol for a photon
$\mathbf{F}_\mathrm{L}$	The Lorentz force
$\mathbf{E}$	An electric field
$\mathbf{B}$	A magnetic field
q_e	The charge of an electron
$\mathbf{v}_\mathrm{e}$	The velocity of an electron
$\mathbf{e}_1$, $\mathbf{e}_2$ and $\mathbf{e}_3$	The Euclidean unit vectors
$v_\parallel$	Velocity component parallel to a magnetic field
$v_\perp$	Velocity component perpendicular to a magnetic field
E_e	Energy of an electron
m_e	Mass of an electron
μ_e	Magnetic moment of the gyration in a magnetic field
R_mag	The magnetic mirror ratio
ω_C	The cyclotron frequency
ω_rf	A microwave frequency
ω_p	The plasma frequency

Chapter 2	

p_v	The vapour pressure
p	A pressure value
R_{gas}	The gas constant
ΔH_{vap}	The enthalpy of vaporization
T	Temperature values
A_{Pb} and B_{Pb}	Measured coefficients for the vapour pressure of lead
J	A particle flux density
m	Mass of a particle
k_{B}	the Boltzmann constant
J_{cond}	The fraction of particles, that condensate when they are hitting the liquid phase
α	The evaporation coefficient
Kn	The Knudsen number
λ	Mean free path of a gas particle
l	Characteristic length of a gas containing system
σ	Cross sectional size of a particle
d	Molecule or atom diameter
θ	An angle
R	An evaporation rate
a and b	Surface areas
d	A distance
x	A distance as shown in figure 3.10
$\mathbf{q}$	The heat flux density vector
$k_{\text{therm.}}$	A bodies thermal conductivity
∇	The nabla operator
P	Power values
ϵ	A bodies emissivity
σ_{B}	The Stefan-Boltzmann constant
A_{surf}	The surface of a body
Q	A heat value
$\mathfrak{F}_{1-2}$	A viewfactor
V	A volume
$a_{\text{cond.2D}}$	Surface area of the conductors in 2D
$r_{\text{rot.}}$	Distance of the surface centre to the symmetry axis

h_{3D} and h_{2D}	Internal heat generation of the conductors in the ANSYS simulation
Chapter 3	
t	A time value
A	Calibration factor for the deposition to evaporation rate conversion
ΔM	Weight change of the crucible over a measurement
I	Integral in equation (4.13)
ρ_{Pb}	Density of lead
c	Detector surface area
Chapter 4	
a_1, b_2, b_3, t_1 and t_2	Fit parameters for the power-time model
r	The oven resistance
H	The Heaviside step function
$\lvert r'_{neg}\rvert$	Negative time derivation of the resistance
$x_{sol.}$	The molar fraction of a solvent
Appendix A	
I	A current value
Appendix B	
L	A length
q	A heat flux
A	Cross sectional area of a body
v	Test functions in the weak formulation of a differential equation
$\mathbf{N}$	Shape functions (vector)
$\mathbf{K}$	The stiffness matrix
$\mathbf{f}$	A vector containing the boundary conditions and loads
$\mathbf{K}_1$	A stiffens Matrix
$\mathbf{a}$	A temperature field
$\mathbf{f}$	A load vector

Abbreviations

CERN	Conseil europeen pour la recherche nucleaire, now European Organization for Nuclear Research
LHC	Large Hadron Collider
AD	Antiproton Decelerator
ELENA	Extra Low ENergy Antiproton ring
SPS	Super Proton Synchrotron
PS	Proton Synchrotron
GTS-LHC	A name referring to Grenoble Test Source and Large Hadron Collider
LEIR	Low Energy Ion Ring
ALICE	A Large Ion Collider Experiment
CEA	Commissariat à l'Énergie atomique
ECRIS	Electron Cyclotron Resonance Ion Source
MHD	Magneto Hydro Dynamics
ECR4	Name derived from ECRIS
CAD	Computer Aided Design
FEM	Finite Element Method
OTS	Oven Test Stand
TC	Thermocouple
PLC	Programable Logic Controller
PC	Personal Computer
CALS	CERN Accelerator Logging Service

Bibliography

[1] The official website of CERN. `https://home.cern.ch`, accessed 2019-10-10.

[2] Tommy Eriksson et al. ELENA - From Installation to Commissioning. In *Proceedings, 8th International Particle Accelerator Conference (IPAC 2017): Copenhagen, Denmark, May 14-19, 2017*, page WEPVA034, 2017.

[3] Davide Gamba, Christian Carli, Tommy Eriksson, Laurette Ponce, and Gerard Tranquille. ELENA Commissioning. In *12th Workshop on Beam Cooling and Related Topics (COOL'19), Novosibirsk, Russia, 23-27 September 2019*, pages 52–54. JACOW Publishing, Geneva, Switzerland, 2019.

[4] Augusto Ceccucci, F Ambrosino, G Anelli, A Antonelli, , M Losasso, et al. Proposal to measure the rare decay $K^+ \to \pi^+ \nu \bar{\nu}$ at the CERN SPS. Technical Report CERN-SPSC-2005-013. SPSC-P-326, CERN, Geneva, Apr 2005.

[5] G. Aad, T. Abajyan, B. Abbott, J. Abdallah, S. Abdel Khalek, et al. Observation of a new particle in the search for the Standard Model Higgs boson with the ATLAS detector at the LHC. *Physics Letters B*, 716(1):1 – 29, 2012.

[6] S. Chatrchyan, V. Khachatryan, A.M. Sirunyan, A. Tumasyan, W. Adam, et al. Observation of a new boson at a mass of 125 GeV with the CMS experiment at the LHC. *Physics Letters B*, 716(1):30 – 61, 2012.

[7] B. Abelev, J. Adam, D. Adamová, A. M. Adare, M. M. Aggarwal, G. Aglieri Rinella, A. G. Agocs, A. Agostinelli, S. Aguilar Salazar, Z. Ahammed, and et al. Net-Charge Fluctuations in Pb-Pb Collisions at $\sqrt{s_{\mathrm{NN}}} = 2.76$TeV. *Physical Review Letters*, 110(15), Apr 2013.

[8] R Alkofer and J Greensite. Quark confinement: the hard problem of hadron physics. *Journal of Physics G: Nuclear and Particle Physics*, 34(7):S3S21, May 2007.

[9] S A Bass, M Gyulassy, H Stöcker, and W Greiner. Signatures of quark-gluon plasma formation in high energy heavy-ion collisions: a critical review. *Journal of Physics G: Nuclear and Particle Physics*, 25(3):R1R57, Jan 1999.

[10] N Angert, M P Bourgarel, Etienne Brouzet, R Cappi, Daniel Dekkers, John Evans, Giovanni Gelato, H Haseroth, Charles E Hill, G Hutter, Jürgen E Knott, Hartmut Kugler, A M Lombardi, Hans Dieter Lustig, E Malwitz, Fritz Nitsch, G Parisi, A Pisent, Ulrich Raich, U Ratzinger, Lodovico Riccati, A Schempp, Karlheinz Schindl, Horst Otto Schönauer, Pierre Têtu, Hans Horst Umstätter, M Van Rooij, David J Warner, and Mario Weiss. *CERN heavy-ion facility design report.* CERN Yellow Reports: Monographs. CERN, Geneva, 1993.

[11] Django Manglunki, Maria Elena Angoletta, Jerome Axensalva, Giulia Bellodi, Alfred Blas, Michael Bodendorfer, Thomas Bohl, Stephane Cettour-Cave, Karel Cornelis, Heiko Damerau, Ilias Efthymiopoulos, Adrian Fabich, Jose Ferreira Somoza, Alan Findlay, Pierre Freyermuth, Simone Gilardoni, Steven Hancock, Eva Barbara Holzer, Steen Jensen, Verena Kain, Detlef Küchler, Alessandra Lombardi, Alice Michet, Michael O'Neil, Sergio Pasinelli, Richard Scrivens, Rende Steerenberg, and Gerard Tranquille. CERN's Fixed Target Primary Ion Programme. (CERN-ACC-2016-275):TUPMR027. 4 p, 2016.

[12] Yves Schutz. Heavy-ion physics at LHC. *Journal of Physics G: Nuclear and Particle Physics*, 30(8):S903–S909, jul 2004.

[13] Hannes Bartosik, Simon Albright, Julie Coupard, Malika Meddahi, Heiko Damerau, Alexander Huschauer, Richard Scrivens, Maria Elena Angoletta, Klaus Hanke, Elena Shaposhnikova, et al. The LHC injectors upgrade (LIU) project at CERN: ion injector chain. 2017.

[14] John Jowett et al. The 2018 heavy-ion run of the LHC. In *Proceedings, 10th International Particle Accelerator Conference (IPAC2019): Melbourne, Australia, May 19-24, 2019*, 2019.

[15] Reyes Alemany-Fernández, Simon Albright, Maria Elena Angoletta, Jerome Axensalva, et al. Performance of the CERN Injector Complex and Transmission Studies into the LHC during the Second Proton-Lead Run. (CERN-ACC-2017-155):TUPVA128. 4 p, 2017.

[16] C E Hill, D Küchler, R Scrivens, D Hitz, L Guillemet, R Leroy, and J Y Pacquet. GTS-LHC: A New Source For The LHC Ion Injector Chain. *AIP Conf. Proc.*, 749(LHC-Project-Report-800. CERN-LHC-Project-Report-800):127–130. 4 p, Sep 2004.

[17] A Beuret, J Borburgh, A Blas, H Burkhardt, Christian Carli, M Chanel, A Fowler, M Gourber-Pace, S Hancock, M Hourican, C E Hill, John M Jowett, K Kahle, D Küchler, A M Lombardi, E Mahner, Django Manglunki, M Martini, S Maury, F Pedersen, U Raich, C Rossi, J P Royer, Karlheinz Schindl, R Scrivens, L Sermeus, Elena Shaposhnikova, G Tranquille, Maurizio Vretenar, and T Zickler. The LHC Lead Injector Chain. (LHC-Project-Report-776. CERN-LHC-Project-Report-776):4 p, Aug 2004.

[18] D. Hitz, A. Girard, K. Serebrennikov, G. Melin, D. Cormier, J. M. Mathonnet, J. Chartier, L. Sun, J. P. Briand, and M. Benhachoum. Production of highly charged ion beams with the Grenoble test electron cyclotron resonance ion source (plenary). *Review of Scientific Instruments*, 75(5):1403–1406, 2004.

[19] R. Geller. *Electron Cyclotron Resonance Ion Sources and ECR Plasmas*. Taylor & Francis, 1996.

[20] Denis Hitz. Recent progress in high frequency electron cyclotron resonance ion sources. *Advances in imaging and electron physics*, 144(1):1–163.

[21] Francis F Chen. *Introduction to plasma physics and controlled fusion*, volume 1. Springer, 1984.

[22] M Bodendorfer, P Wurz, and M Hohl. Global plasma simulation of charge state distribution inside a 2.45 GHz ECR plasma with experimental verification. *Plasma Sources Science and Technology*, 19(4):045024, 2010.

[23] Joseph John Thomson. XLII. Ionization by moving electrified particles. *The London, Edinburgh, and Dublin Philosophical Magazine and Journal of Science*, 23(136):449–457, 1912.

[24] A. Girard, D. Hitz, G. Melin, and K. Serebrennikov. Electron cyclotron resonance plasmas and electron cyclotron resonance ion sources: Physics and technology (invited). *Review of Scientific Instruments*, 75(5):1381–1388, 2004.

[25] Wolfgang Lotz. Electron-impact ionization cross-sections and ionization rate coefficients for atoms and ions from hydrogen to calcium. *Zeitschrift für Physik*, 216(3):241–247, 1968.

[26] David Hugh Crandall. Electron impact ionization of multicharged ions. *Physica Scripta*, 23(2):153, 1981.

[27] Peter F Lang and Barry C Smith. Ionization energies of atoms and atomic ions. *Journal of chemical education*, 80(8):938, 2003.

[28] H. A. Kramers. XCIII. On the theory of X-ray absorption and of the continuous X-ray spectrum. *The London, Edinburgh, and Dublin Philosophical Magazine and Journal of Science*, 46(275):836–871, 1923.

[29] Igor A Kotelnikov and Alexander I Milstein. Electron radiative recombination with a hydrogen-like ion. *Physica Scripta*, 94(5):055403, 2019.

[30] Hendrik Antoon Lorentz. *Versuch einer Theorie der electrischen und optischen Erscheinungen in bewegten Körpern*. E. J. Brill, 1895.

[31] Irving Langmuir. Oscillations in ionized gases. *Proceedings of the National Academy of Sciences of the United States of America*, 14(8):627, 1928.

[32] S. Gammino and G. Caviola. ECR ion sources and scaling laws. *Proceedings of the 14th International Conference on Cyclotrons and their Applications*, 1995.

[33] G Castro, D Mascali, S Gammino, G Torrisi, et al. Overdense plasma generation in a compact ion source. *Plasma Sources Science and Technology*, 26(5):055019, apr 2017.

[34] AG Drentje. Techniques and mechanisms applied in electron cyclotron resonance sources for highly charged ions. *Review of Scientific Instruments*, 74(5):2631–2645, 2003.

[35] G D Shirkov. A classical model of ion confinement and losses in ECR ion sources. *Plasma Sources Science and Technology*, 2(4):250–257, nov 1993.

[36] V Mironov, S Bogomolov, A Bondarchenko, A Efremov, and V Loginov. Numerical simulations of gas mixing effect in electron cyclotron resonance ion sources. *Physical Review Accelerators and Beams*, 20(1):013402, 2017.

[37] H.W. Zhao, A.A. Efremov, and V.B. Kutner. Numerical study on the gas mixing effect in ECR ion sources. *Nuclear Instruments and Methods in Physics Research Section B: Beam Interactions with Materials and Atoms*, 98(1):545 – 548, 1995. The Physics of Highly Charged Ions.

[38] C. Andresen, J. Chamings, V. Coco, C. E. Hill, D. Küchler, A. Lombardi, E. Sargsyan, and R. Scrivens. Characterisation And Performance Of The CERN ECR4 Ion Source. *AIP Conference Proceedings*, 749(1):161–164, 2005.

[39] Detlef Küchler. personal communication.

[40] John Dalton. Experimental essays on the constitution of mixed gases; on the force of steam or vapor from water and other liquids in different temperatures, both in a torricellian vacuum and in air; on evaporation and on the expansion of gases by heat. *Memoirs of the Literary and Philosophical Society of Manchester*, 5(2):535–602, 1802.

[41] Austin Chambers. *Modern vacuum physics*. Masters series in physics and astronomy. CRC Press, Boca Raton, FL, 2005.

[42] Yunus A Cengel and Michael A Boles. *Thermodynamics: an engineering approach; 5th ed.* McGraw-Hill, 2004.

[43] D.R. Lide. *CRC Handbook of Chemistry and Physics, 84th Edition*. Taylor & Francis, 2003.

[44] C. B. Alcock, V. P. Itkin, and M. K. Horrigan. Vapour Pressure Equations for the Metallic Elements: 2982500K. *Canadian Metallurgical Quarterly*, 23(3):309–313, 1984.

[45] Jafar Safarian and Thorvald A. Engh. Vacuum evaporation of pure metals. *Metallurgical and Materials Transactions A*, 44(2):747–753, Feb 2013.

[46] D.F. Heaney. Vacuum sintering. In Zhigang Zak Fang, editor, *Sintering of Advanced Materials*, Woodhead Publishing Series in Metals and Surface Engineering, pages 189 – 221. Woodhead Publishing, 2010.

[47] Dorothy Hoffman, Bawa Singh, and John H Thomas III. *Handbook of vacuum science and technology*. Elsevier, 1997.

[48] George Karniadakis, Ali Beskok, and Narayan Aluru. *Microflows and nanoflows: fundamentals and simulation*, volume 29. Springer Science & Business Media, 2006.

[49] The official MOLFLOW+ website. `https://molflow.web.cern.ch`, accessed 2018-07-31.

[50] Márton Ady. Monte carlo simulations of ultra high vacuum and synchrotron radiation for particle accelerators. page 195, 2016.

[51] The official ANSYS simulation tools website. `https://www.ansys.com`, accessed 2018-08-01.

[52] J González-Leal. Optical functionalities of dielectric material deposits obtained from a lambertian evaporation source. *Optics express*, 15:5451–9, 05 2007.

[53] Young I Cho, James P Hartnett, and Warren M Rohsenow. *Handbook of heat transfer; 3rd ed.* McGraw-Hill, New York, NY, 1998.

[54] Ludwig Boltzmann. Ableitung des Stefan'schen Gesetzes, betreffend die Abhängigkeit der Wärmestrahlung von der Temperatur aus der electromagnetischen Lichttheorie. *Annalen der Physik*, 258(6):291–294, 1884.

[55] C. Fichera, F. Carra, D. Küchler, and V. Toivanen. Numerical study of the thermal performance of the cern linac3 ion source miniature oven. *Nuclear Instruments and Methods in Physics Research Section A: Accelerators, Spectrometers, Detectors and Associated Equipment*, 901:21 – 31, 2018.

[56] W. Hemminger. Thermal conductivity of lead in the range 180 to 500C. *International Journal of Thermophysics*, 10(4):765–777, Jul 1989.

[57] B. Giordanengo, N. Benazzi, J. Vinckel, and L Gasser, Ji. Thermal conductivity of liquid metals and metallic alloys. *Journal of Non-Crystalline Solids*, s 250252:377383, 08 1999.

[58] Table of emissivity of various surfaces, Mikron, Mikron Vertretung Schweiz.

[59] M Quinn Brewster. *Thermal radiative transfer and properties*. John Wiley & Sons, 1992.

[60] Website of the CERN Engineering Data Management Service. `https://edms.cern.ch/`, accessed 2019-08-08.

[61] Information on high performance computing at CERN. `https://twiki.cern.ch/twiki/bin/view/ABPComputing/HpcCERN`, accessed 2019-12-08.

[62] The official Wolfram website. `https://www.wolfram.com`, accessed 2019-10-10.

[63] Siemens. *Siemens Simatic S7-300 Module Data Manual*, February 2013.

[64] R Billen and C Roderick. The LHC Logging Service: Capturing, storing and using time-series data for the world's largest scientific instrument. Technical Report AB-Note-2006-046. CERN-AB-Note-2006-046, CERN, Nov 2006.

[65] C Roderick, R Billen, and D Dinis Teixeira. Instrumentation Of The CERN Accelerator Logging Service: Ensuring Performance, Scalability, Maintenance And Diagnostics. *Conf. Proc.*, C111010(CERN-ATS-2011-208):THCHAUST06. 4 p, Oct 2011.

[66] A.W. Van Herwaarden and P.M. Sarro. Thermal sensors based on the seebeck effect. *Sensors and Actuators*, 10(3):321 – 346, 1986.

[67] Robert L Powell. *Thermocouple reference tables based on the IPTS-68.* Number 125. US National Bureau of Standards, 1974.

[68] EN DIN. 60584-1,(2014): Thermoelemente-Teil 1: Thermospannungen und Grenzabweichungen.

[69] The official INFICON website. `https://www.inficon.com`, accessed 2017-10-03.

[70] Donald M Mattox. *Handbook of physical vapor deposition (PVD) processing.* William Andrew, 2010.

[71] INFICON. *Operating Manual, SQM-160, Multi-Film Rate/Thickness Monitor*, 2012.

[72] Philliptech website on RC crystals and rate spike prevention. `https://www.philliptech.com/rc-crystals/`, accessed 2019-10-02.

[73] Ifan Hughes and Thomas Hase. *Measurements and their uncertainties: a practical guide to modern error analysis.* Oxford University Press, 2010.

[74] Mettler Toledo GmbH, CH-8606 Greifensee, Switzerland. *Operating instructions METTLER TOLEDO AG balances*, 2004.

[75] The official Nova Elements website. `https://www.novaelements.com`, accessed 2019-10-10.

[76] Homepage of the GSI. `https://www.gsi.de/start/aktuelles.htm`, accessed 2019-06-14.

[77] R. Lang, J. Bossler, H. Schulte, and K. Tinschert. Investigation of different oven types for sample evaporation in the caprice electron cyclotron resonance ion source. *Review of Scientific Instruments*, 71(2):651–653, 2000.

[78] FM Raoult. General law of the vapor pressure of solvents. *Comptes Rendus*, 104:1430–3, 1887.

[79] Henry Marshall Leicester and Herbert S Klickstein. *A Source Book in Chemistry, 1400-1900*, volume 5. Harvard University Press, 1952.

[80] L Dumas, C Hill, D Hitz, D Küchler, C Mastrostefano, M O'Neill, and R Scrivens. Operation of the GTS-LHC Source for the Hadron Injector at CERN. Technical Report LHC-PROJECT-Report-985. CERN-LHC-PROJECT-Report-985, CERN, Geneva, Jan 2007.

[81] G. Comini. *Finite Element Analysis In Heat Transfer: Basic Formulation & Linear Problems*. Series in Computational and Physical Processes in Mechanics and Thermal Sciences. Taylor & Francis, 1994.

[82] Klaus-Jürgen Bathe. *Finite element procedures*. Klaus-Jurgen Bathe, 2006.

Acknowledgements

- I would like to thank Dr. Detlef Küchler who supervised my work at CERN. Without him this work would not have been possible. Throughout my time at CERN he was always available to answer my many questions and his friendly persistence probably halved the time the writing of this thesis would have taken otherwise.

- For supervising my work from the university side I would like to express my gratitude to PD Dr. Bernhard Schmidt. He was one of the persons that started my fascination for particle accelerator technology and I could not imagine a more supportive remote supervision.

- For the assistance during my experimental work at the oven test stand I would like to thank Cristiano Mastrostefano, Francesco Di Lorenzo, Michael O'Neil and Sebastien Bertolo. Their friendliness, expertise and solution oriented support made the work at the oven test stand so much easier.

- For the introduction to the oven test stand and his friendly and reliable support during several conference contributions I would like to thank Dr. Ville Toivanen.

- I would like to thank Dr. Claudio Fichera for introducing me to the ANSYS thermal simulations.

- For the introduction to Molflow+ I would like to thank Dr. Roberto Kersevan and Dr. Marton Ady.

- The setup modifications for the oven were only possible because of the help of Didier Steyaert.

- Dr. Fredrik Wenander and Dr. Edgar Mahner together with Dr. Detlef Küchler made the Nitrogen Test at the GTS-LHC ion source possible and helped me to interpret the results.

- Dr. Alessandra Lombardi, as section leader of the Hadron Sources and Linacs team, always showed support for my project and welcomed me to the section warmheartedly.
- I would also like to thank all members of the BE-ABP-HSL section at CERN for integrating me into their team and showing interest and new ideas regarding my work.
- For giving me insights into the oven operation at the GSI and sharing their ideas and thoughts I would like to thank Ralf Lang and the Ion Sources team at the GSI in Darmstadt.
- For making the work enjoyable and for the many, more or less fruitful, discussions during coffee and lunch breaks I would like to thank Dr. Daniel Noll and Hannes Pahl.
- I would also like to thank my parents and my girlfriend for their support throughout the PhD project.

Eidesstattliche Versicherung

Hiermit versichere ich an Eides statt, die vorliegende Dissertationsschrift selbst verfasst und keine anderen als die angegebenen Hilfsmittel und Quellen benutzt zu haben.

Die eingereichte schriftliche Fassung entspricht der auf dem elektronischen Speichermedium.

Die Dissertation wurde in der vorgelegten oder einer ähnlichen Form nicht schon einmal in einem früheren Promotionsverfahren angenommen oder als ungenügend beurteilt.

Genf, den 21. Januar 2020

____

Toke Kövener